Electrical and spin switching effects in high-temperature superconducting devices

Aurélien Lagarrigue

université PARIS-SACLAY

Electrical and spin switching effects in high-temperature superconducting devices

Commutation résistive par effet de champs électriques et de spin dans des dispositifs à base de supraconducteurs à haute température critique

Thèse de doctorat de l'université Paris-Saclay

École doctorale n°564, physique en Île-de-France (PIF)
Spécialité de doctorat : Physique
Graduate School : Physique. Référent : Faculté des sciences d'Orsay

Thèse préparée dans l'unité de recherche
Unité Mixte de Physique CNRS/Thales (Université Paris-Saclay, CNRS, Thales),
sous la direction de **Javier VILLEGAS**, Directeur de recherche,
la co-direction de **Javier BRIATICO**, Directeur de recherche,
le co-encadrement de **Juan TRASTOY**, Ingénieur de recherche,
le co-encadrement de **Salvatore MESORACA**, Ingénieur de recherche,

Thèse soutenue à Palaiseau, le 23 Juin 2023, par

Aurélien LAGARRIGUE

Composition du Jury

Membres du jury avec voix délibérative

Marie POIRIER-QUINOT Professeure, Université Paris-Saclay	Présidente
Alain PAUTRAT Directeur de recherche, Université de Caen Normandie	Rapporteur & Examinateur
Anna PALAU Chargée de recherche (HDR), Institut de Ciencia de Materials de Barcelona	Rapporteur & Examinatrice
Carlos LEÓN Professeur, Universidad Complutense Madrid	Examinateur
Brigitte LERIDON Chargée de recherche (HDR), Sorbonne Université	Examinatrice

THESE DE DOCTORAT

NNT : 2023UPASP058

université PARIS-SACLAY

ÉCOLE DOCTORALE
Physique en Île-de-France (PIF)

Titre : Commutation résistive par effet de champs électriques et de spin dans des dispositifs à base de supraconducteurs à haute température critique

Mots clés : Supraconductivité, Cuprate, Manganite, Memristor, Vanne de spin, Magnétorésistance

Résumé :

Cette thèse porte sur l'étude de dispositifs à base d'oxydes supraconducteurs à haute température, dans lesquels un comportement de commutation de la supraconductivité est produit par application de champs électriques dans des structures de type transistor ou de champs magnétiques dans des vannes de spin.

$YBa_2Cu_3O_{7-x}$ (YBCO) est un cuprate supraconducteur à haute température critique (T_C) avec un diagramme de phase riche et complexe en fonction de la température et du dopage, dont la T_C dépend à la fois du désordre et de la stœchiométrie en oxygène. Un moyen possible pour contrôler sa teneur en oxygène est de déposer par-dessus un matériau réducteur et de profiter de la réaction chimique d'oxydoréduction se produisant spontanément à l'interface. Ce mécanisme est ici exploité dans un dispositif de type transistor dans lequel une grille en aluminium est placée sur un canal d'YBCO. Je démontre que l'application de tensions de grille permet de créer un mouvement d'ions oxygène entre les deux matériaux, produisant un effet memristor réversible et non volatile de la conductance à l'interface. De plus, le canal supraconducteur est affecté de manière irréversible par l'application de la tension de grille : la température critique diminue progressivement jusqu'à ce qu'un état isolant soit atteint. Je montre que cet effet est le résultat d'une migration d'oxygène activée thermiquement par effet Joule. Ces travaux ouvrent la voie à une nouvelle génération de dispositifs à commutation résistive basés sur une transition de phase supraconducteur-isolant activée électriquement.

Dans la deuxième partie, j'exploite l'interaction entre la supraconductivité et le ferromagnétisme, deux phénomènes généralement antagonistes du fait de l'incompatibilité de l'état singulet (spins opposés) des paires de Cooper et de la polarisation de spin induite par l'interaction d'échange ferromagnétique. Ces travaux sont réalisés dans des vannes de spin, qui consistent généralement en deux couches ferromagnétiques séparées par une fine couche d'un matériel non magnétique et sont caractérisées par un état de faible résistivité lorsque les aimantations sont parallèles (pointant dans la même direction) et un état de forte résistivité lorsque les aimantations sont antiparallèles (pointant dans des directions opposées). Dans cette thèse, j'étudie un type spécifique de dispositif vanne de spin, appelé vanne de spin supraconductrice (VSS), dans lequel la couche centrale est constituée d'un matériau supraconducteur. La magnétorésistance de dispositifs formés d'YBCO et de deux couches de manganites demi-métalliques $La_{1-x}Sr_xMnO_3$ (LSMO) ou $La_{1-x}Ca_xMnO_3$ (LCMO) est mesurée lors de l'application d'un champ magnétique orthogonal à la direction du courant. Je mets en évidence une inversion de la magnétorésistance d'un comportement positif vers un comportement négatif, caractérisée par un état faiblement résistif alors que les aimantations des couches ferromagnétiques sont dans la configuration antiparallèle. Cette inversion peut être déclenchée en faisant varier la température, en changeant le sens du courant ou en modifiant l'angle d'incidence du champ magnétique. Bien qu'un tel renversement de la magnétorésistance ait déjà été observé dans des VSS à base de supraconducteurs basse T_C, mon travail démontre non seulement la possibilité de concevoir des dispositifs similaires tout en utilisant des supraconducteurs haute T_C, mais introduit également de nouveaux mécanismes d'inversion, avec des applications potentielles pour les mémoires magnétiques cryogéniques.

université PARIS-SACLAY

ÉCOLE DOCTORALE
Physique en Île-de-France (PIF)

Title: Electrical and spin switching effects in high-temperature superconducting devices

Key words: Superconductivity, Cuprate, Manganite, Memristor, Spin valve, Magnetoresistance

Abstract:

This thesis focuses on the study of devices based on high-temperature superconducting oxides, in which a switching behaviour is produced by exploiting either electric fields in transistor-like structures, or magnetic fields in spin valve schemes.

$YBa_2Cu_3O_{7-x}$ (YBCO) is a high critical temperature (T_C) cuprate superconductor with a rich and complex temperature-doping phase diagram, whose T_C depends both on disorder and oxygen stoichiometry. One possible way to control its oxygen content is to deposit a reducing material on top of it and take advantage of the redox chemical reaction spontaneously occurring at the interface. This mechanism is exploited here in a transistor-like device in which an aluminum gate is placed on a YBCO channel. I demonstrate that application of gate voltages allows oxygen ions to be driven back and forth between the two materials, producing a reversible, non-volatile memristive switching of the interface's conductance. In addition, the superconducting channel is non-reversibly affected by the gating: upon increasing the gate voltage, the critical temperature gradually decreases until an insulating state is reached. I show that this effect is the result of a thermally activated migration of oxygen due to Joule dissipation. This work paves the way for a new generation of resistive switching devices based on an electrically driven superconductor-to-insulator phase transition.

In the second part, I exploit the interaction between superconductivity and ferromagnetism, two phenomena that are generally antagonistic due to the incompatibility of the singlet (opposite spins) Cooper pairing and exchange-field induced spin polarization. This is realized in spin valves, which usually consist of two ferromagnetic layers sandwiching a non-magnetic spacer and are characterized by a low-resistivity state when the two ferromagnetic layers' magnetizations are parallel (pointing in the same direction) and a high-resistivity state when they are antiparallel (pointing in opposite directions). In this thesis, I study a specific kind of spin valve device, called a superconducting spin valve (SSV), in which the spacer is made of a superconducting material. The magnetoresistance of SSV devices made from YBCO and the half-metallic manganites $La_{1-x}Sr_xMnO_3$ (LSMO) and $La_{1-x}Ca_xMnO_3$ (LCMO) is measured while applying an external in-plane magnetic field. I evidence the switching behavior from a positive to a superconducting spin valve effect, characterized by a low-resistive state while the magnetizations of the ferromagnetic layers are in the anti-parallel configuration. This switching mechanism can be triggered by varying the temperature, changing the reading current, or modifying the angle of incidence of the applied magnetic field. Although such a switching has been observed in low-temperature SSV before, my work not only demonstrates the possibility to engineer similar types of devices using cuprate superconductors but also introduces new trigger mechanisms, with potential applications for cryogenic magnetic memories.

Table of contents

Acknowlegments

The three years (almost four years!) that I spent in the Unité Mixte de Physique CNRS/Thales have been filled with so many great moments and memories with so many incredible people that I barely know where to start. But first, I would like to say that I feel lucky and honoured to have been able to obtain this PhD in the first place.

The story begins in Japan: I spent 6 months in Tokyo in 2019, for my master's last year internship, working with Prof. Yoshichika Otani in the Quantum Nano-Scale Magnetism Research team (RIKEN). At this point in my life (since I left high school/"Classes préparatoires", in fact), I knew I wanted to work as a researcher in physics and my mind was already set on finding a PhD in France. The first thing I did was to contact my former teachers from PHELMA and one of them answered and proposed a PhD (in non-linear optics) in Grenoble which I instantly accepted. I was really disappointed, three months later, when I found out that the funding for the PhD has been rejected and that I had to look for another PhD position from scratch. The saving hand came from Prof. Otani, who recommended me to some researchers at the Unité Mixte de Physique CNRS/Thales, which led to my first meeting with Javier V., Javier B. and Juan. I feel it is therefore appropriate to start by thanking Prof. Otani for his recommendation as I would not have obtained this PhD without him. With the benefice of hindsight, I am convinced that the rejection of the first PhD position was for the best: the Unité Mixte de Physique CNRS/Thales is by far the laboratory in which I learned the most, met the most interesting people and had the more fun.

Let me start by thanking all the "Supra Team" (past and present): Javier, Javier bis, Juan, Salvatore, Santiago, Ralph, Vincent, Kevin, Sarah, David, Carolina, Meghan and Hadi. I have so many amazing memories with all of you: the BBQs at Javier's place, conference trips (Chicago with David, Crete with Sarah), playing chess with Kevin (once a week!), drinking beers together etc… Also, thanks to Vincent, Carolina and David, for taking care of my cats when I was away ! A big thank you to Salvatore for teaching me so much during the first 6 months of my PhD on the clean room fabrication and the measurement of the superconducting spin valves. Finally, a big thank you to my four supervisors for their constant support during the thesis, the writing of the manuscript and the preparation for the oral presentation.

I had a lot of fun with the people that I shared the office with: Isabella, Santiago and Ralph, at the beginning, and then Hugo, Adrien, Emma, Oliver and Wafa. Although this office is a nightmare during summer due to unbearable temperatures, spending time in the lab was much easier thanks to you ! Also, I had the chance to be surrounded by amazing other PhD students that I spent a lot of good time with: Diane, Laurette, Yanis, Pauline, Enzo, Julien, Gaetan and Matthieu. In particular, I will remember the numerous game board nights that we had together.

I am really grateful to all the people that helped for the fabrication and characterization of the samples and devices. This work would not have been possible without all of you ! In particular, the team of Prof. Jacobo Santamaria, who provided some of the samples that I measured during my PhD. I really enjoyed the multiple discussions I had with Prof. Santamaria about my results, which helped a great deal in my physical understanding of the observed phenomena. A lot of thanks to Vincent, Florian and Sophie for the multiple magnetron sputtering depositions and Javier B., Anke and Santiago for the various pulsed laser depositions. A big thank you to Aymeric for his help with atomic force microscopy measurements and to Richard for measuring magnetization hysteresis loops for me.

I would like to thank the members of the Jury for agreeing to review my doctoral thesis, in particular Prof. Palau and Prof. Leon for coming all the way from Barcelona and Madrid, respectively,

and Prof. Pautrat and Prof. Palau for their reports, that helped me polishing the thesis manuscript and preparing for the oral defence.

Finally, I finish by thanking my family for their support during all these years. I am the only scientist in the family, and although none of them could even remember the title of the thesis (I think my mother asked me at least 50 times over these years), they were always present in difficult moments. Last but not least, the last four years would have been much more difficult and colourless without the presence of Nolwenn by my side. Thank you for everything: for being patient with me during the last six months of the PhD, which were really stressful, and for lighting up my life.

Thank you all !

Acronyms, symbols and physical constants

Acronym	Meaning	Page(s)
AC	Alternative current	-
AF	Antiferromagnet	50
AFM	Atomic force microscopy	69, 95
AP	Anti-parallel	-
ARPES	Angle-resolved photoemission spectroscopy	49
BCS	Bardeen-Cooper-Schrieffer	43
BTK	Blonder-Tinkham-Klapwijk	45, 59
CAR	Crossed Andreev reflection	130
CIP	Current-in-plane	127
CPP	Current-perpendicular-to-plane	127, 131
CMR	Colossal magnetoresistance	55, 142
CVD	Chemical vapor deposition	66
DC	Direct current	-
DMD	Digital micromirror device	71
DOS	Density of states	51
FFLO	Fulde-Ferrell-Larkin-Ovchinnikov	63
FM	Ferromagnet	-
GL	Ginzburg-Landau	41
GMR	Giant magnetoresistance	35, 123
HEMT	High electron mobility transistor	29
HTS	High-temperature superconductor	25, 46
JA	Jiles-Atherton	187
JJ	Josephson junction	25, 30
KA	Kim-Anderson	187
LCMO	$La_{1-x}Ca_xMnO_3$	55
LSMO	$La_{1-x}Sr_xMnO_3$	55
MBE	Molecular beam epitaxy	66
MEMS	Microelectrochemical switches	29
MR	Magnetoresistance	80
MRAM	Magnetoresistive random-access memory	37, 56
MRI	Magnetic resonance imaging	25
MTJ	Magnetic tunnel junction	56, 124
P	Parallel	-
PBCO	$PrBaCo_2O_{5+x}$	133
PEEM	Photoemission electron microscopy	57
PID	Proportional-integral-derivative	69
PLD	Pulsed laser deposition	66
RF	Radio frequency	-
RSFQ	Rapid single flux quantum	32
SCPW	Superconducting coplanar waveguide	29, 89
SIMS	Secondary ion mass spectrometer	73, 94, 134
SQUID	Superconducting quantum interference device	27

SSV	Superconducting spin valve	124
STO	$SrTiO_3$	67, 134
SVE	Spin valve effect	126
TEM	Transverse electromagnetic	90
TMR	Tunneling magnetoresistance	124, 148
UMR	Unité mixte de physique	-
XMCD	X-ray magnetic circular dichroism	57
YBCO	$YBa2Cu_3O_{7-x}$	47

Symbol	Quantity	Value / Unit
B	Magnetic induction	T
$B_C^{\pm}$	Positive and negative coercive fields	T
$B_S^{\pm}$	Positive and negative switching fields	T
c	Speed of light in vacuum	$3 \times 10^8\ m.s^{-1}$
e	Electron charge	$1.602 \times 10^{-19}\ C$
E	Electric field	$V.m^{-1}$
E_{ex}	Exchange energy	J
f	Frequency	Hz
G	Differential conductance	S
h	Planck constant	$6.626 \times 10^{-34}\ J.s$
ħ	Reduced Planck constant	$1.055 \times 10^{-34}\ J.s$
H	Magnetic field	$A.m^{-1}$
H_C	Superconducting critical magnetic field	$A.m^{-1}$
H_{C1}	Lower critical field	$A.m^{-1}$
H_{C2}	Upper critical field	$A.m^{-1}$
I_C	Superconducting critical current	A
j	Imaginary unit	-
J_C	Superconducting critical current density	$A.m^{-2}$
L_S	Surface inductance	H
m_e	Mass of the electron	9.11×10^{-31}
M	Magnetization	$A.m^{-1}$
n_s	Number of superconducting electrons	-
Q	Quality factor	-
R_S	Surface resistance	Ω
T_B	Superparamagnetic blocking temperature	K
t_C	Reduced critical temperature	-
T_C	Superconducting critical temperature	K
T_{Curie}	Curie temperature	K
v_F	Fermi velocity	$m.s^{-1}$
X_S	Surface reactance	Ω
Z_S	Surface impedance	Ω
Δ	Superconducting gap	eV
λ_L	London penetration depth	m
ξ	Superconducting coherence length	m
μ_0	Vacuum permeability	$H.m^{-1}$
π	Pi	3.14
ρ	Resistivity	$\Omega.m$
Φ_0	Magnetic flux quantum	$2.07 \times 10^{-15}\ Wb$
χ	Magnetic susceptibility	-
ω	Angular frequency	$rad.s^{-1}$

Résumé étendu en français

Commutation résistive par effet de champs électriques et de spin dans des dispositifs à base de supraconducteurs à haute température critique

1. Introduction et aperçu de la thèse

Le concept physique de supraconductivité, qui représente l'objet d'étude principal de cette thèse, fut découvert en 1911 par Heike Kamerlingh Onnes à la suite de travaux révolutionnaires sur la liquéfaction de l'hélium, permettant de refroidir un système physique jusque des températures cryogéniques jusqu'alors inatteignables ($4.13\ K$) [1]. Cet état condensé de la matière est caractérisé par la disparation totale et subite de la résistance en-dessous d'une température critique T_C qui est dépendante du matériau étudié. Ce phénomène est d'une importance capitale pour un grand nombre d'applications puisque l'absence de résistance électrique implique une drastique réduction des pertes énergétiques due à l'effet Joule (phénomènes thermiques), qui permet la réalisation de circuits électroniques à basse dissipation d'énergie. Une autre propriété essentielle des matériaux supraconducteurs est leur capacité d'exclusion totale d'un champ magnétique depuis l'intérieur du supraconducteur (aussi appelé effet Meissner ou encore diamagnétisme parfait), qui fut utilisé historiquement pour le développement de puissants électroaimants pouvant induire des champs magnétiques de plusieurs dizaines de Tesla à basses températures [2,3]. De nombreuses autres technologies peuvent bénéficier des propriétés des supraconducteurs (composants radiofréquences, neuromorphisme, magnétométrie, portes logiques, *etc*), et l'étude de certaines de ces applications est le sujet du premier chapitre (**« Motivations and technological challenges »**), dans le but de motiver les travaux de recherche de cette thèse.

D'une importance particulière dans le cadre de ce projet, les cuprates forment une remarquable famille de matériaux supraconducteurs à haute température critique et furent découverts en 1986 par Müller et Bednorz [4] en étudiant l'évolution de la résistance électrique d'une céramique de $Ba_xLa_{5-x}Cu_5O_{5(3-y)}$ à des températures cryogéniques. Les deux chercheurs furent récompensés par un prix Nobel en 1987 pour cette découverte qui marque le commencement de la course pour de nouveaux matériaux supraconducteurs ayant une T_C de plus en plus élevée, dans le but de découvrir un supraconducteur pouvant opérer à température ambiante. Les oxydes mixtes de baryum, de cuivre et d'yttrium (avec une formule chimique $YBa_2Cu_3O_{7-x}$, abrégée en YBCO) sont particulièrement étudiés dans la littérature depuis les années 80 pour leurs T_C supérieures à la température d'ébullition de l'azote liquide ($77\ K$) [5]. En effet, l'azote liquide est plus simple d'utilisation et moins couteux que l'hélium liquide, deux qualités qui rendent l'utilisation de YBCO adaptée dans des contextes industriels. De plus, ces matériaux peuvent être refroidis dans leur état supraconducteur en utilisant des cryostats beaucoup plus compacts (quelques dizaines de centimètres) avec des puissances de l'ordre de la dizaine de watt, ce qui ajoute à leur potentiel.

Le phénomène de supraconductivité fut un sujet de débat considérable dans le domaine de la physique théorique au cours du vingtième siècle dû à l'incapacité des modèles physique à prédire et quantifier son origine et ses conséquences. En 1962, Bardeen, Cooper et Schrieffer furent les premiers à développer une théorie globale expliquant l'origine microscopique de la supraconductivité à basse température critique [6]. Cette théorie se base sur le fait que des paires d'électrons liés (appelées paires de Cooper) sont générées à basse température par l'intermédiaire de l'interaction électron-phonon. L'état fondamental d'une paire de Cooper est constitué de deux électrons ayant des directions de spin opposées, que l'on nomme état singulet. Cette propriété rend la supraconductivité incompatible avec un fort champ magnétique ou une forte énergie d'échange, par exemple à l'interface avec un matériau ferromagnétique ayant une aimantation permanente. L'étude de la supraconductivité, du ferromagnétisme et de l'interaction entre ces deux états antagonistes est l'objet du second chapitre intitulé **« Theoretical concepts »**.

Cette thèse porte sur l'étude de dispositifs à base d'oxides supraconducteurs à haute température critique dont l'état résistif peut être modifié par effets de champ électrique ou de spin. En particulier, cette propriété de commutation est étudiée dans deux dispositifs spécifiques : des structures de type transistor (**Chapitre 4, « Electrochemical tuning of YBCO's superconducting properties »**) et des vannes de spin supraconductrices (**Chapitre 5, « Magnetic switching in superconducting spin valve structures »**). Ces dispositifs furent fabriqués en salle blanche dans le cadre de cette thèse via des techniques de dépôt (pulvérisation cathodique, ablation laser pulsé et évaporation sous vide), de lithographie optique et de gravure par faisceau ionique. La caractérisation des propriétés de transport électrique et magnétique fut réalisé dans des bâtis de mesure cryogéniques. Les descriptions des techniques de fabrication et des mesures de transport sont développées dans le troisième chapitre intitulé **« Experimental details »**.

2. Contrôle électro-chimique des propriétés supraconductrices de YBCO dans des dispositifs de type transistor

2.1. Introduction

Les cuprates sont extrêmement sensibles au taux de dopage et au désordre structurel, ce qui permet de modifier leurs propriétés de conduction électrique entre des caractères conducteurs, isolants, antiferromagnétiques et supraconducteurs via une modification du nombre de porteurs de charges, par exemple causée par une modification de la stœchiométrie en oxygène. Cette propriété est illustrée en **Fig. 0.1** [7,8], qui montre le diagramme de phase de YBCO en fonction de la température (axe y) et de la concentration de trous p (axe x), représentant le nombre de trous d'électron par atome de cuivre. Ainsi, le premier volet de cette thèse consiste à induire un mouvement d'ions oxygènes (ou, de façon équivalente, de lacunes d'oxygènes) dans la structure cristallographique de YBCO par application de champs électriques, ce qui permet de contrôler localement p dans le but de modifier *in-situ* les propriétés conductrices (et supraconductrices) d'une fine couche d'YBCO de quelques nanomètres.

Cette étude est effectuée dans un dispositif de type transistor (une illustration schématique de la structure est donnée en **Fig. 0.2**), caractérisé par trois terminaux distincts, nommés par analogie avec un transistor classique : la source (S), la grille (G) et le drain (D). La grille est constituée d'une fine

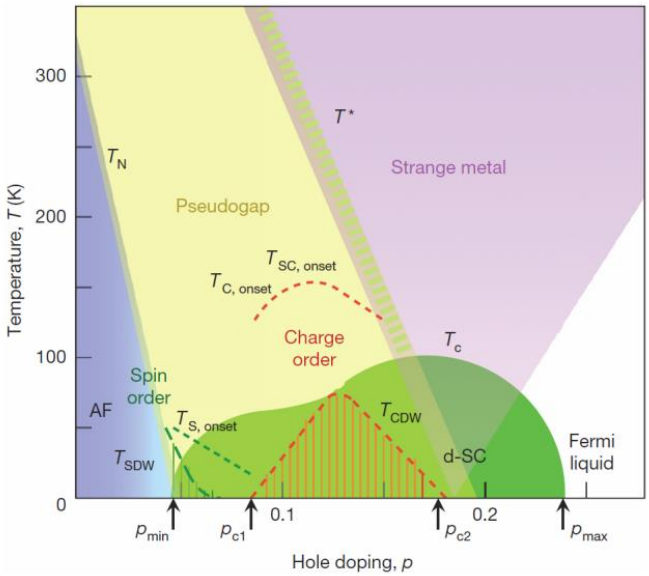

Fig. 0.1: Diagramme de phase de l'YBCO en fonction de la température et de la concentration de dopants p. Pour une température fixée, modifier p permet d'induire une transition de phase entre des comportements métalliques, supraconducteurs (zone verte) et isolants. Schéma provenant de Taillefer et al., Annu. Rev. Condens. Matter. Phys. (2010) [7,8].

couche d'aluminium (Al) et d'or (Au). Etant donné la différence importante entre les potentiels de réduction de l'aluminium et du cuivre [$\Delta E = E^{\circ}(Cu) - E^{\circ}(Al) = 2.4 - (-1.676) \approx 4.1\ eV$] [9], une réaction d'oxydo-réduction est naturellement attendue à l'interface entre ces deux éléments : une fine barrière d'oxide d'alumine AlO_x se forme alors qu'une région déplétée en oxygène apparait à l'intérieur de la couche d'YBCO [voir la zone rouge clair en **Fig. 0.2(a)** et **Fig. 0.2(b)**]. Ainsi, une barrière tunnel se développe du fait du caractère isolant de AlO_x [10] et de YBCO fortement désoxygéné [11]. L'idée principale de ce projet est donc d'inverser cette réaction chimique spontanée en appliquant une tension aux bornes de l'interface qui est supérieure à la différence entre les potentiels de réduction, permettant le contrôle du volume de la barrière isolante et le volume de la partie d'YBCO déplétée en oxygène. Le principe de fonctionnement est représenté schématiquement en **Fig. 0.2(c)**.

Les dispositifs étudiés lors de cette thèse possèdent une géométrie variable, avec les caractéristiques suivantes :

- Epaisseur du canal d'YBCO : $20\ nm < t_{YBCO} < 150\ nm$
- Epaisseur de la couche d'aluminium : $t_{Al} = 0\ nm$ (dispositif témoin), $t_{Al} = 2\ nm$ ou $t_{Al} = 10\ nm$
- Largeur de la grille : $W_{Al} = 5\ \mu m$ ou $W_{Al} = 60\ \mu m$

La caractérisation électrique est divisée en deux types de mesures. Dans un premier temps, une tension de grille V_G est appliquée entre les contacts G et D pour induire un mouvement de lacune d'oxygène à l'interface entre Al et YBCO comme expliqué précédemment [voir **Fig. 0.2(a)**] et symbolisé schématiquement par la zone rouge clair sous la couche d'aluminium. Dans un second temps, la résistance du canal d'YBCO est obtenue en appliquant un courant I_{SD} entre S et D et en mesurant la différence de potentiel V_{SD} aux mêmes bornes [voir **Fig. 0.2(b)**].

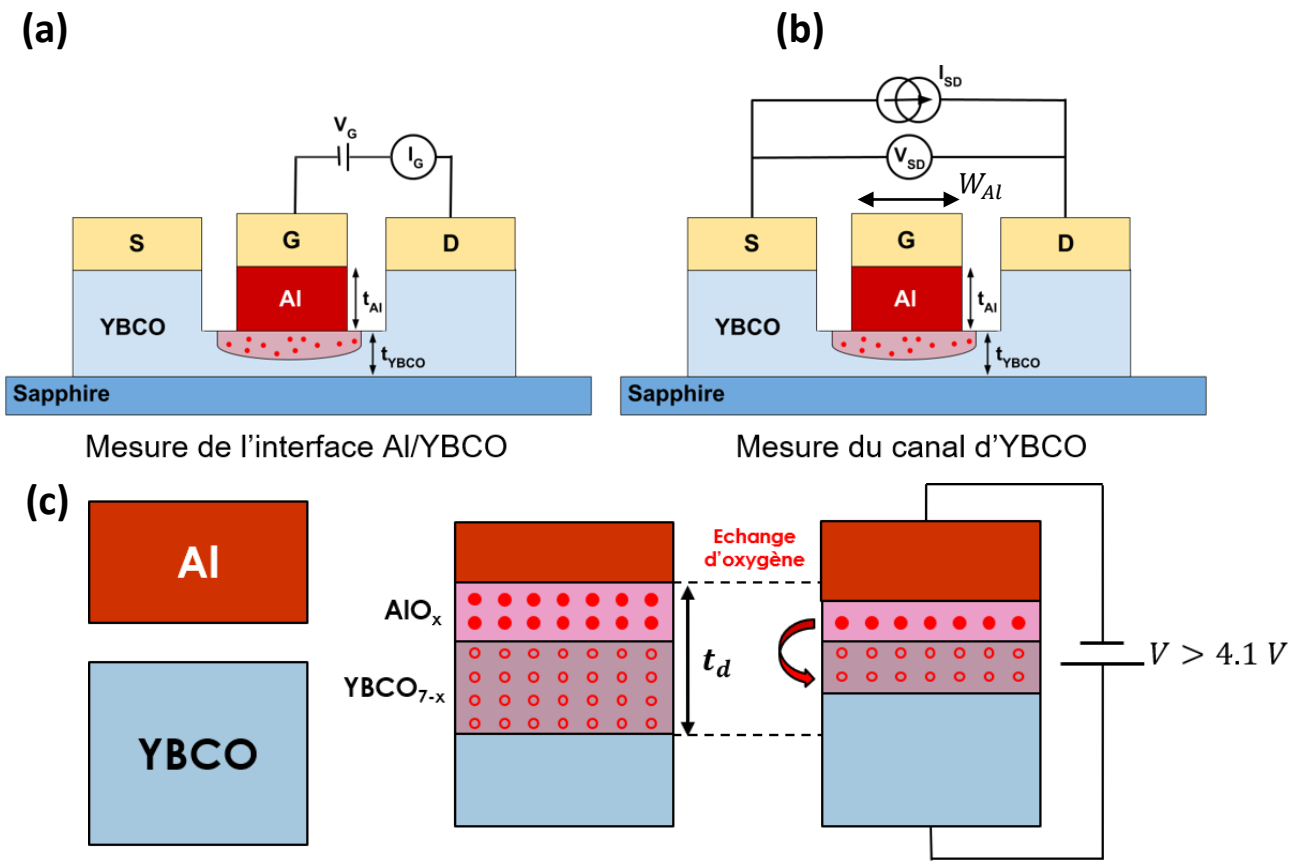

Fig. 0.2: Schéma des deux types de mesures effectuées lors de ce projet pour la caractérisation électrique de dispositif ayant une structure de type transistor. La caractérisation est divisée en deux types de mesures : (a) mesure de l'état à l'interface Al/YBCO, une tension de grille V_G est appliquée entre G et D et le courant est mesuré et (b) mesure de l'état du canal d'YBCO, un courant I_{SD} est appliqué entre S et D et la différence de potentiel est mesurée. (c) Principe de fonctionnement de la réaction d'oxydoréduction. Lorsque Al et YBCO entre en contact direct, une couche d'oxide d'alumine se développe naturellement à l'interface en pompant de l'oxygène de la structure d'YBCO, générant une fine couche (de quelques nanomètres) de barrière isolante. Ensuite, le volume de la barrière peut être contrôlé par application d'une tension qui est supérieure à la différence entre les potentiels de réduction de Al et Cu.

2.2. Comportement memristor de l'interface grille-drain

Pour étudier le comportement de l'interface Al/YBCO, une tension de grille $V_G(t)$ est appliquée entre G et D comme illustré en **Fig. 0.3(a)** : la tension est incrémentée jusqu'à une valeur maximale V_{write} (qui peut être positive ou négative) puis est ramenée à zéro en un temps t_G. La valeur maximale est appelée tension d'écriture V_{write} car, comme il sera démontré plus tard, une V_{write} suffisamment élevée permet de modifier de façon permanente et non-volatile l'état résistif de l'interface. Cette propriété est typique de systèmes memristors : la conductance du système est fonction de son histoire électrique, *i.e.* le niveau de conductance peut être modulé entre un état de forte conductance (aussi appelé état ON), un état de faible conductance (aussi appelé état OFF) ainsi que des états de conductance intermédiaires par application de champs électriques. Ces états sont non-volatiles (ils restent constants dans le temps et ne relaxent pas naturellement vers un état fondamental) pour des températures inférieures à $150\ K$, rendant ce type de dispositif particulièrement intéressant pour un grand nombre d'applications, par exemple en tant que mémoire configurable ou dans le domaine du neuromorphisme.

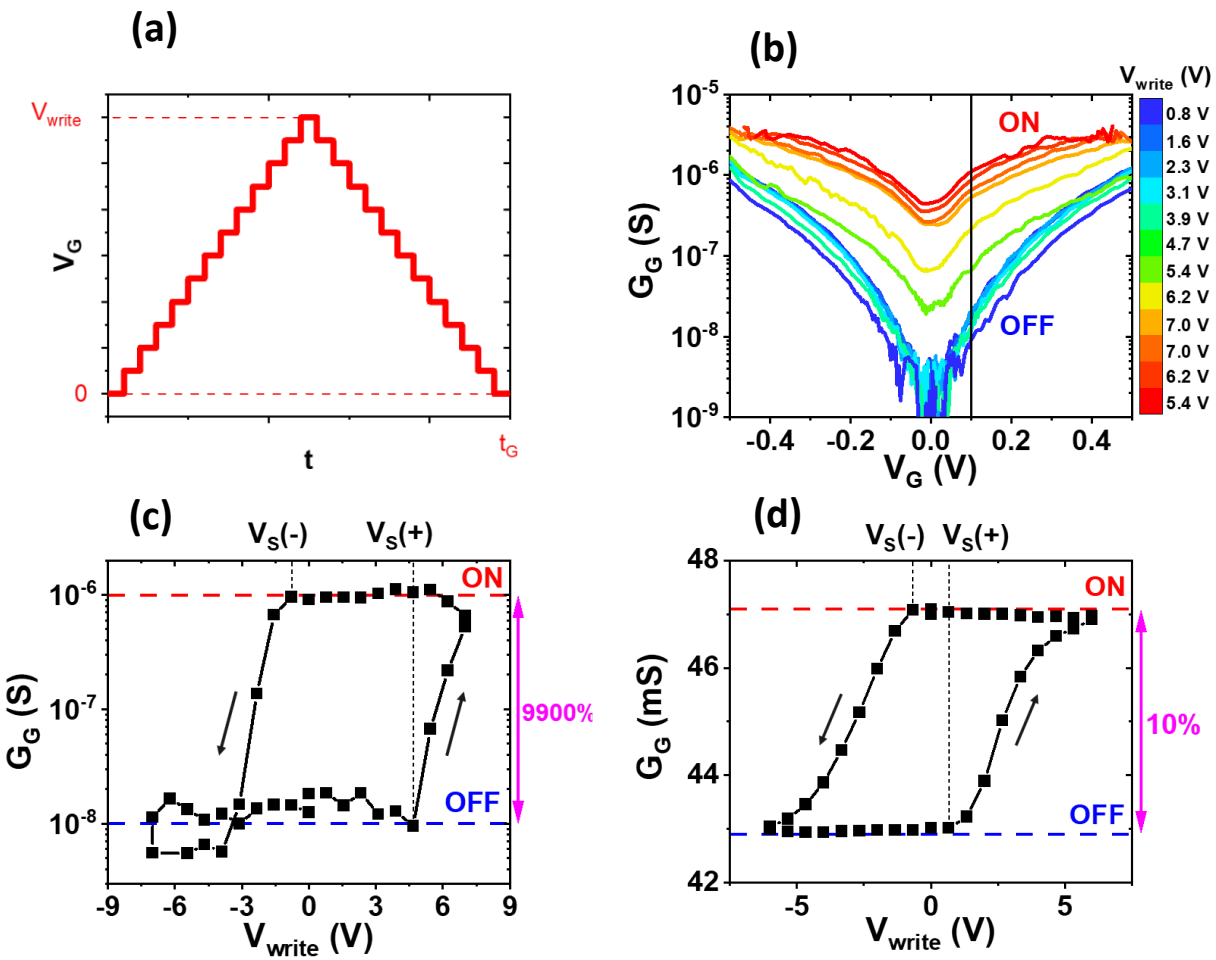

*Fig. 0.3: (a) Forme de $V_G(t)$ qui atteint un maximum V_{write} puis est ramenée vers zéro en un temps t_G. (b) G_G en fonction de V_G pour différentes valeurs de V_{write}. On peut voir une claire transition d'un état de faible conductivité OFF (courbe bleue) vers un état de forte conductivité ON (courbe rouge) en augmentant V_{write}. (c) Evolution de G_G en fonction de V_{write} montrant un effet de commutation memristor entre des états ON, OFF et intermédiaires sur une gamme de plus de deux ordres de grandeur. (d) Expérience identique à celle conduite en **Fig. 0.3(c)** pour un dispositif témoin dont la grille est formée uniquement d'or. Même si un effet de commutation est observé, cet effet est très différent en amplitude et forme comparé au résultat de la **Fig. 0.3(c)**, indiquant que le comportement physique dépend des matériaux à l'interface.*

Cet effet memristor est démontré en **Fig. 0.3(b)**, qui montre la conductance différentielle $G_G = dI_G/dV_G$, pour des tensions entre $-0.5\ V$ et $0.5\ V$, mesurée entre G et D après avoir appliqué des V_{write} de plus en plus élevées (de $0.8\ V$ à $7\ V$, comme indiqué par la légende). Ces résultats ont été obtenus sur un dispositif avec $t_{YBCO} = 50\ nm$, $t_{Al} = 10\ nm$ et $W_{Al} = 60\ \mu m$. On peut observer un effet de commutation de la conductance entre un état OFF (courbe bleue) et un état ON (courbe rouge). De plus, les états intermédiaires sont stables dans le temps, comme indiqué par la symétrie des courbes pour des tensions positives et négatives. Pour étudier ce comportement en fonction de V_{write}, la valeur de G_G est récupérée depuis les courbes de la **Fig. 0.3(b)** pour une tension fixe de $V_G = 100\ mV$ (voir la ligne noire verticale) et le résultat est illustré en **Fig. 0.3(c)**, qui montre l'évolution de $G_G(V_{write})$. Ici aussi, le comportement memristor est particulièrement visible : le cycle est réversible, non-volatile (les états ON et OFF sont constants pour une large gamme de V_{write}) et montre une large modulation de la conductance entre deux niveaux éloignés de plus de deux ordres de grandeurs (de 10^{-8} S à 10^{-6} S).

Cet effet est attribué à une réaction d'oxydo-réduction interfaciale : l'application de V_G permet de contrôler l'épaisseur de la barrière tunnel et donc de contrôler l'état résistif de l'interface. Cette

conclusion est corroborée par de multiples observations. En particulier, **Fig. 0.3(d)** montre le résultat d'une expérience identique à celle effectuée en **Fig. 0.3(c)** pour un échantillon témoin dont la grille est faite uniquement d'or (sans déposition d'aluminium). Même si un effet de commutation entre deux états est visible, la forme ainsi que les ordres de grandeurs sont drastiquement différents : ainsi, on peut conclure que la présence d'un matériau fortement réducteur (tel que l'aluminium) est nécessaire pour observer les effets décris en **Fig. 0.3(c)**. D'autres observations qui soutiennent cette conclusion sont discutées dans le texte principal (**Chapitre 4, Sect. 4.1.1.**), et le lecteur peut se référer à cette section pour plus de détails.

2.3. Modulation non-réversible de l'état supraconducteur du canal d'YBCO

Le deuxième set de mesure correspond à la caractérisation de l'état résistif du canal d'YBCO après application de tensions V_{write} de plus en plus importantes. Ces mesures sont effectuées par l'application d'un courant I_{SD} entre les contacts S et D et la mesure de la différence de potentiel V_{SD} aux mêmes bornes en géométrie deux pointes [voir **Fig. 0.2(b)**]. La résistance $R_{SD} = V_{SD}/I_{SD}$ est calculée en fonction de la température après chaque cycle d'écriture $V_G(t)$ [Fig. **Fig. 0.3(a)**] pour étudier les conséquences de l'application de tensions de grilles sur la conductance du canal. **Fig. 0.4(a)** montre un résultat typique obtenu sur un dispositif avec $t_{YBCO} = 110\,nm$, $t_{Al} = 10\,nm$ et $W_{Al} = 60\,\mu m$ en augmentant V_{write} entre $0\,V$ [aucune tension de grille n'a été appliquée avant la mesure de $R_{SD}(T)$] et $15\,V$. Deux observations principales ressortent de ces courbes. Tout d'abord, l'application de V_{write} croissantes entraine une augmentation de la résistance dans l'état normal, c'est-à-dire au-dessus de T_C, $\sim 10\,\Omega$ pour $V_{write} = 0\,V$ jusque $\sim 40\,k\Omega$ pour $V_{write} = 15\,V$. Deuxièmement, la transition métal-supraconducteur s'élargie jusqu'à ce qu'après application de $V_{write} = 15\,V$, un état isolant soit atteint.

Ce type de mesure a été reproduit à l'identique sur un grand nombre de dispositifs ayant des géométries différentes. Ceci est illustré en **Fig. 0.4(c)**, qui montre la valeur de la température critique effective T_C^* en fonction de V_{write}. T_C^* est définie comme étant la valeur de la température pour laquelle R_{SD} passe sous une température de $1\,\Omega$, qui correspond à la valeur de la résistance de contact mesurée en série due à la géométrie de mesure deux pointes. Ainsi, on observe que T_C^* décroit de façon monotone entre une valeur $\sim 80\,K$ jusque $0\,K$, et que cette diminution dépend principalement de t_{YBCO} : un canal plus fin (t_{YBCO} est faible) entraine une réduction plus rapide de T_C^*. De plus, la suppression du caractère supraconducteur est non-réversible, même après application de tensions négatives.

Cette diminution du caractère supraconducteur du canal d'YBCO lors de l'application de tensions de grille croissantes peut être expliquée par la génération de désordre dans la structure cristallographique du cuprate par effet Joule, menant à la suppression graduelle des propriétés supraconductrices. Cette conclusion est appuyée par le graphe présenté en **Fig. 0.4(b)**, qui montre que dans le cas d'un dispositif témoin, la phénoménologie est identique au cas d'un dispositif ayant une grille faite d'aluminium [voir courbe verte en **Fig. 0.4(c)**]. Ainsi, la présence ou non d'une couche réductrice en contact avec YBCO mène à la même phénoménologie, et donc le phénomène observé ne peut être expliqué par une réaction d'oxydo-réduction. De plus, comme indiqué dans le texte principal (**Chapitre 4, Sect. 3.3.2.**), l'augmentation de R_{SD} apparait comme concomitante aux pics de puissance dissipée dans la grille, pointant vers une origine thermique déterminée par la température locale du canal.

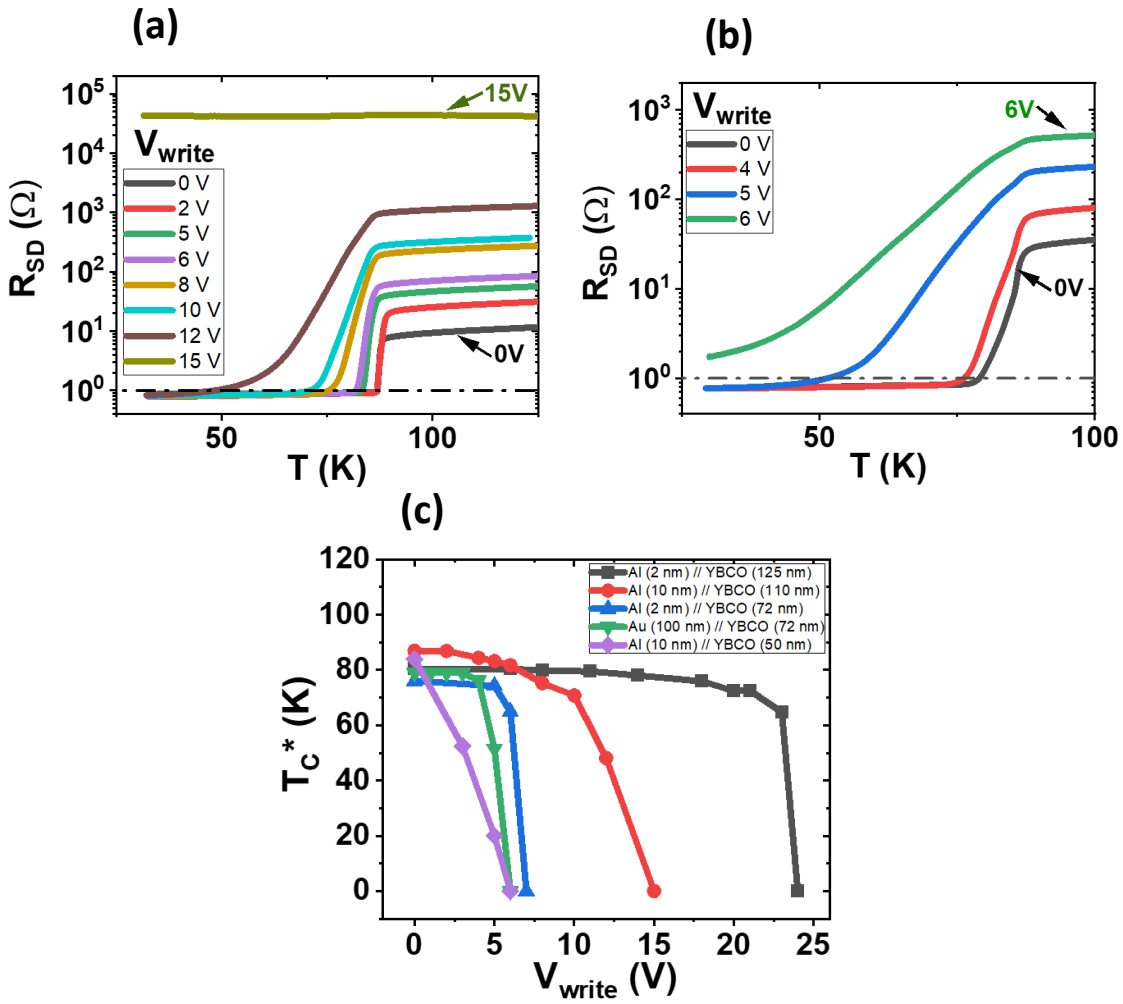

Fig. 0.4: (a) R_{SD} en fonction de la température pour un dispositif avec $t_{YBCO} = 110\ nm$, $t_{Al} = 10\ nm$ et $W = 60\ \mu m$. Cette expérience met en évidence une claire transition entre un état supraconducteur ($V_{write} = 0\ V$, courbe noire) et un état isolant ($V_{write} = 15\ V$, courbe verte) lors de l'application de V_{write} croissants. (b) R_{SD} en fonction de la température pour un dispositif avec $t_{YBCO} = 72\ nm$, $t_{Al} = 0\ nm$ et $W_{Al} = 60\ \mu m$. Le même comportement en fonction de V_{write} est observé comparé à ***Fig. 0.4(a)****. Ce résultat atteste que la présence ou non d'un matériau réducteur mène à la même phénoménologie. (c) T_C^* en fonction de V_{write} pour cinq dispositifs avec des géométries différentes, montrant un comportement identique : le caractère supraconducteur disparait graduellement (de façon monotone) lorsque V_{write} augmente.*

L'étude du contrôle électro-chimique des propriétés supraconductrices de YBCO dans des dispositifs de type transistor est le sujet du chapitre 4 intitulé **« Electrochemical tuning of YBCO's superconducting properties »** et le lecteur est prié de se référer à ce chapitre pour une plus complète analyse et discussion des résultats introduits précedemment.

3. Commutation magnétique de l'état résistif de dispositifs vannes de spin supraconducteurs

3.1. Introduction

Une vanne de spin est formée de deux couches ferromagnétiques séparées par une fine couche non-magnétique (métallique, isolante, semi-conductrice, etc…) et est caractérisée par un état de faible résistance lorsque les aimantations sont parallèles (P, pointant dans la même direction) et un état de forte résistance lorsque les aimantations sont antiparallèles (AP, pointant dans des directions opposées). Cette structure est un dispositif essentiel dans le domaine de la spintronique. L'un des évènements clés dans l'étude des propriétés de transport des vannes de spin fut la découverte en 1988 par Albert Fert [12] et Peter Grünberg [13] de l'effet de magnétorésistance géante (GMR) qui correspond à la modulation géante de la résistance électrique d'une multicouche, alternant couches ferromagnétiques et métalliques, par application d'un champ magnétique externe. Cette découverte marque la naissance du domaine de la spintronique moderne, avec de nombreuses applications telles que les mémoires magnétiques non-volatiles, les qubits ou la simulation de neurones et de synapses dans le domaine du neuromorphisme.

L'objet d'étude de cette seconde partie est une vanne de spin supraconductrice (VSS) : une fine couche supraconductrice (aussi appelée couche séparatrice) placée entre deux couches ferromagnétiques. Ce système fut étudié pour la première fois en 1966 par Pierre-Gilles de Gennes [14], puis plus tard en 1999 par Tagirov [15] et Buzdin [16] qui démontrèrent indépendamment, en utilisant les équations de Usadel et Gor'kov (formalisme des fonctions de Green), qu'un état de forte résistivité est attendu lorsque les aimantations des couches ferromagnétiques sont P, dû à un effet de couplage ferromagnétique au travers de la couche séparatrice qui module ses propriétés supraconductrices. Ainsi, l'effet vanne de spin (EVS) est dit négatif, contrairement à l'effet positif communément observé dans les vannes de spin conventionnelles.

3.2. Description du dispositif

Les propriétés de transports électriques et magnétiques d'une multicouche S ($30\ nm$)/ FM_1 ($15\ nm$)/ S (t_{YBCO})/ FM_2 ($5\ nm$)/ S ($30\ nm$) sont étudiées, S représentant le supraconducteur YBCO (avec $2\ nm < t_{YBCO} < 10\ nm$) et FM une couche ferromagnétique de $La_{1-x}Sr_xMnO_3$ (LSMO) ou $La_{1-x}Ca_xMnO_3$ (LCMO). Cette structure est illustrée en **Fig. 0.5(a)**. LSMO et LCMO sont des manganites demi-métalliques communément employées dans des hétérostructures en combinaison avec YBCO du fait de leurs structures cristallographiques compatibles permettant l'obtention d'interfaces transparentes avec une faible résistance. De plus, LSMO et LCMO ont la propriété d'être isolants pour une direction de spin tout en étant conducteurs pour les électrons de spin opposés (on dit que ces matériaux sont $100\ \%$ polarisés en spin), ce qui permet d'étudier un cas limite fondamental du magnétisme pour des applications de spintronique. Il est important de remarquer que les épaisseurs des couches FM_1 et FM_2 sont différentes ($15\ nm$ et $5\ nm$), de manière à obtenir des champs coercitifs différents et permettre l'apparition d'une configuration antiparallèle par application d'un champ magnétique externe [17,18]. **Fig. 0.5(b)** montre la géométrie de mesure des VSS : la jonction possède la forme d'un pilier vertical de section transverse $10 \times 10\ \mu m^2$ ou $20 \times 20\ \mu m^2$, le courant I est

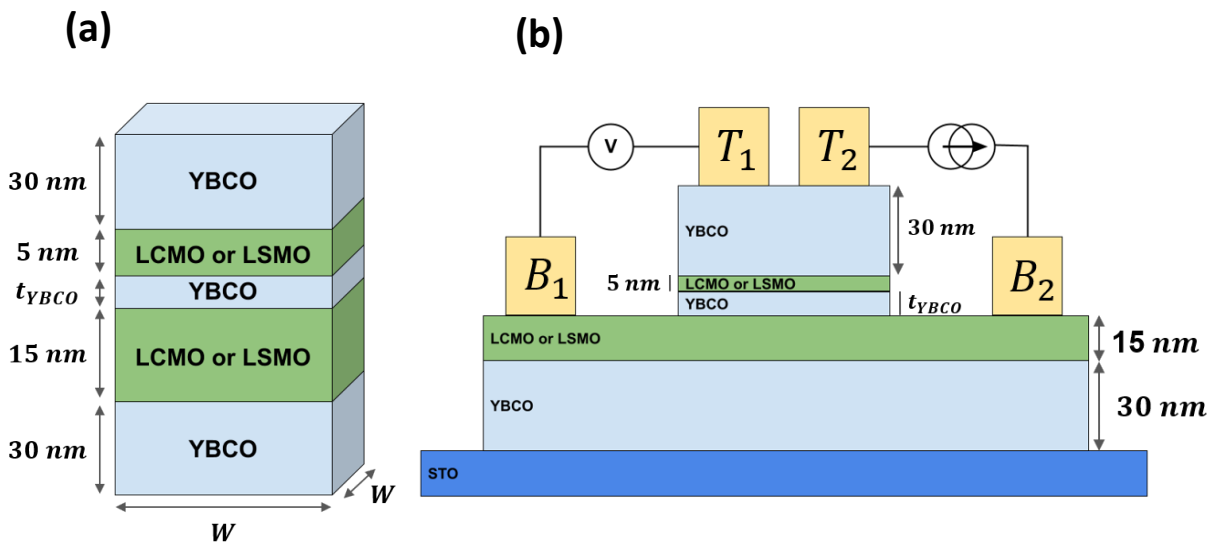

Fig. 0.5: (a) Structure des multicouches S/FM$_1$/S/FM$_2$/S étudiée dans le chapitre 5 ayant la forme d'un pilier verticale avec une section transverse carrée de $W \times W$. Les épaisseurs sont toutes fixées mis à part l'épaisseur de la couche séparatrice d'YBCO, avec $2\ nm < t_{YBCO} < 10\ nm$. (b) Configuration de mesure en 4 pointes. Le courant I est appliqué entre T_2 et B_2 et la différence de potentiel V est mesurée entre T_1 et B_1.

appliqué perpendiculaire aux diverses interfaces entre T_2 et B_2, et la différence de potentielle V est mesurée entre deux contacts distincts T_1 et B_1. Ainsi, cette géométrie autorise une mesure de type quatre pointes, qui permet de se défaire des résistances de contacts pour une mesure plus précise des effets supraconducteurs.

3.3. Résultats des mesures de transport : renversement de l'effet vanne de spin

Le résultat principal de cette étude est le renversement systématique du signe de la magnétorésistance entre un EVS positif et un EVS négatif lorsque la température refroidie sous un seuil qui dépend de la jonction étudiée, appelé température de renversement T_R. Cet effet est démontré en **Fig. 0.6**, montrant la magnétorésistance (la courbe rouge correspond à un balayage décroissant du champ magnétique et la courbe bleu correspond à un balayage croissant) mesurée sur une jonction avec $t_{YBCO} = 8\ nm$ à $100\ K$ [**Fig. 0.6(a), haut**] et à $15\ K$ [**Fig. 0.6(b), haut**] :

(i) Pour $T = 100\ K$, la magnétorésistance présente un comportement linéaire pour des champs magnétiques élevés, signature de l'effet de magnétorésistance colossale typique des manganites [19–24] et deux pics hystérétiques à bas champ, signature de l'effet de magnétorésistance géante.

(ii) Pour $T = 15\ K$, le signe de la magnétorésistance est inverse et l'on observe deux creux de résistances.

De plus, des mesures de cycle d'hystérésis (aimantation M en fonction du champ magnétique B) ont été effectuées sur un échantillon pleine plaque (c'est-à-dire avant la fabrication des jonctions en salle blanche) pour déterminer la valeur des champs coercitifs des couches ferromagnétiques et vérifier que la commutation résistive observée en **Fig. 0.6** est liée à la configuration des aimantations.

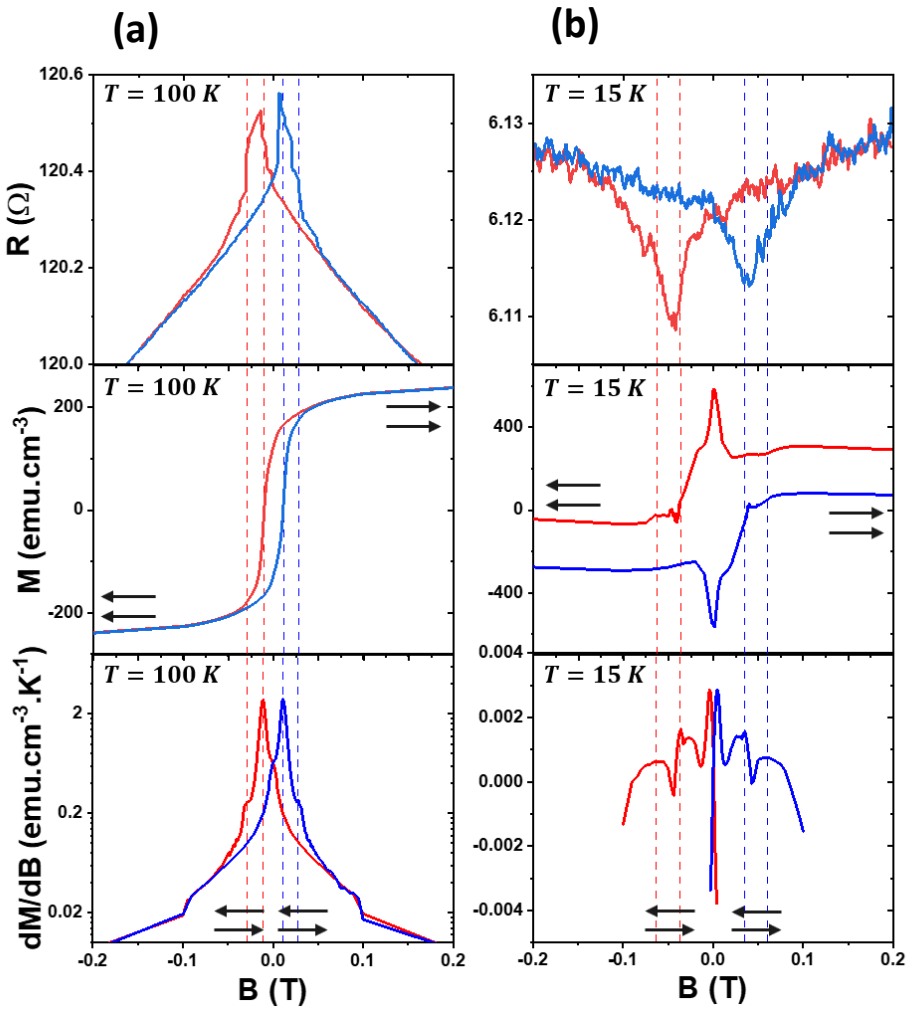

*Fig. 0.6: (a) [haut] Cycle d'hystérésis $M(B)$ à $100\ K$ d'un échantillon YBCO ($30\ nm$)/ LSMO ($15\ nm$)/ YBCO ($8\ nm$)/ LSMO ($5\ nm$)/ YBCO ($30\ nm$) avant fabrication des vannes de spin. Le comportement est typique d'un matériau ferromagnétique (LSMO). Pour des champs élevés, l'aimantation sature, indiquant que les deux couches de LSMO possèdent des aimantations parallèles. [milieu] Dérivée première de $M(B)$, montrant deux maximas distincts pour $B_{C1} = 11\ mT$ et $B_{C2} = 29\ mT$, qui correspondent aux champs coercitifs des deux couches de LSMO : pour un champ magnétique compris entre ces deux valeurs, la vanne de spin est dans un état antiparallèle, i.e. les aimantations des deux matériaux ferromagnétiques pointent dans des directions opposées. [bas] Magnétorésistance d'un dispositif montrant une hystérésis située exactement entre les deux champs coercitifs calculés précédemment via la première dérivée. (b) Même type de mesures que **Fig. 0.6(a)** pour une température de $15\ K$. Le cycle d'hystérésis montre une claire réponse supraconductrice, indiquée par les deux maximas à bas champ magnétique.*

Ces mesures sont réalisées à l'aide d'un magnétomètre SQUID et les résultats sont tracés en [**Fig. 0.6(a), milieu**] et [**Fig. 0.6(b), milieu**] à $100\ K$ et $15\ K$, respectivement, dans la même fenêtre de champs magnétiques.

Pour $T = 100\ K$, le cycle d'hystérésis est typique d'un système ferromagnétique [25], avec une saturation de l'aimantation à haut champ magnétique (voir les flèches noires parallèles), ainsi qu'un renversement de l'aimantation de positive à négative pour des champs faibles. Le champ magnétique nécessaire pour obtenir une aimantation nulle en partant de l'état saturé est appelé champ coercitif et se note B_C. [**Fig. 0.6(a), bas**] montre la dérivée première du cycle $M(B)$: deux pics distincts pour des champs $B_{c1} = 11\ mT$ et $B_{c2} = 29\ mT$ sont obtenus, et ces deux valeurs correspondent aux champs coercitifs des deux couches ferromagnétiques. En effet, un champ coercitif plus important ($B_{c2} = 29\ mT$) est attendu pour la couche ferromagnétique la plus fine (FM_2 avec une épaisseur de $5\ nm$).

Pour $T = 15\ K$ (*i.e.* dans le régime supraconducteur de la jonction), le cycle d'hystérésis possède une forme non conventionnelle : un pic d'aimantation est observé pour un champ très faible ($\sim \pm 3\ mT$), qui correspond à l'apparition de vortex supraconducteurs car YBCO est un supraconducteur de type II [26]. Néanmoins, la dérivée première du cycle $M(B)$ illustrée en [**Fig. 0.6(b), bas**] montre une fois de plus des pics distincts que l'on peut interpréter comme les champs coercitifs des deux couches ferromagnétiques à cette température : on observe un accroissement des champs coercitifs avec $B_{c1} = 37\ mT$ et $B_{c2} = 63\ mT$. Notez que les deux pics de dM/dB à bas champs magnétiques correspondent au caractère supraconducteur de la multicouche et donc ne sont pas pris en compte dans l'analyse des champs coercitifs.

Ainsi, il est possible de définir une gamme de champ magnétique pour laquelle la configuration des aimantations du dispositif est AP, c'est-à-dire $11\ mT < B < 29\ mT$ pour $T = 100\ K$ et $37\ mT < B < 63\ mT$ pour $T = 15\ K$. Il est important de remarquer que les extrema de la magnétorésistance se situent exactement dans ces gammes de champs magnétiques pour les deux températures (voir les lignes pointillées verticales rouge et bleu en **Fig. 0.6**). Par conséquent, on peut conclure que l'effet de commutation de la résistance dans les dispositifs vannes de spin est directement lié à l'orientation relative des aimantations des deux couches ferromagnétiques.

Ce renversement de la magnétorésistance est uniquement observé pour des épaisseurs intermédiaires de la couche d'YBCO centrale $5\ nm < t_{YBCO} < 8\ nm$: dans le cas d'une épaisseur trop mince ou trop épaisse, seul un EVS positif est observé (à l'exception d'un seul dispositif dans le cas de $t_{YBCO} = 10\ nm$). Ceci est démontré en **Fig. 0.7**, qui montre les valeurs de T_R mesurées pour un grand nombre de dispositifs VSS provenant de quatre échantillons différents (REAL1, REAL2, REAL3 et REAL4)

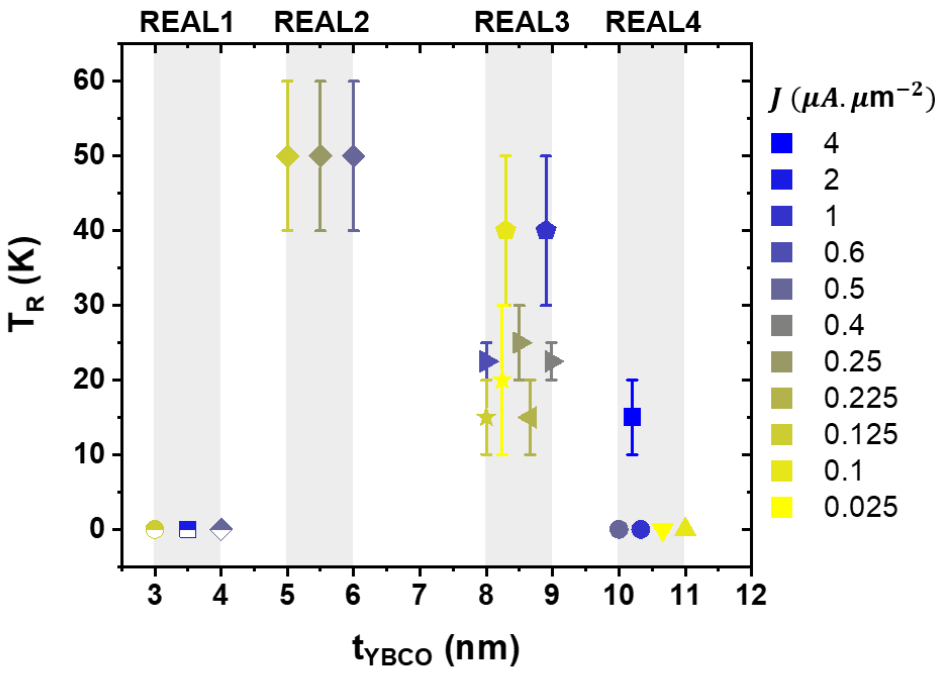

Fig. 0.7: Valeurs de T_R en fonction de t_{YBCO} mesurées sur quatre échantillons différents avec des densités de courant variables. Une valeur $T_R = 0\ K$ indique que pour cette jonction et cette densité de courant, seulement un EVS positif a été observé lors des mesures de magnetoresistance pour des températures supérieures à 6 K (minium de température atteignable par le cryostat).

en fonction de t_{YBCO} pour des densités de courant différentes. Pour éviter le recouvrement des points et faciliter la lecture de cette figure, la valeur de t_{YBCO} est arbitrairement choisie entre $[t_{YBCO}, t_{YBCO} + 1]$: par exemple, les points situés entre $5\,nm$ et $6\,nm$ correspondent à des T_R obtenues sur l'échantillon REAL2 avec $t_{YBCO} = 5\,nm$.

Par conséquent, l'épaisseur de la couche séparatrice est d'une importance fondamentale pour l'apparition d'un EVS négatif. Ce dernier est attribué à la modulation des propriétés supraconductrices de la couche séparatrice d'YBCO par un couplage d'échange ferromagnétique : dans l'état P, les aimantations se couplent et se renforcent mutuellement, générant une énergie d'échange plus importante qui mène à la suppression du caractère supraconducteur. Cette conclusion est cohérente avec les résultats en fonction de l'épaisseur : lorsque l'épaisseur est trop faible, YBCO n'est pas supraconducteur [27] et lorsque l'épaisseur est trop importante, les deux couches ferromagnétiques sont trop éloignées pour que l'effet de couplage module de manière visible les propriétés supraconductrices. En effet, le champ d'échange h est proportionnel à $\propto \frac{\cos(\delta/2)}{t_{YBCO}}$ [28], avec δ l'angle formé par les aimantations des deux couches ferromagnétiques.

L'étude de la commutation magnétique de l'état résistif de dispositifs vannes de spin supraconducteurs est le sujet du chapitre 5 intitulé **« magnetic switching in superconducting spin valve structures »** et le lecteur est prié de se référer à ce chapitre pour une plus complète analyse et discussion des résultats introduis précedemment.

Chapter 1: Motivations and technological challenges

This doctoral thesis focuses on the study of devices based on high-temperature superconducting oxides, in which a resistive-switching behaviour is produced by exploiting either electric fields or magnetic fields. The first chapter is dedicated to an introduction of high-temperature superconductivity from the viewpoint of practical applications to motivate the research that was conducted during this thesis. After briefly describing the main concepts of superconductivity, the description of a particular set of applications will be given, namely superconducting RF components, superconducting quantum sensing as well as promising novel applications related to superconducting resistive-switching devices. In each case, indications of how the main results of the present work can be applied to these technologies are discussed, yielding enhanced properties and/or new functionalities.

1. Historical overview

In 1908, Heike Kamerlingh Onnes achieved the feat of liquefying helium for the first time [1], allowing scientists to study the physical properties of materials at yet unachieved low temperatures. Soon followed the ground-breaking discovery of superconductivity in 1911 [29,30], which consists in the sudden drop of the electrical resistance of various metals to zero below a critical temperature T_C, characteristic of the material. Another signature of the superconducting condensed state is the expulsion of the magnetic field from the interior of the material when cooled below the superconducting critical temperature, also known as the Meissner effect. The complete disappearance of the resistance implies that a current can flow indefinitely within a superconducting wire without power dissipation, a feature of great technological importance. However, it was soon realized that, analogous to T_C, there exist a critical current J_C and a critical external magnetic field H_C above which a superconductor loses its superconducting properties [see **Fig. 1.1(a)**], considerably reducing the technological impact of such materials.

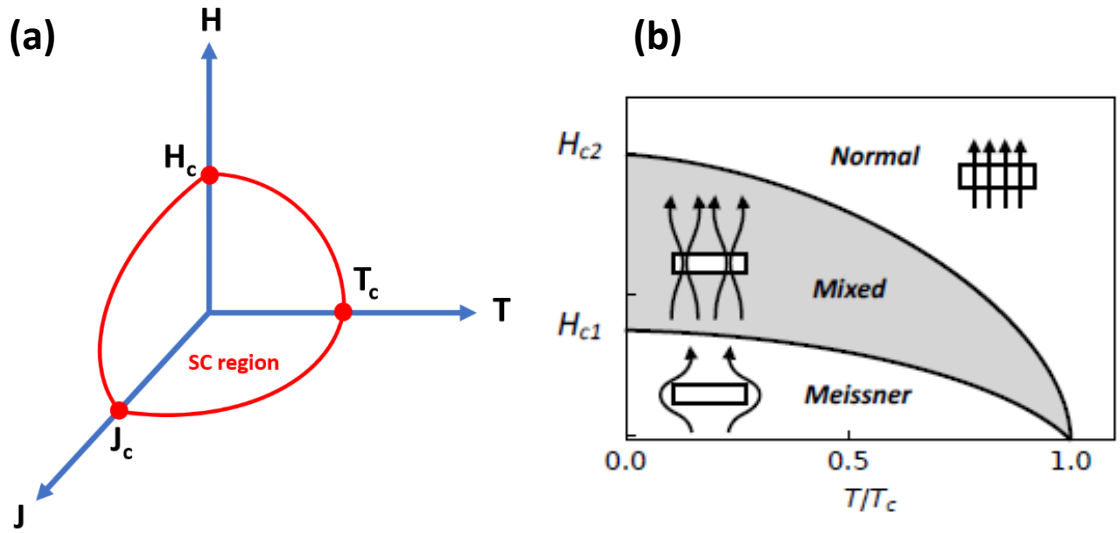

Fig. 1.1: (a) The superconducting phase as a function of the three main critical parameters: T_C, J_C and H_C. (b) Behaviour of a type-II superconductor as a function of the normalized temperature (x-axis) and the external magnetic field (y-axis). The Meissner phase consists in a purely superconducting state, and the external magnetic field is completely screened out from the material's interior (Meissner effect). The mixed phase is characterized by partial flux penetration. Figure taken from Palermo, PhD thesis (2019) [32].

A second breakthrough happened in the 1930s when Shubnikov and Rjabinin experimentally discovered type-II superconductors, defined by the appearance of an intermediate state between two critical fields denoted as H_{c1} and H_{c2} [31]. In this intermediate "mixed state", the material experiences partial flux penetration in a regular array of flux tubes, each tube carrying a magnetic flux quantum $\Phi_0 = hc/2e \approx 2.07 \times 10^{-15}\ Wb$ [as shown in **Fig. 1.1(b)** [32]]. This property, later demonstrated theoretically by Abrikosov in 1957 [33], enables this new family of superconductors to hold a much stronger external magnetic field H_{c2} allowing for the design of superconducting electromagnets. The first superconducting electromagnet was engineered in 1955 using niobium wires and provided a field of $0.7\ T$ at $4.2\ K$ [2]. A few years later, a field as high as $8.8\ T$ was achieved with niobium and tin alloys (Nb_3Sn) [3]. Nowadays, being able to control precisely strong magnetic fields is of paramount importance for numerous practical applications such as magnetic resonance imaging (MRI) [34], mass spectrometry [35] or for particle accelerators [36].

A theoretical microscopic understanding of superconductivity emerged in the late 50s with the work of three American physicists Bardeen, Cooper and Schrieffer [6]. In particular, Cooper hypothesized and later demonstrated that superconductivity can be caused by a relatively small attractive interactions between electrons, leading to the formation of Cooper pairs [37]. These Cooper pairs refer to pairs of bound electrons with opposite spins' directions. In 1962, Brian Josephson predicted the possibility for a supercurrent (a flow of Cooper pairs) to tunnel through a weak non-superconducting link, a phenomenon now known as the Josephson effect [38]. It was not long before this effect was confirmed experimentally by Anderson and Rowell [39] and studied extensively as a building block for precision magnetometers, among many other applications [40–42].

The most impractical aspect of superconductivity in the early 50s and 60s was the need to cool down devices to temperature below $10\ K$, requiring the use of liquid helium. Therefore, real life applications were hindered by the cost of such cryocooling systems, as well as the unreliability of the process. A major step in the history of superconductivity was achieved in 1986, when Müller and Bednorz discovered the emergence of superconductivity in a new type of ceramic materials below a critical temperature of $30\ K$ [4]. They were jointly awarded the Nobel Prize in Physics for this discovery one year later. Shortly after, the first ever superconductor able to transition above the liquid nitrogen boiling point at ambient pressure ($YBa_2Cu_3O_{7-x}$ with $T_C \approx 93\ K > 77\ K$) was unveiled [5]. This foundational moment marked the beginning of the still raging race for new high-T_c superconductors (HTS), summarized in **Fig. 1.2** [43], showing T_C for various materials as a function of the year of discovery. Even though the microscopic mechanisms allowing for superconductivity to appear in such materials remain a long-standing problem, HTS have been a vivid subject of debate for their immense potential for practical applications.

Nowadays, the field of superconducting electronics is well anchored in numerous applications [44]. Cuprate superconductors, made of alternating layers of copper oxides CuO_2 and other metal oxides, are promising materials for future applications despite difficult fabrication processes due to their sensibility of minute variations in their oxygen content, as well as a very strong anisotropy of properties. The work presented in this thesis demonstrates the possibility to tune and control the superconducting properties of the archetypal cuprate high-T_C superconductor $YBa_2Cu_3O_{7-x}$ (YBCO) by application of (i) electric or (ii) magnetic fields:

(i) As stated above, cuprate superconductors are strongly sensitive to disorder and oxygen stoichiometry, allowing for an *in-situ* tuning of the superconducting phase via a controlled motion of negatively charged oxygen ions. This motion of oxygen is induced by applying a voltage bias onto a gate made of an oxygen-hungry material (in the present case,

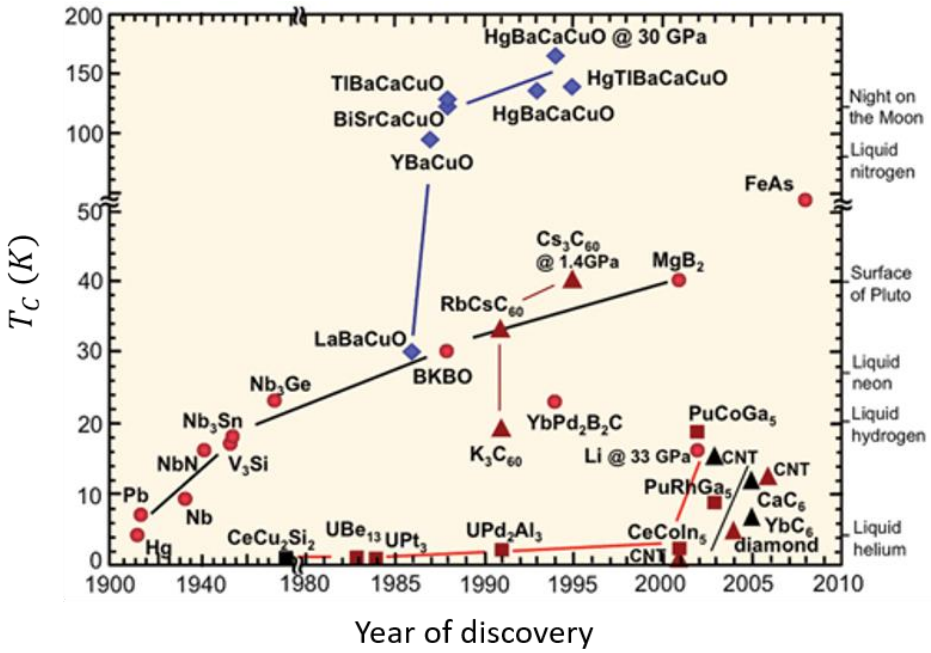

Fig. 1.2: T_C of various superconductors as a function of the year of discovery. Figure taken online from superconductivity, present and future applications (2014) [43].

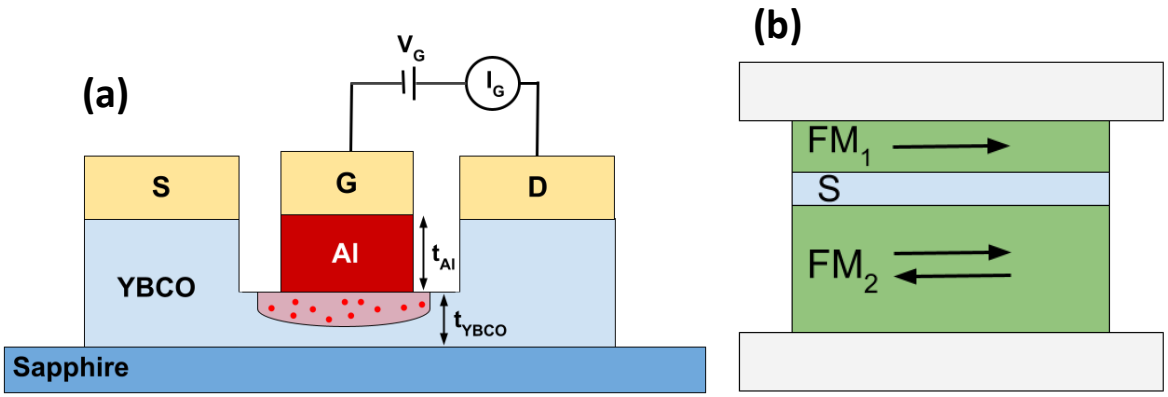

Fig. 1.3: Schematic of two types of devices that are studied in this thesis. (a) 3-terminal transistor-like structure made from the HTS cuprate superconductor YBCO and Al. In this structure, the superconducting ground state of YBCO can be controlled via application of V_G, inducing an oxygen-depleted region in the YBCO channel, depicted by the red shaded area. (b) Superconducting spin valve $FM_1/S/FM_2$ made of two ferromagnets (FM) sandwiching a superconducting layer (S). The conducting state of the device can be controlled by changing the relative orientations of the magnetizations of the FM layers, represented by the black arrows.

aluminium) in a superconducting transistor-like structure, illustrated schematically in **Fig. 1.3(a)**. These devices exhibit strong reversible and non-volatile memory effects, typical of memristive systems, as well as a non-reversible tuning of the YBCO channel's T_C. This study is the topic of **Chapter 4** entitled "Electrochemical tuning of YBCO superconducting properties".

(ii) Superconducting spin valve structures, consisting of two ferromagnets on each side of a superconducting spacer, yield different conducting states depending on the relative orientations of the ferromagnets' magnetizations, which can be controlled externally via magnetic fields [see **Fig. 1.3(b)**]. The possibility to control the magnetoresistance of such devices, demonstrated through magneto-transport experiments, make them promising candidates for low power-consuming non-volatile memories for information storage applications. These devices will be studied in **Chapter 5** on the "Magnetic switching in superconducting spin valve structures".

The results of these two distinct projects and the characterization of the resistive-switching devices can prove an important contribution for a plethora of already existing as well as novel technological applications in the field of superconducting electronics.

2. Superconducting electronics

Superconducting electronics can be defined as functional electronic circuits made of active (nonlinear) and/or passive (linear) elements that are superconducting below a critical temperature, possibly combined with non-superconducting components such as amplifiers and power sources [44]. The basic passive superconducting components include coils for the generation of magnetic fields, resonators, filters, antennas and transmission lines. Another well-studied application of superconducting electronics is the possibility to accurately measure very small magnetic fields with superconducting quantum interference devices (SQUIDs) made of two Josephson junctions in parallel within a superconducting loop.

2.1. Superconducting RF components

2.1.1. Superconducting resonator

The ability of superconductors to withstand very high current densities while displaying extremely low losses has been used extensively to engineer passive devices working in the microwave frequencies range. While operating at non-zero frequencies, superconductors are best characterized by their complex surface impedance Z_S :

$$Z_S = R_S + jX_S = R_S + j\omega L_S \tag{1.1}$$

where R_S, X_S and L_S represent the surface resistance, the surface reactance and the surface inductance respectively and $\omega = 2\pi f$ is the angular frequency related to the frequency f. While superconductors only show a zero dissipation at zero frequency, it was demonstrated experimentally by London in 1941 [45], studying the resistance of tin at high-frequencies ($f = 1.46\ GHz$), that the losses are orders of magnitude lower for superconductors below T_C compared to the best normal metals such as copper. This property is of crucial importance for the fabrication of high-quality superconducting resonators.

Let's consider a superconducting microwave cavity of volume V and surface area S. It is possible to show that the quality factor of the cavity can be approximated as follows [46]:

$$Q = \frac{energy\ stored}{energy\ lost\ per\ cycle} = \frac{\omega V}{2S}\frac{\pi}{c^2 R_S} \tag{1.2}$$

where c is the velocity of light. As can be seen from **Eq. 1.2**, the quality factor (Q factor) is inversely proportional to the surface resistance R_S leading to very high Q factors even in the case of small effective areas. Q factors as high as 10^7 were obtained experimentally for cavities made of niobium at $0.5\ K$ [47].

2.1.2. Superconducting bandpass filter

One of the most important application of high-quality superconducting resonators is the possibility to engineer high-performance bandpass filters composed of resonators coupled in series. As the performance of the filter is proportional to the number n of resonators (commonly referred as the number of poles), superconductors make ideal materials for compacity purposes combined with high quality factors. **Fig. 1.4** shows an example of the behaviour of the insertion loss in dB as a function of the frequency for different number of poles [44]. For the three examples showed in **Fig. 1.4**, the bandwidth is identical but the transitions between bandstop and bandpass frequencies δf are getting sharper as the number of poles is increased, improving the quality of the filter.

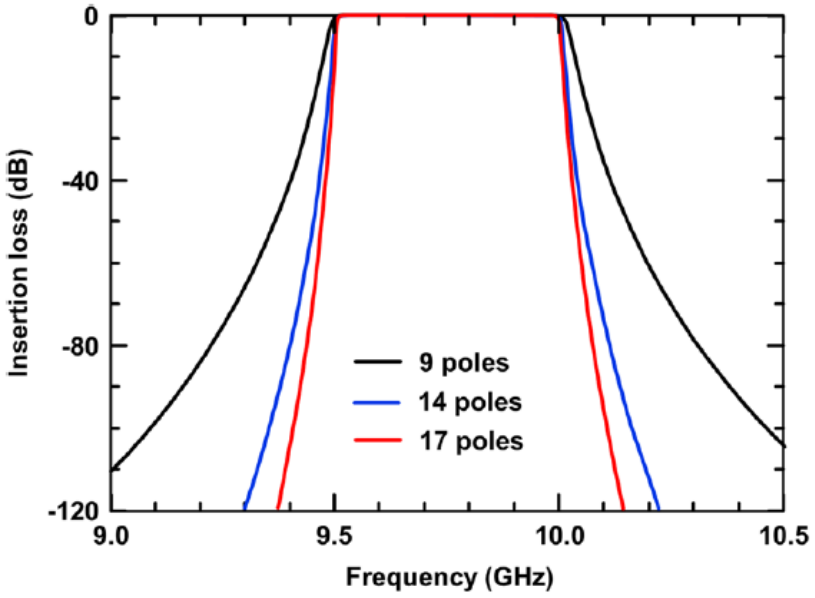

Fig. 1.4: Behaviour of the insertion loss in dB of a RF filter as a function of the frequency for different values of $n = 9, 14,$ and 17. Figure adapted from Braginsky et al., Supercond. Nov. Magn. (2019) [44].

Superconducting filters are widely used in wireless telecommunications, although mostly as front-end receivers, owing to their very low power handling capability making them unfit as transmitters. In particular, YBCO has been mostly exploited due to its critical temperature above the nitrogen boiling point as well as its very low surface resistance R_S [48]. Filters made of YBCO yield ultra-selective bandpass properties, extremely low insertion losses and very compact structures down to the millimetre size [49,50].

2.1.3. RF switches

An RF switch is a device used to route microwave signals through transmission lines to connect antennas, amplifiers and filters. As the market surrounding microwave applications is rapidly growing, the need for efficient, reliable, fast and low energy-consuming RF switches operating at cryogenic temperatures is becoming more and more crucial. As of today, the best RF switches available on the market are the PIN diodes, consisting of an intrinsic semiconducting region surrounded by a P-doped region on one side and a N-doped region on the other side, usually made from gallium arsenide (GaAs). A PIN diode allows the current to flow in one direction when forward biased but not in the other when

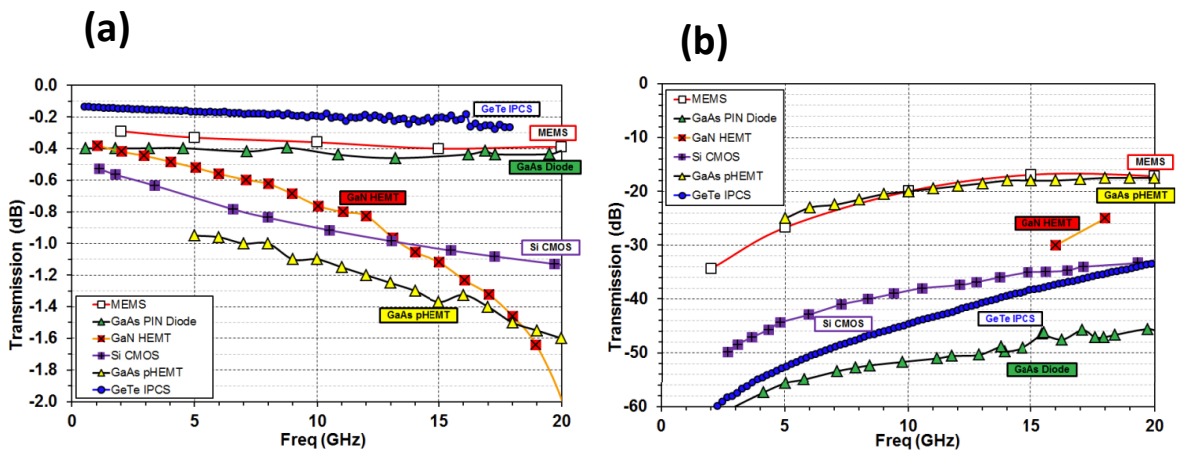

Fig. 1.5: (a) Transmission and (b) isolation in dB as a function of the frequency for the main currently available RF switches. Figure taken from El Hinnawy et al., IEEE (2014) [51].

reverse biased. Alternatively, the market is composed of two other technologies: gallium nitride high electron mobility transistors (GaN HEMTs) and RF microelectromechanical switches (MEMS). As can be seen from **Fig. 1.5** [51], the PIN diode is currently the technology displaying the best characteristics in terms of transmission and isolation for a wide range of frequencies. However, in the frame of compact cryogenic applications, PIN diodes present a big problem due to a high dissipation of energy caused by the large constant DC current needed to bias the diode in the ON state. As an example, mobile phones typically transmit RF signals of $1\ W$. In a standard $50\ \Omega$ system, this power translates to a peak-to-peak voltage of $V = 2\sqrt{2}\sqrt{50} \approx 20\ V$. Therefore, the control voltage must be greater than $20\ V$, leading to energy dissipation and heating via Joule effect.

The work on the electrical control of the superconducting phase of YBCO (**Chapter 4**) provides an interesting alternative to the already existing RF switches operating at very-low temperatures. One can envision a new type of RF switch in the shape of a superconducting coplanar waveguide (SCPW) with an active element shorting the signal and the ground planes, as depicted in **Fig. 1.6(a)**. The attenuation of the transmission line can be tuned by changing the resistive state of the active element. The behaviour of the attenuation in dB of the SCPW as a function of the active element's resistance R_{ae} is displayed in **Fig. 1.6(b)**, showing that changing R_{ae} between a few ohms to a few tens of ohms can drastically alter the attenuation of the transmission line, reaching performances competitive with

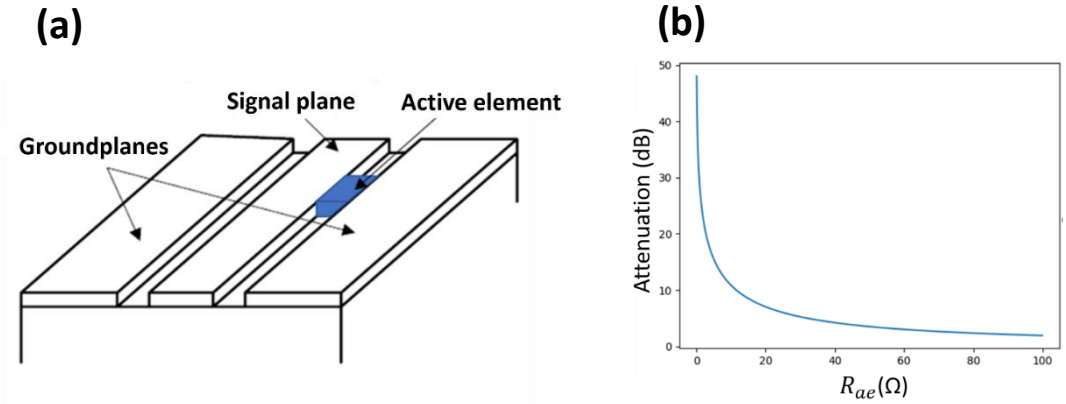

Fig. 1.6: (a) Schematic representation of a superconducting RF switch in the shape of a superconducting coplanar waveguide. The active element, represented in blue, shorts the signal plane to the ground plane. (b) Attenuation of the transmission line as a function of the active element's resistance R_{ae}.

those of the currently used RF switches described above. During this PhD, the results obtained in **Chapter 4** contributed to the invention of a device that exploits the controlled superconductor-to-insulator phase transition of the cuprate superconductor YBCO to engineer such an RF switch in a SCPW geometry. A patent to protect this invention has been filled. This device should require little to no energy as fast voltage pulses are needed to switch the resistive state of the active element, greatly enhancing the viability of RF switch at cryogenic temperatures. The working principle of this RF switch and the active element will be discussed in more details in **Chapter 4, Sect. 1.2.**

2.2. Superconducting quantum sensing

2.2.1. Josephson junctions (JJ)

A Josephson junction consists of two superconducting electrodes separated by any non-superconducting thin spacer or weak link (for example an insulator, a metal or a ferromagnet) [38]. It is characterized by a flow of supercurrent (or tunnelling of a supercurrent) between the junction electrodes in the absence of an applied voltage due to the phase difference of the wave functions in both superconductors. Moreover, when a voltage is applied to the junction, the current oscillates at a characteristic frequency that is voltage dependent. This effect is called the Josephson effect and is typically described by a set of two equations called the DC and AC Josephson equations:

$$I(t) = I_c \sin(\varphi(t)) \tag{1.3}$$

$$\frac{\partial \varphi}{\partial t} = \frac{2eV(t)}{\hbar} \tag{1.4}$$

where I and V represent the current and the voltage across the junction respectively, φ is the Josephson phase, I_c is the critical current and $\hbar = {}^{h}/_{2\pi}$ is the reduced Planck constant. The Josephson effect is one example of a superconducting macroscopic quantum phenomenon, the manifestation of quantum behaviours at the macroscopic scale rather than at the atomic scale. This effect is the basis of a plethora of different applications in the field of superconducting electronics [44].

The Josephson effect has drastically changed the field of metrology, the scientific study of measurements and fundamental constants [52]. In fact, when the Josephson junction is exposed to electromagnetic radiation at the frequency f, the current-voltage characteristic of the junction displays regions of constant voltage at specific values $V_{step} = nhf/2e$, with h the Planck constant, e the elementary charge and n an integer. This phenomenon was experimentally demonstrated by Shapiro in 1963 [53]. This very important relationship proportionally relates the Volt to the second only through fundamental constants, making this effect of great significance in the measurement of voltage standards.

As of today, JJs made from cuprate superconductors are mostly designed by step-edge processes [54] or through ion irradiation [55]. Step-edge junctions, also called grain boundary junctions, consist of the epitaxial growth of a high-T_C superconductor on a previously step-etched substrate, leading to a local decrease of the superconducting properties close to the etched step

pattern. Another option for the design of HTS JJs is called masked ion irradiation [55]. The sample is first coated with a photoresist for protecting the cuprate superconductor from the ion irradiation and electron beam lithography is performed to open slits. Then, the sample is irradiated by accelerated oxygen ions that create disorder and modulate the T_C of the irradiated areas.

The possibility to tune *in-situ* the superconducting properties of YBCO (**Chapter 4**) by applying voltage pulses onto an aluminium gating allows the design of electrochemically configurable high-T_C JJs. Such a property can be used to train JJ on-demand for specific applications by controlling the strength of the barrier of the non-superconducting weak link and therefore altering the Josephson coupling between the superconducting electrodes.

2.2.2. SQUIDs magnetometers

The main application of the Josephson effect is in the fabrication of superconducting quantum interference devices (SQUIDs). A SQUID is made from a superconducting loop containing one or two JJs and was invented in 1964 at the Ford Scientific Laboratory [56]. SQUIDs are widely used as extremely precise magnetometers for a broad range of applications, spanning from bio-medical applications (for instance for magnetoencephalography, the mapping of the magnetic fields of the brain) to geophysical measurements (measurements of the time dependence of the earth's magnetic field). Basically, a SQUID is a magnetic flux to voltage converter having an extremely low magnetic flux noise.

The most common implementation of a SQUID is the so-called DC SQUID, made of two JJs placed in parallel inside a superconducting loop as shown in **Fig. 1.7**. By biasing a SQUID with a constant current exceeding the sum of the critical currents of both JJs, the voltage across the SQUID is a periodic function of the external magnetic field applied to the device with a period equal to the magnetic flux quantum Φ_0. This phenomenon arises due to screening currents flowing through the superconducting loop to complement or oppose the external applied field so that the flux through the SQUID is exactly Φ_0. Therefore, SQUIDs are sensitive to magnetic fields of the order of magnitude of the magnetic flux

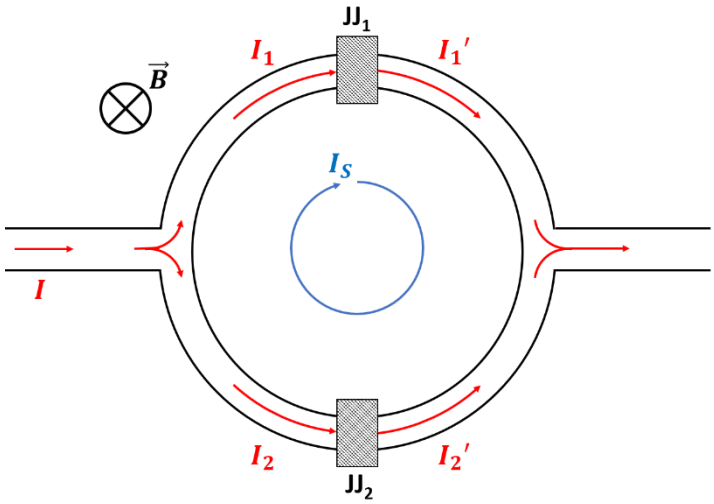

Fig. 1.7: Schematic of a DC SQUID. JJ_1 and JJ_2 denote the two JJs forming the SQUID's structure. The supercurrent I flows from the left end side and divides into I_1 and I_2 in the superconducting loop. The two JJs induce a change in the Josephson phase of the signals. When $\vec{B}$ is applied, a screening current I_S flows around the loop to complement or compensate for the magnetic field due to magnetic flux quantization. The voltage across the SQUID oscillates at a period equal to the magnetic flux quantum Φ_0.

quantum, *i.e.* $\sim 2.07 \times 10^{-15}\ T.m^2$. Nowadays, SQUIDs are mostly made from low-T_C superconductors like niobium or lead alloys and can read magnetic fields as low as $5.10^{-14}\ T = 0.5\ fT$ with white noise levels of the order of a few $fT.H^{-1/2}$ [57,58]. For comparison purposes, the magnetic field induced by a human brain ranges between $10\ fT$ to $10^3\ fT$ while the earth's magnetic field at its surface varies from $25\ \mu T$ to $65\ \mu T$ [59,60]. These values lead to the need of magnetic shielding to be able to measure magnetoencephalograms without being disturbed by the time dependence of the earth's magnetic field of typically $\pm 1\ nT$ over a few seconds [61].

Since the beginning of the 1990s, SQUIDs made from high-T_C superconductors are being experimentally investigated [62–64]. Although their sensitivity and white noise levels are inferior to their low-T_C counterparts, SQUIDs made from YBCO offer the possibility to perform extremely precise magnetic field measurements operating at liquid nitrogen temperature [65–68]. In particular, Faley *et al.* [68] demonstrated in 2013 the possibility to obtain magnetic field resolutions as low as $\sim 4\ fT.H^{-1/2}$ at $77\ K$ for SQUIDs made from a $150\text{-}nm$ thick layer of YBCO with two $1.5\text{-}\mu m$-wide step-edge Josephson junctions. Another advantage of high-T_C SQUIDs is that the cryogeny can be scaled down and, for example for magnetoencephalography, the SQUID can be closer to the patient's head, therefore receiving stronger signals [69].

Another thoroughly-studied type of SQUID is the so-called radio frequency SQUID (or RF SQUID), necessitating only one JJ inside a superconducting loop by exploiting the AC Josephson effect (**Eq. 1.4**). These SQUIDs exhibit sensitivities lower than the DC SQUIDs due to flux trapping while cooling but are cheaper and easier to produce and might be useful for specific applications that does not require the precision of DC SQUIDs. RF SQUIDs made from YBCO can display magnetic field sensing sensitivities around $1\ pT$ with white noise levels as low as $90\ fT.H^{-1/2}$ [70–73].

The range of applications for SQUID devices is vast and encompass a large number of emerging technologies, for example quantum dots and Rapid single flux quantum (RSFQ) systems. Quantum dots are nanostructured semiconducting devices having unique optoelectronic properties described by quantum mechanics [74,75]. They have first been theorized in 1982 [76] and have since proven to be a promising field of research for multiple applications, such as bioimaging [77], photovoltaic [78] and quantum computing [79]. In the last 20 years, much attention has been dedicated to the study of hybrid superconducting-quantum dots SQUID systems to possibly enhance their functionalities. Van Dam *et al.* [80] studied in 2006 a SQUID made from a superconducting aluminium loop with semiconducting weak links made from indium arsenide, controlled by aluminium top gates (see **Fig. 1.8**), showing a switching between a normal to a π-junction. A π-junction corresponds to a JJ which has a phase φ equal to π in the ground state in the absence of external magnetic fields. Such hybrid systems are promising entities for the study of novel physical phenomena, for example Yu-Shiba-Rusinov states, [75] Kondo physics [81] and quantum entanglement [81]. SQUIDs can also be implemented in RSFQ systems, a digital superconducting electronic device used to process logic operations in the form of magnetic flux quanta exchanges based on flux quantization [82,83]. This technology can perform similar tasks as the analogous CMOS technology, with SFQ pulses of the order of $1\ ps$ accompanied by the unique ability to drastically reduce dispersion, Joule heating and power consumption. However, such circuits are still hindered by complex and unreliable fabrication processes due to the required high density of chips [84]. Moreover, this technology is limited to low temperatures and subjected to perturbations from the earth magnetic field, requiring the implementation of a magnetic shielding [84].

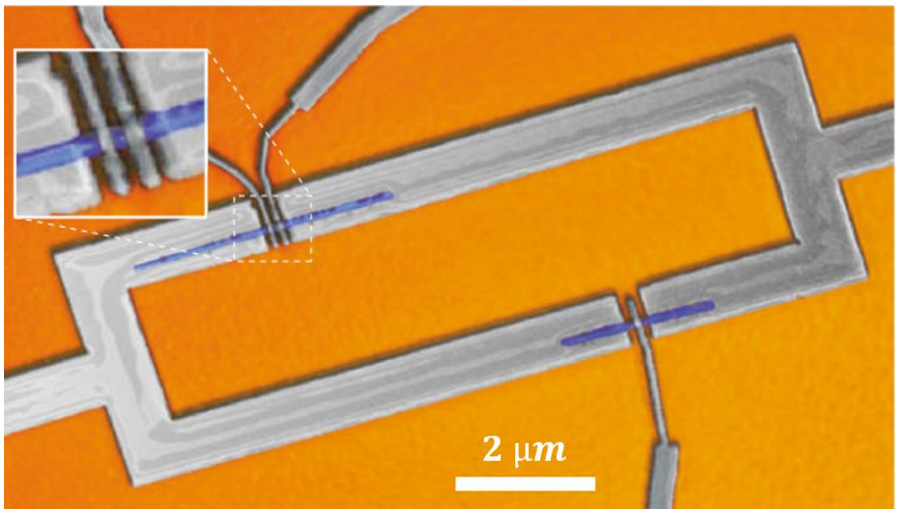

Fig. 1.8: Microscope picture of a hybrid superconducting-quantum dot SQUID system made from aluminium (superconducting loop) and indium arsenide weak links (blue). The quantum dot is controlled by applying a negative voltage bias into the top gate contacts L and R. Figure taken from Van Dam et al., Nature *(2006) [80].*

3. Novel superconducting applications

3.1. Memristive devices for neuromorphic computing

A memristor (abbreviation for "memory resistor") is a two-terminal non-linear electrical component with a tunable resistance that depends on its past dynamics. It was defined and described in 1971 by Leon Chua from the study of symmetries in electrical devices and measured experimentally for the first time in 2008 in devices made of titanium dioxide (TiO_2) [85–87]. Memristors are characterized by a low conducting state (denoted as OFF state) and a high conducting state (denoted as ON state), as well as a number of intermediate states, that can be accessed through application of external stimuli such as voltage bias or magnetic fields. Generally, the ON and intermediate states relax into the OFF state over a characteristic time, which can be shorter or longer depending on the conductance switching mechanisms. However, the lifetime can be so long that the conductance states are virtually non-volatile. Thus, memristors offer the possibility to design non-volatile solid-state memories with potential applications in data storage [88,89], signal processing [90,91] and reconfigurable computing [92]. In other cases, the conductance states relax into the OFF state at a relatively fast pace, for instance in the presence of strong thermal activation [93].

Memristors have gathered a lot of attention lately for their potential use in the field of neuromorphic computing to try to reproduce the way the brain works with solid state components [94]. Indeed, the brain has the capability to execute complex operations such as pattern recognition with less than $20\ W$ of power consumption in a very small volume and with very little delay [95]. Although today's machine learning is reaching processing capabilities close or superior to those of humans, the volume needed as well as the energy consumption of such devices is orders of magnitude higher than those of the brain because of the conventionally used von Neumann architecture of computers with separate memory and processing units (usually referred as the "von Neumann bottleneck").

A brain is composed of billions of neurons communicating together via electrical signals (or spikes) send through synapses, the point of connection between two neurons. The synapse acts as a variable resistance: depending on its weight and the intensity of the incoming spike, the signal may or may not be transmitted to other neurons. One of the most studied neuron model is called the leaky integrate-and-fire model [96]. In this model, the neuron emits a spike with a shape culminating at a specific intensity after some time, then an exponential decay over time [see the shape of a pulse in **Fig. 1.9(a)**]. This spike is modulated through synapses and sent to adjacent neurons. Thus, a neuron receives a weighted sum of spikes that raises its electrical potential and once this potential overcomes what is commonly referred as the firing threshold, the neuron emits in turn a spike that will travel to subsequent neurons. In 2022, Samardzic *et al.* [97] demonstrated theoretically and experimentally (using oxide materials) the possibility to engineer leaky integrate-and-fire neurons using volatile memristors to mimic temporal integration, firing function and signal decay. This phenomenon is summarized schematically in **Fig. 1.9(a)**, showing the behaviour of the conductance of a volatile memristor as a function of time while consecutive pulses are applied to it with the emission of an electrical spike after the fourth stimulus. On the other hand, non-volatile memristive systems can store information in their resistance states and are ideal devices for emulating the main attributes of a synapse, paving the way for neuromorphic computing applications [94]. The weight is encoded in the resistive state, effectively mimicking the strength of the synapse.

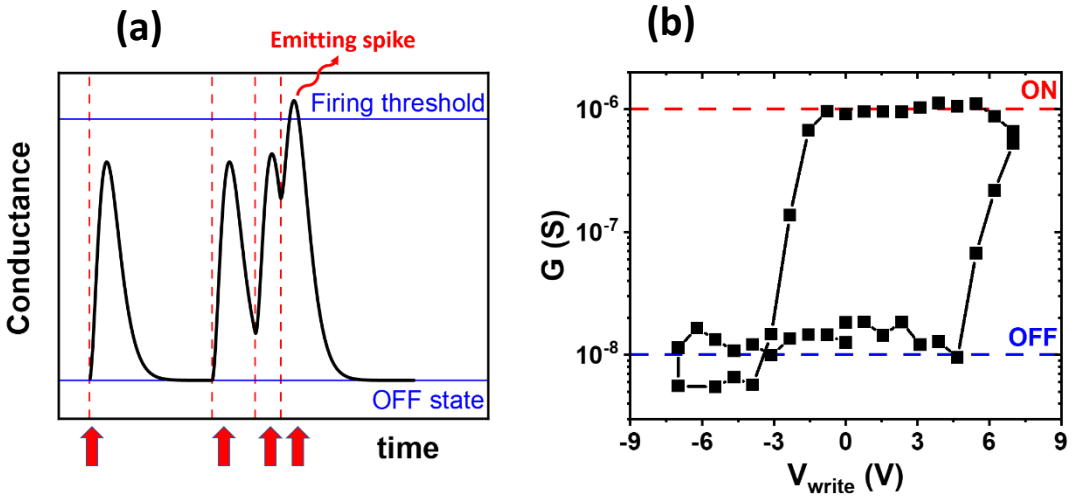

Fig. 1.9: (a) The conductance as a function of time of a volatile memristor when subjected to multiple external pulses . The red arrows represent the time of the incoming external pulses and the memristor emits a signal after the fourth pulse once the firing threshold is overcome. (b) Differential conductance of the interface between YBCO *(50 nm) and* Al *(10 nm) as a function of V_{write} at 35 K. The graph demonstrates the reversible and non-volatile switching of the interface's conductance between ON and OFF states. See* ***Chapter 4, Sect. 3.2.1.*** *for more details about the graph and the measuring method.*

In the experiments as detailed in **Chapter 4**, it will be shown that the interface between YBCO and aluminium displays a strong memristive behaviour: the reversible switching of the conductance within a continuum of states via application of external writing voltage cycles as shown in **Fig. 1.9(b)**. Therefore, the resistance of the interface can be tuned on-demand between two conducting levels that are more than two orders of magnitude apart. This effect is non-volatile at temperatures below $200\ K$ and becomes volatile at higher temperatures due to the spontaneous thermal relaxation of the oxygen ions. Therefore, these memristors display both non-volatile and volatile regimes depending on the temperature, and can be used to emulate the behaviour of both neurons and synapses.

3.2. Superconducting spintronics

Spintronics (abbreviation for "spin electronics") is the scientific study of spin-dependent electron transport in solid-state devices [98]. Whereas conventional electronics only use the electrical charge of the electron, being able to carry information in both the charge and the spin allows various unique functionalities for a wide range of applications. One of the foundations of spintronics is the discovery of the giant magnetoresistance (GMR) effect by Albert Fert [12] and Peter Grünberg [13], making possible the fabrication of magnetic field sensors used to read data in hard disk drives [99]. GMR devices are made by alternating ferromagnetic layers with non-magnetic materials in a spin valve structure or superlattice. The conducting state of the multilayer is controlled by changing the relative orientations of the ferromagnetic layers' magnetizations resulting in a difference in resistance between the parallel and the anti-parallel states. Julliere *et al.* [100] were the first to experimentally investigate a spin valve device made of Fe/ Ge/ Co trilayers, demonstrating a modulation of the magnetoresistance of the stack as high as $14\ \%$ at $4.2\ K$ between the parallel and anti-parallel alignments [101].

Ferromagnetism and conventional superconductivity are two antagonistic phenomena: the electron pairing in the form of singlet (opposite spins) Cooper pairs in the superconducting phase is non-compatible with the ferromagnetic order that tends to align all spins in the same direction. Yet, interfaces between materials with radically different physical properties are known to give rise to fascinating phenomena. Due to the inherent non-locality of electrons in quantum mechanics, the transport properties of electrons cannot abruptly change at a given interface between materials of different natures, leading to the so-called proximity effect; the properties of both materials become mixed near the interface. Therefore, even though Cooper pairs can only be created in the interior of a superconductor, a superconducting pairing can be induced in a non-superconducting material via proximity effect. In a ferromagnet (FM), however, the strong ferromagnetic exchange interactions act as a de-pairing mechanism for the Cooper pairs, breaking apart the electrons of opposite spins and reducing the distance over which the superconducting correlations enter the ferromagnet. **Fig. 1.10** shows the probability amplitude $|\Psi|^2$ of the induced superconducting wavefunction Ψ as a function of the distance x in the case of superconductor/normal metal (SC/N) and superconductor/ferromagnet (SC/FM) interfaces [102]. As mentioned above, the induced superconducting state decays much faster in the ferromagnetic region than in the normal metal as indicated by the shorter coherence length $\xi_F \ll \xi_N$.

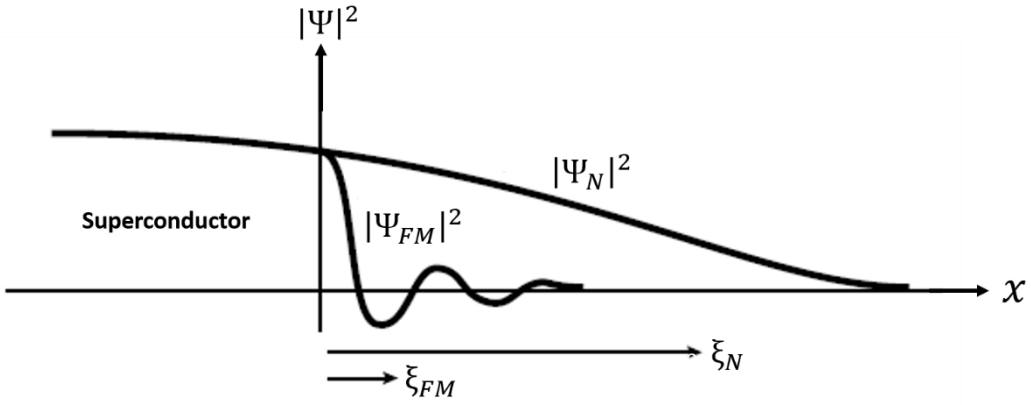

Fig. 1.10: Probability amplitude of the superconducting wavefunction at the interface between a normal (N) metal and a ferromagnet (FM) as a function of the distance x. $|\Psi|^2$ rapidly decreases to zero in the case of a FM due to the exchange energy inherent to the ferromagnetic phase ordering. .Figure taken from Flokstra, PhD thesis (2010) [102].

In the last decade, a lot of work has been dedicated to the creation and the control of superconducting triplet correlations (equal-spin Cooper pairs) to rectify the antagonism between superconductivity and ferromagnetism [103,104]. Most known superconductors only support the transport of singlet Cooper pairs made of paired electrons of opposite spins, making them unstable under application of magnetic fields and exchange interactions. However, it has been shown that equal-spin electrons can be paired together at carefully engineered interfaces between some superconductors and ferromagnetic materials through spin mixing and spin rotation mechanisms as illustrated in **Fig. 1.11** [104], produced by magnetic inhomogeneities at the interface. The mechanism that allows the generation of triplet Cooper pairs will be further detailed in **Chapter 2, Sect. 4.3.** Owing to the equal spins' direction, triplet Cooper pairs can coexist with a magnetic field, and therefore the ferromagnetic exchange field, increasing the distance over which they can survive inside a FM by orders of magnitude, allowing the generation and the control of long-range spin polarized supercurrents. Spin polarized supercurrents constitute the basis of the emerging field of superconducting spintronics [104]. Spin lifetimes in conventional spintronics are short due to spin-orbit and spin-flip scattering processes that lead to spin randomization, greatly limiting spintronics applications. Superconducting spintronics offer the possibility to enhance these lifetimes by orders of magnitude while suppressing the energy dissipation due to Joule effects. The first experimental demonstration of a long-range supercurrent was published by Keizer *et al.* [105] in 2006 while studying the interface between the s-wave superconductor NbTiN and the half-metallic ferromagnet CrO_2. Since this discovery, a lot more studies were conducted on a plethora of different systems and attested of long-range triplet correlations at various interfaces such as $YBa_2Cu_3O_{7-x}$/ $La_{1-x}Sr_xMnO_3$ [106], and multi-layered spin valve structures [107–109], among others [110–112].

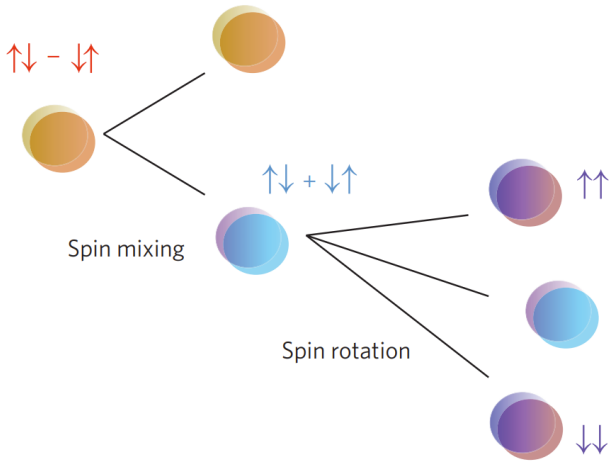

Fig. 1.11: Schematic description of spin mixing and spin rotation mechanisms. Starting with a spin-singlet $S = 0$ Cooper pair $\uparrow\downarrow - \downarrow\uparrow$, spin-mixing and spin-rotation can lead to the generation of triplet $S_Z = \pm 1$ correlations $\uparrow\uparrow$ and $\downarrow\downarrow$. Triplet Cooper pairs are promising for practical applications as they can coexist with an external magnetic field. More details about the equal-spin triplet generation is given in ***Chapter 2, Sect. 4.3.2.*** *Figure taken from Linder et al., Nat. Phys., (2015) [104].*

As will be studied in more details in **Chapter 5**, the possibility to produce magnetoresistance switching effects in superconducting spin valve structures made from the high-T_C superconductor YBCO in contact with half-metallic ferromagnets ($La_{1-x}Sr_xMnO_3$ and $La_{1-x}Ca_xMnO$) is promising for various applications, in the field of information storage for example. Half-metallic ferromagnets have attracted a great deal of interest since the 1980s for their ability to act as a conductor for one spin direction while behaving as an insulator for the other. In particular, LSMO and LCMO provide the convenient property to crystallize in a perovskite-based structure, making them perfectly fit to share interfaces with YBCO and reducing interface disorder to a minimum [106,113]. The magnetoresistance exhibits a unique property: a reversal behaviour between a positive spin valve effect (with maxima of

the resistance in the anti-parallel configurations) to a negative spin valve effect (with minima of the resistance in the anti-parallel configurations) depending on the temperature, the current flowing through the junction as well as the angle of the incident external magnetic field. These results are summarized in **Fig. 1.12**, showing typical measurements of the magnetoresistance for the studied devices. Because of the shown memory effects, the spin valves are interesting candidates to implement functions analogous of that of magnetoresistive random-access memory (MRAM) in superconducting electronic circuits, where not only they would bring low power dissipation, but also add an additional functionality via the possibility to reverse from a positive to a negative magnetoresistance.

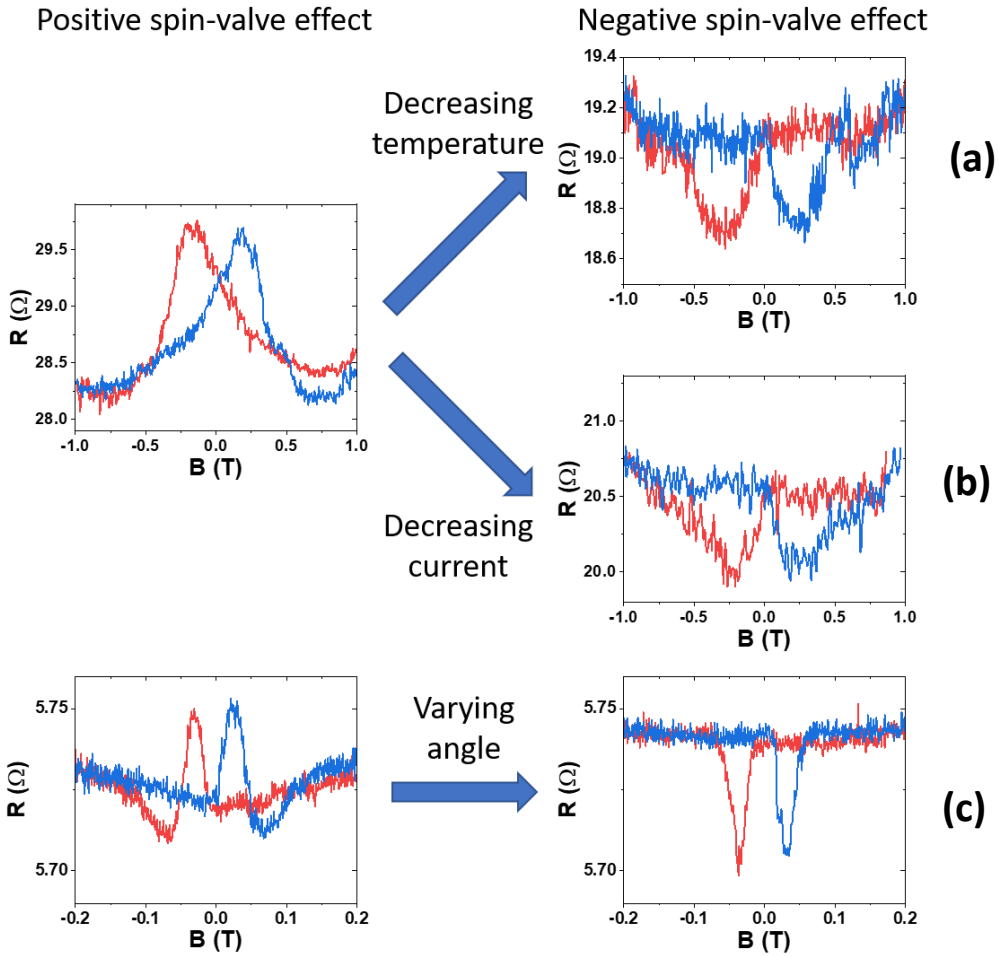

Fig. 1.12: Typical behaviour of the magnetoresistance profiles of superconducting spin valves made from the cuprate superconductor YBCO and half-metal ferromagnets obtained within the framework of this thesis. The results show a clear reversal from a positive spin valve effect to a negative spin valve effect by (a) decreasing the temperature, (b) decreasing the injected current and (c) varying the angle. The details about these results, the related experiments and the origins can be found in ***Chapter 5****.*

4. General outline

High-T_C cuprate superconductors provide a wide range of functionalities useful for numerous applications. This thesis has been focused on the control of the superconducting ground state of YBCO through application of electric and magnetic fields, to lay the basis for the realization of high-temperature superconducting switches, memories and field sensors.

After this application-centred introduction, **Chapter 2** will be dedicated to the description and discussion of the most important theoretical concepts useful for the scope of this thesis, namely high-T_C superconductivity, ferromagnetism (in particular in manganite half-metallic materials LSMO and LCMO) and the superconducting proximity effects at various interfaces. In **Chapter 3**, the different techniques that were used for the fabrication and characterization of the devices will be presented, including a description of the deposition methods (magnetron sputtering and pulsed laser deposition), the typical clean-room processes (optical lithography, ion beam etching…) and the low-temperature transport and magneto-transport measurements.

As was introduced in this chapter, the nature of the superconducting pairing mechanism in cuprates has not yet been explained theoretically to this day, but it is well established that the CuO_2 planes forming the perovskite structure play a key role, making cuprates extremely sensitive to structural disorder as well as oxygen stoichiometry. This property is generally considered detrimental to the technological impact of YBCO but can be used as a tuning parameter to control its superconducting properties. However, such control can be achieved electrically via the application of voltages, allowing the fabrication of a new generation of field-effect resistance switching memories based on superconductor-to-insulator phase transitions. In **Chapter 4**, this effect is exploited at the interface between a reducing material (aluminium) and YBCO in a transistor-like geometry, as depicted in **Fig. 1.3(a)**. The transport measurements demonstrate that the gate-drain channel exhibits strong memristive effects: the reversible and non-volatile switching of the differential conductance within a continuum of stable conducting states. Concomitantly, the transistor's channel experiences a gradual and monotonic non-reversible decrease of the superconducting properties, a phenomenon that is attributed to the thermomigration of oxygen ions under high temperature gradients leading to a local disordering of YBCO's crystal structure. Being able to control *in-situ* the superconducting ground state of YBCO, although in a non-reversible way, can be used to train YBCO layers on-demand for specific applications, for instance for the fabrication of electrochemically reconfigurable Josephson junctions and SQUID systems.

Finally, **Chapter 5** will be focused on the study of vertical superconducting spin valve structures made of alternating layers of YBCO and the half-metallic ceramics $La_{1-x}Sr_xMnO_3$ (LSMO) and $La_{1-x}Ca_xMnO_3$ (LCMO). The fabrication of such vertical junctions is challenging, owing to the numerous lithography and etching steps involved in the clean-room micro-patterning. In particular, contact resistances must be optimized to yield optimal interfaces' transparencies, and the first part of the chapter will be dedicated to the optimization of the fabrication process to yield reliable and reproducible 4-probe transport measurements. The magnetoresistance measurements display a unique property: the ability to reverse between a positive to a negative spin valve effect depending on the temperature, the current flowing through the junction and the angle of incidence of the external magnetic field (**Fig. 1.12**). This property is explained through what is commonly referred as the superconducting exchange coupling mechanism: in the parallel configuration of the spin valve, superconductivity in the spacer's layer is suppressed and the resistance is higher than in the anti-parallel configuration. In fact, the spin-polarized perturbations of the pairing functions for both ferromagnetic layers couple and enhance each other, effectively breaking apart Cooper pairs and quenching superconductivity in the middle layer. Moreover, the magnetoresistance relative change in percentage can be enhanced at very low temperature via the negative spin valve effect, a property of great interest for the engineering of non-volatile cryogenic magnetic memories.

Chapter 2: Theoretical concepts

1. Conventional description of superconductors

The discovery of superconductivity in 1911 by Heike Kamerlingh Onnes [1] triggered a great deal of interest in the scientific community for its incredible potential for practical applications (see **Chapter 1**) as well as its implications from a theoretical standpoint. The theoretical understanding of the electronic properties of materials was, at the time, unable to explain the two main consequences of superconductivity, namely the perfect conductivity (zero resistance state) and perfect diamagnetism (the total screening of the magnetic field in the interior of the superconductor) below the critical temperature T_C. This paragraph is aimed at briefly describing the history of superconductivity from a theoretical point of view as it was developed during the 20th century. Although the complete derivation of the theories cannot be done succinctly enough to be added to this manuscript, this sub-chapter will be necessary for the definition and introduction of the most important parameters that are needed to understand the basic phenomena of superconductivity and will be used intensively throughout the thesis.

The essential understanding of superconductivity was derived and developed mainly during the 20th century, in several very important successive steps as shown in **Fig. 2.1**, representing a simplified timeline of the most crucial theories of superconductivity that will be discussed below.

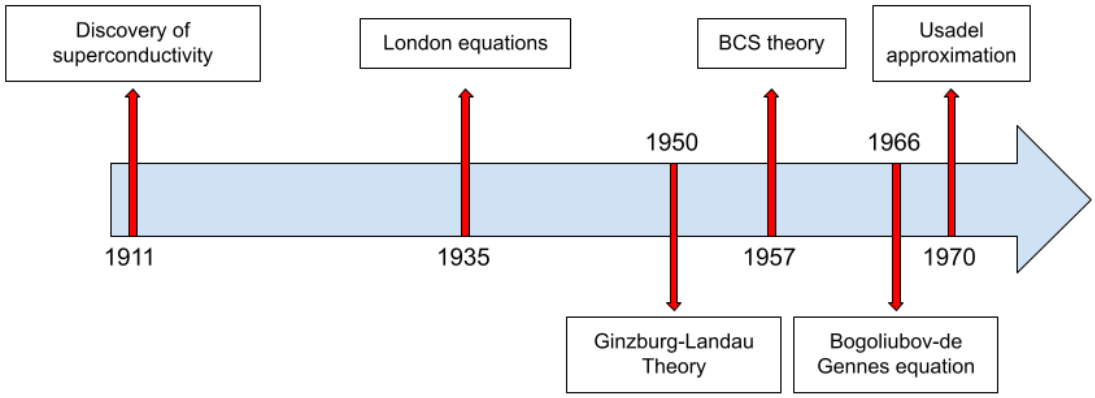

Fig. 2.1: Timeline of the most important theories on conventional superconductivity developed during the 20th century.

1.1. London equations

In 1935 (24 years after the discovery of superconductivity!), Fritz and Heinz London [114] derived the first basic equations accurately describing a superconducting material by incorporating perfect conductivity and perfect diamagnetism into a single theoretical body. These two equations relate the superconducting current (or supercurrent) $\overrightarrow{J_S}$ to the electromagnetic field $(\vec{E}, \vec{H})$ and are commonly written as:

$$\vec{E} = \frac{\partial}{\partial t}\left(\frac{4\pi {\lambda_L}^2}{c^2}\overrightarrow{J_S}\right) \tag{2.1}$$

$$\vec{H} = -c.\overrightarrow{curl}\left(\frac{4\pi {\lambda_L}^2}{c^2}\overrightarrow{J_S}\right) \tag{2.2}$$

where $\overrightarrow{curl}\vec{A} = \vec{\nabla} \times \vec{A}$ is the curl vector operator with $\vec{\nabla} = \left(\frac{\partial}{\partial x} \quad \frac{\partial}{\partial y} \quad \frac{\partial}{\partial z}\right)$ the Nabla matrix.

In particular, **Eq. 2.2** implies that an external magnetic field is exponentially expelled from the interior of the superconductor with a typical screening length equal to λ_L. Solving **Eq. 2.2** using Maxwell equations in one dimension, one can obtain that the magnetic field $\vec{H}$ inside the superconductor has a spatial dependence described by:

$$H(x) = H(0)e^{-x/\lambda_L} \tag{2.3}$$

where λ_L is called the superconducting London penetration depth and indicates how deep an external magnetic field can penetrate inside a superconducting material. The value of the London penetration depth is temperature dependent and typically ranges from a few tens of nm (for instance, $\lambda_L = 15\ nm$ for bulk aluminium [115]) to a few hundreds of nm [for instance, $\lambda_L = 430 \pm 50\ nm$ for $Fe(Se_{0.5}Te_{0.5})$ single crystals [116]] at $0\ K$ for most superconducting materials.

Being able to accurately predict and measure the penetration depth of superconductors is of great importance for testing theoretical models, giving us crucial information for the understanding of more complex superconducting systems such as the mechanisms behind high-T_C superconductivity. There exist various experimental techniques to measure the London penetration depth. Muon spin spectroscopy is mostly used and consists in the measurement of the depolarizing rate of a spin-polarized muon current injected through a superconductor, giving information on the local dependence of the magnetic field [117]. Another method to determine λ_L is the measurement of the resonance frequency shift of a microwave cavity or a tunnel diode oscillator after inserting the studied material inside the cavity [118].

Even though conventional superconductors display an isotropic London penetration length, cuprate superconductors show an anisotropic behaviour of λ_L as a result of their anisotropic crystalline structure (with stronger superconducting properties along the CuO_2 ab-planes) as well as the d-wave pairing symmetry. These two concepts will be discussed in more details later in **Sect. 2.2.** while studying the crystalline structure of YBCO and its superconducting characteristics. The value of the London penetration depth reported in the literature for YBCO is typically of $\lambda_L^a(0) \approx 126\ nm$ and $\lambda_L^b(0) \approx 105\ nm$ measured with low-energy muon spectroscopy [117] and an average value of $\lambda_L(0) \approx 148\ nm$ measured using a tunnel diode resonator [118]. It is important to mention that the value of λ_L is closely related to the quality of the sample, which is why the dispersion of the values reported in the literature can be really high (values $\lambda_L^a(0) \approx 160\ nm$ and $\lambda_L^b(0) \approx 80\ nm$ were reported in 1998 by Kamal et al [119]) due to difficult fabrication processes and aging effects.

1.2. The phenomenological Ginzburg-Landau (GL) theory

The next main step in the general understanding of superconductivity was achieved at the end of the 40s by Vitaly Ginzburg and Lev Landau [120,121]. This so-called Ginzburg-Landau (GL) theory was proposed as a phenomenological theory of superconductivity based on experimental observations of the mixed state of type-II superconductors in which spatial inhomogeneities play a dominant role. They introduced a pseudo wavefunction $\vec{\Psi}(\vec{r})$ to describe the spatial dependence of the density of superconducting electrons $n_s(\vec{r}) = \left|\vec{\Psi}(\vec{r})\right|^2$, *i.e.* the number of electrons participating to the supercurrent. Even though this theory provided a solid theoretical background for the study of the

intermediate state of type-II superconductors and for the fabrication of extremely strong electromagnets, the Ginzburg-Landau theory was mostly regarded as an incomplete macroscopic description of a more microscopic mechanism.

The GL theory was derived by assuming a series expansion of the thermodynamic Gibbs free energy adequate for temperatures as close to the superconducting critical temperature as possible. By minimizing the energy of the system (*i.e.* by applying a variational principle), they were able to obtain the GL differential equation:

$$\alpha\vec{\Psi}(\vec{r}) + \beta\left|\vec{\Psi}(\vec{r})\right|^2\vec{\Psi}(\vec{r}) + \frac{1}{2m^*}\left(\frac{\hbar}{j}\vec{\nabla} - \frac{e^*}{c}\vec{A}\right)^2\vec{\Psi}(\vec{r}) = \vec{0} \tag{2.4}$$

where $m^* = 2m_e$ and $e^* = 2e$ to account for the Cooper pairs, m_e is the mass of an electron, α and β represent the coefficients in the series expansion of the free energy, $\vec{A}$ is the vector potential and j is the imaginary unit.

The most important consequence of the GL theory was the introduction of a new parameter called the Ginzburg-Landau coherence length ξ_{GL}, that can be derived in the absence of any applied field in **Eq. 2.4** and considering only a 1D problem, giving rise to a real second order linear differential equation in the form of:

$$\frac{\hbar^2}{2m^*|\alpha(T)|}\frac{d^2\Psi(x)}{dx^2} + \Psi(x) - \Psi(x)^3 = 0 \tag{2.5}$$

We can easily see that the differential equation of **Eq. 2.5** allows the introduction of a coherence length ξ_{GL} over which $\Psi(x)$ typically varies, defined as:

$$\xi_{GL}(T) = \sqrt{\frac{\hbar^2}{2m^*|\alpha(T)|}} \tag{2.6}$$

In the 1930s, Shubnikov and Rjabinin experimentally discovered type-II superconductors, defined as materials that show an intermediate state between two critical fields denoted as H_{c1} and H_{c2} [31]. In

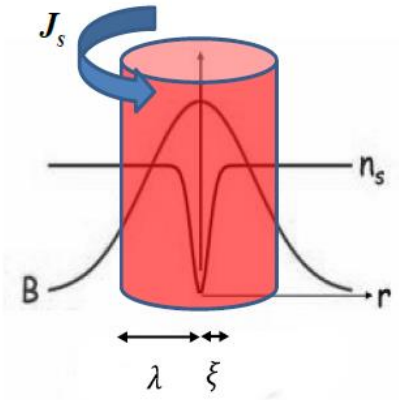

Fig. 2.2: Representation of a vortex. n_S represent the number of superconducting electrons and collapses to zero within the core of the vortex. The radius of the vortex is typically equal to the London penetration depth λ_L while the radius of the core typically varies over the coherence lenght ξ_{GL}. The blue arrow J_S corresponds to the screening current circulating around the vortex. Figure taken from Trastoy, PhD thesis (2014) [122].

this intermediate "mixed state", the material experiences partial flux penetration in a regular array of vortices, each vortex carrying a magnetic flux quantum $\Phi_0 = hc/2e \approx 2.07 \times 10^{-15}\, Wb$. **Fig. 2.2** represents a schematic of a typical Abrikosov vortex [122], depicted as a red cylinder with a radius equal to the London penetration length λ_L. The vortex's core, *i.e.* the region for which the superconducting pseudo wavefunction collapses (the number of superconducting electrons n_S tends to 0), typically varies over a distance equal to ξ^{GL}. Consequently, the GL coherence length appeared of particular interest in the definition of type-I and type-II superconductors, when Abrikosov showed in 1957 [33] that type-II superconductors correspond to materials in which $\kappa = \lambda_L/\xi_{GL} > 1/\sqrt{2}$. These two very important spatial parameters and a visual definition of types I and II superconductors are summarized in **Fig. 2.3**, showing an interface between a superconductor and a normal metal with the corresponding penetration and coherence lengths [46].

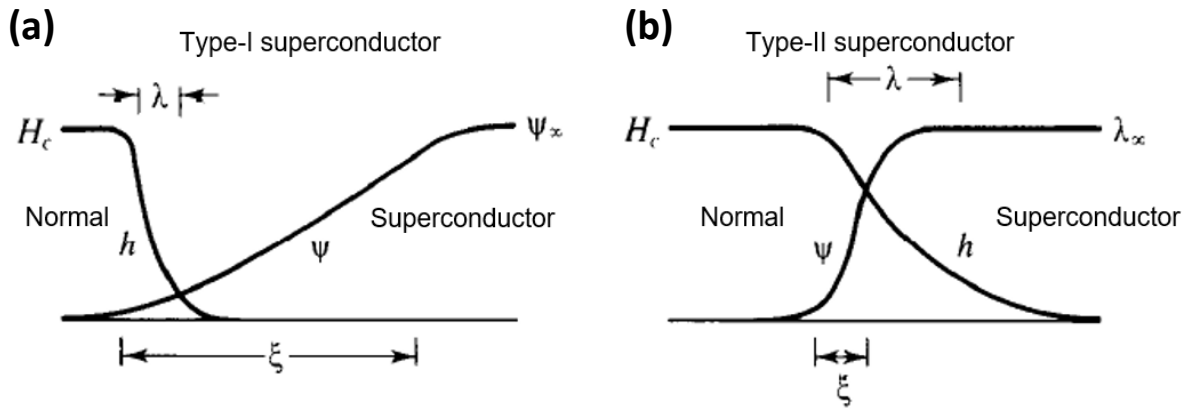

Fig. 2.3: Schematic of the coherence and penetration lengths at the interface between a superconductor and a non-superconducting material showing the difference between (a) type-I and (b) type-II superconductors. Figure adapted from Tinkham (1996) [46].

As was the case for the penetration depth, the coherence length of YBCO is anisotropic, giving different values when measured along the ab-plane or along the c-axis of the crystalline structure. Abou *et al.* [123] reported in 2021 measurements of YBCO's coherence length, giving the estimated values of $\xi_{GL}^{ab}(T = 0\,K) \approx 2.41\,nm$ measured along the ab-plane and $\xi_{GL}^{c}(T = 0\,K) \approx 0.684\,nm$ along the c-axis. As this value is indicative of the strength of a Cooper pair and therefore the quality of the superconducting properties, we can see that the ab-plane is showing stronger superconducting behaviour compared to the c-axis. These values are much smaller than the coherence length of conventional superconductors such as niobium (with $\xi_{GL}(T = 0\,K) \approx 14\,nm$ according to Asada *et al.* [124]), implying that YBCO is more sensitive to disorder and impurities, emphasizing the complexity and importance of the fabrication processes.

1.3. The microscopic Bardeen-Cooper-Schrieffer (BCS) theory

The first microscopic quantum theory of superconductivity emerged in the late 50s under the work of three American physicists, John Bardeen, Leon Cooper and John Robert Schrieffer (the BCS theory) [6]. They were conjointly awarded the Nobel prize in 1972 for this ground-breaking discovery and its incredible consequences for the global understanding of superconductivity. The BCS theory is based upon the fact that even under a small attractive potential, the Fermi surface becomes unstable against the formation of what is commonly referred as a Cooper pair: the electrons condense into a

new state of matter, pairing themselves into pairs of opposite spins' orientations (also called singlet Cooper pairs). This phenomenon was described for the first time by Leon Cooper in 1956 [37]. He demonstrated that, following an idea formulated in 1952 by Frölich [125], this attractive potential could be explained through interactions with the lattice deformation (phonons). Bardeen, Cooper and Schrieffer showed that under these assumptions, it was possible to reproduce the Meissner effect, the calculations of specific heat and penetration depths, validating the veracity of the theory.

In the BCS theory, the Hamiltonian of the system describing the energy levels, valid for a superconductor in equilibrium at zero temperature experiencing a constant attractive potential V is defined as:

$$H_{BCS} = \sum_{k\sigma} \varepsilon_k n_{k\sigma} + \sum_{kk\prime} V c^{\dagger}_{k\uparrow} c^{\dagger}_{-k\downarrow} c_{-k\prime\downarrow} c_{k\prime\uparrow} \tag{2.7}$$

where $c^{\dagger}_{k\sigma}$ and $c_{k\sigma}$ are the creation and annihilation operators respectively, $n_{k\sigma} = c^{\dagger}_{k\sigma} c_{k\sigma}$ counts the number of particles in the specific state of wave vector $\vec{k}$ and spin σ ($\sigma = \uparrow$ or $\sigma = \downarrow$) and $\epsilon_{k\sigma}$ is the corresponding kinetic energy of that state.

The first term in **Eq. 2.7** corresponds to the kinetic energy of the system while the second term describes the behaviour of the Cooper pairs. As can be seen from this Hamiltonian, the electrons forming a Cooper pairs and described by the creation operators $c^{\dagger}_{k\uparrow} c^{\dagger}_{-k\downarrow}$ have opposite spins. We say that they form a singlet Cooper pair, which is commonly written in the Dirac formalism as the quantum state $|\uparrow\downarrow - \downarrow\uparrow\rangle$. This specific pairing mechanism is responsible for the Meissner effect: an external magnetic field will tend to align the spins of the electrons in a Cooper pair, meaning that it is energetically more favourable to screen out a small magnetic field to keep the pairing of the electrons intact than to let the field enters the superconductor. When the external magnetic becomes too strong, the superconductor starts to lose its superconducting properties, leading to the existence of the critical magnetic field H_C.

In 1959, Gor'Kov [126] made the discovery that the GL equation (**Eq. 2.4**) can be derived as a limiting case of the microscopic BCS theory, giving a new life to the GL theory and confirming the intuition of Ginzburg and Landau when, seven years before the BCS theory, they came up with this equation.

A crucial prediction of the BCS theory is the existence of an energy gap $\Delta(T)$ that represents the minimum amount of energy needed to break a Cooper pair into two distinct excitations for a given temperature. This energy gap is equal to 0 for a temperature above T_C (as the material in non-superconducting) and increases for decreasing temperatures until it reaches a maximum value at $T = 0\ K$ (as shown in **Fig. 2.4** [127]) which depends on T_C through the relation:

$$\Delta(T = 0\ K) = 3.528 k_B T_C \tag{1.8}$$

Although this theory was a formidable display of physical intuition and mathematical calculations, it still fails to explain the superconducting behaviour of high-T_C superconductors, which is the reason for their denomination as unconventional superconductors. In the BCS theory, the energy gap $\Delta(T)$ is constant in space, whereas the d-wave pairing symmetry in cuprate superconductors induces an anisotropic energy gap, making the BCS theory unfit to accurately predict the behaviour of such materials.

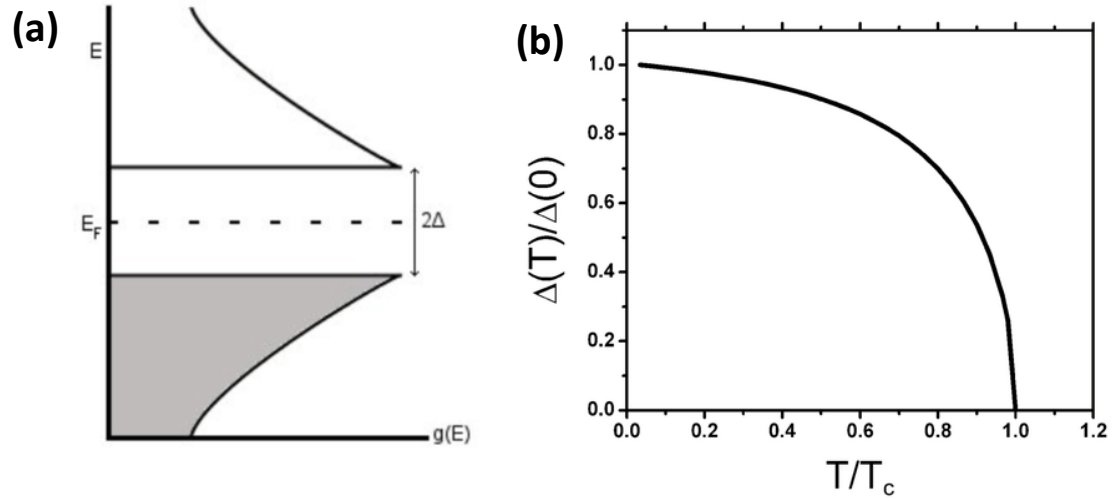

Fig. 2.4: (a) Energy as a function of the density of states of a superconductor, displaying the superconducting gap equals to Δ around the Fermi energy E_F. (b) Behaviour of the normalized superconducting gap as a function of the normalized temperature. The gap is zero for $T = T_C$ (and above) and reaches a maximum value for $T = 0\ K$. Figure taken from Le Quang et al. (2011) [127].

1.4. Overview of modern descriptions of superconductivity

The advancement of the theoretical understanding of superconductivity did not stop at the BCS theory, although it was a big step toward a complete understanding of conventional superconductivity. In particular, the implementation of the particle creation and annihilation operators in **Eq. 2.7** and the fact that the Hamiltonian is only valid for zero temperature, make the use of the BCS theory very cumbersome for finite temperatures. Bogoliubov and de Gennes introduced the concept of mixed particule-hole excited states forming quasiparticles now known as the bogoliubons [46]. They developed together in 1966 the self-consistent field method, widely used nowadays to describe inhomogeneous superconductors with a non-uniform in space potential $V(\vec{r})$, leading to the Bogoliubov-de Gennes equation:s

$$(E - \mu_S)\begin{pmatrix} u \\ v \end{pmatrix} = \begin{pmatrix} H + V & \Delta \\ \Delta^* & -(H^* + V) \end{pmatrix}\begin{pmatrix} u \\ v \end{pmatrix} \qquad (2.8)$$

where H is the one-electron Hamiltonian $H = \frac{(p-eA)^2}{2m_e} + e.V - \mu_S$, μ_S the chemical potential and u and v represent the electron-like part and the hole-like parts of the bogoliubons, respectively.

The self-consistent field method was key to the development in 1982 of the BTK theory (the Blonder-Tinkham-Klapwijk theory) accurately describing the behaviour of the current-voltage characteristics at the interface between a normal metal and a superconductor by solving the Bogoliubov-de Gennes equation [128].

However, one aspect is missing from the Bogoliubov-de Gennes equation, limiting its accuracy to predict real-life behaviours of superconductivity: the equation doesn't incorporate the effects of scattering processes due to impurities. In order to circumvent this limitation, a lot of work has been dedicated between 1966 and 1970 by Gor'kov and Usadel to the formulation of the Bogoliubov-de Gennes equation with the help of the Green's functions formalism, leading to the Gor'kov equation, later simplified using a quasiclassical approximation proposed by Eilenberger and using the diffusive

limit by Usadel in 1970 [126,129–131]. We shall not delve more into the intricacies of such theories as they are far beyond the theoretical scope of this work.

2. High-T_C superconductivity

The main goal of this thesis is to study the superconducting properties of the high-T_C superconductor YBCO under application of external stimuli. This material is part of the cuprate family with a critical temperature of approximately $92\ K$. The conventional theories described above are unable to predict how and why superconductivity emerges in such materials. The next paragraphs will be centred on the description of high-T_C superconductivity while focusing more particularly on the cuprate sub-family.

2.1. Discovery and first descriptions

High-T_C superconductivity (HTS) is a type of unconventional superconductivity (it cannot be described by the BCS theory) referring to superconductors with a critical temperature above the liquid nitrogen boiling point ($T = 77\ K$). Historically, the first high-T_C superconductor was discovered by Bednorz and Müller [4] in 1986 while studying the transport properties of new ceramic materials. These materials offer the obvious advantage to operate at temperatures above the boiling point of liquid nitrogen, a less expensive and easier to handle coolant compared to liquid helium, paving the way for more practical applications. Most high-T_C superconductors are type-II superconductors, exhibiting very high upper critical fields H_{C2} (approximately $20\ T$ at $0\ K$ in the case of YBCO [132]). Importantly, high-T_C superconductors have been extensively used to engineer high-field electromagnets for a wide range of applications.

Cuprates [133] represent the most thoroughly studied unconventional superconductors owing to their early discovery in 1986 and very high critical temperatures. The highest critical temperature for cuprate superconductors at ambient pressure belongs to mercury barium calcium (HGBC-CO) with $T_C = 133\ K$ [134]. They are related to the broader family of transition metals, which are strongly correlated systems with the chemical formula ABO_3 (perovskite structure) with A a rare earth element, B a transition metal with a partially filled 3d electronic band and O representing oxygen ions. Transition metal oxides [135] have been a hot topic of research for the last 30 years for their plethora of interesting physical effects and ground states (superconducting [133], ferroelectric [136], ferromagnetic, antiferromagnetic [137], half-metallic [138], Mot insulators [139], semiconducting [140] among others) which, in addition to their fundamental interest, can have various applications for technological devices (for examples, for memory devices [141], electronics and spintronics applications [142], neuromorphic [94], and many more).

In addition to cuprates, many other families of high critical temperature superconductors have been discovered along the years including iron-based superconductors [143], nickelates [144] and carbon-based superconductors [145], which, in some cases, are suspected to share physical mechanisms with the cuprates. Iron-based superconductivity was discovered during the late 2000s by Kamihara *et al.* [146] while studying LaFePO below 4 K and designate materials compounds made of layers of iron and a pnictogen (a chemical element in group 15 of the periodic table, typically arsenic or phosporous). These materials display critical temperatures up to 111 K, as was reported by Jian-

Feng *et al.* [147] in 2015 in single-layer FeSe thin films on $SrTiO_3$, making iron-based superconductors the family with the second highest superconducting critical temperature after the cuprates.

2.2. The archetypal cuprate superconductor YBCO

2.2.1. Crystallographic description

Yttrium barium copper oxide ($YBa_2Cu_3O_{7-x}$ or YBCO) is characterized by a structure related to the perovskites, made of alternating layers of copper oxides plane CuO_2 and other metal oxides as depicted in **Fig. 2.5(a)** [148]. It crystallizes in an orthorhombic geometry, with lattice parameters $a = 3.82$ Å, $b = 3.89$ Å and $c = 11.68$ Å. The two main features of the structure are the CuO_2 planes and the so-called CuO chains alongside the b crystallographic direction. The CuO chains are thought to act as a charge reservoir for electrons to be transferred to the CuO_2 planes [149].

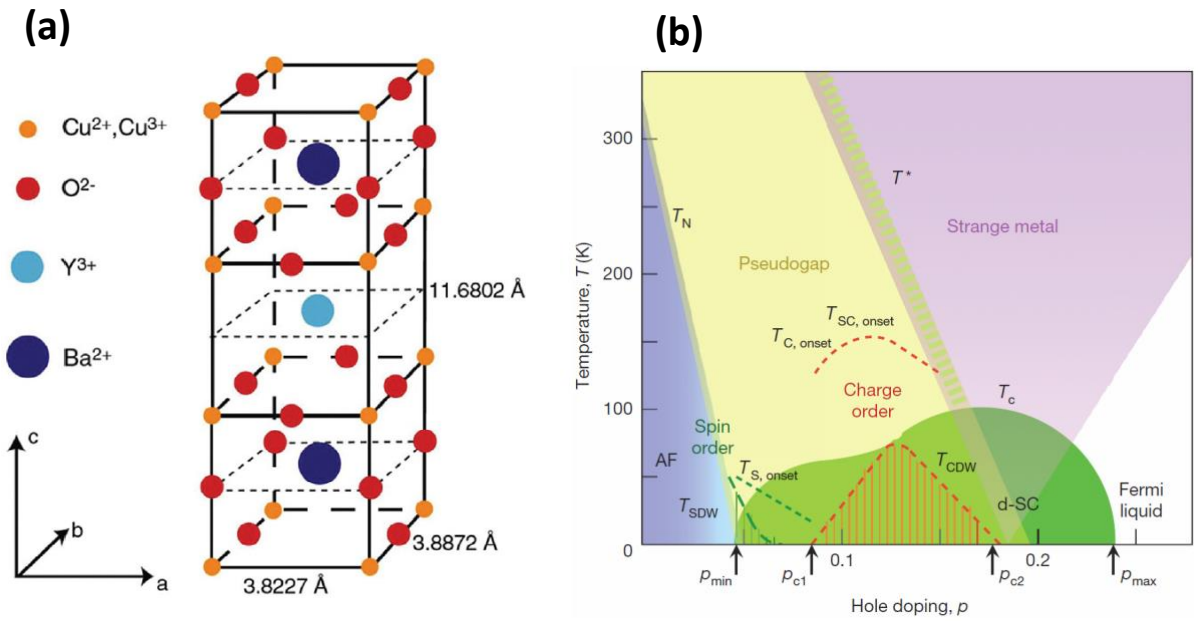

Fig. 2.5: (a) Crystallographic structure of YBCO with alternating layers of CuO_2 planes with Y and BaO layers. Figure taken from Ainslie, PhD thesis (2016) [148]. (b) Schematic temperature-doping phase diagram of YBCO exhibiting various different phases such as the insulating AF region, the pseudogap phase or the strange metal phase. The superconducting dome (in green) appears for doping values between $p_{min} = 0.05$ and $p_{max} = 0.24$, showing that there exists an optimal value of the doping $p = 0.18$ yielding a maximum critical temperature $T_C = 92\ K$. Figure taken from Taillefer et al., Annu. Rev. Condens. Matter. Phys. (2010) [7,8].

2.2.2. Phase diagram and different exotic phases

All cuprate superconductors have a similar temperature-doping phase diagram, schematically illustrated in **Fig. 2.5(b)** [7,8], showing the different conducting phases of YBCO as a function of the temperature (y-axis) and the hole doping concentration p (number of holes per copper atom, x-axis) within the structure. Therefore, p is a parameter of crucial importance for the superconducting properties of cuprates. The parent undoped compound of YBCO ($p = 0$) is an antiferromagnetic Mott

insulator having a Néel temperature $T_N = 500\ K$ [150], above which the antiferromagnetic order collapses and the material becomes paramagnetic. For higher doping content, and sufficiently low temperature, the phase diagram exhibits what is referred as the superconducting dome: for $0.05 < p < 0.24$, YBCO is superconducting, and T_C reaches a maximum value of $92\ K$ for an optimal doping $p = 0.18$. There exist multiple strategies for locally modifying YBCO's hole doping concentration, for example through a controlled motion of oxygen ions [151] that can be triggered by annealing [152], illumination [93], redox reactions [153,154] or high current-densities [155–157]. In fact, the CuO_2 planes (a feature common to all cuprate superconductors) play a key role in the emergence of superconductivity in the cuprates, making them extremely sensitive to oxygen stoichiometry [158]: changing the amount of oxygen in the structure translates to modifying the charge carrier density and the hole doping p. The controlled motion of oxygen ions within the crystalline structure of YBCO is the topic of **Chapter 4**, where the possibility to modulate YBCO's superconducting properties through the thermomigration of oxygen will be demonstrated.

Although the phase diagram of YBCO has been extensively studied for several decades, the origin of the different exotic phases for high doping and temperature above T_C remains a major puzzle in condensed matter physics. The strange metal phase is characterized by a linear-in-T behaviour of the resistivity as long as superconductivity is suppressed [133]. Whereas this linearity is also observed in some normal metals for very high temperatures where phonon scattering dominates the transport properties [159], cuprates uniquely show this linearity for low temperatures. The strange metal phase is lost for extremely high doping content where YBCO acts as a usual Fermi liquid, displaying a T^2-dependence of the resistivity. This elusive phase is generally attributed to strong quantum fluctuations associated with the quantum critical point denoted as p_{c2} in **Fig. 2.5(b)**.

Another very interesting phase is the so-called pseudogap phase, arising for temperature above T_C and a doping level intermediate between the AF Mott insulating phase and the strange metal phase. In this state, YBCO exhibits a partial gapping of the conduction electrons [160]. The mechanism behind this very controversial phase is still a hot topic of debate, as many physicists are giving multiple possible explanations. As a matter of fact, it is not even known if this gap is related to superconducting properties or not. Some studies [161,162] show that this phase could be the pre-manifestation of the Cooper pairing mechanism: electrons may condense into pairs below a transition temperature T^* (the pseudogap temperature) and the pseudogap is produced by incoherent fluctuations of the pairing field at high temperatures

2.2.3. S-wave and d-wave pairing mechanisms

In conventional superconductors, described by the BCS theory, the pairing mechanism responsible for the electrons to condense into singlet Cooper pairs is mediated by a phonon-induced attractive force, *i.e.* through lattice deformations. Within this framework, it is assumed that the Fermi surface is spherical and isotropic in $\vec{k}$-space, as is depicted in **Fig. 2.6(a)** [163]. This property leads to an isotropic superconducting gap $\Delta(T)$ and explains most of the exotic properties of conventional low critical temperature superconductors. This conventional type of superconductivity is known as s-wave superconductivity.

However, it was soon realized after the discovery of cuprate superconductors that the BCS theory could not fully describe the appearance of superconducting correlations in these materials and that the nature of the pairing mechanism must have a different origin. Bickers *et al.* [164] first proposed in

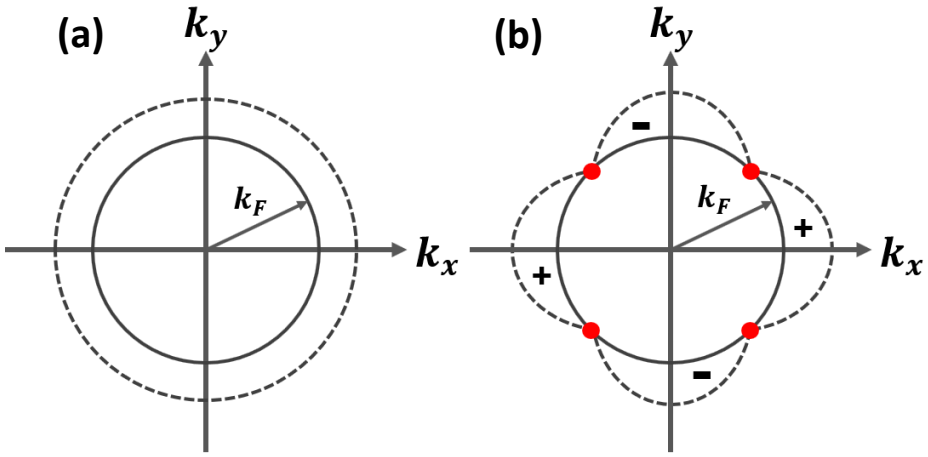

Fig. 2.6: Fermi surface representation in $\vec{k}$-space of a (a) s-wave superconductor and a (b) d-wave superconductor. In the case of a s-wave superconductor, the Fermi surface is isotropic whereas for a d-wave superconductor, the Fermi surface, as well as the superconducting gap Δ are anisotropic: there exist four nodal points where the superconducting gap reduces. Figure adapted from Armitage et al., online (2011) [163].

1987 a d-wave pair symmetry of the cuprate superconductors and a few important theories followed, using spin-fluctuation theory to account for a $d_{x^2-y^2}$ symmetry [164–166]. Derived from these theories, the superconducting gap of d-wave superconductors was shown to exhibit an anisotropic behaviour in the form of:

$$\Delta(\vec{k},T) = \Delta_0(T)\left|\cos(k_x a) - \cos(k_y a)\right| \tag{2.9}$$

where $\vec{k} = (k_x, k_y)$ is the wavevector, $\Delta_0(T)$ is the maximum value of the energy gap at a fixed temperature T and a is the distance between two adjacent copper atoms in a CuO plane. The d-wave symmetry is schematically shown in **Fig. 2.6(b)**, showing the Fermi surface in a $d_{x^2-y^2}$ symmetry [163]. The most important feature of this pairing symmetry is the existence of favoured directions for which the superconducting gap is drastically reduced around four nodal points, depicted with red points in **Fig. 2.6(b)** [163]. After these theoretical predictions, the d-wave properties of cuprate superconductors have been experimentally verified through multiple experiments, notably through angle-resolved photoemission spectroscopy (ARPES) [167], penetration lengths measurements [168] and by measuring the angular dependence of the Josephson critical current density [169].

One important consequence of the d-wave pairing mechanism is the extreme sensibility of a cuprate's superconducting correlations to structural disorder [158]. In fact, the anisotropic profile of the superconducting gap implies that scattering events due to isolated impurities lead to a fast decrease of the critical temperature. The impurities act as depairing centers due to the strong anisotropy of the wave vector [170]. This effect was experimentally investigated by Lesueur *et al.* [158] in 1990 while studying the consequences of an irradiation-induced disorder on the critical temperature of YBCO thin films.

3. Fundamentals of ferromagnetism

3.1. Microscopic description of itinerant ferromagnetism

Magnetism is a macroscopic quantum-mechanical phenomenon that is intrinsic of any material and originates from the dynamics of the magnetic moments of the atoms' orbiting electrons. All existing substances are susceptible to magnetic fields, although most of the time the magnetic response is so small that it can only be measured with extremely sensible sensors, and these substances are often qualified as non-magnetic in everyday life. There exist different types of magnetism, depending on how the electrons' magnetic moments interact together. We can distinguish between five main categories, namely diamagnetism, paramagnetism, antiferromagnetism [**Fig. 2.7(a)**], ferrimagnetism [**Fig. 2.7(b)**] and ferromagnetism [**Fig. 2.7(c)**].

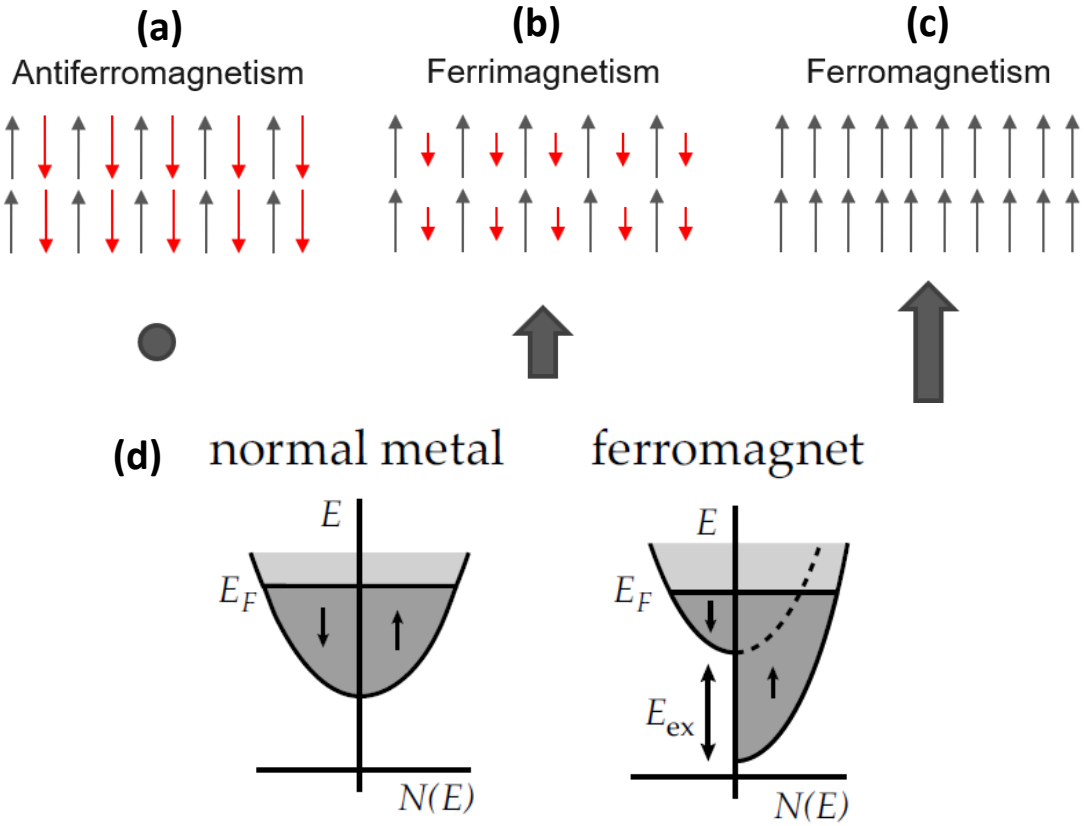

Fig. 2.7: Schematic description of the spin ordering in a (a) antiferromagnet, (b) ferrimagnet and (c) ferromagnet. (d) Filling of the density of states E vs. $N(E)$ for a normal metal and a ferromagnet, with E_F the Fermi energy and E_{ex} the exchange energy. In the case of a ferromagnet, the shift in the density of states for spin up and spin down leads to an imbalance between the two populations: they are designed as the majority and minority charge carriers, respectively. Figure taken from Flokstra, PhD thesis (2010) [102].

The magnetic description of a material requires two main vectors: the magnetic field $\vec{H}$ measured in $A.m^{-1}$ and the magnetic flux density $\vec{B}$ measured in T. These two vectors are linked through a third quantity, known as the magnetization $\vec{M}$, which is defined as the density of microscopic magnetic moments per volume unity. These three vectors relate through the relation (using SI units):

$$\vec{B} = \mu_0(\vec{H} + \vec{M}) = \mu_0(1 + \chi_V)\vec{H} \qquad (2.10)$$

where μ_0 is the vacuum permeability and χ_V is the volume magnetic susceptibility. The magnetic susceptibility represents a measure of how strongly a material will magnetize under an applied external magnetic field.

Whereas diamagnetism and paramagnetism do not exhibit a net magnetization in the absence of an applied external magnetic field, ferromagnetic materials are characterized by their spontaneous magnetization. Ferromagnetism and antiferromagnetism arise from the exchange coupling mechanism, a quantum phenomenon that describes the interactions between two neighbouring spins S_1 and S_2 through the Hamiltonian [171]:

$$H = -2J\hat{S}_1 \times \hat{S}_2 \tag{2.11}$$

where J is the coupling constant and $\hat{S}_1$ and $\hat{S}_2$ are dimensionless spin operators. The derivation was first done by Heisenberg [172] and the details of the derivation can be found in Coey (2010) [171]. The nature of the spins' interactions depends on the sign of the coupling constant: $J < 0$ leads to a ferromagnetic phase ordering, whereas $J > 0$ leads to an antiferromagnetic ground state. Therefore, electrons in ferromagnetic materials tend to align in the same direction under the action of the exchange field, contributing to a collective net magnetic moment, depicted in **Fig. 2.7(c)**. The most common ferromagnets are the transition metals (such as iron, cobalt and their alloys) and alloys of rare-earth metals. Alloys of neodymium and iron ($Nd_2Fe_{14}B$) are particularly well-known for their very strong ferromagnetic order, allowing for the engineering of permanent magnets with a magnetic remanence up to $1.4\ T$. In the rest of this sub-chapter, the basics of itinerant ferromagnetism will be addressed: the magnetic properties of the material are transported by the spins of electrons within the conduction band. This theory is well fitted to describe the magnetic behaviour of iron, cobalt, nickel and their alloys, as well as some half-metallic materials, which will be the subject of **Sect. 3.5.**

Fig. 2.7(d) shows the filling of the density of states (DOS) of a normal metal (left) and a ferromagnet (right) [102]. In a normal metal, the two spin bands for electrons with a spin up or a spin down are equally filled up to the Fermi energy, whereas in a ferromagnet, the ordering of the spins creates an asymmetric shift of the two spin bands' populations. One spin band is favoured (the majority band), with a higher number of electrons, while the other (the minority band) contains a lower number of electrons. Exchanges in ferromagnetic materials create a spin-splitting of the conducting bands by a factor E_{ex}, called the exchange energy. The net spin polarization P is expressed using the density of state for each spin population $N_\uparrow(E)$ (density of states of spin up electrons for a given energy E) and $N_\downarrow(E)$ (density of states of spin down electrons for a given energy E), yielding the equation:

$$P = \frac{N_\uparrow(E_F) - N_\downarrow(E_F)}{N_\uparrow(E_F) + N_\downarrow(E_F)} \tag{2.12}$$

Ferrimagnetic materials, on the other hand, are antiferromagnetic materials with uncompensated lattices. In fact, the spins' interactions are dictated by an antiferromagnetic ordering $(J > 0)$ but one spin direction has a lower magnetic moment than the other (uncompensation), as depicted in **Fig. 2.7(b)**, leading to magnetic properties closely related to ferromagnetism. In fact, ferromagnetism and ferrimagnetism were thought to be a unique phenomenon before Louis Néel and Charles Guillaud discovered in 1936 that ferromagnetism could not explain the magnetic behaviour of Mn_2Sb and introduced the theoretical concept of ferrimagnetism [173,174].

3.2. Curie temperature

The ferromagnetic order onsets at a temperature above which the thermal energy will lead to the randomization of the spins' directions, effectively suppressing the ferromagnetic properties. This temperature is referred to as the Curie temperature T_{Curie} named after the French physicist Pierre Curie following the discovery that the net magnetization of permanent magnets is lost above a specific temperature, characteristic of the material. It corresponds to the phase transition between a ferromagnet and a paramagnet, and is analogous to the Néel temperature of antiferromagnets.

While in the paramagnetic state, for a temperature above the Curie temperature, the susceptibility of a ferromagnet is described by the Curie-Weiss law

$$\chi(T) = \frac{C}{T - T_{Curie}} \tag{2.13}$$

where C is a material-specific constant.

The typical T_{Curie} of single elements ferromagnets varies between a few Kelvin to a few thousands. As an example, gadolinium exhibits a T_{Curie} of $\sim 292\ K = 19\ °C$ while cobalt is known for having a relatively high T_{Curie} of $\sim 1394\ K = 1121\ °C$.

3.3. Switching of magnetic domains

At equilibrium, the magnetization inside a ferromagnet is generally not uniform: it is energetically more favourable to reduce the magnetostatic energy by sectionalizing the magnetic background into smaller regions having uniform magnetizations, known as magnetic domains. Each domain has a single orientation of the magnetization vector, and the regions separating the magnetic domains are referred to as domain walls. As any physical phenomenon, the transition of the magnetization between the value of one domain to the value of the other cannot happen abruptly at the domain wall. We can distinguish between two main types of domain walls depending on their spin texture, namely Bloch walls and Néel walls. **Fig. 2.8** shows a schematic representation of these two types of walls [175]. A Bloch wall [**Fig. 2.8(a)**] is characterized by a spin rotation axis being orthogonal to the wall, while in a Néel wall [**Fig. 2.8(b)**], the magnetization rotates alongside an axis which is parallel to the wall. The size d_{wall} and the type of a domain wall depends mainly on the magneto crystalline anisotropy of the ferromagnet (the magnetic field needed to magnetize the material is lower in certain directions) and the strength of the exchange interactions (meaning the value of E_{ex}) as well as the film's thickness [176]. The density of defects in the material can also induce local changes in the formation and structure of domain walls [177]. d_{wall} typically range between $5\ nm$ to hundreds of nm [178].

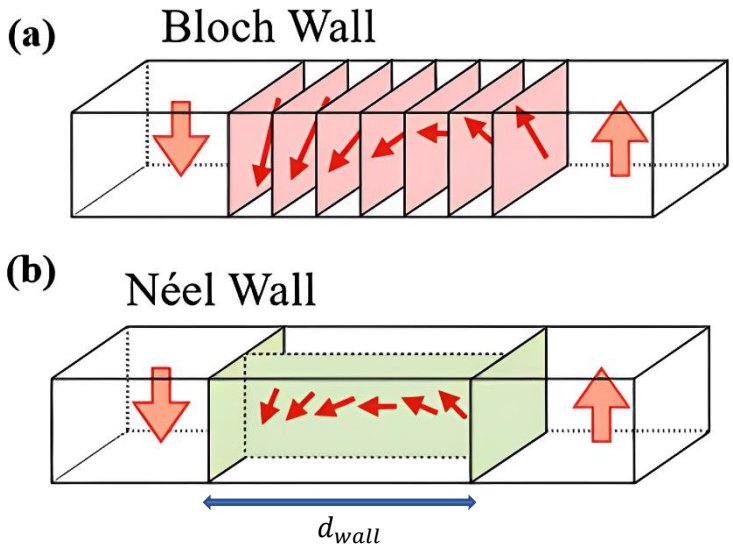

Fig. 2.8: (a) Schematic representation of a Bloch wall, displaying a smooth transition between the two magnetisations on each side with a rotation axis orthogonal to the wall (b) Schematic representation of a Néel wall, the rotation axis of the transition being parallel to the wall. Figure adapted from Seki (2015) [175].

3.4. Magnetization reversal and hysteresis loop

The characterization of the typical properties and parameters of ferromagnetic materials is usually studied through magnetization hysteresis loops $M(B)$ measurements and an example of such a loop is depicted in **Fig. 2.9**. This experiment allows to define and quantify three very important properties of ferromagnets: coercivity, remanence and saturation. Magnetic saturation is the magnetic state defined by a constant magnetization and is reached after increasing the external magnetic field over the saturation field B_{sat}. The coercive field B_C of a ferromagnet is defined as the field necessary to restore zero magnetization from saturation (Aschroft [179], Solid State Physics, p. 722). The coercive

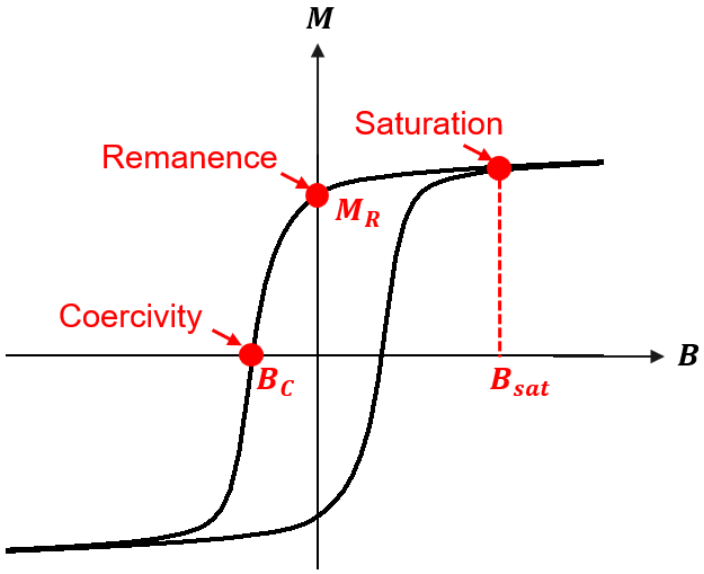

Fig. 2.9: Typical magnetization vs magnetic field hysteresis loop of a ferromagnetic material, showing three of the most important properties of ferromagnets: coercivity, remanence (or retentivity) and saturation.

field of a ferromagnet thin film depends on multiple parameters, such as the temperature and the thickness of the film [17,18]:

- The thinner the ferromagnetic layer, the larger B_C becomes.
- The coercive field of ferromagnetic materials is expected to increase at low temperatures as a consequence of the lowering of the thermal fluctuations, enhancing the magnetic field required to switch magnetic domains' magnetizations.

Finally, remanence represents the magnetization M_R that a ferromagnet can naturally exhibit after the removal of the external magnetic field.

3.5. Half-metallic ferromagnetic materials

3.5.1. Definition

Half-metallic materials, discovered in 1983 by de Groot *et al.* [180], correspond to ferromagnets acting as an insulator to one spin orientation while acting as a conductor for the other [181]. It corresponds to the extreme case of a ferromagnet with an exchange energy being large enough to allow one spin band population to shift above the Fermi energy, as depicted in **Fig. 2.10(a)** in the filling of the DOS [182]. The half-metallic property of magnetic materials is usually deduced from spin resolved photoemission spectroscopy, a technique probing the spin dependent elastic and inelastic scattering processes between photoelectrons and electrons [183]. These materials are of great theoretical and practical interest because charge carriers are $100\ \%$ spin-polarized ($P = 1$ in **Eq. 2.12**) for vanishing temperatures, although the spin-polarization might be lower for non-zero temperatures due to spin-orbit interactions. Nowadays, a few families of materials have shown half-metallic properties, the most studied ones being the Heusler alloys, manganites and chromium dioxide [184–187].

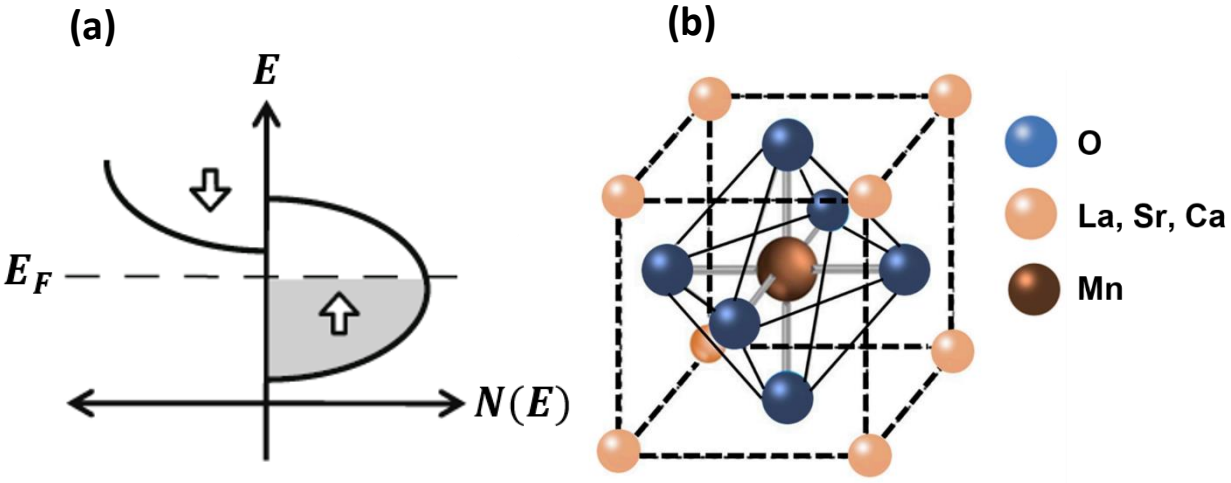

Fig. 2.10: (a) Filling of the density of states E vs. $N(E)$ for a half-metallic material. In the case represented here, the material is acting as an insulator for spin down electrons, while acting as a conductor for spin up electrons. Figure taken from Korkin (2008) [182]. (b) Representation of the unit cell for LSMO and LCMO crystals. They both share a perovskite crystal structure, as is the case for YBCO. Figure adapted from Md Saif Hasan et al., Processes (2022) [188].

3.5.2. Manganite half-metals: LSMO and LCMO

Chapter 5 will be dedicated to the study of heterostructures made from YBCO and two half-metallic manganites, namely $La_{1-x}Sr_xMnO_3$ (LSMO) and $La_{1-x}Ca_xMnO_3$ (LCMO). Manganite materials have a general chemical formula $T_{1-x}D_xMnO_3$ where T is a trivalent ion and D a divalent ion. They crystallize in a perovskite structure, making them perfectly fit to share epitaxial interfaces with YBCO [see **Fig. 2.10(b)** for a schematic figure of a unit cell for these kind of materials [188]]. They both display very intricates phase-diagrams, illustrated in **Fig. 2.11**, showing that depending on the doping level and the temperature, it is possible to induce ferromagnetic to antiferromagnetic as well as metal to insulator phase transitions [189,190]. Importantly, they both have a relatively high Curie temperature of $T_{Curie}^{LSMO} \approx 350\ K$ in the case of LSMO and $T_{Curie}^{LCMO} \approx 280\ K$ in the case of LCMO, for optimally doped materials. Especially, LSMO's Curie temperature is above room temperature for a wide range of strontium concentration, greatly enhancing the potential for technological applications. Note that in **Fig. 2.11**, T_C represents the Curie temperature and not the superconducting critical temperature.

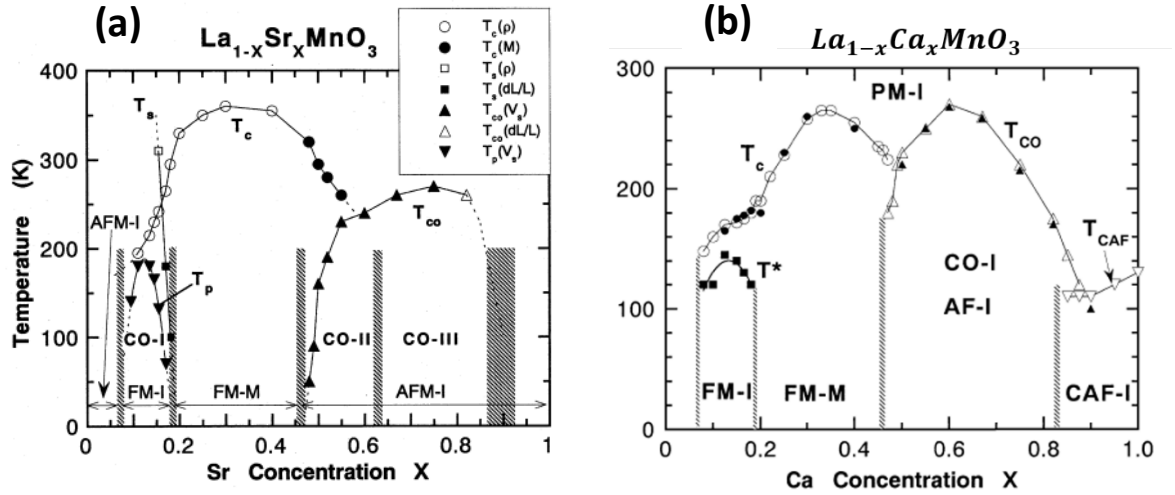

Fig. 2.11: (a) Temperature-doping phase diagram of LSMO for a strontium doping between 0 and 1. Figure taken from Fujishiro et al., Phys. Soc. Japan (1998) [189]. (b) Temperature-doping phase diagram of LCMO for a calcium doping between 0 and 1. Figure taken from Fujishiro et al., Phys. Soc. Japan (2001) [190].

3.5.3. Colossal magnetoresistance

One of the most important property of manganite half-metals is the so-called colossal magnetoresistance (CMR), which describes a drastic change of the resistivity upon application of an external magnetic field. This behaviour may be promising for various applications in data storage or magnetic field sensing [186]. The most complete understanding of this phenomenon is achieved through an interplay between double-exchange mechanisms and Jahn-Teller effects [191]:

(i) **Double-exchange mechanism:** magnetic interactions arising between two ions with different oxidation states, *i.e.* when one atom has one more electron compared to the other [192].

(ii) **Jahn-Teller distortion:** geometrical distortion of the crystal's lattice in order to lower its ground state energy [193].

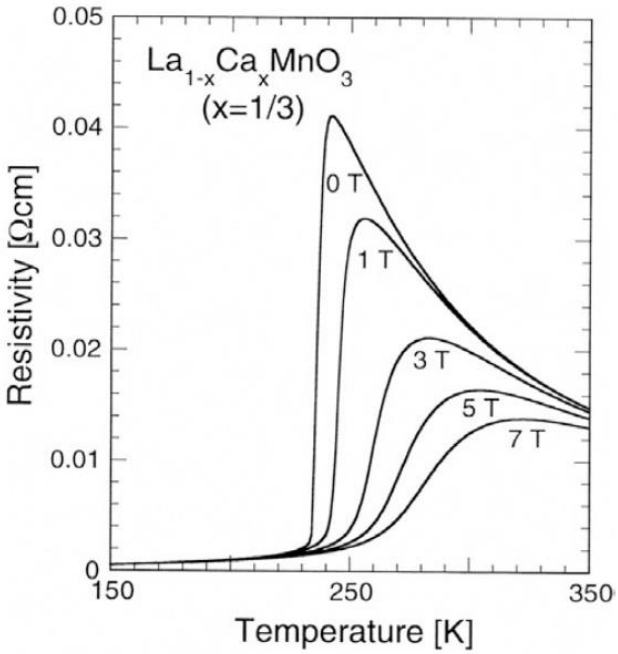

Fig. 2.12: Resistivity in $\Omega.cm$ of a LCMO thin film ($x = 0.33$) as a function of the temperature for different fixed values of the external magnetic field. As the field is ramped up from $0\ T$ to $7\ T$, we see a decrease of the resistivity particularly pronounced close the Curie temperature of LCMO, $T_{Curie}^{LCMO} \approx 280\ K$, typical of the colossal magnetoresistance effect. Figure taken from Tokura, Reports on progress in physics (2006) [194].

Fig. 2.12 illustrates the CMR effect measured on a LCMO crystal ($x = 0.25$) for different constant external magnetic fields [194]. One can observe that the highest change of the resistivity as a function of the magnetic field is confined near LCMO's curie temperature, $T_{Curie}^{LCMO} \approx 280\ K$.

3.5.4. Magnetic tunnel junctions made from half-metallic ferromagnets

Manganites are ideal candidates for the engineering of spin valve structures and magnetic tunnel junctions due to the 100 % spin-polarized property of the conducting electrons, a property of great technological importance in the field of spintronics. Spin valve structures, made of two magnetically active conducting electrodes sandwiching a non-magnetic thin layer (often referred to as the spacer), are devices whose resistance can be tuned between a high-resistive state and a low-resistive state by changing the relative orientations of the magnetizations of the magnetic layers. If the spacer is insulating, the spin valve is called a magnetic tunnel junction (MTJ).

In particular, Bowen *et al.* [195,196] investigated in 2007 the evolution of the electrical resistance upon application of a magnetic field on a LSMO/$SrTiO_3$/LSMO MTJ, showing a tunnelling magnetoresistance as high as $\sim 1850\ \%$ at $T = 4\ K$ and demonstrating the possibility to reach a spin polarization of $99\ \%$. More experiments on magnetic tunnel junctions include, for example, LSMO/$SrTiO_3$/$Co_{1-x}Cr_x$ trilayers [197], $MnGeSe_3$/CrI_3 heterostructures [198] or NiMnSb/Mo/NiMnSb trilayers [199], among many other studies. Therefore, magnetic tunnel junctions made from half-metallic materials are very promising candidates for a plethora of technological applications in the fields of non-volatile magnetic memories (magnetic random access memory, MRAM) [200], sensing [201] and neuromorphic [94], to cite a few.

3.5.5. Magnetic domains' structure

Of great interest in this thesis, more precisely in **Chapter 5** while studying spin valve structures made from superconductors and half-metallic materials, is the magnetic structure of the manganite while in contact with YBCO, *i.e.* the typical size of a magnetic domain and the corresponding domain walls properties. Photoemission electron microscopy (PEEM) and X-ray magnetic circular dichroism (XMCD) experiments were performed by Sanchez *et al.* [19] in Madrid, measuring magnetic profiles of a thin layer of LSMO deposited on top of YBCO after applying a fixed in-plane magnetic field of $B = 0.125\ T$. The results are displayed in **Fig. 2.13**, showing two magnetic profiles for temperatures of $T = 45\ K$ [**Fig. 2.13(a)**] and $T = 120\ K$ [**Fig. 2.13(b)**], above and below the superconducting transition, respectively. The main conclusions of this experiment are:

(i) The domains have a filamentary structure, developing perpendicular to the applied external magnetic field, alongside the [110] crystallographic direction. This direction is known to be one of the typical easy axis of a thin manganite layer. The typical domain width is approximately of 1-2 microns, while the size of a domain wall amounts for a few tens of nanometres. The domain walls were found to be of Bloch-type in LSMO in the experiments illustrated in this section [19].

(ii) The density of magnetic domains increases drastically below the superconducting critical temperature.

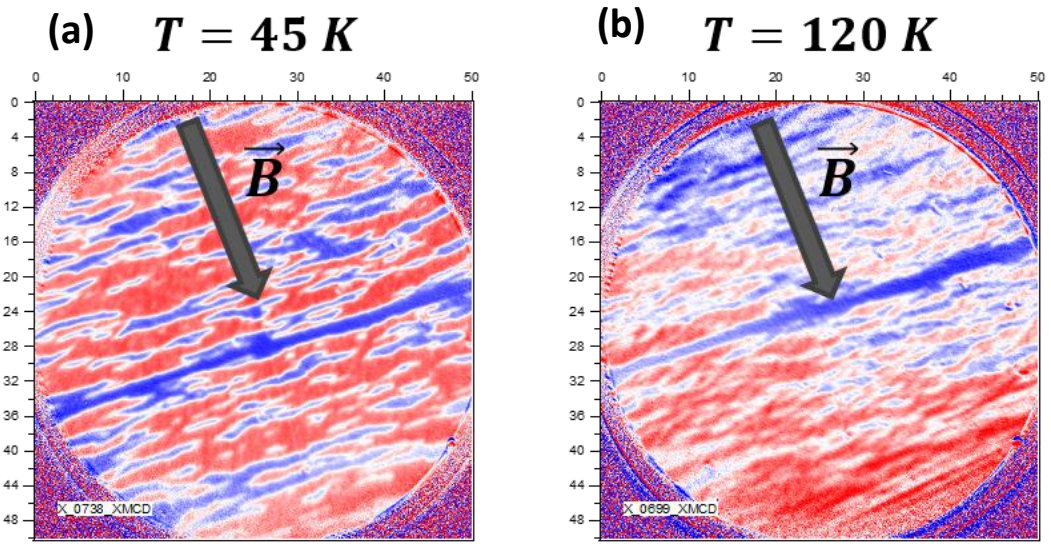

Fig. 2.13: Images of a thin layer of LSMO deposited on top of a YBCO layer after application of an in-plane magnetic field equals to $B = 0.125\ T$ for a temperature of (a) $T = 45\ K$ and (b) $T = 120\ K$. We observe the formation of magnetic domains with a magnetic contrast being calculated using X-ray magnetic circular dichroism (XMCD). The size of one picture is $50 \times 50\ \mu m^2$. Figures adapted from Sanchez, PhD thesis (2021) [19].

4. Superconducting proximity effect

Interfaces made from materials with different physical properties (*e.g.* a superconductor and a metal), or even antagonistic phase ordering (*e.g.* a superconductor and a ferromagnet), always are interesting systems to study from a theoretical point of view. Mixing very different states of matter

can help understanding the underlying properties of both materials independently, and sometimes gives rise to novel effects and fields of research. In this section, the basics of the superconducting proximity effect will be reviewed: although a Cooper pair can only be formed in the interior of a superconductor (as being an eigen-function of the system's Hamiltonian), it can be transferred into an adjacent layer via the mechanism of Andreev reflections.

4.1. Andreev reflections

Andreev reflection describes an interface mechanism via which a flow of electrons (an electrical current) is converted into a supercurrent carried by Cooper pairs [46]. This effect is summarized schematically in **Fig. 2.14(a)**, depicting an interface between a superconductor (S) on the left and a normal metal (N) on the right. An incoming electron with an energy inferior to the superconducting gap Δ coming from N will form a Cooper pair at the interface, by retroreflecting a hole with opposite spin and opposite velocity. The inverse process, with an incoming Cooper pair is also possible via time-reversal symmetry. This mechanism allows a supercurrent to be converted into a normal electrical current at a well-designed interface. On the other hand, if the interface transparency between both materials is too low, Andreev reflections are hindered and instead, conventional electron-retroreflection is promoted. Each Andreev reflection correspond to a transfer of a charge 2e across the interface.

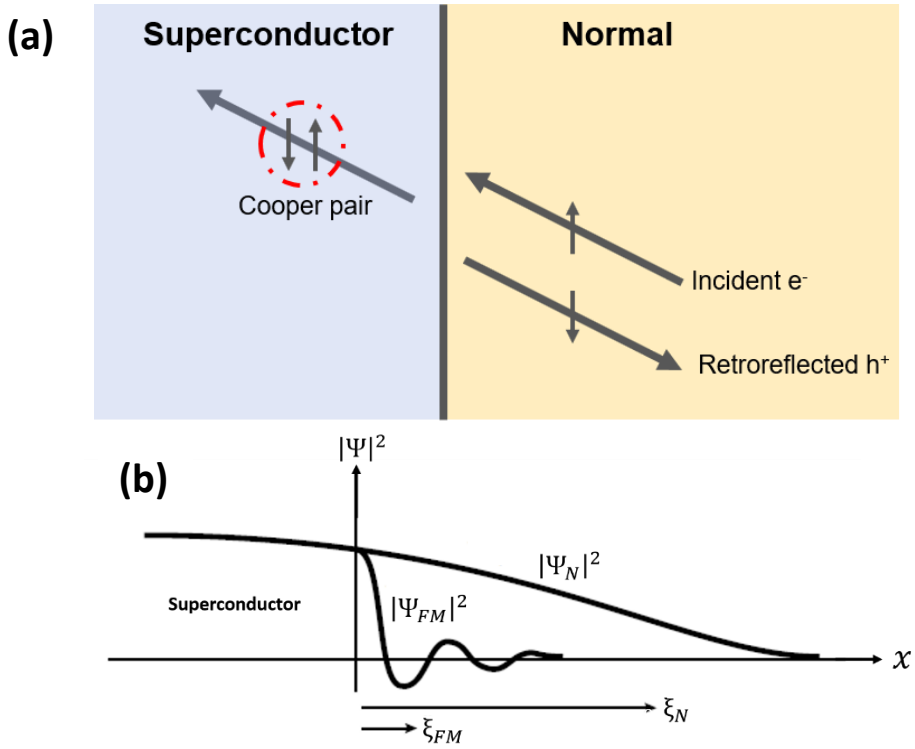

Fig. 2.14: (a) Schematic representation of the Andreev reflection mechanism at a superconductor/normal interface. This process involves an incoming spin up (down) electron e^- arriving at the interface from the N layer, generating a Cooper pair within the superconductor by reflecting a spin down (up) hole h^+ in the opposite direction with opposite velocity. (b) Probability amplitude of the superconducting wavefunction Ψ as a function of the distance x in the case of S/N and S/FM interfaces. The probability to find a Cooper pair within the ferromagnetic region decays much faster compared to the case of a normal metal. Moreover, the probability amplitude oscillates, indicating that the nature of the proximity effect is different in both cases. Figure adapted from Flokstra, PhD thesis (2010) [102].

Andreev reflection is the phenomenon responsible for the proximity effect in metals in contact with superconductors. The consequences of the proximity effect are twofold: the leakage of the superconducting correlations inside the adjacent non-superconducting layer, as well as a reduction of the interfacial superconducting pair-density inside the superconducting layer. This is shown in **Fig. 2.14(b)** [102], displaying the pair density (the squared modulus of the superconducting wavefunction Ψ) at the interface between a superconducting and another material: $|\Psi_N(x)|^2$ corresponds to the probability to find Cooper pairs at a distance x from an S/N interface, while $|\Psi_S(x)|^2$ is a similar quantity in the case of a S/FM interface [102]. We can notice that in the case of a ferromagnet, the supercurrent cannot survive as long as in a normal metal. This is due to the pair breaking effect of the exchange field, which tends to align electronic spins and is thus antagonistic with the singlet (opposite spins) pairing. This phenomenon decreases the distance ξ_F over which the supercurrent can survive inside the ferromagnet. The stronger the exchange field, the shorter the distance ξ_F.

4.2. Proximity effect at S/N interfaces

4.2.1. Case of an s-wave superconductor in contact with a normal metal

The bias-dependent differential conductance of an interface between an s-wave superconductor and a normal metal has been theoretically studied in 1982 by Blonder, Tinkham and Klapwijk and is known as the BTK model [128]. It accurately predicts the behaviour of the S/N interface by considering a non-ideal contact with the occurrence of both Andreev reflections and retroreflections, for example due to impurities at the interface, as well as electrons transmission above the superconducting energy gap. The derived equation for the differential conductance for $T = 0\ K$ takes the form:

$$G_{SN}^{S} = \frac{dI}{dV} = G_N[1 + |a(E,Z)|^2 - |b(E,Z)|^2] \tag{2.14}$$

where G_N is the conductance of the interface in the normal state, $a(E,Z)$ describes the probability for Andreev reflections to occur and $b(E,Z)$ the probability for normal reflections to occur. These two functions are found through solving the Bogoliubov-de Gennes equation and the parameter Z accounts for the transparency of the barrier at the interface. In fact, $Z = 0$ corresponds to a perfectly transparent interface, while the case $Z \gg 1$ corresponds to a low transparency interface that behaves as a tunnel barrier. Both functions $a(E,Z)$ and $b(E,Z)$ tend toward 0 for high values of the energy, yielding $\lim_{E\to\infty}(G_{SN}^{S}) = G_N$.

Fig. 2.15 shows the normalized differential conductance calculated from **Eq. 2.14** plotted as a function of the normalized value of the energy for two different cases: **Fig. 2.15 (a)** corresponds to the perfectly transparent case while **Fig. 2.15 (b)** corresponds to an insulating contact [32]. We observe that for $Z = 0$, the sub-gap conductance is fully explained by Andreev reflections, as the differential conductance below the superconducting gap is governed by Cooper pairs with a charge of $2e$ and single electrons above the gap. For $Z \gg 1$, the BCS differential conductance is retrieved.

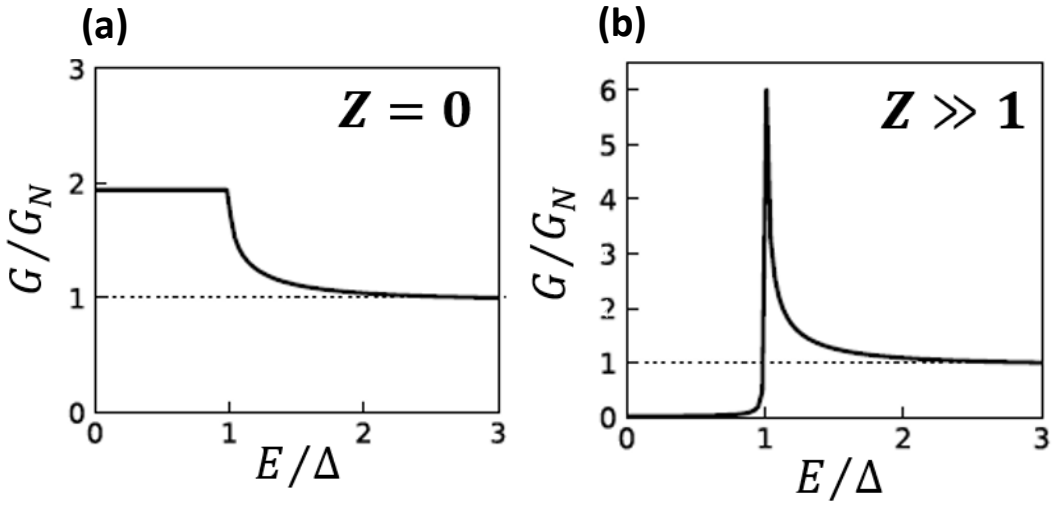

Fig. 2.15: Normalized differential conductance (divided by the conductance in the normal state G_N) as a function of the normalized energy (divided by the superconducting gap) at the interface between an s-wave superconductor and a normal metal for two different interface's transparencies: (a) completely transparent interface with $Z = 0$ and (b) insulating barrier with $Z \gg 1$. Figures adapted from Palermo, PhD thesis (2019) [32].

4.2.2. Case of a d-wave superconductor in contact with a normal metal

To account for the anisotropic behaviour of the superconducting gap in the case of a d-wave superconductor, Tanaka and Kashiwaya developed in 1995 an extension of the BTK theory [202,203]. The differential conductance at 0 K is now anisotropic and is dependent on the angle θ through the relation:

$$G_{SN}^{d}(\theta) = \frac{dI}{dV}(\theta) = G_N[1 + |a'(E,Z,\theta)|^2 - |b'(E,Z,\theta)|^2] \tag{2.15}$$

where the functions $a'(E,Z,\theta)$ and $b'(E,Z,\theta)$ are defined in the same way as in **Eq. 2.15** but now follow an angular dependence. θ represents the angle between the a-axis of the cuprate superconductor and the direction of the applied current. The exact formulation and derivation of these functions are detailed in the original paper by Tanaka and Kashiwaya [202]. **Fig. 2.17** depicts the behaviour of the normalized differential conductance as a function of the energy E normalized with respect to the superconducting gap for $Z = 0$ and $Z \gg 1$ in the case of an interface between a d-wave superconductor and a normal metal [32]. These graphs have been calculated for an interface orthogonal to the c-axis of the crystallographic structure. The general shapes of the tunnelling spectra observed in are similar to the ones of **Fig. 2.15**, although the features appear less sharp that in the case of an s-wave superconductor: the superconducting gap Δ is not as well-defined and the transitions between the normal and superconducting properties happen on a larger energy range. However, as a consequence of the asymmetry of the d-wave pairing mechanism, the conducting properties of the interface are expected to be largely dependent on the probing direction within the $\vec{k}$-space, especially along the nodal [110] and anti-nodal [100] directions, as depicted in **Fig. 2.16(a)**. The simulated normalized differential conductance of the d-wave S/N interface (for $Z \gg 1$) in the nodal [110] direction and the anti-nodal [100] direction are depicted in **Fig. 2.16 (b)** and **Fig. 2.16(c)**, respectively [204]. For the nodal configuration, the tunnelling spectrum is identical to the one of a typical BCS superconductor, as shown in **Fig. 2.15(b)**. However, in the case of the anti-nodal configuration, the pairing potentials experienced by the electron-like and hole-like quasiparticles are

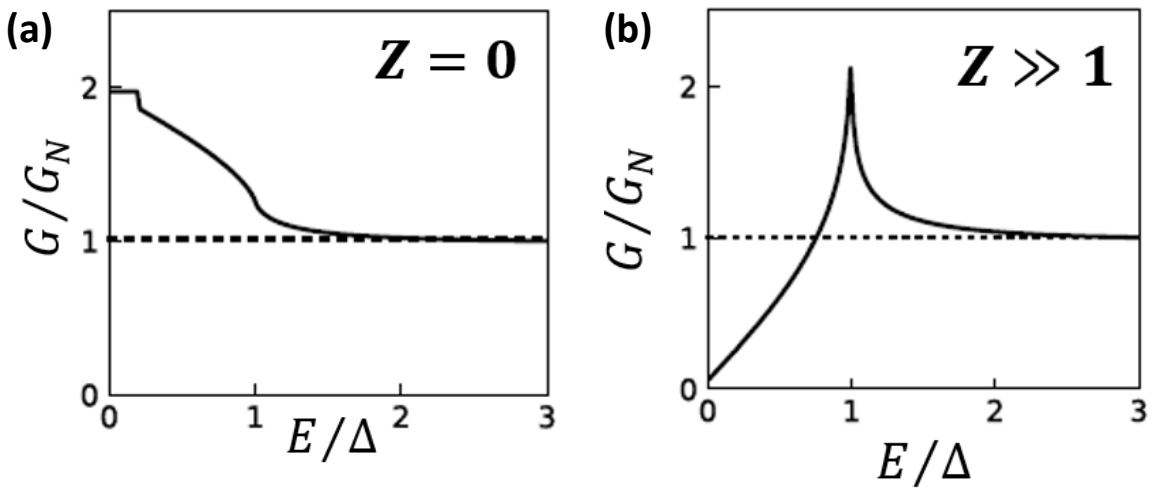

Fig. 2.17: Normalized differential conductance as a function of the normalized energy at the interface between a d-wave superconductor and a normal metal for two different interface's transparencies: (a) completely transparent interface with $Z = 0$ and (b) insulating barrier with $Z \gg 1$. Figures adapted from Palermo, PhD thesis (2019) [32].

opposite, leading to the existence of an Andreev bound state (zero-energy surface state), giving rise to a zero-energy conductance peak. This zero-bias conductance peak has been observed in a plethora of physical systems, including cuprate superconductors [205,206], Dirac semimetals [207] or topological insulators [208], among many others, and is an active topic of research for the characterization of unusual properties of electronic superconducting systems, for instance for the demonstration of Majorana bound states [209].

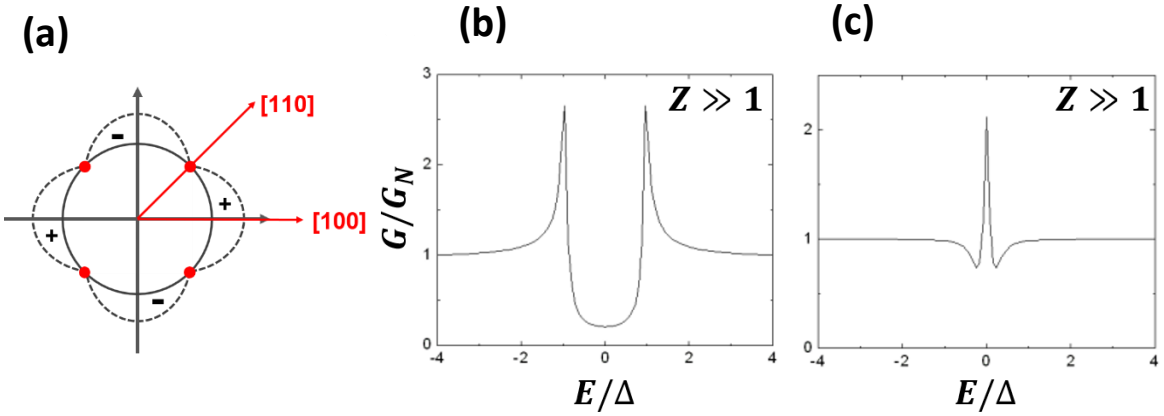

*Fig. 2.16: (a) Fermi surface representation in k-space of a d-wave superconductor, showing the nodal [110] and anti-nodal [100] directions along which the tunnelling spectra of **Fig. 2.16**(b) and **Fig. 2.16**(c) are simulated. (b) and (c) Normalized differential conductance as a function of the normalized energy at the interface between a d-wave superconductor and a normal metal for $Z \gg 1$ along the (a) nodal [100] direction and (b) anti-nodal [100] direction. Figure adapted from Chen, PhD thesis (2006) [204].*

4.3. Proximity effect at S/F interfaces

The ferromagnetic order, as seen previously in **Fig. 2.14(b)**, is incompatible with conventional (opposite spins) Cooper pairs. The exchange energy of a ferromagnet acts as a depairing mechanism on singlet Cooper pairs as it tends to align the electrons' spins in the same direction. Lately, a lot of attention has been brought to the creation and control of equal-spin triplet correlations that circumvent the antagonism between superconductivity and ferromagnetism.

4.3.1. Singlet proximity effect

In the case of a singlet superconductor/ferromagnet (S/FM) interface, the probability amplitude to find Cooper pairs in the ferromagnetic layer decays in a damped oscillatory manner away from the interface, as was shown in **Fig. 2.14 (b)**. This oscillatory property is a consequence of the finite center-of-mass momentum acquired by the Cooper pairs due to the different spin population for spin up and spin down electrons [210]. The distance ξ_F over which the superconducting correlations travel inside the ferromagnet is given by:

$$\xi_F = \frac{\hbar v_F}{2E_{ex}} \tag{2.16}$$

where v_F is the Fermi velocity and E_{ex} is the exchange energy of the involved ferromagnet. Typically, this value amounts for a few nm in the case of strong ferromagnets and vanishes for half-metals, in which the density of minority spins is nearly zero (strictly zero in perfect materials) thus precluding Andeev reflections. For comparison, a superconducting correlation can typically propagate a few hundreds of nm into normal metals.

4.3.2. Triplet proximity effect

At specific well-engineered S/FM interfaces, it has been shown that triplet correlations can be formed through spin-dependent scattering caused by magnetic inhomogeneities [105,106,111,112,211]. The process of creation of a triplet correlation can be understood through the mechanisms of spin mixing and spin rotation, depicted in **Fig. 2.18(a)** [104]. The wavefunction associated to a singlet Cooper pair can be written as:

$$\Psi^{singlet} = \sqrt{1/2}\,.\left(|\uparrow,\vec{k}\rangle|\downarrow,-\vec{k}\rangle - |\downarrow,\vec{k}\rangle|\uparrow,-\vec{k}\rangle\right) = \uparrow\downarrow - \downarrow\uparrow \tag{2.17}$$

where the quantum states $|x,y\rangle$ are written in the usual Dirac notation, x being the spin direction while y is the wavevector, and the second equality represent a typical simplified notation useful for clarity purposes. This quantum state exhibits a total net spin component $S = 0$, therefore is strongly affected by any exchange energy and magnetic field.

When a singlet Cooper pair arrives at a magnetically active interface with a ferromagnetic material, spin-dependent scattering can occur due to the Zeeman field that splits the majority and

minority spin carriers. Thus, the wavefunction experiences a spin-dependent shift of the phase, that can be written through the relations $|\uparrow,\vec{k}\rangle \propto e^{i\theta_\uparrow}|\uparrow,-\vec{k}\rangle$ and $|\downarrow,\vec{k}\rangle \propto e^{i\theta_\downarrow}|\downarrow,-\vec{k}\rangle$. Applying these two relations to **Eq. 2.17** yields a new wavefunction Ψ_n equal to:

$$\Psi_n = \alpha\cos(\Delta\theta)\Psi^{singlet} + \beta\sin(\Delta\theta)\Psi^{triplet}_{short} \tag{2.18}$$

where $\Delta\theta = \theta_\uparrow - \theta_\downarrow$, $\Psi^{triplet}_{short} = \uparrow\downarrow + \downarrow\uparrow$ and α and β are complex numbers. If $\Delta\theta = 0$, *i.e.* if the interface doesn't induce a shift of the wavefunction's phase, the triplet component disappears and only the singlet component remains.

We see from **Eq. 2.18** that the new wavefunction is a linear combination of a singlet state $\Psi_n = \uparrow\downarrow - \downarrow\uparrow$ and a triplet state $\Psi^{triplet}_{short} = \uparrow\downarrow + \downarrow\uparrow$. This triplet state corresponds to a quantum state with a net spin component $S_Z = 0$. It is sometimes referred to as the FFLO state in today's literature, named after P. Fulde, A. Ferrell, A. Larkin and Y. N. Ovchinnikov [212,213]. Because this triplet state doesn't carry a net spin polarization, it does not survive much longer into a ferromagnet compared to singlet correlations and thus is of low interest for superconducting spintronics applications. **Fig. 2.18(b)**

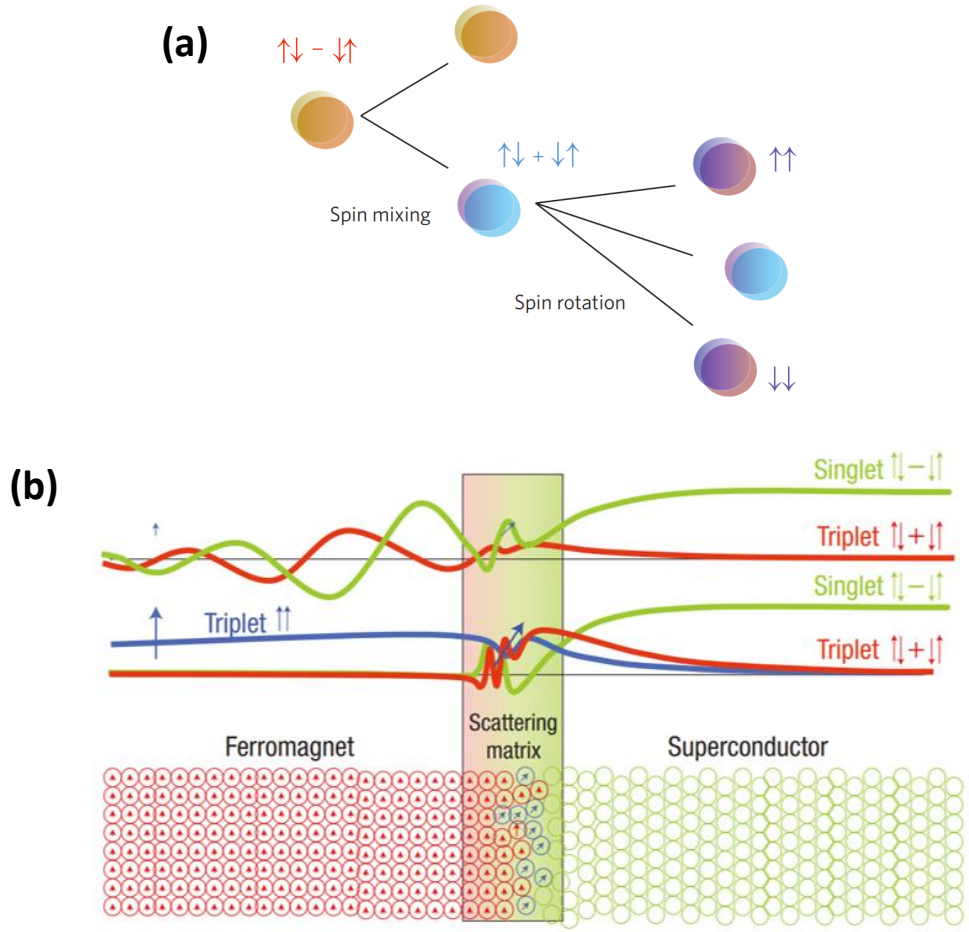

Fig. 2.18: (a) Schematic showing the creation process of equal-spin triplet Cooper pairs through spin mixing and spin rotation mechanisms. Spin mixing is caused by the Zeeman field that splits the majority and minority spin carriers causing a spin-dependent shift of the superconducting wavefunction's phase. Spin rotation is a consequence of the randomized magnetisations' directions at a magnetically active interface, causing the spins of the spin-zero triplet Cooper pairs to align. Figure taken from Linder et al., Nature Physics (2015) [104]. (b) Probability densities of the superconducting wavefunction in the case of a singlet $S = 0$ pairing (green curve), a spin-zero $S_Z = 0$ triplet pairing (red curve) and a equal-spin $S_Z = \pm 1$ triplet pairing (blue curve) at the interface between a ferromagnet and a superconductor. The scattering matrix represent the magnetically active interface required to observe the spin mixing and spin rotation mechanisms. Figure adapted from Eschrig, Nat. Phys. (2008) [214].

illustrates this property by showing a schematic of a SC/F interface with an active magnetic barrier (or scattering matrix) between both [214]. The red and green lines depict the probability amplitude of the superconducting wavefunction in the case of a singlet pairing and a spin-zero triplet pairing respectively. For both systems, the supercurrent vanishes in the ferromagnet's and superconductor's bulks.

Spin rotation is the mechanism through which a spin-zero triplet state can be transformed into an equal-spin triplet state with $S_Z = \pm 1$. This mechanism is made possible through a magnetically textured scattering matrix at the interface, with randomized local magnetizations, causing the spins of a Cooper pair to align, thus creating equal-spin triple states $\Psi_{S_Z=1}^{triplet} = \uparrow\uparrow$ or $\Psi_{S_Z=-1}^{triplet} = \downarrow\downarrow$. These triplet Cooper pairs can coexist with external magnetic fields and exchange fields because Zeeman interactions no longer have a pairbreaking effect. Therefore, the propagation length of such triplet correlations in ferromagnets is enhanced by orders of magnitude, as is depicted by the blue line in **Fig. 2.18(b)** [214].

Being able to generate and control equal-spin triplet Cooper pairs has promising implications for practical applications in the field of superconducting spintronics as it mixes the advantages of both spintronics (spin-polarized transport) and superconductivity (resistance-less phase-coherent transport). Thus, triplet Cooper pairs can expectedly enhance the lifetime of polarized current while suppressing energy dissipation due to Joule heating.

Chapter 3: Experimental details

This chapter is aimed at describing the techniques used during this thesis for the fabrication processes and the transport measurements of the devices. The first part of the chapter will be dedicated to a succinct explanation of the methods used for the growth and thickness characterization of the samples: pulsed laser deposition (PLD) and sputtering for the deposition of materials, and atomic force microscopy (AFM) to precisely measure the devices' thicknesses. Although I have not conducted myself the depositions and the AFM measurements, I have assisted to the experiments. Optical lithography was exclusively used for the micro-patterning of the devices studied in this thesis and a brief introduction to these techniques and the clean-room apparatus will be also detailed in this chapter. Finally, this thesis mainly focuses on the electrical characterization of various experimental devices, and therefore, an overview of the typical transport experiments (resistance vs. temperature, voltage vs. current and magnetoresistance) and important experimental parameters will be addressed.

1. Pulsed Laser Deposition (PLD)

Pulsed Laser Deposition (PLD) is a widely used deposition technique consisting in focusing a high-power pulsed laser beam onto a target, breaking apart the target's molecules in the form of a plasma plume that is used to deposit thin films in a ultra-high vacuum chamber [215]. The main advantage of PLD compared to other deposition techniques such as Molecular beam epitaxy (MBE) or Chemical vapor deposition (CVD) is its ability to accurately reproduce the stoichiometry of the target's material and allow epitaxial growth, which is crucial in the case of oxide materials (cuprate superconductors and manganite half-metals for example), for which the crystal structure is of paramount importance in the transport properties. Moreover, this technique also allows to operate the deposition process in an oxygen-controlled atmosphere, a parameter of great significance while depositing YBCO, whose superconducting properties are extremely sensitive to oxygen stoichiometry.

Fig. 3.1(a) shows a picture of the PLD apparatus used during this thesis for the deposition of heterostructures made of $YBa_2Cu_3O_{7-x}$ (YBCO), $La_{1-x}Sr_xMnO_3$ (LSMO) and gold (Au), while **Fig. 3.1(b)** is a schematic representation of the working principle of a PLD process with the main chamber's components [216]. The UV laser beam (in our case $\lambda = 248\ nm$, provided by a Kr/F excimer laser) comes from outside the vacuum chamber and is focused onto a moving target holder to prevent from

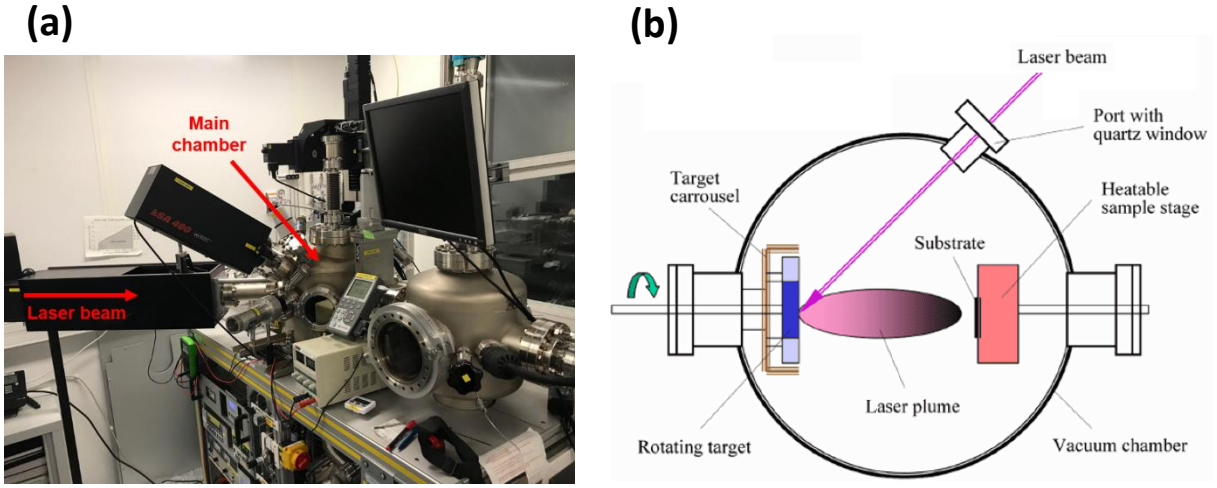

Fig. 3.1: (a) Picture of the PLD apparatus. We can distinguish the laser beam path and the main chamber. (b) Working principle of a PLD. The laser beam is focused onto a moving target, then the plasma plume develops and deposit the desired material onto the substrate in a high-vacuum chamber. Figure taken online from Oxford Instrument Andor [216].

quick erosion, breaking apart the target's molecules and starting the vaporization process. A plasma plume, with a shape depending on the oxygen chamber's pressure, is then created perpendicular to the target's surface due to Coulomb repulsion. The substrate, placed in front of the plasma plume, is usually mounted on a heated plate in order to facilitate the thermal diffusion of the deposited material for optimal crystalline properties.

The profile of the deposited material is also crucial for the clean-room patterning and the quality of devices. To improve the profile's uniformity in the centre of the sample, the point of focus of the laser beam is slightly offset while the sample rotates during the deposition. This effect is represented in **Fig. 3.2**, showing the deposited profile for a perfectly centred case [**Fig. 3.2(a)**] and a slightly misaligned case [**Fig. 3.2(b)**]. When an offset is applied, the thickness uniformity of the profile is greatly enhanced in the centre of the substrate.

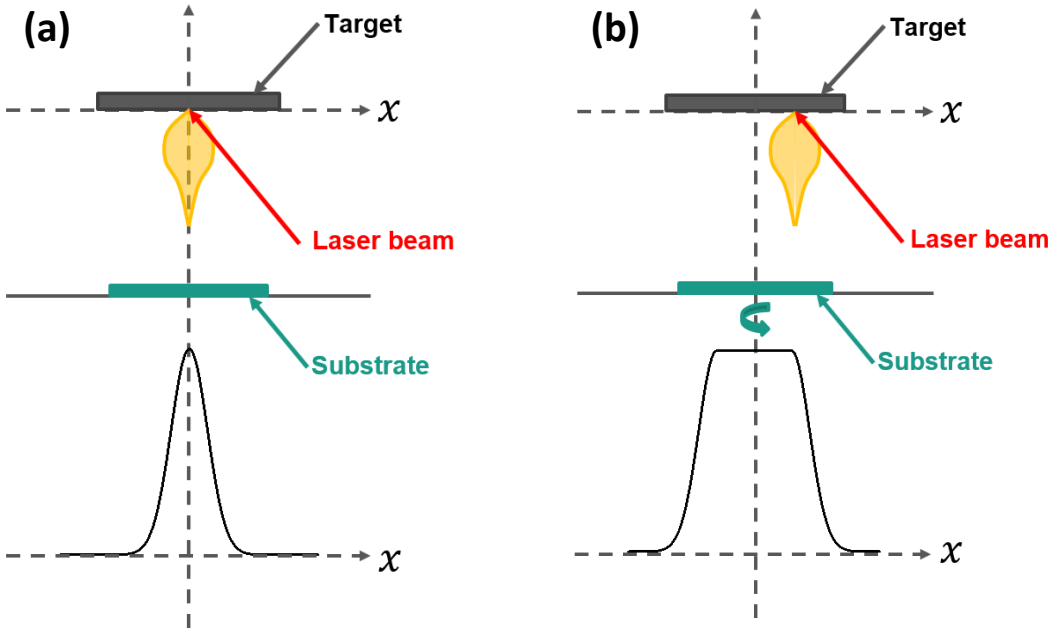

Fig. 3.2: Schematic representation of the deposited profile for (a) a perfectly centred laser beam and (b) a slightly misaligned laser beam with a rotated substrate. One can see that the profile is improved in (b), leading to a more uniform repartition of the material in the centre of the sample.

Some of the samples studied in **Chapter 5** have been deposited by PLD (see batches 3 and 4 in **Chapter 5, Sect. 2.2**). The samples are made of alternating thin layers of YBCO and LSMO on a (001)-oriented STO substrate. On some samples, a layer of gold was deposited *in situ* for contact purposes. The typical growth parameters for these materials have been optimized to obtain the best transport properties (an optimal T_C of YBCO for example) and reduce the number of surface outgrowths for better deposition conditions. The most important parameters involved in the PLD deposition are the deposition time t_{PLD}, the oxygen pressure P_{O_2}, the distance between the target and the sample d_{ts}, the energy density of the laser beam ρ_{laser} at the target's surface and the sample surface's temperature $T_{surface}$ (as measured by a pyrometer). For the depositions of interest for this thesis, the parameters chosen were:

(i) **For the deposition of YBCO:** $t_{PLD} = 3\,min$ for $\sim 30\,nm$, $P_{O_2} = 0.36\,mbar$, $d_{ts} = 50.85\,mm$, $\rho_{laser} = 8.5\,mJ.mm^{-2}$, $T_{surface} \approx 680\,°C$.

(ii) **For the deposition of LSMO:** $t_{PLD} = 2\,\mathrm{min}\,15\,s$ for $\sim 15\,nm$, $P_{O_2} = 0.2\,mbar$, $d_{ts} = 54.85\,mm$, $\rho_{laser} = 27.5\,mJ.mm^{-2}$, $T_{surface} \approx 660\,°C$.

(iii) **For the deposition of Au:** $t_{PLD} = 10\,min$ for $\sim 30\,nm$, $P_{O_2} = 2 \times 10^{-6}\,mbar$, $d_{ts} = 43.85\,mm$.

2. Magnetron sputtering

Magnetron sputtering (or simply sputtering) is a physical vapor deposition technique consisting in bombarding a target with highly energetic ions to detach atoms from the target's surface in an argon-filled chamber at very low pressure. The ions come from a discharge argon plasma generated by high DC or AC voltages and are directed toward the target's surface using an electric field. The plasma is confined in the vicinity of the target by applying a strong magnetic field with a magnetron sputter source placed next to it to protect the substrate from being in direct contact with the plasma, thus avoiding re-sputtering of the samples' surface. It also allows to increase the plasma's density to achieve higher deposition rates. A picture of the sputtering apparatus is displayed in **Fig. 3.3(a)** while a schematic of the working principle is shown in **Fig. 3.3(b)** [217].

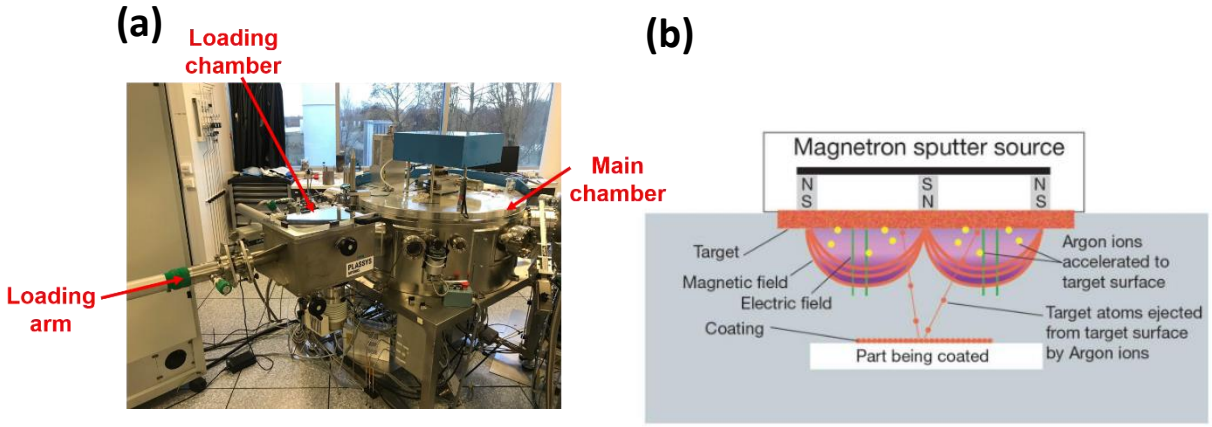

Fig. 3.3: (a) Picture of the magnetron sputtering apparatus. The sample is brought inside the main chamber via a mechanical loading arm that stretches on the left end side. (b) Schematic representation of the interior of a sputtering machine. The argon plasma is generated by a high DC electric field and is confined next to the target via a strong magnetic field. Then the argon ions are accelerated to the target's surface and the sputtered atoms deposit on top of a facing substrate. Figure taken online from Horiba Scientific [217].

Sputtering has been extensively used in the semiconductor industry for the deposition of thin films for integrated circuitry. It has the unique ability to allow the deposition of materials with a high melting temperature, as the working principle is distinct from the one of typical evaporation techniques. Moreover, sputtering is easier, faster and cheaper compared to other deposition techniques, making this deposition technique of particular interest from an industrial point of view [218]. Sputtering is also compatible with reactive gases such as oxygen, making it possible to engineer complex oxides (such as YBCO, LCMO and LSMO) film deposition in oxygen-controlled chambers. This is the technique used in Madrid by the group of Santamaria Jacobo and some of the samples studied in this thesis in **Chapter 5** have been ordered and deposited there (see batches 1 and 2 in **Chapter 5, Sect. 2.2**).

During this thesis, sputtering was used mostly for the deposition of contact layers, more specifically for the fabrication of transistor-like structures that will be presented in **Chapter 4**. These contacts are made of a thin layer of aluminium ($2\,nm$ or $10\,nm$) topped with a 100-nm thick capping layer of gold. The most important parameters used for the depositions are the chamber's pressure P,

the RF power P_W, the argon flow rate $d_m(Ar)$ and the deposition rate τ. For the depositions involved in this thesis, the parameters were:

(i) **For the deposition of aluminium:** $P = 2.5 \times 10^{-3}\ mbar$, $P_W = 65\ W$, $d_m(Ar) = 60\ sccm$ and $\tau = 1.25\ \text{Å}.s^{-1}$.

(ii) **For the deposition of gold:** $P = 2.5 \times 10^{-3}\ mbar$, $P_W = 95\ W$, $d_m(Ar) = 60\ sccm$ and $\tau = 9\ \text{Å}.s^{-1}$.

3. Atomic Force Microscopy (AFM)

Atomic Force Microscopy (AFM) is a scanning probe microscopy technique used to analyse surfaces' topography with a nanometric precision, with a more than 1000 times higher resolution compared to optical microscopes [219]. A cantilever with a sharp tip is attached to a mechanical arm and is used to scan the surface of a sample. The sample is placed on a piezoelectric holder that can be controlled via electric currents with a proportional-integral-derivative (PID) controller. To assess the movement of the cantilever while probing the surface, a laser is focused onto the cantilever's tip and the deflection is analysed by a photodetector. Typically, 3 different working modes for an AFM measurement exist:

(i) **Contact mode:** The tip is in direct contact with the surface and the feedback loop calculates and keeps constant the force and deviation of the cantilever. The cantilever deflection is then calculated and allows to reconstruct the sample's surface.

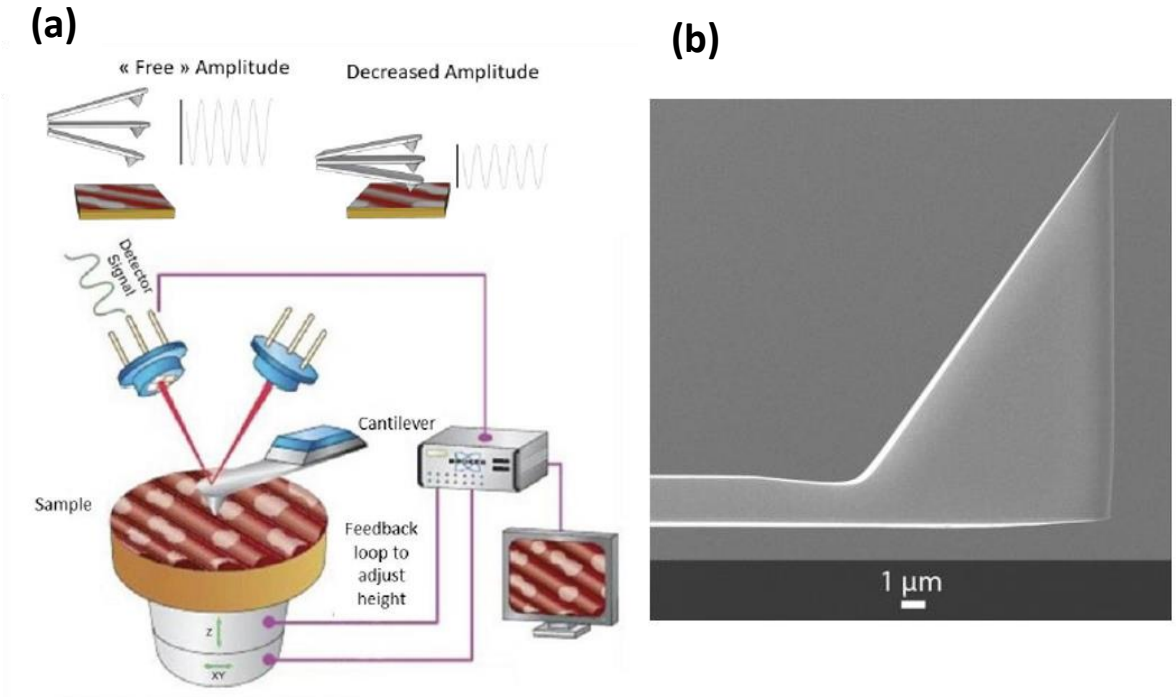

Fig. 3.4: (a) Scheme of an AFM apparatus showing on top the free amplitude of the cantilever far from the surface and the decreased amplitude while performing a scan in tapping mode. The cantilever is brought close to the surface while oscillating at its resonant frequency and a feedback loop controls the piezoelectric holder to keep the AFM station in tapping mode. (b) Picture of the cantilever used during this thesis for the AFM characterization (OPUS 160AC-NA). A lot of different geometries and materials exist with a variety of prices, depending on the desired utilization. Figure taken online from Opus [220].

(ii) **Non-contact mode:** The cantilever oscillates close to the sample's surface but is never in direct contact with it. When the tip approaches the surface, Van der Waals forces induce a decrease of the resonant frequency that can be used to image the surface.

(iii) **Tapping mode:** The cantilever oscillates at its resonant frequency and slightly touch the sample's surface during the scan. Therefore, the changes in the oscillation amplitude can be used to assess the surface topography. An increase of the oscillation amplitude corresponds to a gap in the surface's topography while a decrease relates to a bump. The working principle of an AFM in tapping mode is shown in **Fig. 3.4(a)**. The free amplitude of the cantilever when operating far from the surface is approximately $\sim 50\ nm$.

For this work, tapping mode was used to characterize the surface topography of the studied devices. The cantilever used for the AFM characterization of the devices is shown in **Fig. 3.4(b)**, corresponding to a Opus 160AC-NA with a resonant frequency of $300\ kHz$ [220]. AFM was performed to precisely measure the height and thicknesses of the devices in **Chapter 4**, a parameter of great significance when studying and analysing the results of the transport measurements. The results of the AFM characterization will be explained in more details in **Chapter 4, Sect. 2.2.** while describing the fabrication process of these devices.

4. Clean-room techniques for device fabrication

The clean-room fabrication of multiple devices has been an important part of this thesis and all the micro-patterning steps leading to the design of the devices studied in **Chapter 4** and **Chapter 5** were conducted in the clean-room of the UMR CNRS/Thales. Typical clean-room fabrication techniques include photolithography for the patterning, ion beam etching (IBE) for the design of the measuring bars and junctions as well as plasma cleaning for surface cleaning.

4.1. Photolithography techniques

Photolithography is the term employed to describe techniques that use light to pattern thin films. The main ingredients are a photoresist and a mask. The photoresist is a light-sensitive material (in our case, UV-sensitive) that will become vulnerable to (in the case of a positive photoresist) or robust against (in the case of a negative photoresist) certain etching chemicals (called developers) after being exposed to specific wavelengths. The mask with the desired pattern (physical or digital) is used to protect part of the resist from being exposed to light, effectively transposing a motif onto the substrate. This technique is pivotal for clean-room micro and nanofabrication processes and exist in various forms. During this thesis, I mostly used two types of photolithography techniques, namely optical projection lithography and laser lithography. Both methods do not require the use of a physical mask and therefore are denoted as maskless photolithography.

4.1.1. Optical projection lithography

The projection lithography system that was used for the lithography steps of the fabrication processes is shown in **Fig. 3.5**. The model is a SMART PRINT UV lithography system developed and

commercialized by microlight 3D in Grenoble. The system is compatible with 4 lenses (x1, x2.5, x5 and x10), depending on the precision desired and the minimum feature size that can be achieved is approximately $2\ \mu m$ with a x10 lens. The wavelength of the light source used for the exposure is $385\ nm$, corresponding to ultraviolet radiations, and the average writing speed is $\sim 100\ mm^2.min^{-1}$. The photoresist used during the fabrication was SPR700, a multiwavelength positive photoresist compatible with a wide variety of developers. The projection method is based on a digital micromirror device (DMD) projection technology, consisting in a chip composed of hundred thousand micromirrors arranged in a rectangular array. Each of these microscopic mirrors can be tilted by an angle of $\sim \pm 10°$, reflecting the light source onto the coated substrate or not and transposing the mask onto its surface.

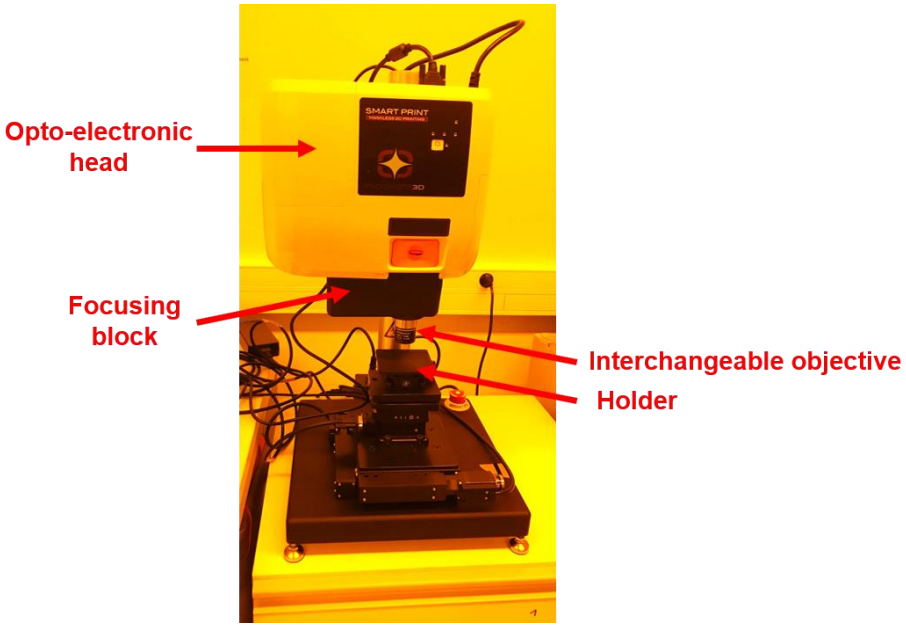

Fig. 3.5: Picture of the SMART PRINT UV maskless optical projection lithography that was used for the clean-room fabrication processes. The yellowish background colour is due to the light in the clean-room, with specific wavelengths that prevent the photoresist to be exposed unintentionally.

The main advantage of this system compared to commonly used hard mask lithography systems is the possibility to use a digital mask making it less costly and more flexible. However, this technique requires "stiching", meaning that the final pattern is divided into sub-areas that are exposed one by one. As a consequence, the stitching process must be effective to avoid misalignments and offsets between sub-areas. In practice, a misalignment of a few pixels (approximately $\sim 1\ \mu m$) is typical for our system. For this work, optical projection lithography was used for the micro-patterning of the devices that will be studied in **Chapter 4**. Due to the large sizes of the patterns (a few tens or hundreds of micrometres), the x5 lens was used, and the structures were kept within the size of one stiching area at a time, *i.e.* the misalignment due to the stiching process did not hinder the fabrication process. The digital masks used during the clean-room fabrication were designed using the software Klayout.

4.1.2. Laser lithography

Laser photolithography has also been performed for the fabrication of the devices. The apparatus is a DILASE 650 multifunction maskless lithography equipment developed by KLOE and is based on direct laser writing. The laser (with a wavelength of $375\ nm$) has a 1-μm wide spot that can be reshaped into a 100-μm wide laser spot using an optical treatment line. The linear writing speed can

be as high as $500\ mm.s^{-1}$. This technique, unlike optical projection lithography, does not require the use of stitching, meaning that a more precise alignment on wide areas can be achieved. Alignment is essential for the fabrication of the superconducting spin valves that will be studied in **Chapter 5**: consequently, during this thesis, laser lithography was exclusively used for the fabrication of such devices.

4.2. Ion Beam Etching (IBE)

Ion beam etching (IBE) is a physical dry etch process involving the bombardment of a substrate with an ionized beam to sputter surface atoms in a highly anisotropic manner inside a low-pressure chamber. The ion beam is created by ionizing a noble gas, argon in this case, using a field emission gun (simply referred as an electron gun) made of tungsten. Then, the ions are directed and accelerated toward the substrate with an electric field. The picture of the IBE apparatus available in the clean-room in Thales is shown in **Fig. 3.6(a)**, and a drawing of the working principle is displayed in **Fig. 3.6(b)** [221]. The sample is placed on a temperature-controlled holder, cooled down to prevent the sample from

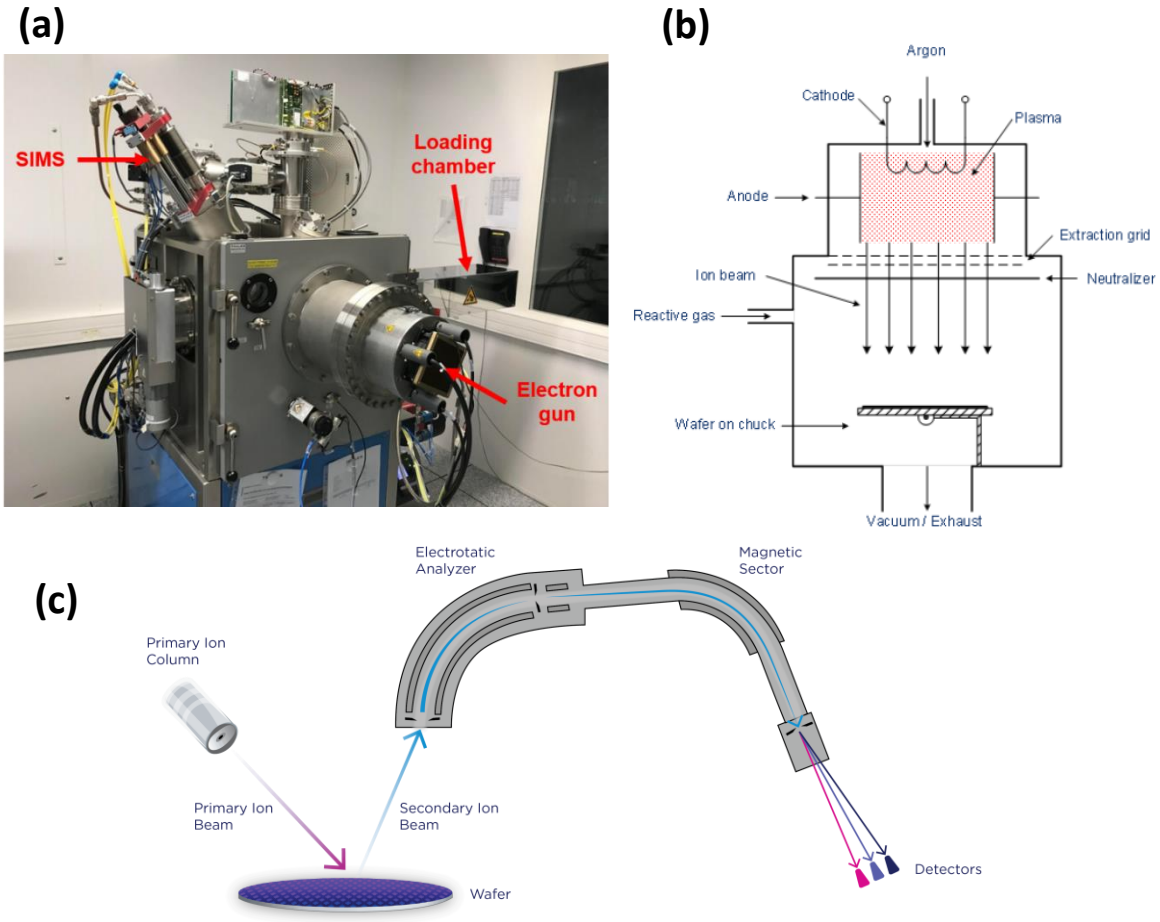

Fig. 3.6: (a) Picture of the ion beam etching (IBE) apparatus. A secondary ion mass spectrometer (SIMS) is present in the top left, monitoring the sputtered materials during the etching process. The model shown in this picture correspond to a Plassys MU600s. (b) Schematic representation of the main chamber of an IBE setup. Figure taken online from Semiconductor Technology [221]. (c) Working principle of a SIMS. The sputtered ions are picked up by an electrostatic analyser and then subjected to a magnetic field, effectively splitting the ions of different charge and mass, making it possible to distinguish ions and atoms from one another. The SIMS used during the IBE process was a Hiden Analytical, model IMP-EPD.

overheating during the etching process due to high energies. A tilt of the holder as well as a rotation is also applied to help the homogenization of the etching profile.

Additionally, a secondary ion mass spectrometer (SIMS) has been added to the apparatus to monitor in real time the materials being etched inside the chamber. A schematic of a typical SIMS system is showed in **Fig. 3.6(c)**. The molecules and atoms sputtered from the sample's surface by the primary ion beam are picked up by an electrostatic analyzer that lead the particles in a magnetic field. The motion of a charged particle inside a magnetic field is well-known to have a circular shape, with a radius r equal to:

$$r = \frac{mv}{qB} \tag{3.1}$$

where m is the mass of the particle, q its charge, v its velocity and B is the magnetic induction.

Therefore, particles will not be deflected in the same way depending on the mass and the charge it carries. Then, detectors at the exit of the magnetic channel extract the mass and the charge to identify the nature of the particle. This tool is extremely important for the fabrication processes involved in this thesis. In fact, the SIMS allows to precisely know which materials are being sputtered from the sample in real time, allowing to stop the etching process after the desired layer has been etched completely. An example of a SIMS signal as a function of time during a typical etching process is given in **Fig. 3.7**, showing the etching of (in chronological order): $30\ nm$ of gold, $30\ nm$ of YBCO, $5\ nm$ of LSMO, $8\ nm$ of YBCO and a few nm of LSMO. This etching was performed on a sample used for the characterization of superconducting spin valves as will be discussed in full details in **Chapter 5**.

Important parameters when operating ion beam etching are the voltage V and the current I used for the accelerating field, the tilt angle θ and the sample holder's temperature T. In all the etching performed during this thesis, the values were chosen to be $V = 300\ V$, $I = 50\ mA$, $\theta = 30\ °$ and $T = 5\ °C$.

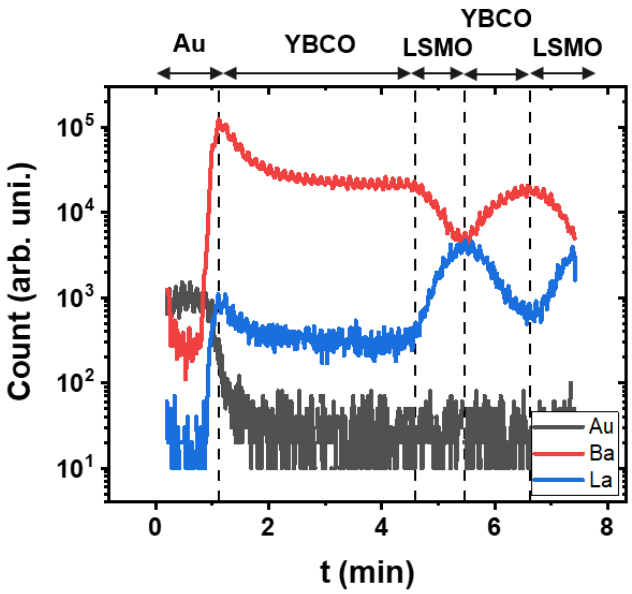

Fig. 3.7: Typical shape of the signal acquired by the secondary ion mass spectrometer (SIMS) during the etching of 30 nm of gold, 30 nm of YBCO, 5 nm of LSMO, 8 nm of YBCO and a few nm of LSMO. In total, the etching process lasted for 7 minutes and 30 seconds.

4.3. Plasma cleaning

Clean-room processes may have undesirable surface effects on some materials via interactions with the chemical developers and ionic bombardment. In addition, residues of the different chemicals, and particularly of the photolithography resist, can remain on the sample's surface even after acetone and propanol cleaning. An important fabrication step is the cleaning of damaged surfaces using a dry etching NANOPLAS DSB9000 system (shorten as plasma cleaning system). Damaged surfaces may have different transport properties and crystal structures; thus, depositing another material on top of it may yield high contact resistances (low transparency). Plasma cleaning is particularly interesting for organic cleaning, isotropic etching and reoxygenation. The energy of the cleaning process is chosen to be very low to prevent for an unwanted etching of the surface.

This fabrication step consists in inducing a chemical reaction between radicals or ions coming from a plasma and the sample's surface atoms to turn them into volatile compounds that are evacuated by pumping. The plasma is generated inside a vacuum chamber via six inductively coupled plasma sources, made of electromagnetic coils, connected to an RF generator. The system is linked to 4 different gas lines: N_2, O_2, Ar and SF_6. Each line is monitored by a flow measurement unit, controlled via a feedback loop to keep the flow equal to the setpoint value.

The important parameters to track for a successful nanoplasma cleaning are the chamber's pressure P, the duration of the cleaning t_{np}, the RF power P_W and the flow rates d_m of the different gases. The recipe used every time for the nanoplasma cleaning was defined by the parameters: $P(O_2) = 0.2\ Torr, P_W = 1000\ W, t_{np} = 10\ min, d_m(Ar) = 14\ sccm$ and $d_m(O_2) = 100\ sccm$. This cleaning step ensured better surface properties in view of subsequent deposition or lithography processes.

5. Cryostats

Following the fabrication of the samples, transport measurements were carried on the devices. Of course, a stable temperature is of paramount importance while studying superconducting behaviours, requiring the use of a cryostat. A cryostat is an apparatus able to keep samples at cryogenic temperature while allowing for electrical and magnetic characterizations. Mainly, two different cryostats were used for the transport measurements of the various samples: an Oxford cryostream system and a Janis SHI-950T refrigerator system. This paragraph is aimed at describing the main characteristics of both cryostats.

5.1. Oxford cryostream system

This cryostat is based on an Oxford cryostream closed cycle refrigerator system made of a two stage coldhead model 6/30 and a compressor. Although they require a large amount of electrical power to operate, closed cycle cryostats do not require a refill of helium to run as the helium flows in a closed gas line. The coldhead is fixed at the bottom of the metallic armature seen in **Fig. 3.8** and is able to cool down the chamber to a base temperature of $10\ K$ under a pressure of $\sim 10^{-4}$ bar. A turbo-pump adixen drytel 1025 is used for pumping the interior of the chamber. The sample's holder is made

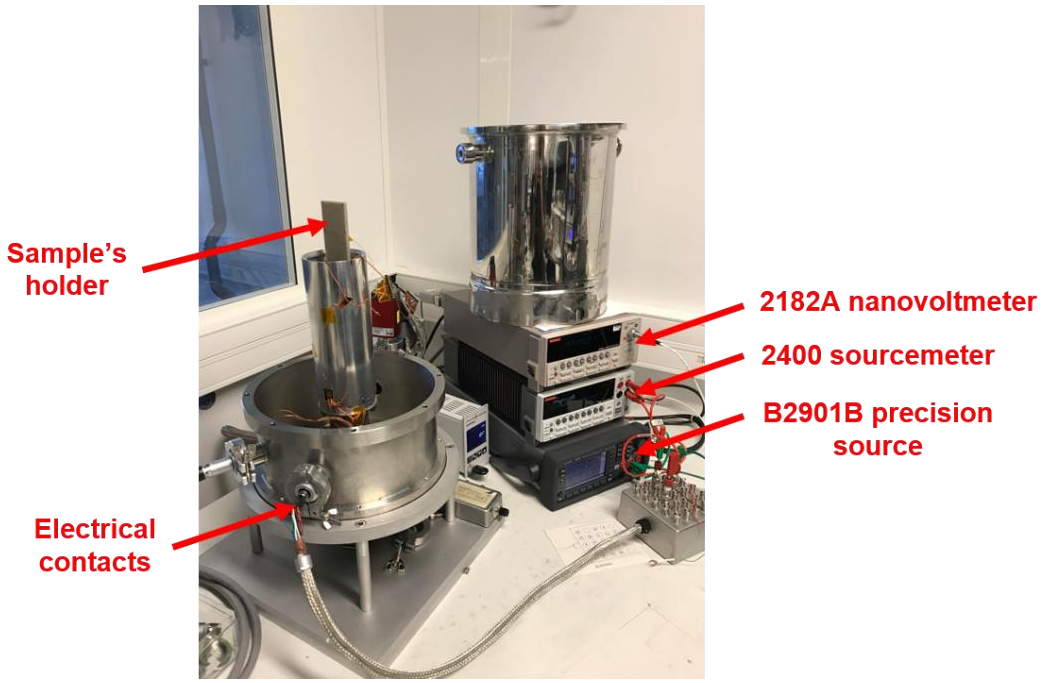

*Fig. 3.8: Picture of the Oxford Cryostream system used for the transport measurements of the transistor-like devices that will be studied in **Chapter 4**. The system is composed of a two stage coldhead, a compressor and a turbo-pump that pumps the interior of the chamber.*

of aluminium nitride, an electric insulator known to have a very high thermal conductivity of $\kappa \approx 300\ W.m^{-1}K^{-1}$ at room temperature that drastically increases with a decrease of temperature ($2000\ W.m^{-1}K^{-1}$ at $T = 100\ K$), particularly interesting while working at cryogenic temperatures for thermal homogenization [222]. Temperature is supervised via a PID controller (Lakeshore 336 Temperature Controller) and is measured with a silicon diode temperature sensor placed on the sample's holder next to the sample. It is possible to add a coil for the generation of a magnetic field, although for the scope of this thesis, no magnetic characterization was needed while using this system.

5.2. Janis model SHI-950T refrigerator system

The Janis model SHI-950T system is also a closed cycle refrigerator system that is designed to function from $4\ K$ to room temperature. A picture of the Janis cryostat is displayed in **Fig. 3.9**, showing the principal components that are detailed below. The temperature is controlled via a LakeShore 336 Temperature Controller, monitoring the temperature of the first stage, the second stage and the sample's temperature.

The main components of this cryostat are:

(i) **Compressor:** The compressor recovers and controls the flow of helium from the gas line to supply the cold head with high-pressure helium and is water cooled to prevent overheating. The compressor is manufactured by Sumitomo Heavy Industries (SHI).

(ii) **Cold Head:** The model is an RDK-408D2 Expander developed by SHI. It is a two-stage cryogenic refrigerator based on the Gifford-McMahon refrigeration cycle using the helium gas coming from the compressor to generate cryogenic temperatures. The helium gas is

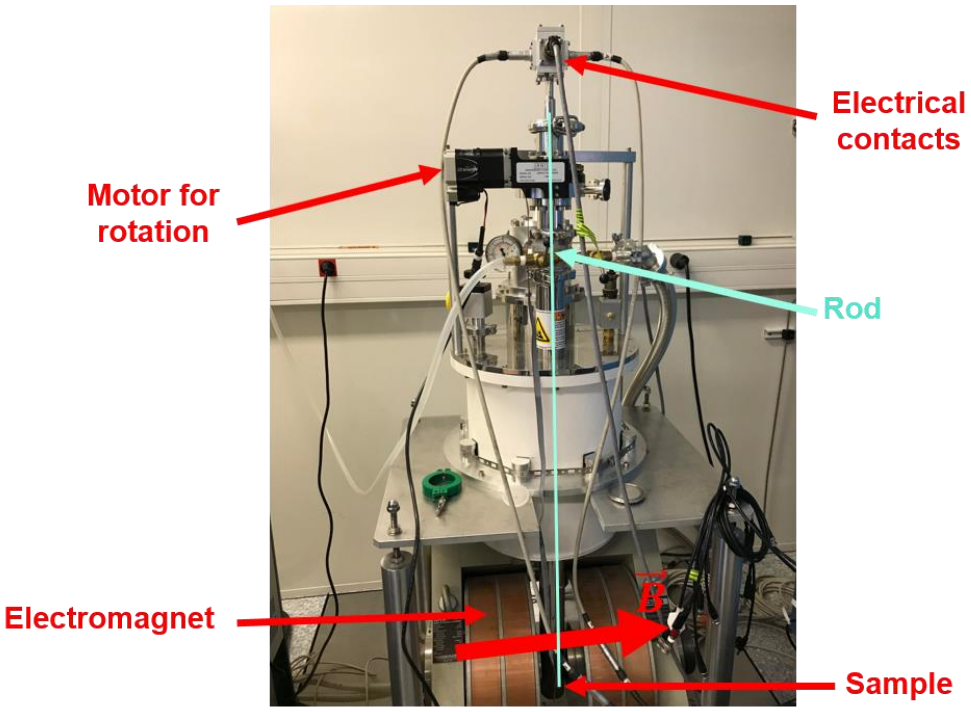

*Fig. 3.9: Picture of the Janis SHI-950T closed cycle refrigerator used for the transport and magneto-transport measurements of the superconducting spin valves in **Chapter 5**.*

expanded inside the displacer-regenerator assembly to cool down the system and is subsequently reinjected into the gas line toward the compressor.

(iii) **Vacuum jacket and radiation shield:** These two components represent the protective layers surrounding the whole apparatus. The jacket is a thin layer with a high-pressure that insulates the inside chamber from the outside and prevent temperature diffusion and convection. The shield protects the sample from temperature radiations.

(iv) **Loading rod:** The rod is used to load the sample inside the main chamber. It is composed of a head with electrical contacts for the transport measurements on one end and a sample holder on the other end. A temperature sensor is placed next to the sample holder to measure the temperature of the device.

(v) **Electromagnet:** The generation of the magnetic field is performed through a GMW electromagnet system (Model 3472-70). The electromagnet is controlled via a GMW 231HC bipolar current amplifier for the power supply and can apply magnetic fields between $-1\ T$ and $1\ T$. Two different holders for the rod are available to be able to apply in-plane or out-of-plane magnetic fields.

(vi) **Motor:** A motor has been integrated to the system to allow for the rotation of the rod and therefore the rotation of the sample. This can allow the characterization of the magnetic properties of a junction with varying incident angles of the magnetic field, particularly interesting while studying ferromagnetic materials.

During this thesis, the Janis cryostat was used for the study of the electrical and magnetic transport properties of the vertical superconducting spin valve junctions that will be the topic of **Chapter 5**. The junctions are made of alternating layers of YBCO with a half-metallic material, LSMO or LCMO. The possibility to apply a rotation of the sample around the rod's axis is particularly adapted while studying devices made from ferromagnetic materials: depending on the angle of incidence of the magnetic field, the magnetic domains behave differently. This is due to the existence of easy and hard axes for the magnetization and will be discussed in more details in the aforementioned chapter.

6. Transport measurements

Transport measurements consist in the characterization of the electrical properties of a device while varying the current, temperature, magnetic field etc… In this section, the most common transport measurements that will be presented throughout the next chapters are reviewed with a description of how to extract typical quantities such as the critical temperature T_C and the critical current I_C of a superconducting device. The automation of all the transport measurements was performed using the software LabView.

6.1. Electrical resistance measurements

The electrical resistance of a device can be measured via three different methods, depending on the context:

(i) **Simple measurement:** The voltage V is measured while applying a positive or a negative current I, and the resistance is equal to $R = V/I$.

(ii) **Zero-bias offset corrected measurement:** After each measurement, the voltage V_{0A} at zero-bias (for a current equal to $0\ A$) is measured, and the corrected value of the resistance is $R = (V - V_{0A})/I$.

(iii) **Current inversion method:** The voltage is measured for a positive and a negative current (with the same absolute value) and the average of both values is calculated. This technique allows to get rid of any voltage offset created by the experimental setup. In the end, the resistance is retrieved using the relation:

$$R = \frac{V_+ - V_-}{2|I|} \tag{3.2}$$

where V_+ and V_- are the voltages measured by applying $+I$ and $-I$, respectively.

Additionally, the measurement can be conducted in a 2-point or a 4-point probing configuration. The 4-point measurement setup consists in separating the contacts used to apply a current and the ones used to measure the voltage and allows to get rid of the parasite contact resistances. This type of measurement is particularly interesting while studying superconducting devices whose resistance is orders of magnitude lower than the contact resistances.

6.2. Resistance as a function of temperature

One of the most common type of transport measurement consists in measuring the resistance of a device as a function of the temperature [also shorten as $R(T)$]. This measurement has been used historically to define and distinguish the different families of materials: insulators, semiconductors and normal metals. In fact, the resistance of a normal metal increases with increasing temperatures due to a larger number of collisions between charge carriers caused by lattice vibrations. On the other hand, a semiconductor will experience a lowering of the resistance with increasing temperatures. This phenomenon is caused by the electronic band structure of semiconductors: the electrons cannot jump from the valence to the electronic band without a high enough thermal energy.

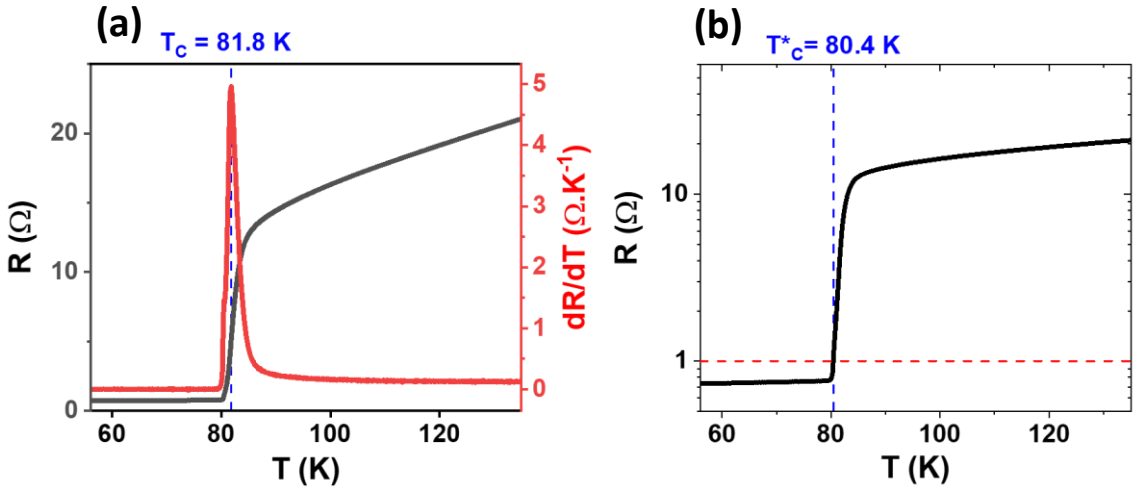

Fig. 3.10: Measurements done on a $125\ nm$*-thick layer of YBCO for a current of* $10\ \mu A$ *using the simple measurement method (**Sect. 6.1.**). (a) Resistance (black curve) and its first derivative (red curve) vs temperature. The maximum of the first derivative is reached for a value of* $T_C \approx 82\ K$*. (b) Example of calculation of* T_C^* *with a* $1\ \Omega$ *threshold criterion, yielding a value of* $T_C^* \approx 80\ K$*.*

Superconductors exhibit a critical temperature below which the resistance of the material completely vanishes. For the rest of the manuscript, the critical temperature T_C of a device is defined as the temperature for which the first derivative of the resistance reaches a maximum. This criterion is presented in **Fig. 3.10(a)**, showing the resistance of a YBCO thin film (with a thickness $t_{YBCO} = 125\ nm$) measured in a 2-point configuration as a function of the temperature in black (linked to the left y-axis) while the first derivative is plotted in red (linked to the right y-axis). The maximum of dR/dT is reached for a value of $T_C = 81.8\ K$.

Additionally, as will be helpful later in this thesis, I define the effective critical temperature T_C^* to be the first temperature for which the resistance of the device goes below a resistance threshold, as depicted in **Fig. 3.10(b)** for the same set of data as **Fig. 3.10(a)** for a $1\ \Omega$ threshold. This method yields an effective critical temperature of $T_C^* = 80.4\ K$. The remnant resistance of approximately $\sim 0.7\ \Omega$ below the critical temperature is a consequence of the 2-point measurement setup, as the contact resistances are measured in series. T_C^* will be used in the rest of this thesis only when the shape of the $R(T)$ does not allow for the calculation of the T_C from the first method. In particular, this will be the case in **Chapter 4, Sect. 3.3.1.**, where a gradual superconductor-to-insulator phase transition leads to unusual shapes of the $R(T)$.

Finally, I define the parameter ΔT_C as the width of the superconducting transition from metallic to superconducting. This width is calculated by fitting the linear parts of the $R(T)$ curve well above and well below the superconducting transition. This is illustrated by the coloured dashed lines in **Fig. 3.11**. Then, the resistance at $20\ \%$ ($80\ \%$) is calculated from the low-temperature (high-temperature) fit, as shown by the red and blue full lines in **Fig. 3.11**, and the width of the transition is obtained by retrieving the intersections between these lines and the $R(T)$ curve. The mathematical derivation in the particular case of the $R(T)$ curve of **Fig. 3.11** yields a final value of $\Delta T_C = 4.2\ K$.

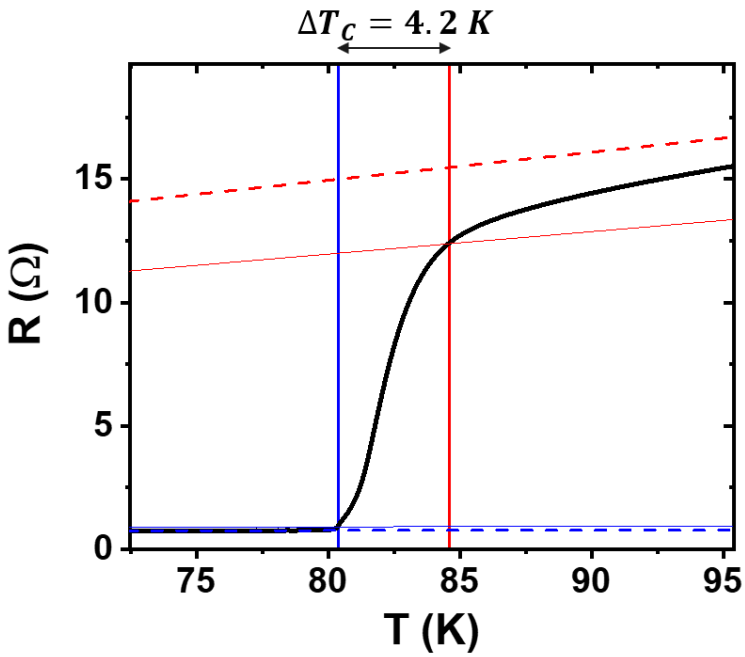

*Fig. 3.11: Example of calculation of the superconducting transition width ΔT_C for a $125\ nm$-thick layer of YBCO measured with a current of $10\ \mu A$ using the simple measurement method (**Sect. 6.1.**). A fitting of the linear parts of the graph is performed at high and low temperatures and the resistance at $20\ \%$ ($80\ \%$) is calculated below (above) T_C. This example yields a result of $\Delta T_C \approx 4\ K$.*

6.3. Current-voltage characteristics

Another very typical set of transport measurements important for the scope of this thesis corresponds to the current-voltage characterization of a device (shorten as I-V characteristic). This measurement can be achieved by measuring the voltage while sweeping the applied current or inversely. **Fig. 3.12** shows the regular shape of a superconducting I-V characteristic (in black) of a spin valve structure with a clear superconducting critical current below which the voltage (and therefore the resistance) is almost zero. The value of the critical current I_C can be deduced from the I-V curve by

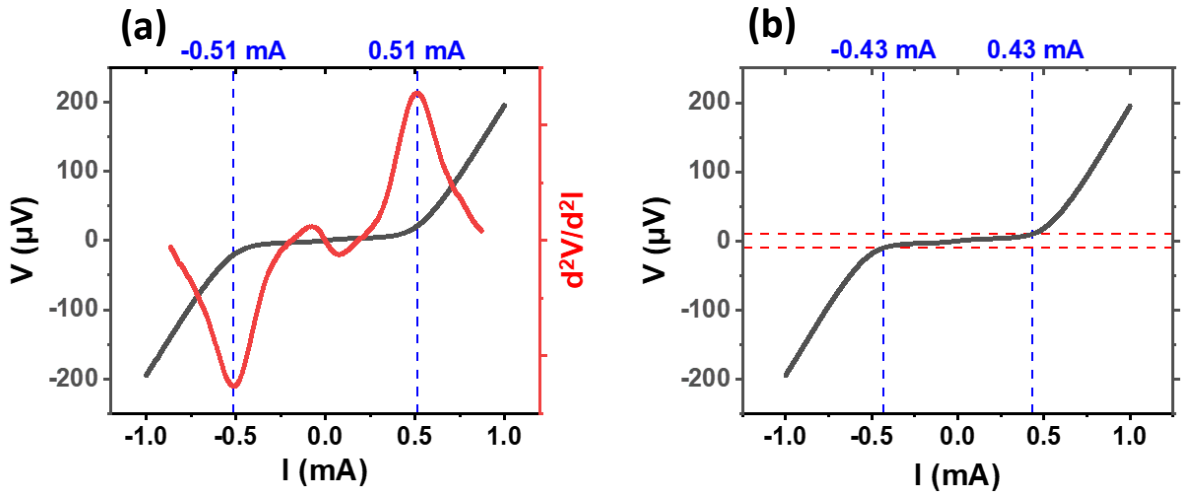

*Fig. 3.12: I-V characteristic measured on a superconducting spin valve junction made of YBCO (30 nm)/LSMO ($5\ nm$)/YBCO ($8\ nm$)/LSMO ($15\ nm$)/YBCO ($30\ nm$) in a 4-point configuration at 10 K (see **Chapter 5**). (a) Calculation of I_C from the extremum of the second order derivative of the I-V characteristic. (b) Example of calculation of I_C^* with a $\pm 10\ \mu V$ threshold criterion.*

calculating the second order derivative and retrieving the values of the currents for which the derivative reaches an extremum. In the example given in **Fig. 3.12(a)**, the value of the critical current is found to be equal to $I_C = 0.51\ mA$.

A related value, denoted as the effective critical current (shorten as I_C^*), is defined as the value of the current for which the absolute value of the voltage goes below a specific threshold, as is illustrated in **Fig. 3.12(b)** in the case of a $\pm 10\ \mu V$ threshold. The value of I_C^* calculated from **Fig. 3.12(b)** is equal to $I_C^* = 0.43\ mA$. Analogous to T_C^*, this criteria will only be used when the shape of the I-V characteristics does not allow for the clear calculation of the critical current via the first method, for example if the superconducting features are too faint or if the number of measured points is too low.

6.4. Magnetoresistance

Magnetoresistance (MR) is defined as a change of the electrical resistance of a material under application of an external magnetic field. This type of transport measurement is of particular interest for the scope of this thesis, for the study of the spin valve vertical junctions made of the superconductor YBCO and the half-metallic ferromagnets LSMO and LCMO. These experiments were carried on the Janis refrigerator system described above, and the magnetic field was applied (either in-plane or out(of-plane) via an electromagnet, yielding fields between $-1\ T$ and $1\ T$.

Fig. 3.13 shows the typical behaviour of the magnetoresistance of a spin valve device in a 4-point configuration using the current inversion method (see **Sect. 6.1.**) for the measurement of the resistance. As the magnetizations of the ferromagnetic layers reverse via the application of an external magnetic field, the device switches between a parallel (P) to an anti-parallel (AP) configuration. The

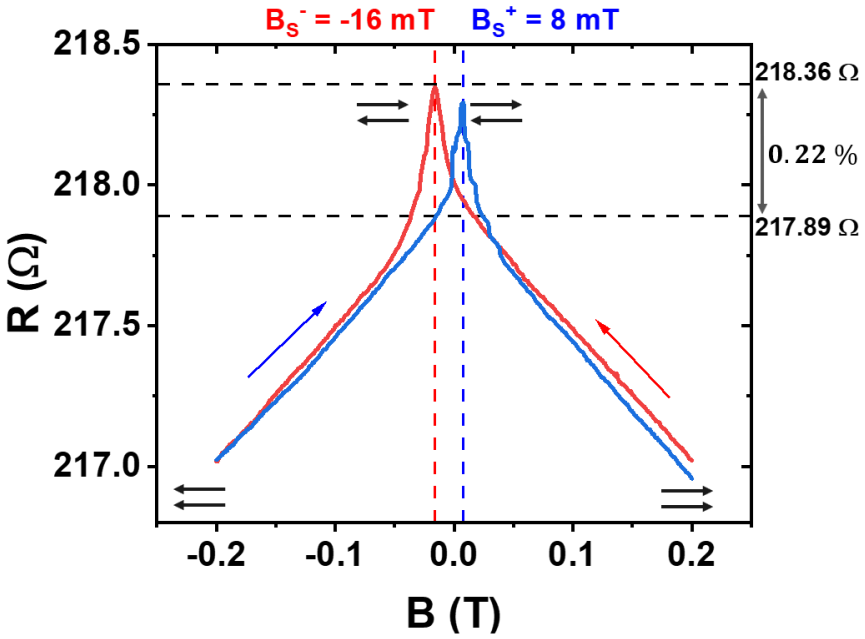

*Fig. 3.13: Magnetoresistance measurement performed on a superconducting spin valve junction made of YBCO ($30\ nm$)/LSMO ($5\ nm$)/YBCO ($8\ nm$)/LSMO ($15\ nm$)/YBCO ($30\ nm$) in a 4-point configuration at $120\ K$ using the current inversion method (**Sect. 6.1.**). The red curve corresponds to the value of the resistance measured while sweeping the magnetic field from $+0.2\ T$ to $-0.2\ T$, while the blue curve corresponds to the resistance measured while sweeping the magnetic field in the other direction, as illustrated by the coloured arrows. The double black arrows represent the relative orientations of the magnetizations of the ferromagnetic layers, defining the parallel and anti-parallel configurations.*

red curve corresponds to the value of the resistance measured while sweeping the magnetic field from $0.2\ T$ to $-0.2\ T$, while the blue curve corresponds to the resistance measured while sweeping the magnetic field in the other direction, as indicated by the blue and red arrows in **Fig. 3.13**. I define in these experiments the switching fields B_S^- and B_S^+ to be the value of the magnetic field for which the magnetoresistance reaches an extremum for decreasing magnetic fields (red curve) and for increasing magnetic fields (blue curve), respectively. In the case of the magnetoresistance experiment of **Fig. 3.13**, we obtain values of $B_S^+ = 8\ mT$ and $B_S^- = -16\ mT$.

Magnetoresistance (MR) in percentage is defined as:

$$MR = 100 \times \frac{R_{AP} - R_P}{R_P} \tag{3.3}$$

with R_{AP} and R_P the resistance of the device in the anti-parallel and parallel configuration, respectively. The maximum value of the MR for the particular case of **Fig. 3.13** is observed for $B = B_S^- = -16\ mT$ and is equal to $MR = \frac{218.36-217.89}{217.89} \approx 0.22\ \%$. Therefore, MR corresponds to the relative height of the hysteresis peaks observed in the magnetoresistance for $B = B_S^{\pm}$.

6.5. Instruments

The instruments that were used during this thesis for the transport measurements are the following:

(i) **For the electrochemical tuning of YBCO superconducting properties in Chapter 4:** the current was generated with a Keithley K6220 precision current source, and the voltage was measured with a Keithley K2182A nanovoltmeter or a Keithley K2700 multimeter data acquisition system. The temperature was controlled via a Lakeshore 336 temperature controller. The rotation of the rod was done with a motor and monitored with a K2200-20-5 programmable power supply.

(ii) **For the magnetic switching in superconducting spin valve structures in Chapter 5:** the gate voltage was applied with a Keithley K2400 sourcemeter while the current was measured in 2-point with the same instrument. The channel's resistance was measured by applying a current with a Keysight B2901B precision source/measure unit and the voltage was measured using a Keithley K2182A nanovoltmeter.

Chapter 4: Electrochemical tuning of YBCO's superconducting properties

1. Introduction

Cuprate superconductors, discovered in 1986 by Müller and Bednorz [4], have been extensively studied for their high superconducting critical temperature T_C, above the boiling point of liquid nitrogen $(77\ K)$, and their unusual properties, such as a strong anisotropy arising from the superconducting d-wave pairing mechanism (see **Chapter 2, Sect. 2.2.3.**). $YBa_2Cu_3O_{7-x}$ (YBCO) is a commonly-used cuprate for a plethora of practical applications, spanning from superconducting resonators and band-pass filters to magnetic field sensors in the form of SQUIDs, as discussed in **Chapter 1**. YBCO crystallizes in a perovskite crystal structure, consisting of alternating CuO_2 planes and yttrium and barium planes. Although there is no consensus to this day on the mechanism allowing superconductivity in such materials, it is known that the CuO_2 planes, a common feature of all cuprate superconductors, play a key role in the superconducting properties of YBCO and similar materials. The temperature-doping phase diagram of YBCO is given in **Fig. 4.1** [7], showing the different phases as a function of temperature (y-axis) and the hole doping p (x-axis), *i.e.* the number of holes per copper atom, and was already described in **Chapter 2, Sect. 2.2.2.** The green area, defined for a hole doping between p_{min} and p_{max} at low temperatures, represents the very important superconducting phase, and the purple area, for strongly underdoped YBCO ($p < p_{min}$), consists of an antiferromagnetic (AF) insulating phase. Therefore, for a fixed temperature, the ability to control the hole doping concentration may allow the development of superconducting devices based on superconductor-to-insulator phase transitions, and this is the focus of this chapter.

There exist multiple strategies for locally modifying YBCO's hole doping concentration, for example through a controlled motion of oxygen ions [151] that can be triggered by annealing [152], illumination [93] or electrical fields [153–157]. In fact, the superconducting ground state of YBCO is heavily dependent on the oxygen stoichiometry [223]: changing the amount of oxygen in the structure translates to modifying the charge carrier density and the hole doping p, allowing to scan through the temperature-doping phase diagram by inducing a back and forth movement of oxygen ions. Historically, cuprates' high sensitivity to oxygen stoichiometry has been widely regarded as a hindrance

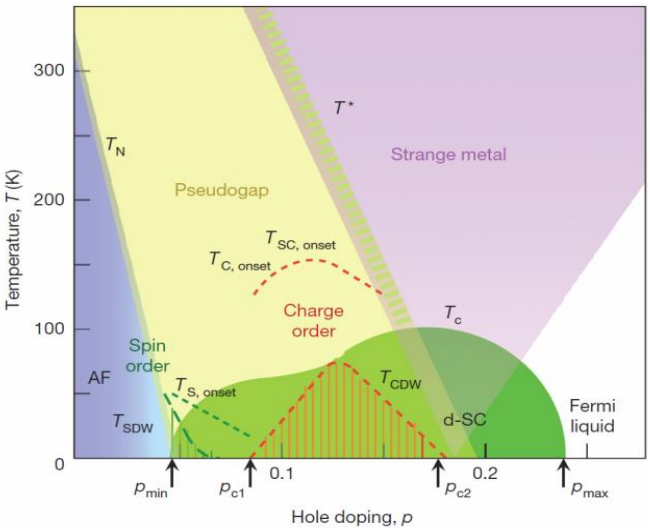

Fig. 4.1: Temperature-doping phase diagram of YBCO with various different phases such as the insulating antiferromagnetic Mott phase for low doping concentration ($p < p_{min}$), the pseudogap phase or the strange metal phase. The superconducting dome (green area) appears for doping values between $p_{min} = 0.05$ and $p_{max} = 0.24$, showing that there exists an optimal value of the hole doping $p = 0.18$ yielding a maximum $T_C \approx 93\ K$. Figure taken from Taillefer et al., Annu. Rev. Condens. Matter. Phys. (2010) [7,8].

and a limiting factor in term of practical applications, adding additional challenges for the fabrication. For example, YBCO thin films must be grown epitaxially on specific substrates and deposited in a chamber with a high oxygen concentration in order to get optimally doped YBCO samples with optimum superconducting properties [224].

Such a sensitivity, on the other hand, can be used to electrically tune *in-situ* the superconducting properties of YBCO via chemical redox reactions or via oxygen migration triggered by high current densities and/or high thermal gradients**.** The next section will be dedicated to the review of some of the different strategies that can be implemented to control the flow of oxygen ions while giving a state-of-the-art description for each of them. Then, the main envisioned application and the proof-of-concept device that will be studied extensively throughout this chapter will be introduced.

1.1. Strategies for the *in-situ* control of the oxygen content in cuprates

1.1.1. Redox chemical reactions

The term "redox reaction" (for reduction-oxidation reaction) describes a specific type of chemical reaction where an exchange of either oxygen atoms, hydrogen atoms or electrons induce a change in the oxidation number of the participating chemical species. This phenomenon is very common in nature and has tremendous implications in very basic physical effects, such as the rusting of iron in contact with water, the browning of fruits or in the process of combustion [225]. Redox reactions can spontaneously appear at the interface between materials with different reduction potentials: the material with a higher reduction potential reduces while the material with a lower reduction potential oxidizes. As a result, a thin oxygen-depleted layer is expected at one side of the interface, and conversely, an oxide layer will form at the other side, leading to the appearance of an electron tunnelling barrier.

While the importance of oxygen migration in cuprates is a well-known property for more than 30 years [226], the control of the superconducting properties of a cuprate superconductor through redox reactions has not been investigated until recently [153,154,227–229]. In 2018, Palau *et al.* [153] studied the transport properties of YBCO thin films (with thicknesses ranging between $50\ nm$ and $250\ nm$) in contact with silver in a transistor-like geometry. They measured a reversible and non-volatile switching of the resistance at the interface between YBCO and silver, attributed to the controlled tuning of the charge carrier density in the superconducting layer. In 2020, Murray *et al.* [229] showed that depositing a thin layer of gadolinium of $20\ nm$ on top of a 100-nm thick layer of YBCO was enough to reduce the critical temperature of the film to $0\ K$ and induce a superconductor-to-insulator phase transition, without the application of any voltages. They attributed this modulation to the chemical migration of oxygen from the YBCO to the Gd layer, locally modifying the YBCO microstructure and conducting properties. While studying tunnel electroresistance junctions made of $Mo_{80}Si_{20}$ (MoSi), $BiFeO_3$ (BFO) and YBCO, Rouco *et al.* [154] demonstrated that redox chemical reactions can be directly induced at the interface between YBCO and MoSi. **Fig. 4.2** presents some of the most important results from the paper of Rouco *et al.* [154], showing the reversible switching behaviour between non-volatile low-conductance and high-conductance states, as well as intermediate states, for junctions made of MoSi ($100\ nm$)/BFO (t_{BFO})/YBCO ($30\ nm$) at $3.2\ K$, with $t_{BFO} = 0, 3 \text{ and } 15\ nm$. Importantly, **Fig. 4.2(a)** and **Fig. 4.2(d)** illustrate that the switching is observed

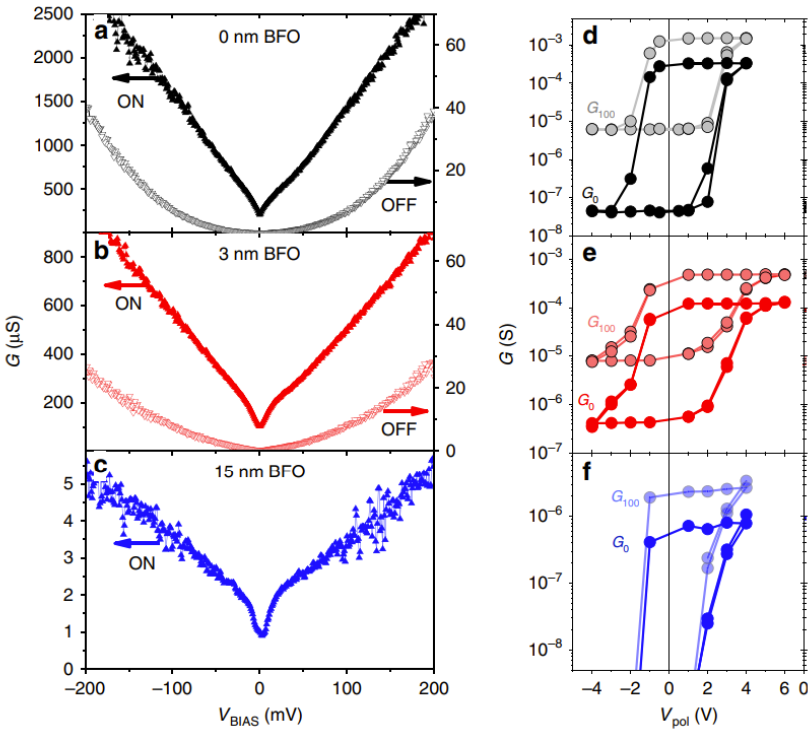

Fig. 4.2: G of a MoSi $(100\ nm)$/BFO (t_{BFO})/YBCO $(30\ nm)$ micro-junction measured at $4.2\ K$ as a function of V_{BIAS} and V_{pol} for three different BFO thicknesses: $t_{BFO} = 0\ nm$ [(a) and (d)], $t_{BFO} = 3\ nm$ [(b) and (e)] and $t_{BFO} = 15\ nm$ [(c) and (f)]. For more information about the experimental details and the graphs, refer to the paper of Rouco et al. Nat. commun. (2020) [154].

at the interface between MoSi and YBCO without the need to include a thin layer of BFO. Finally, although redox reactions are typically triggered by a voltage bias, el Hage *et al.* [93] demonstrated in 2022 the possibility to induce a back and forth motion of oxygen between YBCO and the transparent semiconductor indium tin oxide (ITO) via light illumination in the visible and UV range, paving the way for novel superconducting optical field-effect devices. The authors attribute this switching to redox reactions and photovoltaic effects taking place simultaneously, whose balance determine the direction of the oxygen motion.

1.1.2. Electromigration

Electromigration corresponds to the forced diffusion of ions into metals due to electric fields and high current densities [230]. Well-known in the semiconductor industry, Moore's law predicts that the number of transistors in an integrated circuit doubles every year, giving rise to higher current densities due to increasingly smaller devices. Therefore, electromigration represents one of the main causes of failure in today's integrated electronics and can lead to the degradation of materials over time and the occurrence of unwanted short circuits [231]. Although this phenomenon has been studied extensively to improve semiconducting technologies' efficiency and reliability, it remains to this day a challenging topic, owing to its various origins and potential factors, such as grain structure [232], defects, thermal effects or stresses [233]. As one of the most important failure mechanisms in the nanoscale technologies' industry, the electromigration of oxygen ions mediated by high current densities in cuprate superconductors has been thoroughly investigated in the literature [155,156,241,242,157,234–240]. In 1990 (only 4 years after the discovery of cuprate superconductors), Vitta *et al.* [234] reported scanning electron microscope pictures of electromigration failure in highly oriented YBCO thin films [235]. The following years, many papers

were published on the study of electromigration in nanobridges made of YBCO, demonstrating that the current density necessary for starting the electromigration of oxygen is approximately equal to $J_C \approx 8\ MA.cm^{-2}$ [155–157]. Especially, Baumans *et al.* [156] showed that partial recovery of the superconducting state was achievable by applying opposite voltages onto a YBCO nanobridge with an in-plane area of $\sim 5\ \mu m^2$ and a thickness of $100\ nm$, as depicted in **Fig. 4.3(c)**.

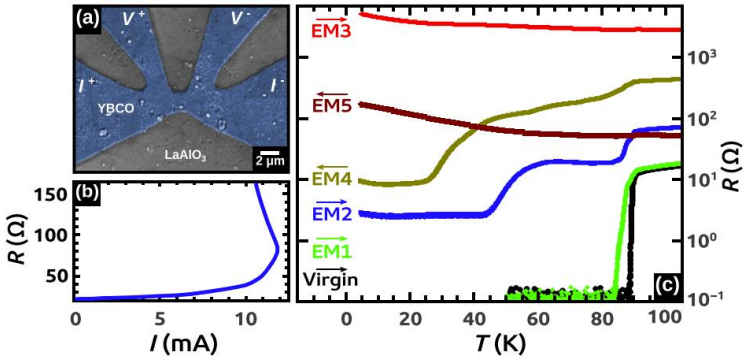

Fig. 4.3: (a) Scanning electron microscopy image of a YBCO nanobridge with a central area of approximately $5\ \mu m^2$. (b) Resistance of the nanobridge as a function of the current during an electromigration (EM) process. (c) Resistance of the nanobridge as a function of temperature after consecutive electromigration experiments, displaying partial recovery of the superconducting state between $\overrightarrow{EM3}$ and $\overrightarrow{EM4}$. Figure taken from Baumans et al., Appl. Phys. Lett. (2019) [156].

1.1.3. Thermomigration

A third strategy for the *in-situ* control of the oxygen stoichiometry in YBCO is to induce a forced motion of oxygen triggered by high thermal gradients, denoted as thermomigration. Contrarily to redox reactions and electromigration processes, experimental studies on the thermomigration of oxygen ions in cuprate superconductors have been relatively limited [155,157,243]. In 2020, it has been shown by finite element simulations conducted with COMSOL [244] by Marinkovic *et al.* [155] that the thermomigration of oxygen ions inside YBCO's crystalline structure starts at approximately $673\ K$. Then, in 2021, Trabaldo *et al.* [157] attributed the gradual decrease of the critical temperature of a YBCO nanobridge while applying RF currents (with the shape of a square wavefunction of frequency $1\ kHz$) to the controlled thermomigration of oxygen ions. Finally, in 2023, Marinkovic *et al.* [243] experimentally investigated the migration of oxygen vacancies in untwinned YBCO thin films under application of high current densities and demonstrated (with the support of numerical simulations) that the flow is ultimately triggered by a local Joule heating mediated by the dissipated power. The authors demonstrate a non-reversible increase of the device's resistivity with a different current threshold that depends on the direction of the applied current alongside distinct crystallographic directions. This effect is illustrated in **Fig. 4.4** [243], showing the evolution of the resistivity ρ of a $5 \times 2\ \mu m^2$ YBCO bridge while injecting a current alongside the a-axis, b-axis and 45 °-axis: ρ first slightly decreases above a specific threshold before abruptly increasing.

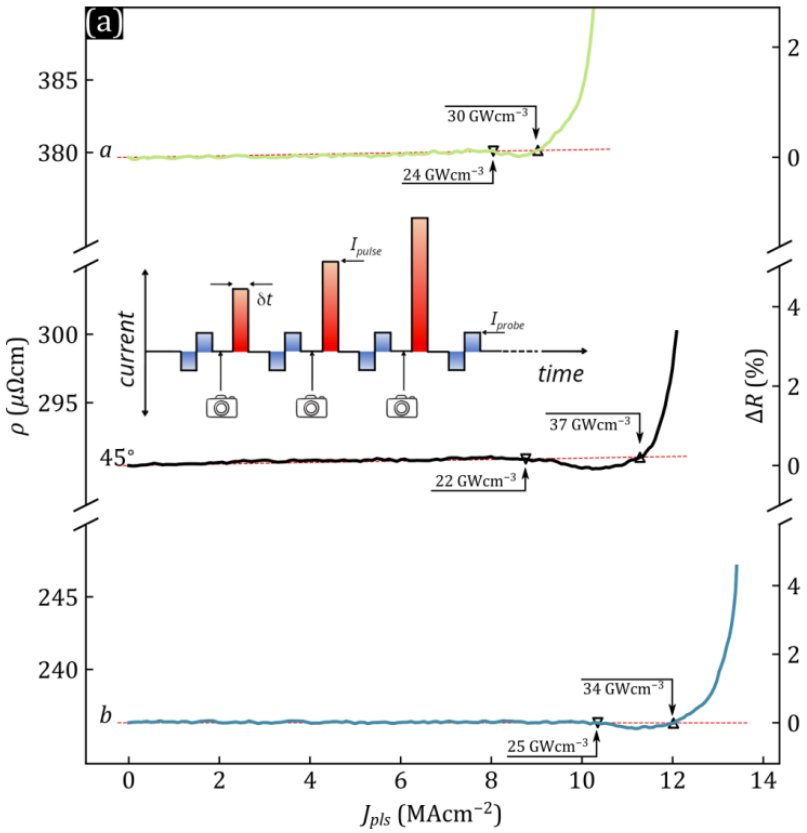

Fig. 4.4: Resistivity ρ of a YBCO transport bridge $(5 \times 2\ \mu m^2)$ *as a function of the applied current density* J_{pls} *alongside three different crystallographic orientations : (top) [100] a-axis, (middle) [110]* $45\ °$*-axis and (bottom) [010] b-axis. After a first current threshold (pointing down triangle), the resistivity first undergoes a small decrease before rapidly increasing after a second threshold (pointing up triangle). Figure taken from Marinkovic et al., Phys. Rev. B (2023) [243].*

1.2. Envisioned goal application: cryogenic radiofrequency switch

The three strategies described above (redox reactions, electromigration and thermomigration) correspond to the three main mechanisms allowing for an electrically triggered movement of oxygen ions within YBCO's crystal structure. The envisioned goal application of this chapter is a superconducting radiofrequency switch (RF switch), exploiting a controlled superconductor-to-insulator phase transition in a superconducting coplanar waveguide (SCPW) geometry based on a controlled motion of oxygen ions that locally modifies the hole doping concentration of a high-T_C superconducting thin film of YBCO in contact with aluminium (Al). Within the framework of this thesis, I contributed to the invention of such a device and a patent to protect this invention has been filed.

An RF switch is a device used to route microwave signals through transmission lines to connect antennas, amplifiers and filters. As the market surrounding microwave applications is rapidly growing, the need for efficient, reliable, fast and low energy-consuming RF switches operating at cryogenic temperatures is becoming more and more crucial. As described in more details in **Chapter 1, Sect. 2.1.3.**, currently available RF switches are unable to fill these conditions for a wide range of frequencies at very low temperatures due to high-power dissipation.

A SCPW is a very common planar transmission line characterized by a superconducting centre strip between two ground planes on top of a dielectric substrate, as depicted in **Fig. 4.5(a)**. This geometry is widely used for various applications such as amplifiers [245], mixers [246] or superconducting qubits [247]. Commonly in these types of transmission lines, the dielectric constant of the substrate is

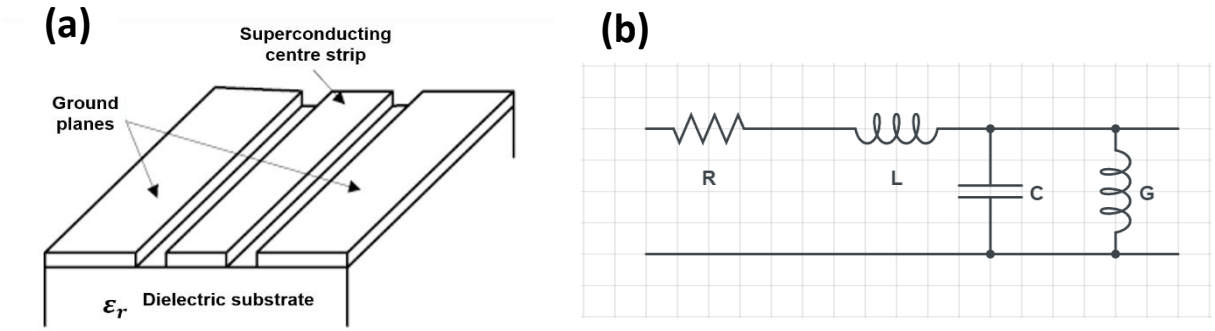

Fig. 4.5: (a) Schematic picture of a typical superconducting coplanar waveguide (SCPW). A SCPW consists in a superconducting centre strip between two ground state on a dielectric substrate. (b) Equivalent circuit of a superconducting coplanar waveguide. R represents losses caused by a non-zero resistance of the guide, while G is the non-zero conductance of the substrate.

much larger than that of the air. Consequently, SCPWs cannot support perfect transverse mode (TEM) but can be considered as quasi-TEM waveguides at low frequencies. Another possible geometry for a SCPW is the so-called conductor-backed coplanar waveguide, with a third ground plane covering the back-face of the dielectric substrate, yielding a better overall transmission.

The equivalent circuit of a coplanar waveguide is given in **Fig. 4.5(b)**, with a total equivalent impedance:

$$Z_0 = \sqrt{\frac{R + jL\omega}{G + jC\omega}} \tag{4.1}$$

where R and G represent losses coming from a non-zero resistance in the guide and a non-zero conductance in the substrate, respectively. In the case of a superconducting coplanar waveguide, the losses are reduced to a minimum and it is possible to consider the simplifications $R \ll L\omega$ and $G \ll C\omega$, leading to the simplified equation:

$$Z_0 \approx \sqrt{\frac{L}{C}} \tag{4.2}$$

The RF switch envisioned for this project consists of a typical SCPW with an additional characteristic: an active element connecting the signal plane to the ground plane [**Fig. 4.6(a)**]. The active element will act as a short between the lines and being able to control the active element's resistance will allow to tune the waveguide's attenuation, therefore engineering an RF switch made of superconducting materials**.** The equivalent circuit of such SCPW with the active element becomes the one shown in the inset of **Fig. 4.6(b),** with R_w the resistance of the SCPW and R_{ae} the resistance of the active element. This system leads to the following equation for the attenuation of the waveguide in a standard 50-ohm system:

$$A = \frac{2}{2 + \frac{R_w}{R_{ae}} + \frac{R_w}{50} + \frac{50}{R_{ae}}} \tag{4.3}$$

The attenuation of the SCPW, calculated from **Eq. 4.3**, is plotted in **Fig. 4.6(b)** as a function of the active element's resistance R_{ae} for an arbitrary low value for the resistance of the superconducting transmission line. We observe that being able to tune the resistance of the active element between a few ohms to a few tens of ohms can lead to a drastic decrease of the attenuation, with performances

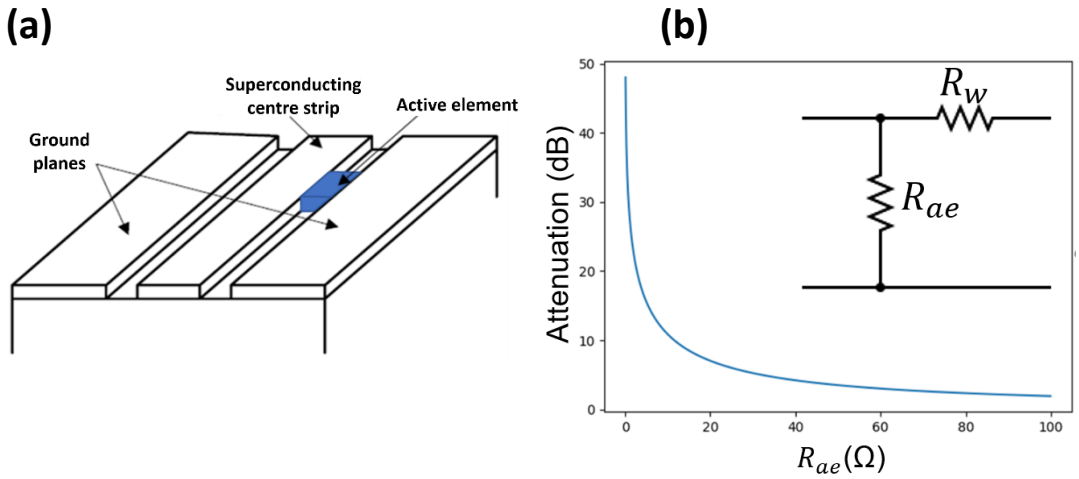

Fig. 4.6 : (a) Schematic picture of a superconducting coplanar waveguide with an additional active element, represented in blue, shorting the signal plane with the ground planes. Tuning the attenuation of the SCPW is possible via a control of the active element's resistance. (b) Attenuation of SCPW as a function of R_{ae}. The inset shows the equivalent circuit with the resistance of the waveguide R_w in parallel with R_{ae}.

competitive to the ones of currently available RF switch technologies (see **Chapter 1, Sect. 2.1.3.**), while offering the additional advantage of being able to operate at cryogenic temperatures.

1.3. Proof-of-concept: superconducting transistor-like device

Characterizing the behaviour of the resistance of the active element and determining the optimal geometric parameters is the first step towards the fabrication of the RF switch described in the previous section. This chapter is aimed at measuring the transport properties of a resistance switching proof-of-concept device that could be implemented as the active element in **Fig. 4.6(a)**.

The schematic representation of the proof-of-concept device is shown in **Fig. 4.7(a)** and consists in a transistor-like structure made from the high-T_C superconductor YBCO and the metal Al on a sapphire substrate. The gold electrodes are named by analogy with a conventional field-effect

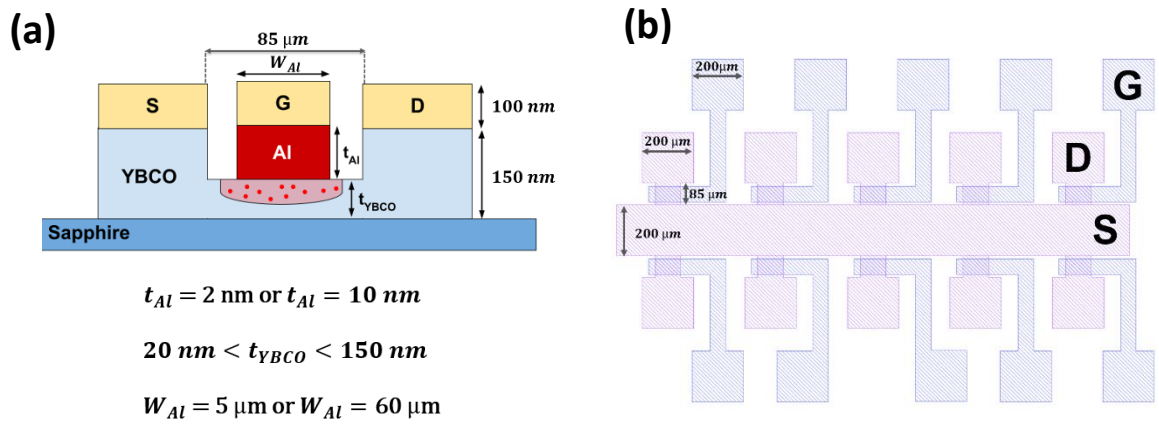

*Fig. 4.7: (a) Schematic representation of the active element of the RF switch in a transistor-like geometry. The electrical contacts are defined by analogy with a conventional field-effect transistor: source (S), gate (G) and drain (D). The three varying geometric parameters (t_{Al}, t_{YBCO} and W_{Al}) and their respective values are summarized below the structure. (b) View from above of a measuring bar with typical in-plane distances. One measuring bar is composed of ten proof-of-concept devices as the ones presented in **Fig. 4.7(a)**.*

transistor, with the source (S), gate (G) and drain (D) contacts. For all the studied devices in this chapter, three geometric parameters are varying: the YBCO channel has a thickness of $20\ nm < t_{YBCO} < 150\ nm$, the layer of Al has a thickness of $t_{Al} = 2$ or $10\ nm$ and the width of the gate is $W_{Al} = 5$ or $60\ \mu m$. All the other parameters are fixed and summarized in **Fig. 4.7(a)**. Such a device allows to take advantage of the redox reactions scenario described in **Sect. 1.1.1.**: the redox reaction should naturally reduce the material with a higher reduction potential (here YBCO, given the high reduction potential of copper $E^{\circ}(Cu) = 2.4\ eV$) and oxidize the material with a lower reduction potential (Al, with $E^{\circ}(Al) = -1.676\ eV$) [9], generating an oxygen depleted region within the YBCO layer close to the Al/YBCO interface, depicted as a light red area in **Fig. 4.7(a)**. This will allow the modulation of the channel's conducting properties. In addition, applying electric fields should lead to the control of the volume of the oxygen-depleted region and therefore tune the channel resistance, thus engineering the working principle of the active element for cryogenic RF switching applications.

The values for the thickness of Al were chosen by calculating the expected volume of the YBCO oxygen depleted region by simple crystallographic arguments: aluminium oxide (Al_2O_3) is created at the interface by pumping one oxygen atom per unit cell from YBCO down to a characteristic t_d thickness (see **Fig. 4.8**). The full calculations are given in **Annexes, Sect. 1.2.**, yielding a final value of:

$$t_{Al} = \frac{t_d \times v_{Al}}{3v_{YBCO}} \tag{4.4}$$

where t_d is the thickness of the oxygen depleted region within the YBCO layer and v_{YBCO} (v_{Al}) is the volume of the crystallographic unit cell of YBCO (Al). Therefore, as $20\ nm < t_{YBCO} < 150\ nm$, the minimum thickness of aluminium needed to completely deplete $20\ nm$ of YBCO is equal to $t_{Al} = 9.9\ nm$. For this work, a value of $t_{Al} = 10\ nm$ was chosen. Moreover, multiple samples have also been prepared with a thickness $t_{Al} = 2\ nm$ for comparison purposes. Although these simple calculations give a rough approximation of the volume of aluminium needed for a complete deoxygenation of the YBCO layer, it is important to mention that it has been shown in a previous experiment that the depleted region caused by redox reactions at this type of interface (YBCO/MoSi) should have a thickness of approximately $2\text{-}3\ nm$ [154]. However, this paper does not consider the impact of electromigration and thermogradient when a current is injected across a metal/cuprate interface,

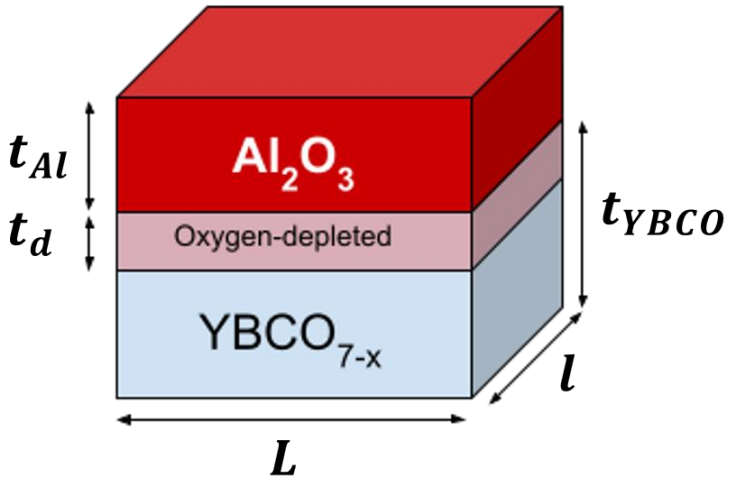

Fig. 4.8: Representation of the interface between Al and YBCO used for the mathematical calculation of the aluminium thickness. Al spontaneously oxidizes into Al_2O_3 at the expense of YBCO, generating an oxygen-depleted region represented in light red.

which will be discussed later in this chapter.

The global shape and in-plane distances of a measuring bar were chosen in the light of the final envisioned goal: a superconducting coplanar waveguide for cryogenic applications. This is illustrated in **Fig. 4.7(b)**, showing a view from above of the shape of the measuring bar, with distances of the order of a few tens or hundreds of micrometres, typical of coplanar waveguides. Each measuring bar is composed of ten proof-of-concept devices.

2. Samples fabrication and description

2.1. Fabrication steps

The fabrication was performed on commercial 150 nm-thick YBCO (001) grown on r-cut sapphire (Al_2O_3) substrates of $10 \times 10\ mm^2$ (CERACO ceramic coating GmbH). A buffer layer of cerium oxide (CeO_2) is included between the YBCO and sapphire layers to reduce the structural parameters mismatch. The samples are also capped with $100\ nm$ of gold for protection and contact purposes. **Fig. 4.9** shows the 3-step process leading to the fabrication of the transistor-like devices. Each step (represented by a, b and c in chronological order) is depicted by a schematic side-view of the multilayer (left) as well as a microscope top view (right) of the measuring bar taken after completion of the respective fabrication step.

The first step [**Fig. 4.9(a)**] consists of the etching of the devices' layout. One wafer contains twelve bars as the one shown in the picture, and each bar contains ten devices. The bars were patterned using

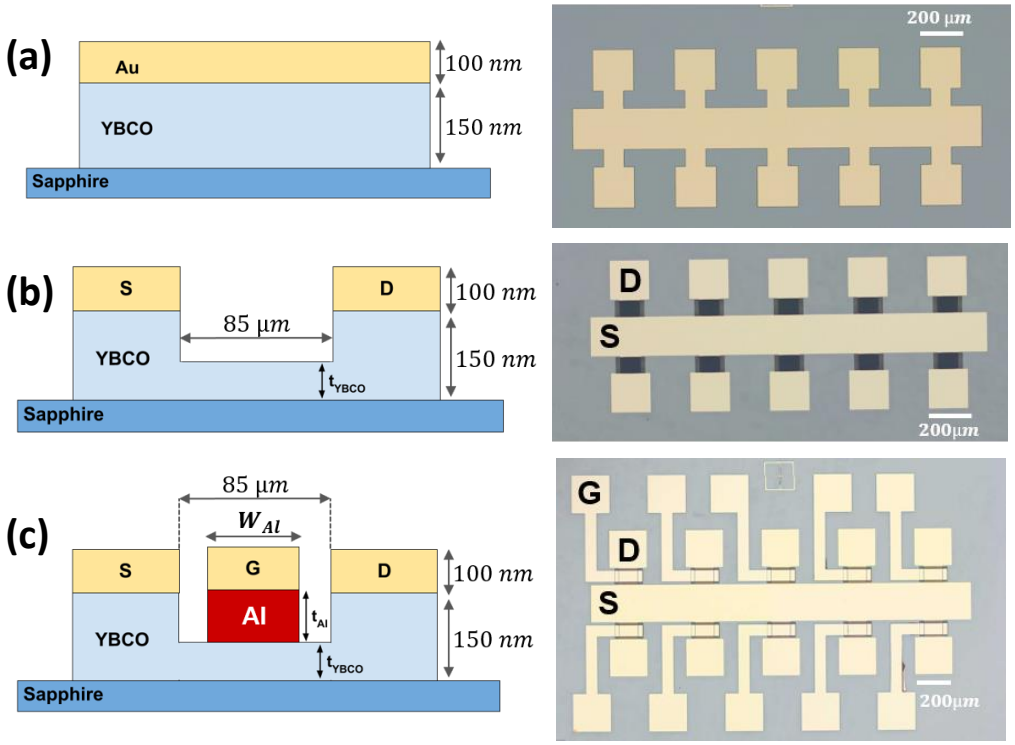

*Fig. 4.9 : 3-step fabrication process of the transistor-like structures. The fabrication recipe is described in full details in **Annexes, Sect. 1.1.** (a) Step 1: etching of the YBCO measuring bar using optical photolithography and IBE. (b) Step 2: etching of the transistor channel using optical photolithography and IBE to reduce YBCO's thickness down to the desired value by adjusting the etching time. (c) Step 3: sputtering deposition of the Al/Au gate on top of the transistor's channel.*

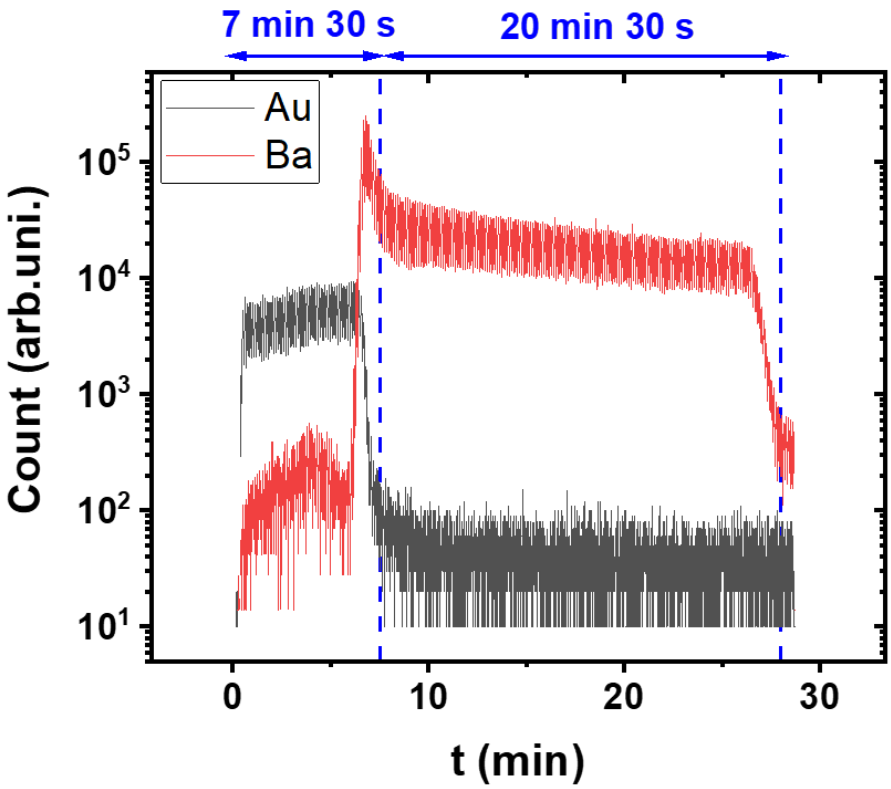

Fig. 4.10: Typical SIMS signal corresponding to the first microfabrication step, showing the number of counts in arbitrary units as a function of time during the etching process for gold (black) and barium (red). The etching times were approximately 7 min 30 sec and 20 min 30 sec for the $100\ nm$*-thick gold layer and the* $150\ nm$*-thick YBCO layer, respectively.*

conventional optical projection lithography (**Chapter 3, Sect. 4.1.1.**) and ion beam etching (IBE, **Chapter 3, Sect. 4.2.**), monitored by a secondary ion mass spectrometer (SIMS). **Fig. 4.10** shows the typical behaviour of the SIMS' signal for gold and barium while etching down to the cerium oxide layer. It is possible to calculate from this graph the etching rates for gold and YBCO for our set of etching parameters, $\sim 13.3\ nm/min$ and $\sim 7.3\ nm/min$, respectively. The etching was stopped according to the change of the barium signal: when it falls back down to a low count value, the YBCO layer can be considered as completely etched (see second vertical blue dotted line in **Fig. 4.10**).

The second microfabrication step defines the source (S) and drain (D) contacts by applying the same process of optical projection lithography and IBE etching as the first step. The gold layer is removed and the thickness of YBCO is reduced down to a certain thickness (t_{YBCO}) between the S bar and the D contacts, as shown in **Fig. 4.9(b)**. The desired t_{YBCO} (ranging from $20\ nm$ to $150\ nm$) is attained by a time-controlled IBE etching with etching rates inferred from the previous step. The actual thickness has been subsequently measured using atomic force microscopy (AFM) and the details can be found in the next section. Finally, the third step [**Fig. 4.9(c)**] consists of the elaboration of the gate (G) contacts via projection lithography and sputter deposition. The gate is made of a thin layer of aluminium ($t_{Al} = 2\ nm$ or $t_{Al} = 10\ nm$) with a gold capping of $100\ nm$ and have been deposited after 30 seconds of argon ion milling for cleaning residues of resist from the lithography steps and remove the first atomic layers that have been damaged during the previous IBE etching process. These contacts have been deported away from the channel to avoid damaging the Al/YBCO interface while bonding the samples.

Fig. 4.11(a) shows a top-view microscope picture of the shape of a final device, while **Fig. 4.11(b)** is the schematic side-view already described in **Fig. 4.7(a)** reported again here for clarity. Full details

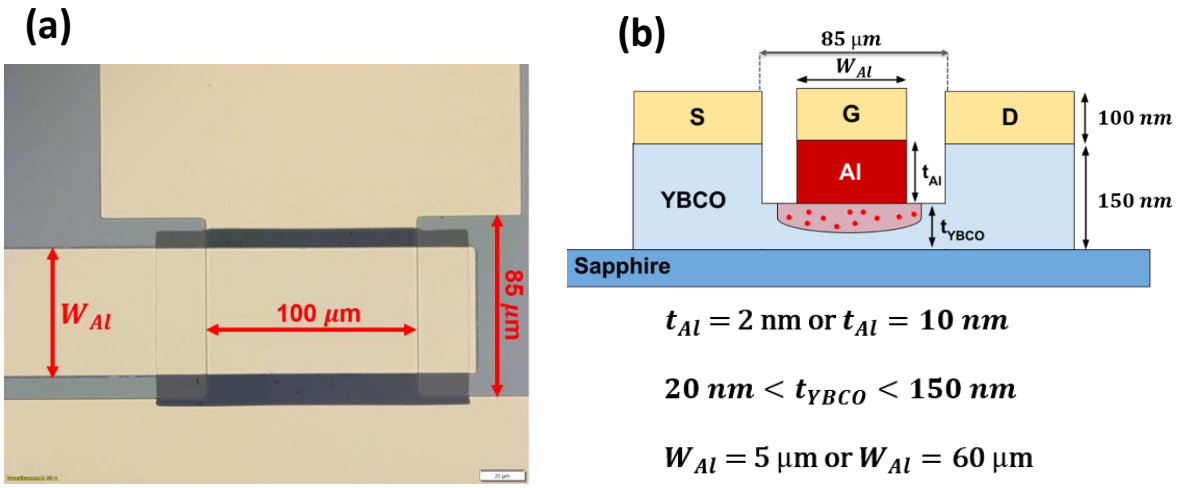

Fig. 4.11 : Summary of the important geometric parameters of the transistor-like structures. (a) Microscope top-view of a device after deposition of the Al/Au gating. The distance between the source and drain contacts $(85\ \mu m)$ *and the lateral dimension of the channel* $(100\ \mu m)$ *will be fixed throughout the whole chapter, while the distance* W_{Al} *will be equal to* $5\ \mu m$ *or* $60\ \mu m$*. (b) Side-view schematic picture of the device and a summary of the typical distances.*

about the fabrication process, the clean-room recipes and the machines' parameters can be found in **Annexes, Sect. 1.1**.

2.2. AFM thickness measurements

Following step 2 of the fabrication process, AFM measurements were conducted to determine precisely the thickness t_{YBCO} of the superconducting channel after the etching of the gold and YBCO layers. Each AFM measurement consists of three scans, measured at three different locations on the sample's surface, as depicted in **Fig. 4.12(a)**. These scans allow for the calculation of the thickness via two different methods: on one hand, the thickness of the YBCO layer must be equal to the difference between step 1 and step 2, and on the other hand, it must also be found by subtracting the two steps'

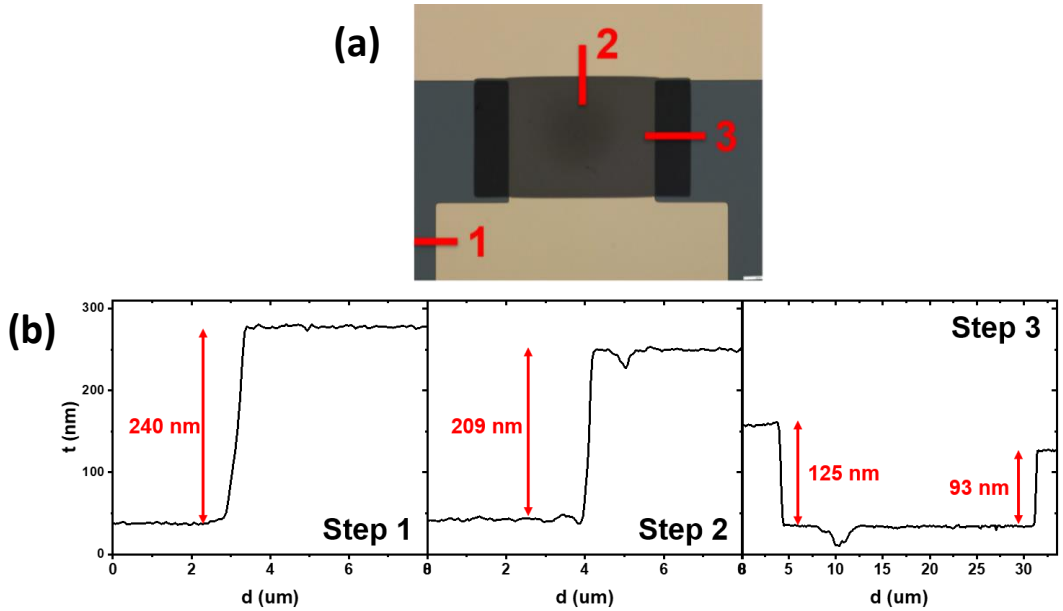

Fig. 4.12: (a) Microscope picture of a fabricated device before the gate deposition during step 3, showing the three locations where the steps were measured with AFM. (b) Example of typical AFM measurements consisting in a set of three graphs, allowing for the precise calculation of t_{YBCO}*.*

heights of step 3. In the example given in **Fig. 4.12(b)**, the AFM measurements yield consistent results with $t_{YBCO} = 31\ nm$ for the first method and $t_{YBCO} = 32\ nm$ for the second method.

2.3. Superconducting properties of the YBCO channel

An important preliminary measurement consists of measuring the resistance R_{SD} of the YBCO channel after the etching process of the second microfabrication step, *i.e.* before the deposition of the Al/Au gate electrodes of step 3. **Fig. 4.13(a)** shows the 2-probe resistance R_{SD} as a function of the temperature measured for decreasing t_{YBCO} (or, equivalently, for increasing etching times). As the thickness reduces, the resistance of the channel in the normal state (above T_C) increases, while T_C decreases. The critical temperature, calculated as the value of the temperature for which the derivative of the $R(T)$ curve reaches a maximum [see an example in the inset of **Fig. 4.13(b)**], is plotted in **Fig. 4.13(b)** as a function of t_{YBCO}. One can see that, even for $t_{YBCO} \approx 34\ nm$, the resistance shows a clear transition between a metallic to a superconducting state, with a superconducting transition of about $\Delta T_C \approx 8\ K$ at a critical temperature of $T_C \approx 72\ K$. For $T < T_C$, a very small resistance between $0.1\ \Omega$ and $1\ \Omega$ still remains. This small residual resistance is a consequence of the 2-probe configuration of the measuring setup which senses the contact resistances.

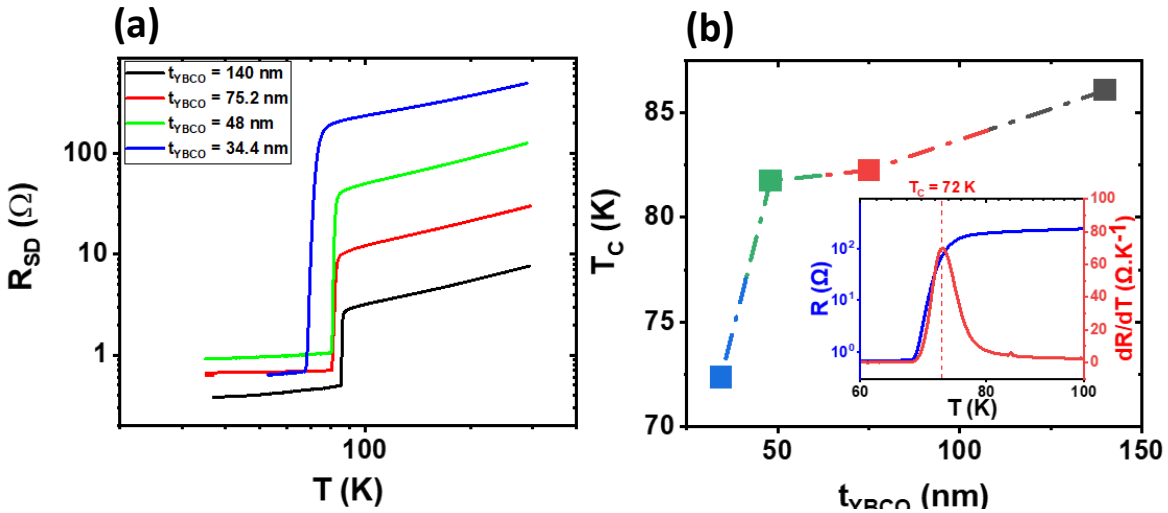

*Fig. 4.13: Measurements done on multiple measuring bars of sample X1. (a) 2-probe resistance R_{SD} for $I = 10\ \mu A$ as a function of temperature measured for devices with $34.4\ nm < t_{YBCO} < 140\ nm$. As t_{YBCO} diminishes, T_C also decreases, while the resistance in the metallic phase $T > T_C$ increases. (b) T_C as a function of t_{YBCO} calculated from the curves presented in **Fig. 4.13(a)** with a matching color-coding. The inset shows an example (for $t_{YBCO} = 34\ nm$) of the calculation of T_C by taking the maximum of the first derivative.*

3. Transport measurements of the transistor-like devices

This section is now aimed at the description of the transport measurements conducted on the proof-of-concept devices introduced in **Sect. 1.3.** First, a summary of all the samples with the most important thicknesses and distances as well as a description of the measuring setup will be given. Then, the results of the transport experiments and how the conducting properties of the devices can be tuned through the application of specific voltages will be illustrated and discussed.

3.1. Samples summary and measuring setup

For this project, different samples with varying geometries were measured, as was indicated in the description of the fabrication process and summarized in **Fig. 4.11**. A complete outlook of all the studied samples is given in **Tab. 4.1**. While presenting data in the remaining paragraphs of this chapter, the names and important thicknesses of the measured samples will be indicated in the text and the figures' captions. The reader may come back to this section to check the different thicknesses and distances.

Note that a typical sample is made of twelve measuring bars, each bar containing ten devices. The samples and measuring bars with their respective t_{YBCO}, t_{Al} and W_{Al} used for this work are listed in the following table in chronological order of fabrication:

Sample's name	Measuring bar	t_{YBCO} (AFM) [nm]	t_{Al} [nm]	W_{Al} [µm]
X1	X1A	140	2	60
	X1B	75	2	
	X1C	48	2	
	X1D	34	10	
	X1E	30	10	
X2	X2A	110	10	60
	X2B	50		
X2WAl	X2WAlA	125	0	60
	X2WAlB	72		
	X2WAlC	57		
X3	X3A	125	2	60
	X3B	112		
	X3C	57		
	X3D	47		
	X3E	31		
X4	X4A	125	10	5
	X4B	87		
	X4C	53		

Table 4.1: Summary of the samples and measuring bars studied for this project, with a description of the important distances and parameters. The third sample X2WAl (represented with a grey shading) is a control sample without aluminium gating ($t_{Al} = 0\ nm$) for comparison purposes.

It is important to mention that the third sample (X2WAl), highlighted in a grey shading in **Tab. 4.1**, is designed as a control sample. In fact, the G contact for this particular sample is made entirely of gold (a noble metal), without aluminium, and will thus be used for comparison purposes when necessary, in particular to help identify the origin of the observed physical phenomena.

The rest of this chapter will be dedicated to the analysis and discussion of the transport measurements that were conducted on the samples introduced above. The devices' characterization is divided into two different sets of measurements, as shown in **Fig. 4.14**:

(i) **Gate measurements** [**Fig. 4.14(a)**]**:** the first set consists of the transport measurements between the gate and drain contact pads which probe the Al/YBCO interface in series with part of the transistor's channel, as we apply voltage cycles $V_G(t)$ to trigger redox chemical reactions and measure the current I_G in 2-probe.

(ii) **Source-drain channel measurements** [**Fig. 4.14(b)**]**:** the second set probes the source-drain channel conductance to analyse the consequences of the voltage gating on the superconducting properties of the YBCO channel. A current I_{SD} is applied between the source and drain contacts and the voltage V_{SD} is measured in 2-probe.

In both cases, we will monitor how the gate and channel transport properties change upon (or after) application of relatively large gate voltages (typically up to $\sim 20 - 30\ V$). Importantly, both sets are measured independently and consecutively. In the rest of this chapter, to avoid confusion, the subscript 'SD' will be used when describing any physical quantity that was measured while probing the source-drain channel, whereas the subscript 'G' will be used for gate-related quantities. All the electrical measurements in this chapter were performed using a 2-probe configuration.

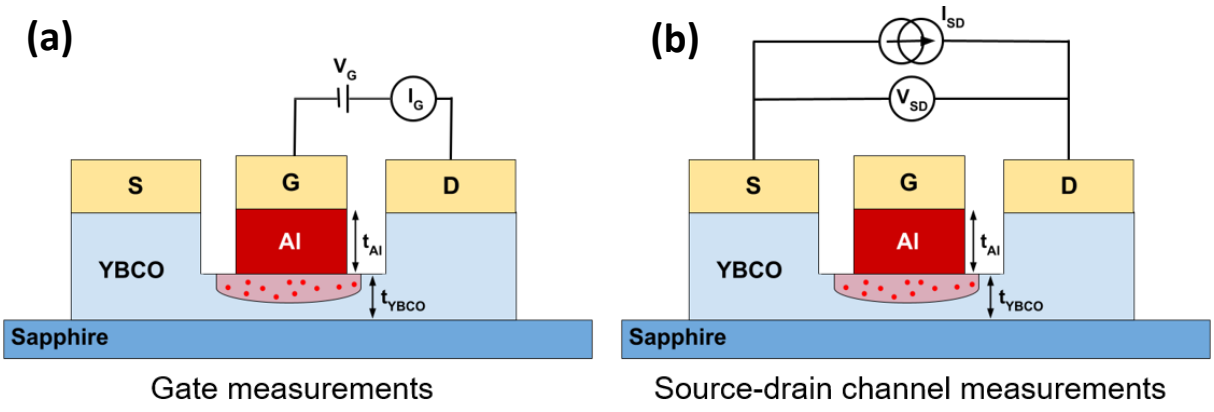

Fig. 4.14: Schematic representation of the transport measurements' experimental setup. (a) Gate measurements: a voltage V_G is applied between the G and D contacts and the current I_G is measured in a 2-probe configuration. (b) Source-drain channel measurements: a current I_{SD} is applied between the S dans D contacts and the voltage V_{SD} is measured in a 2-probe configuration. All the electrical measurements in this chapter were performed in a 2-probe configuration.

3.2. Gate-drain measurements: memristive behaviour

For the first set of measurements, the current is measured while a voltage cycle is applied between the gate and drain contacts [see **Fig. 4.14(a)**] using a Keithley 2400 sourcemeter in a 2-probe configuration. It is important to notice that, because of the 2-probe configuration, the measurement is probing not only the interface between aluminium and YBCO but also part of the transistor's channel in series. The shape of the applied voltage cycles is shown in the inset of **Fig. 4.15(a)**: the gate voltage V_G is ramped up in steps from $0\ V$ to a target voltage that we call V_{write} (which can be positive or negative) and decreased down to $0\ V$ in a fixed time t_G and a fixed number of steps. Usually, unless written otherwise in the text and figures, the time of application of the cycles will be 20 seconds while the number of steps will be 100. As will be shown below, the denomination "writing voltage" V_{write} is adopted because, depending on its magnitude, the gate-drain conductance is set to different non-volatile conductance levels.

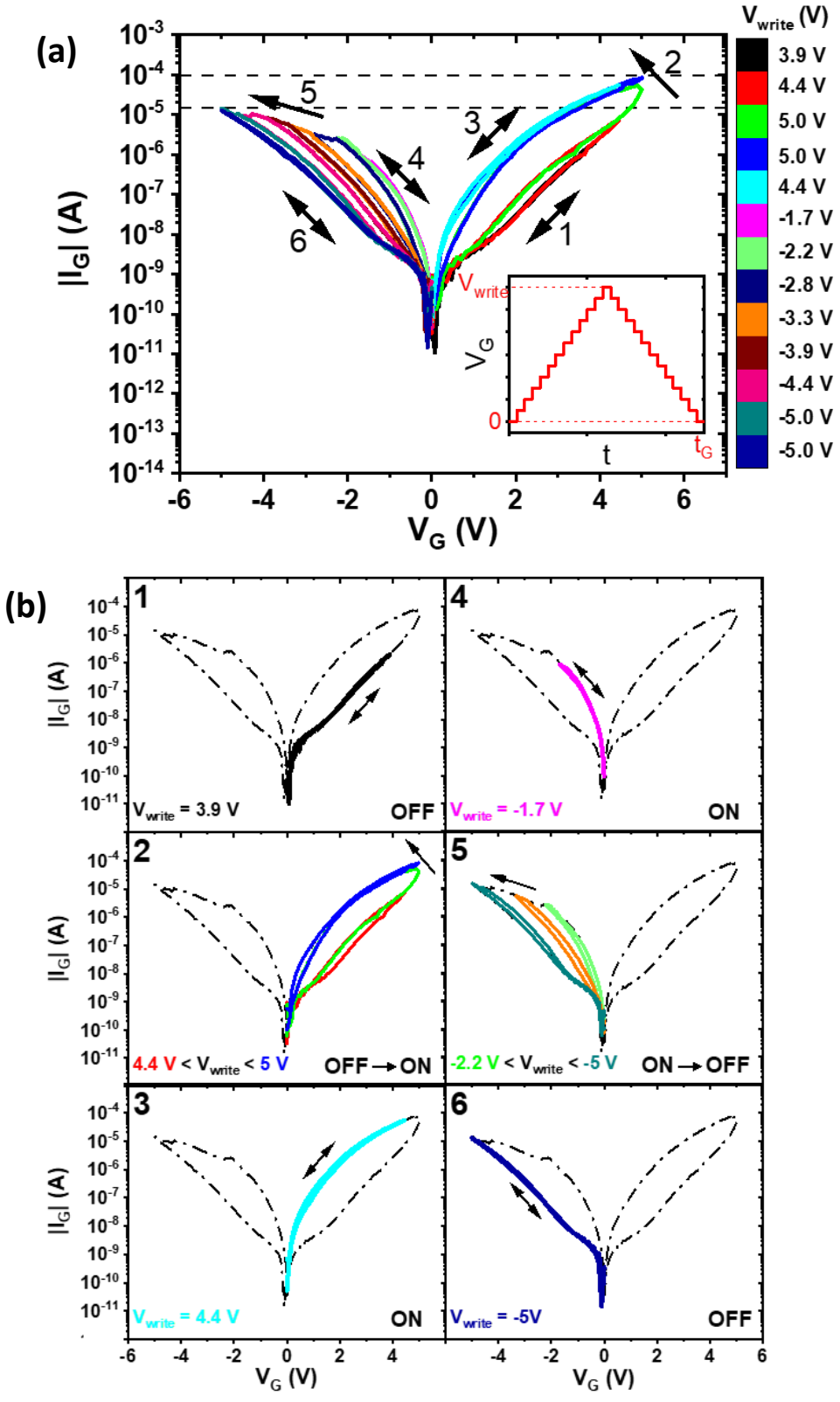

Fig. 4.15: Measurements done on a device with $t_{Al} = 10\,nm$ and $t_{YBCO} = 110\,nm$ at $40\,K$ (X2A). (a) Typical I_G-V_G characteristics of the gate switching process between $-5\,V$ and $+5\,V$. The inset shows the shape of a voltage cycle going from $0\,V$ to V_{write} and back to $0\,V$ in a given time t_G and a fixed number of steps. (b) Splitting of the switching effect into six consecutive regimes. For clarity, the outline of the I-Vs is plotted as a guide to the eye. Regime 2 demonstrates the switching from the low conducting state (OFF state) to the high conducting state (ON state) for $4.4\,V < V_{write} < 5\,V$ and $5\,V$, whereas regime 5 shows the opposite switching as negative $-5\,V < V_{write} < -2.2\,V$ are applied.

3.2.1. Gate conductance switching

3.2.1.1. Current-voltage characteristics and switching

Fig. 4.15(a) displays typical gate current-voltage (I-V) characteristics (the absolute value of the measured current is shown in logarithmic scale as a function of the applied voltage) measured on a device with $t_{Al} = 10\,nm$ and $t_{YBCO} = 110\,nm$ for a fixed temperature of $40\,K$. One set of measurements is usually composed of around 40 or 80 cycles of different V_{write}, although in the figure, only the measurements for a selected subset of V_{write} are shown for clarity. A clear switching between two distinct conductive states can be observed depending on V_{write}. As is usual for devices displaying memristive behaviours, the low (high) conducting state will be denoted as the OFF (ON) state in the rest of the chapter. To better depict this phenomenon, six distinctive V_{write} regimes (labelled from 1 to 6) are displayed in **Fig. 4.15(b)**. In each of these graphs, the outline of the set of I-Vs is plotted in black dotted lines as a guide to the eye.

In particular, regime 1 corresponds to cycles with a writing voltage V_{write} between $0\,V$ and $3.9\,V$. For this range of voltages, the I-V characteristics are perfectly reversible: the current measured while ramping up the gate voltage from $0\,V$ to $3.9\,V$ is equal to the current measured while decreasing it back to $0\,V$. This reversible effect is denoted by a double-headed arrow. While increasing the excursions of the voltage above the $3.9\,V$ threshold, the switching process starts: a clear change of the I-V characteristics between the OFF to the ON state can be seen in regime 2. The switching process is characterized by a lower value of the conductance in the increasing branch $0\,V \rightarrow V_{write}$ and a higher conductance in the decreasing branch $0\,V \rightarrow V_{write}$ and is therefore denoted by a single-headed arrow to emphasize the non-reversibility of the mechanism. Regimes 3 and 4 consist in a new stable ON state of the device while keeping V_{write} between $4.4\,V$ and $-1.7\,V$. Regime 5 shows the inverse switching mechanism for negative values of the voltage. Finally, we reach a new stable OFF state during regime 6 as the voltage cycles are gradually decreased to $0\,V$.

Another recurring effect of this type of measurement is the diode-like behaviour of the I-V characteristics or in other words, the asymmetry of the curves for positive and negative voltages. Note in particular that for the same absolute value of $|V_G| = 5\,V$, the currents measured for positive and negative voltages can be one order of magnitude apart [see the horizontal dotted lines in **Fig. 4.15(a)**]. This behaviour will be addressed later as we delve further into the intricacies of the system.

The reversible switching mechanism described above is almost invariably observed in all the devices studied, independently of t_{Al} and t_{YBCO}. Moreover, similar switching behaviours are observed for temperatures above and below the T_C of the YBCO channel, although the current levels and resistances are different. As an example, **Fig. 4.16** shows the switching of the gate-drain Al/YBCO interface for a device with $t_{Al} = 10\,nm$ and $t_{YBCO} = 53\,nm$ for a temperature of $87\,K > T_C$. The switching is similar in shape to the one observed in **Fig. 4.15(a)**, allowing for the distinction between six identical regimes, as indicated by the black arrows and numbers.

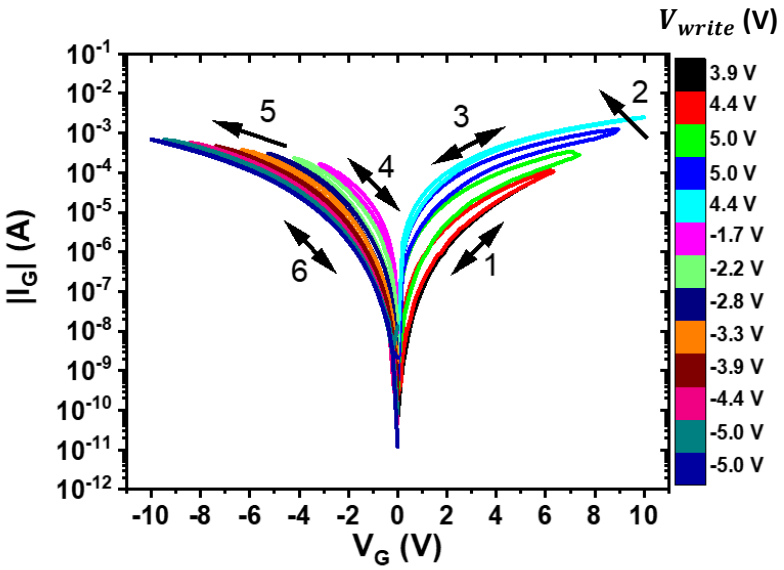

*Fig. 4.16: Switching effect similar to the switching observed in **Fig. 4.15(a)** for a device with $t_{Al} = 10\ nm$ and $t_{YBCO} = 53\ nm$ at $87\ K$ (X4C), illustrating that the switching has an similar shape above and below the superconducting transition. The arrows and corresponding numbers indicate the 6-regime switching in the same way it was described in **Fig. 4.15**.*

3.2.1.2. Low-bias measurements: characterization of the remnant state

The reversible switching behaviour of the Al/YBCO interface is more accurately characterized by measuring a low-bias I_G-V_G characteristic of the gate-drain junction to study its remnant conducting state. After each writing cycle, corresponding to one excursion in **Fig. 4.15(a)**, a characteristic of the gate is measured between $0.5\ V$ and $-0.5\ V$ with an increased number of points for a more precise measurement. This range of voltages is low enough to avoid switching the interface's conducting state while measuring. The differential conductance $G_G = dI_G/dV_G$ is then calculated, and the results are plotted as a function of V_G in **Fig. 4.17(a)**, color-coded per values of V_{write}, for a device with $t_{Al} = 10\ nm$ and $t_{YBCO} = 50\ nm$ at $35\ K$. The set of measurements typically contains 40 to 80 curves and only a selected subset is displayed. This experiment demonstrates the switching from the OFF state (blue curve) to the ON state (red curve) as V_{write} is increased from $0.8\ V$ to $5.4\ V$. Moreover, the intermediate states are perfectly stable during the time of the I-V measurement (typically of a few minutes), as indicated by the symmetry of the $G_G(V_G)$ curves for positive and negative V_G.

Subsequently, $G_G(V_{write})$ is calculated for a fixed value of $V_G = 100\ mV$ [indicated by the vertical black line in **Fig. 4.17 (a)**] and shown in **Fig. 4.17(b)** . Here again, the non-volatile switching between two states $G_{ON} \approx\ 1\ \mu S$ and $G_{OFF} \approx\ 0.01\ \mu S$, as high as two orders of magnitude (an increase of 9900 %) can be seen. It is worth noting that the amplitude of the switching is substantially higher for lower V_G and reduces for higher V_G; the maximum switching amplitude that was observed in these experiments was as high as three orders of magnitude. The switching is non-volatile; the conductance states are stable over times of the order of a few hours for temperatures below $200\ K$. However, the high conductance and intermediate states relax to the low conductance states at higher temperatures. This thermally activated relaxation process of the conducting state of the Al/YBCO interface will be discussed in more details later in the chapter (**Sect. 3.2.2.**).

The switching voltages $V_S(+)$ and $V_S(-)$ are defined as the values of the voltage for which the switching process is launched for positive and negative voltages, respectively. Therefore, $V_S(+)$

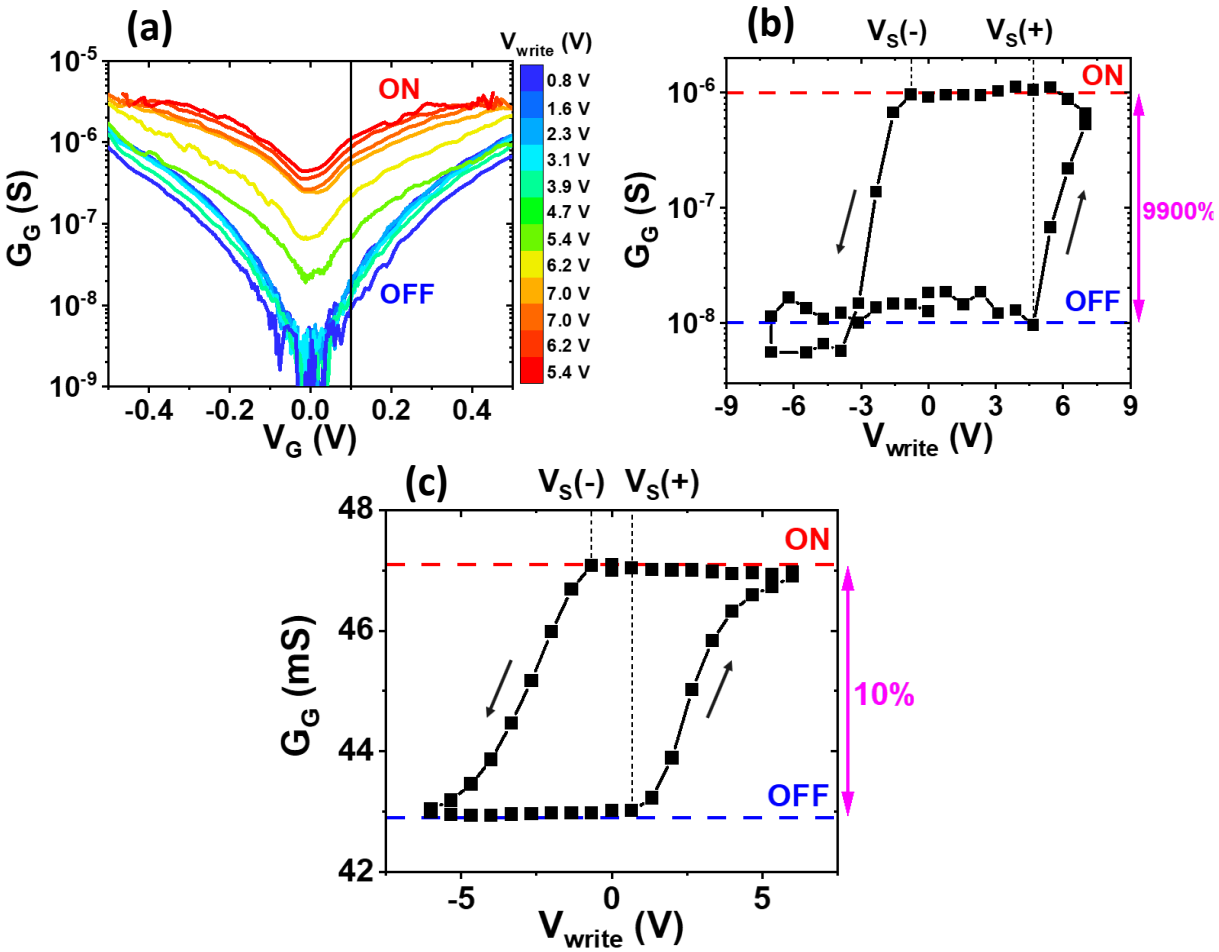

*Fig. 4.17: Measurements done on a device with $t_{Al} = 10\ nm$ and $t_{YBCO} = 50\ nm$ at $35\ K$ (X2B). (a) G_G of the Al/YBCO interface as a function of V_G between $-0.5\ V$ and $0.5\ V$ showing a clear switching from the OFF state (blue curve) to the ON state (red curve) as well as intermediate stable states. The vertical black line represents the chosen value of V_G along which **Fig. 4.17 (b)** is calculated. (b) G_G as a function of V_{write} for a fixed $V_G = 100\ mV$ demonstrating the reversible switching behaviour of the gate's conductance between two non-volatile ON and OFF states. (c) G_G as a function of V_{write} for a control sample with $t_{YBCO} = 72\ nm$ at $90\ K$ (X2WAlB), calculated in the same way as **Fig. 4.17(b)**. G_G also shows a small switching, but its amplitude is two orders of magnitude smaller (only $10\ \%$) compared to the one observed in **Fig. 4.17(b)**.*

corresponds to the minimum value of the voltage needed to start a switching from the OFF to the ON state, while $V_S(-)$ is the minimum value of the voltage required to start the opposite switching. The asymmetry between these two voltages, as illustrated in **Fig. 4.17(b)**, is invariably seen in all the measured devices and always show the same relation: $V_S(+) > |V_S(-)|$. In the particular case of **Fig. 4.17(b)**, the switching voltages are equal to $V_S(+) \approx 4.7\ V$ and $V_S(-) \approx -0.7\ V$. This is a consequence of the OFF state being the fundamental state of the junction and therefore, the energy barrier to overcome while going from the OFF state to the ON state must be higher than the one from the ON state to the OFF state. This feature is reminiscent of previously reported differential conductance switching loops measured at various interfaces between YBCO and other oxides [93,154,248].

Control samples with an Au gate instead of Al were also studied. **Fig. 4.17(c)** displays the differential conductance G_G vs. V_{write}, typical of those control devices. There are three notable differences with respect to the Al-gated devices. First, the conductance is orders of magnitude higher than the conductance observed in the case of Al-gated devices. Second, a very small conductance switching is observed (with an amplitude of only $10\ \%$, as opposed to $9900\ \%$). Third, the conductance vs. V_{write} loop is perfectly symmetric (with $V_S(+) = |V_S(-)| \approx 0.7\ V$), at variance with the behaviour

already discussed in **Fig. 4.17(b)**. These features show that having a low reduction potential metal in contact with YBCO is key to produce the large conductance switching effects observed in **Fig. 4.17(b)**, suggesting that they are linked to oxygen exchange between YBCO and Al.

3.2.2. Relaxation measurements

The ON and intermediate states of a memristor generally relax into the OFF state over a characteristic time, which can be shorter or longer depending on the conductance switching mechanisms. However, the lifetime can be so long that the conductance states are virtually non-volatile. Understanding and characterizing relaxation is of great importance for memristive systems and practical applications. Some of them require the memristor to possess non-volatile ON and OFF states, such as in the case where the memristor acts as a memory [88,89]. Any loss of information with time is then prohibited, and the conducting state must remain constant for a timescale of a few hours to a few months [94]. On the other hand, some technologies take advantage of the volatile aspect of the system [94,97]. In neuromorphic computing [249] for instance, the leaky integrate-and-fire model, introduced in **Chapter 1, Sect. 3.1.**, uses the natural thermal relaxation of a memristor to mimic the forgetting behaviour of biological neurons and synapses.

Relaxation measurements consist in measuring the time-dependent differential conductance in the ON state for different fixed temperatures and are conducted as follows:

(i) The temperature is set to 35 K and the device is in the OFF state.

(ii) A positive writing cycle is applied to set the device into the ON state (typically voltage cycles with $V_{write} \approx 8 - 10\ V$). At this low temperature, the ON state is stable within laboratory observation times (hours).

(iii) The temperature is ramped up as quickly as possible to the desired value of the temperature.

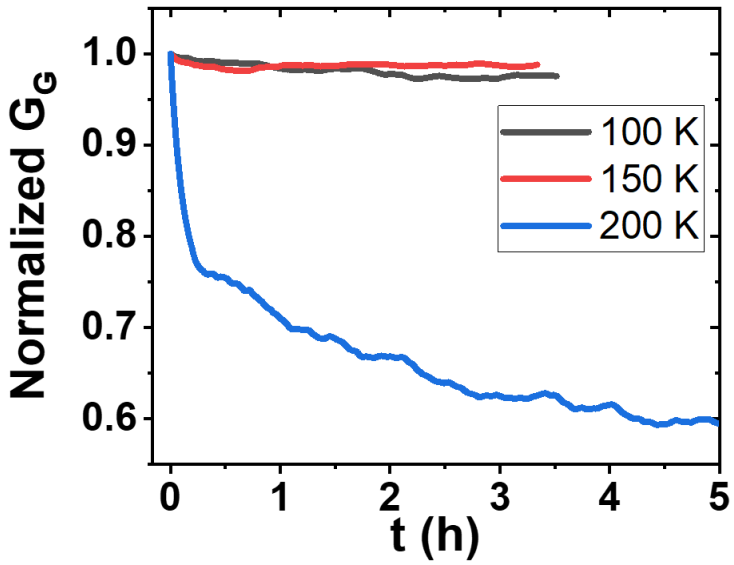

Fig. 4.18: Normalized G_G (smoothed using a Savitsky-Goley filter for clarity) in the ON state in arbitrary units as a function of time, showing the natural relaxation for different temperatures measured on a device with $t_{Al} = 10\ nm$ and $t_{YBCO} = 30\ nm$ (X1E). For temperatures below $200\ K$, no relaxation is observed as the differential conductance stays stable for more than three hours while a clear relaxation from the ON to the OFF state can be seen at $200\ K$.

(iv) When the final temperature is reached and stable, I-V characteristics of the gate are measured for low reading voltages of $-0.5\,V$ to $0.5\,V$ for a few hours. Then, the differential conductance is calculated from the I-V curves and reconstructed for a fixed $V_G = 100\,mV$ value.

Fig. 4.18 shows the results of the relaxation experiments in the form of the normalized value of G_G as a function of time, conducted on a device with $t_{Al} = 10\,nm$ and $t_{YBCO} = 30\,nm$. The values are normalized to allow for a direct comparison of the different curves, as the conducting state (and therefore the ON and OFF states) is temperature-dependent. The curves corresponding to temperatures of $100\,K$ and $150\,K$ show no sign of relaxation: after more than 3 hours, the transport properties of the Al/YBCO interface are mostly unchanged. However, relaxation starts to play a role at $200\,K$ and above, as can be seen from the blue curve in **Fig. 4.18**; the differential conductance has been reduced by $40\,\%$ in 5 hours. As a conclusion, the natural relaxation of excited states (ON and intermediate states) into the low-energy OFF state can be thermally activated: for temperatures above $200\,K$, the dynamics of the relaxation is enhanced and accelerated by the thermal energy $E = k_B T$, with k_B the Boltzmann constant [248].

3.3. Source-drain measurements: non-reversible tuning of YBCO superconducting properties

For the second set of measurements, the transport properties of the superconducting channel were investigated by applying a current I_{SD} with a Keysight B2901B precision current source and measuring the voltage V_{SD} with a Keithley 2182A nanovoltmeter between the source and drain contacts [see **Fig. 4.14(b)**].

3.3.1. Superconductor-to-insulator transition

The resistance $R_{SD} = V_{SD}/I_{SD}$ of the source-drain channel as a function of temperature was measured following gate-drain switching cycles as shown in **Sect. 3.2.1.** The resistance as a function of the temperature for a device with $t_{Al} = 10\,nm$ and $t_{YBCO} = 110\,nm$ for increasing values of V_{write} applied between the gate and drain contacts is shown in **Fig. 4.19(a)**. The pristine device, before application of any gate voltages, displays a critical temperature of $T_C \approx 87\,K$ and presents a very sharp superconducting phase transition with $\Delta T_C \approx 2\,K$ (see **Chapter 3, Sect. 6.3.** for the calculation method). Two main features can be deduced from this figure:

(i) The increase of the resistance in the normal state as V_{write} is ramped up, from $R(T = 100\,K) \approx 10\,\Omega$ for $V_{write} = 0\,V$ to $R(T = 100\,K) \approx 43\,k\Omega$ for $V_{write} = 15\,V$; the change in resistance spans over more than 4 orders of magnitude.

(ii) The broadening of the normal-to-superconducting phase transition until, after applying $15\,V$, an insulating state is reached.

These two effects are non-reversible, regardless of the application of negative V_{write}. The effective critical temperature T_C^* is defined for this experiment as the first value of the temperature for which the resistance of the channel goes below a $1\,\Omega$ threshold as depicted in **Fig. 4.19(a)** and **Fig. 4.19(b)** by the black dotted horizontal line (see **Chapter 2, Sect. 6.2.** for the definition of the different critical

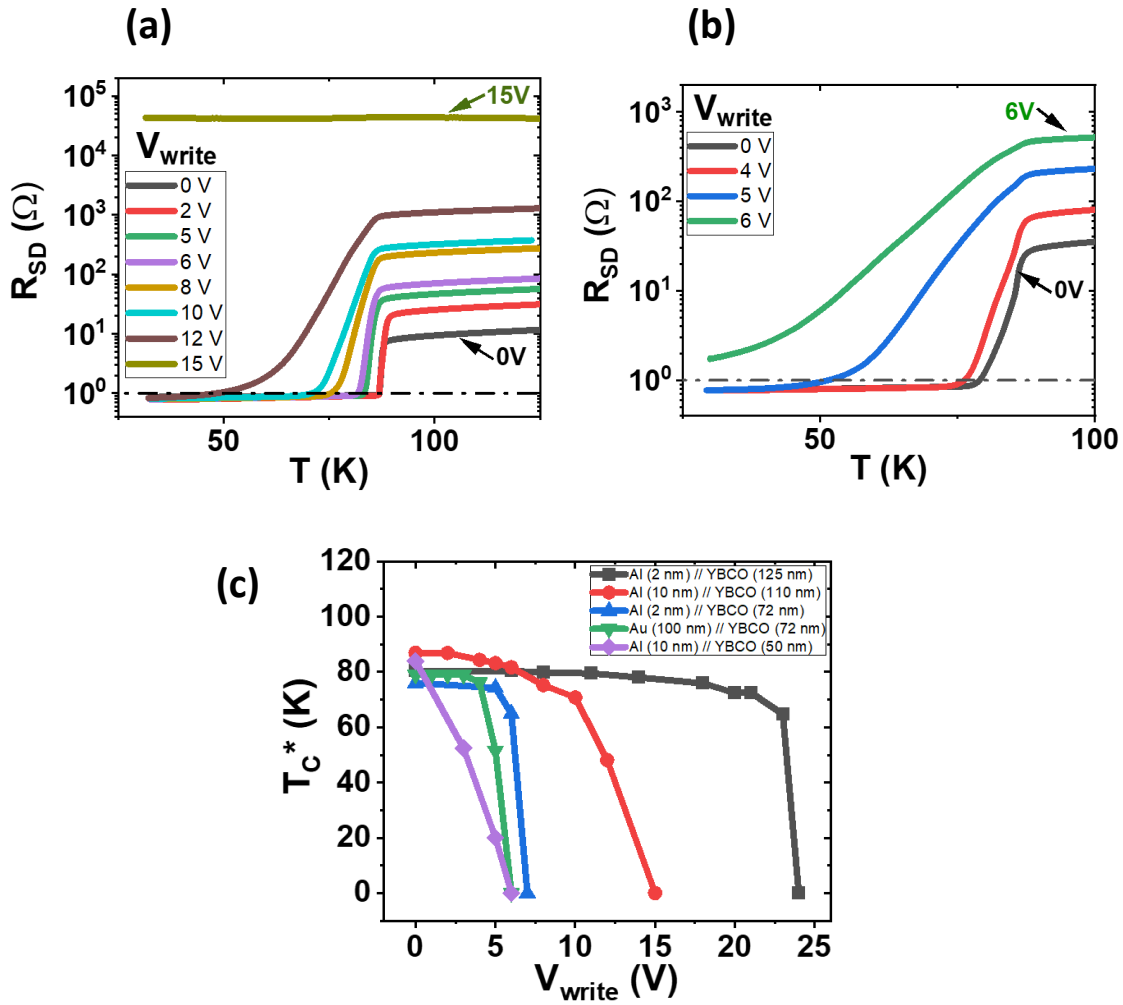

Fig. 4.19: (a) Resistance R_{SD} in semi log scale as a function of the temperature for increasing values of V_{write} measured on a device with $t_{Al} = 10\ nm$ and $t_{YBCO} = 110\ nm$ (X2A). As the voltage V_{write} increases, we observe a gradual and non-reversible modulation of the superconducting ground-state until an insulating state is reached for $V_{write} = 15\ V$. (b) Resistance R_{SD} in semi log scale as a function of the temperature for a control device with no aluminium gating and $t_{YBCO} = 72\ nm$ (X2WAlB). (c) T_C^* as a function of V_{write} for different device geometries.

temperatures). T_C^* was measured as a function of V_{write} for various devices with different geometries and the results are summarized in **Fig. 4.19(c)**. One can observe a monotonic non-reversible decrease of T_C^* until the superconducting state is suppressed. The behaviour depends on the YBCO thickness: the thicker the YBCO layer, the more robust the superconducting properties against V_{write}. In fact, the V_{write} needed to completely suppress T_C^* in the case of a 125-nm thick layer of YBCO is approximately equal to $24\ V$ while applying only $6\ V$ is enough to suppress T_C^* in a device with $t_{YBCO} = 50\ nm$.

Fig. 4.19(b) shows the same set of measurements as the one from **Fig. 4.19(a)** carried on a control device with $t_{Au} = 100\ nm$ and $t_{YBCO} = 72\ nm$, showing the same behaviour as V_{write} is increased to $6\ V$. The green curve in **Fig. 4.19(c)** corresponds to the T_C^* of the control sample presented in **Fig. 4.19(b)**. The shape of $T_C^*(V_{write})$ is identical for Al-gated samples and the control device. In fact, the green and blue curves in **Fig. 4.19(c)**, with an equal YBCO thickness, are very much overlapping, highlighting the obvious similarities between both measurements. We can conclude that the monotonic and non-reversible depression of T_C^* doesn't require the presence of a reducing material, and therefore indicates that the origin of this effect cannot be explained through the process of chemical redox reactions.

3.3.2. Relation between the non-reversible effects and the dissipated power

3.3.2.1. Role of the dissipated power

These gate conductance switching (reversible) and the gradual depression of the channel's conducting (and superconducting) properties (irreversible) occur within a similar range of voltages V_{write} that depends on the YBCO thickness, typically between $4\ V$ and $20\ V$. In order to understand these two effects in detail, the correlation between the superconducting source-drain resistance R_{SD} and the gate switching behaviours were investigated. **Fig. 4.20** shows an example of a typical measurement, displaying both reversible and non-reversible effects simultaneously, measured on a

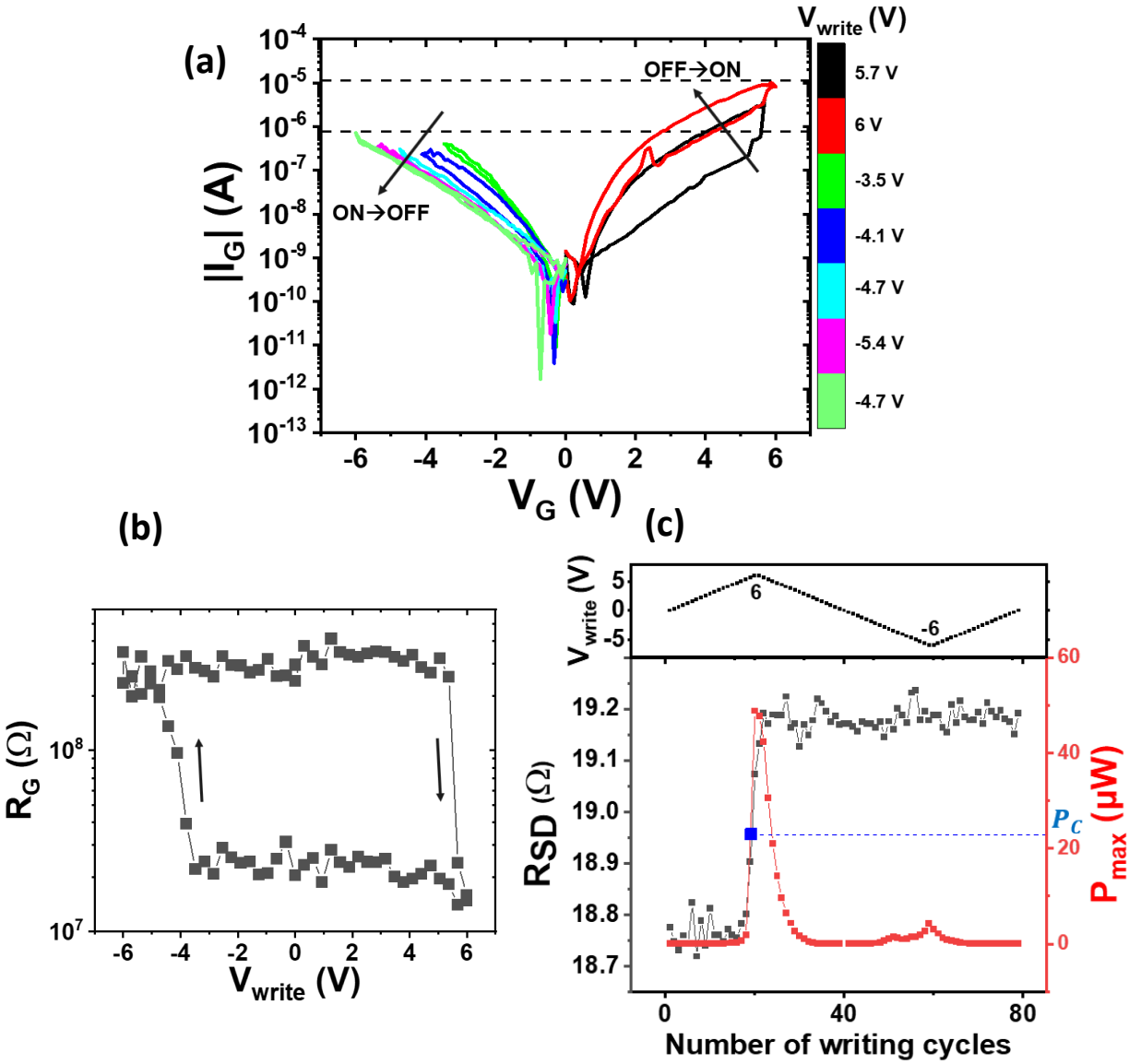

Fig. 4.20: Measurements done on a device with $t_{Al} = 10\ nm$ and $t_{YBCO} = 87\ nm$ at $87\ K$ (X4B). (a) I_G-V_G characteristics during the switching process for $-6\ V < V_{write} < 6\ V$. (b) R_G in log scale as a function of V_{write} for $I = 1\ \mu A$.. R_G is switching between an ON and an OFF state. (c) On top, V_{write} as a function of the number of writing cycles for $-6\ V < V_{write} < 6\ V$. On the bottom, the resistance R_{SD} in black (linked to the left y-axis) and P_{max} in red (linked to the right y-axis) as a function of the number of writing cycles. For positive V_{write}, the dissipated power is much higher than the one calculated for negative V_{write}, and an increase of R_{SD} from $\sim 18.75\ \Omega$ to $\sim 19.2\ \Omega$ is observed concomitantly to high dissipated powers. The blue point corresponds to the minimum dissipated power ($P_C = 23\ \mu W$) that is required to trigger the abrupt change of R_{SD}.

device with $t_{Al} = 10$ nm and $t_{YBCO} = 87$ nm at 87 K, for a writing cycle between $-6\,V < V_{write} < 6\,V$.

A selected subset of the writing I-V characteristics corresponding to this particular set are first displayed in **Fig. 4.20(a)**. The resulting graph yields identical observations and conclusions as the similar plots shown in **Sect. 3.2.1.**, with a clear reversible memristive behaviour of the YBCO/Al interface: the switching between the non-volatile ON and OFF states. Moreover, the diode-like behaviour is clear again, with very different measured I_G for positive and negative V_G, illustrated by the horizontal black dotted lines. The resistance R_G of the gate-drain junction as a function of the V_{write} is plotted in **Fig. 4.20(b)**, depicting the reversible switching of the gate between the ON and OFF states. R_{SD} was measured for a fixed value of the current $I_{SD} = 1\ \mu A$ after applying each V_{write}, *i.e.* after every voltage excursion in **Fig. 4.20(b)**. The succession of applied V_{write} is displayed in the top graph of **Fig. 4.20(c)** and the bottom graph shows the measured resistance R_{SD} as a function of the number of writing cycles applied to the device. The maximum dissipated power in the gate $P_{max} = V_{write}.I(V_{write})$ [right, red axis in **Fig. 4.20(c)**] is calculated from I_G-V_G curves showed in **Fig. 4.20(a)**.

An abrupt increase of R_{SD} occurs as the power dissipated across the gate rises, as demonstrated in **Fig. 4.20(c)**. I define the critical power P_C as the minimum power required to trigger the abrupt increase of R_{SD}, represented as a blue point in **Fig. 4.20(c)**, found to be $P_C = 23\ \mu W$ for this particular set of measurements. Notice that the dissipated power peak is much higher for a positive $V_{write} = 6\,V$ than for a negative $V_{write} = -6\,V$, highlighting the diode-like behaviour of the Al/YBCO interface. This effect is explained by the change in the resistive state while the switching occurs at the Al/YBCO interface. In fact, positive voltages correspond to the switching from the OFF state to the ON state, and, as a consequence, to a decrease of the resistance, while negative voltages produce the opposite effect. By looking at the I_G-V_G characteristics of **Fig. 4.20(a)**, one can see that the current that flows within the gate is higher while applying positive voltages ($|I_G| \approx 11.4\ \mu A$ for $V_G = 6\,V$ compared to $|I_G| \approx 0.8\ \mu A$ for $V_G = -6\,V$) leading to higher dissipated powers for the OFF → ON switch.

The type of measurement illustrated in **Fig. 4.20** was reproduced for various V_{write} cycles of increasing amplitudes. The results are presented in **Fig. 4.21**, showing from top to bottom:

(a) V_{write} as a function of the number of writing cycles.
(b) The gate and the source-drain resistances R_G and R_{SD} as a function of the number of writing cycles, displaying both the reversible and non-reversible effects simultaneously. R_G is calculated as $R_G = V_G/I_G$ for $I_G = 1\ \mu A$. This current is the same as the one used to measure R_{SD}, which allows for a direct comparison between both.
(c) The power dissipated $P_{max} = V_{write}.I(V_{write})$ as a function of time, showing prononced periodic peaks. The peaks corresponding to positive voltages are always higher in amplitude compared to the ones corresponding to negative voltages due to the already mentionned diode-like behaviour of the Al/YBCO interface. As was observed in **Fig. 4.20(c)**, the jumps of the source-drain channel's resistance R_{SD} coincide with the peaks of dissipated power for positive voltages (see the vertical red dotted lines). The blue points correspond to the critical power level P_C that is required to trigger the non-reversible increase of R_{SD}.

A clear correlation between the dissipated power peaks and the irreversible increase of R_{SD} is revealed in **Fig. 4.21**, suggesting a process linked to Joule heating. This effet is illustrated by the evolution of the critical power P_C in **Fig. 4.21(c)**: P_C increases with consecutive switching, indicating that the R_{SD} changes are cumulative. Once a R_{SD} level is established, further increase requires application of a higher P_C. For this reason, applying a negative V_{write} does not produce changes in R_{SD}, since the power dissipated is lower than the P_C established in the previous cycle.

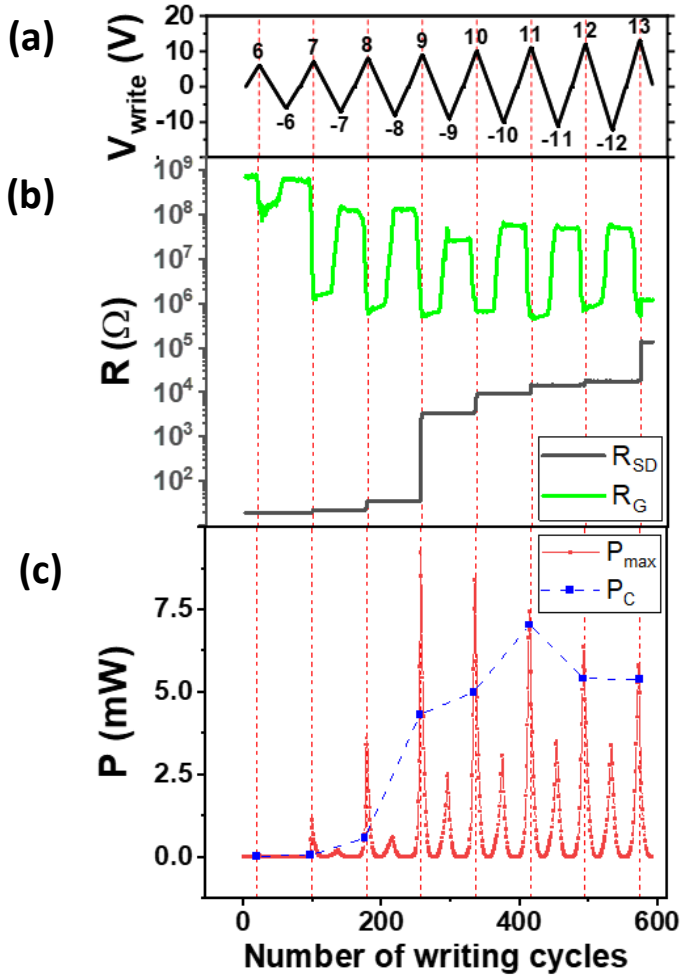

*Fig. 4.21: Measurements done on a device with $t_{Al} = 10\ nm$ and $t_{YBCO} = 125\ nm$ at 87 K (X4A). (a) V_{write} as a function of the number of writing cycles for $-6\ V < V_{write} < 13\ V$. (b) Evolution of R_{SD} and R_G as a function of the number of writing cycles. R_G is switching reversibly between two resistive levels while R_{SD} increases irreversibly from 20 Ω to 0.1 MΩ. (c) P_{max} as a function of the number of writing cycles. The highest peaks correspond to P_{max} calculated while applying positive V_{write} (vertical red dotted lines), whereas the small peaks correspond to P_{max} calculated while applying negative V_{write}. The blue dots represent the minimum value of P_{max} required to induce a jump of R_{SD} in **Fig. 4.21(b)**, as was previously defined in **Fig. 4.20**.*

3.3.2.2. Varying the voltage cycles' application time: the dissipated energy

In the experiments discussed so far, the time of application of the writing voltage cycles was always $t_G = 20$ seconds. Here, I present the same set of measurements as the one described in **Fig. 4.21** conducted on an identical device for $t_G = 40$ seconds. The results are displayed in **Fig. 4.22**, showing V_{write} as a function of the number of writing cycles from $-3\ V < V_{write} < 3\ V$ to $-13\ V < V_{write} < 13\ V$ [**Fig. 4.22 (a)**] and the values of the resistances R_G and R_{SD} for $t_G = 20$ seconds (black curves) and $t_G = 40$ seconds (red curves). As the times of application of the writing cycles are different, the x-axis represents the number of cycles to allow for a direct comparison of the resistance increase. Even though R_G is similarly switching between an ON and an OFF state for both devices, the resistance R_{SD} is increasing much faster in the case of 40-second cycles than in the case of 20-second cycles: the non-reversible increase starts while applying writing voltages of approximately $4\ V$ in the first scenario, whereas in the second scenario, at least $7\ V$ is required. This behaviour suggests that the increase of

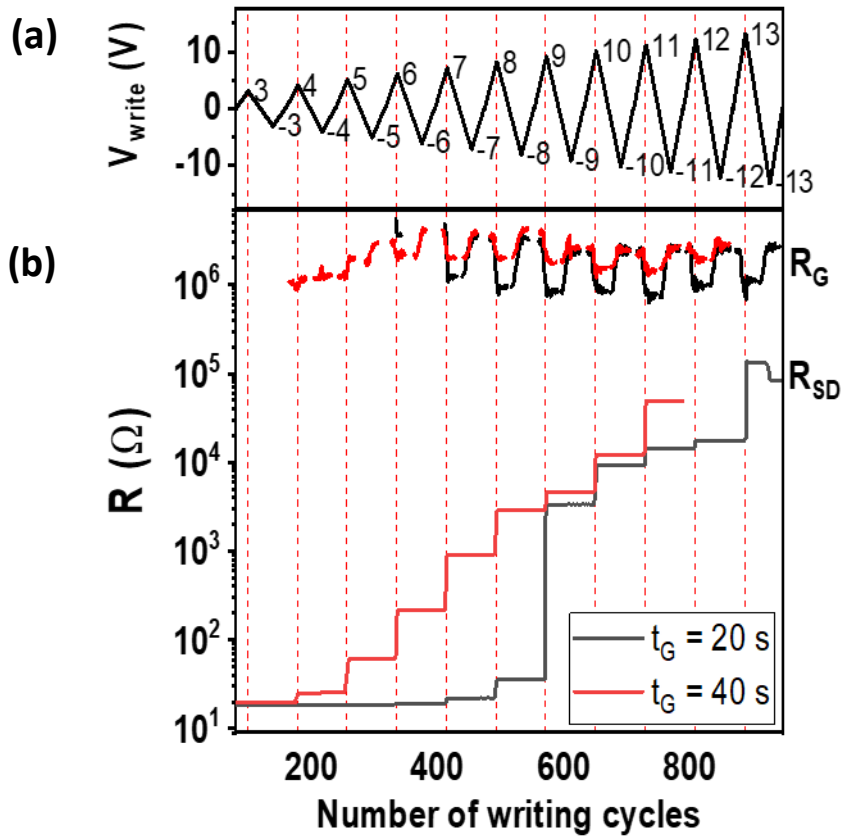

Fig. 4.22: Measurements done on two identical devices with $t_{Al} = 10\ nm$ and $t_{YBCO} = 125\ nm$ at 87 K (X4A). (a) V_{write} as a function of the number of writing cycles for $-3\ V < V_{write} < 13\ V$. (b) Evolution of R_{SD} and R_G as a function of the number of writing cycles for $t_G = 20\ s$ (black curve) and $t_G = 40\ s$ (red curve). We can observe that in the case of $t_G = 40\ s$, the onset of the R_{SD} increase is lower and evolves to higher values faster than for the case of $t_G = 20\ s$.

R_{SD} is not caused directly by the dissipated power, but by the dissipated energy $E = P \times t_G$. In fact, for both devices presented in **Fig. 4.22**, the minimum dissipated energy that is required to induce a noticeable R_{SD} increase can be calculated from dissipated power curves similar to the one presented in **Fig. 4.21(c)**, yielding in the case of 20-second cycles (resp. 40-second cycles) a value of the minimum energy $E_{min} = 9.7\ mJ$ (resp. $E_{min} = 11.4\ mJ$). These two very similar values indicate that the increase of the channel's resistance is ultimately triggered by the dissipated energy.

4. Discussion

The transistor-like devices display simultaneously a reversible (and non-volatile) tuning of the conducting state of the Al/YBCO interface and a non-reversible degradation of the conducting (and superconducting) properties of the YBCO channel for a wide range of voltages between $\sim 4\ V$ to $\sim 15\ V - 30\ V$, depending on the specific device. The first part of this discussion will be focused on the understanding of these two concomitant behaviours; and it will be shown that both effects are caused by a motion of oxygen ions inside YBCO's crystal structure, triggered by different mechanisms. Then, this conclusion will be illustrated and further verified by presenting the typical behaviour of the devices under application of higher voltages and current densities that will highlight the intertwined character of the reversible and non-reversible effects.

4.1. Transistor-like device: simultaneous reversible and non-reversible effects

4.1.1. Memristive behaviour

The reversible, non-volatile and large switching of the conductance of the devices for temperatures below $200\ K$ between ON, OFF and intermediate states [**Fig. 4.17(b)** as an example] can be explained by an interfacial redox reaction between Al and YBCO, analogous to the memristive effects observed in YBCO/MoSi [130], NdNiO3/MoSi [248] and Ag/YBCO [153] systems. This large switching can be as high as three orders of magnitude (with values typically ranging between $0.1\ \mu S$ and $100\ \mu S$) and was invariably seen on all the studied devices, attesting the reproducibility of the measurements. Due to the low reduction potential $E^{\circ}(Al) = -1.676$ of Al and the high reduction potential $E^{\circ}(Cu) = 2.4$ of copper, an oxygen-depleted region within the YBCO layer forms as the Al layer's first crystallographic planes oxidize, as illustrated by the schematic of **Fig. 4.23(a)**. Because both oxygen-depleted YBCO and AlO_x are insulating [10,11], an electron tunnel barrier forms at the interface which strongly reduces the conductance. This explains the low-conductance OFF state. This redox reaction can be reversed by the application of a voltage that exceeds the difference between the reduction potentials, very much as a battery can be charged, leading to oxygen transfer from AlO_x into $YBCO_{7-x}$ and thus to a thinning of the oxygen-depleted AlO_x tunnelling barrier. This lowering of the interfacial conductance is depicted in **Fig. 4.23(b)**, showing the thinning of the $YBCO_{7-x}$ depleted region. This phenomenon explains the high-conductance ON state. The width of the tunnelling barrier can be controlled by applying voltage biases V_{write} between the gate and drain contacts, leading to a back-and-forth motion of oxygen between YBCO and AlO_x. This process thus explains the switching behaviour from the OFF to the ON state in the gate measurements.

This chemical redox scenario is supported by various key observations:

(i) The switching behaviour of the differential conductance as high as 3 orders of magnitude as well as the asymmetric shape is reminiscent of previously reported results on redox chemical reactions [93,153,154,229,248]. Starting from the low conducting state, the

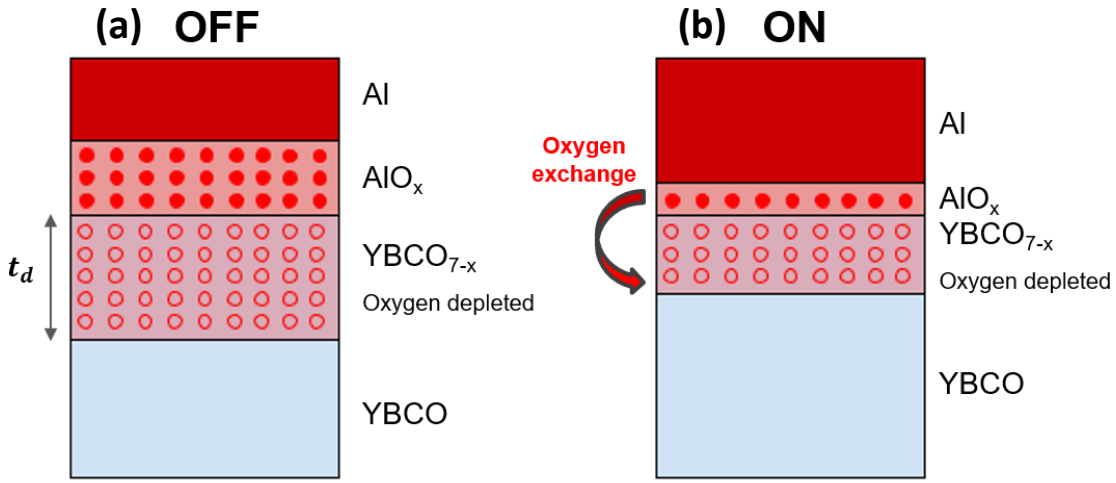

Fig. 4.23: Schematic of the YBCO/Al interface showing the thickness of the aluminium oxide and the YBCO depleted region in the (a) low-conductance OFF state and the (b) high-conductance ON state. The switching process is a consequence of the thinning of the oxidized and oxygen-depleted regions triggered by the applied V_{write}.

energy barrier to overcome by the redox reaction is given by the difference between the reduction potentials of copper and aluminium as follows [9]:

$$\Delta E = E^{\circ}(Cu) - E^{\circ}(Al) = 2.4 - (-1.676) = 4.076\ eV \quad (4.5)$$

This value is consistent with the value of $V_S(+) \approx 4.7\ V$ that was determined in **Fig. 4.17(b)**. An excess voltage of nearly $\sim 0.7\ V$ is required to overcome the barrier for oxygen ion diffusion, that is, to accelerate the dynamics of the electrochemical reaction. This is consistent with the value of the voltage $V_S(-) \approx -0.7V$ required to switch back into the OFF state, which is spontaneous from the electrochemical point of view and thus only requires activation over the barrier for oxygen ion diffusion.

(ii) The control samples with no aluminium gating presented in **Fig. 4.17(c)** only display a very small switching (approximately 10 %) compared to the very high switching (approximately 10000 %) of aluminium-gated samples. This small switching is probably the consequence of the local redistribution of oxygen vacancies in YBCO due to electric fields, slightly modifying the conducting properties of the YBCO channel with respect to the applied V_{write}. Note that in **Fig. 4.17(c)**, we can observe $V_S(+) = |V_S(-)| \approx 0.7\ V$; this voltage corresponds to the excess voltage presented above, further supporting the conclusions of (i).

(iii) The memristive properties can be observed below and above the critical temperature of YBCO [**Fig. 4.15(a)** and **Fig. 4.16**], pointing towards a physical phenomenon that is not governed by superconductivity.

(iv) The switching can be thermally activated for temperatures above $200\ K$ without applying any voltage, as was illustrated in the relaxation-over-time measurements of **Fig. 4.18**, with the gradual relaxation of the ON state into the OFF state. Similar relaxation measurements were reported by Humbert *et al.* [248] in 2022 while studying memristive $NdNiO_3/Mo_{80}Si_{20}$ tunnel junctions. As was demonstrated in this paper, fitting the relaxation curves with an Arrhenius law for many temperatures leads to a global activation energy of $E_a = 0.31\ eV$ which was consistent with the switching voltage of the observed switching loops. Moreover, the authors found that the typical temperature needed to start the relaxation process for their devices was around $150\ K$, which is slightly less than the value of $200\ K$ found in the present experiments. Therefore, the relaxation measurements support the redox scenario.

4.1.2. Non-reversible depression of YBCO's superconducting properties

Concomitantly, the YBCO superconducting channel exhibits a strong non-reversible modulation of the superconducting properties. This superconductor-to-insulator phase transition is characterized by the gradual lowering of T_C^* and the increase of the normal-phase resistance, as demonstrated by **Fig. 4.19(a)**. Redox reactions can be ruled out from playing a major role in this phenomenon, as is suggested by **Fig. 4.19(b)**, showing identical results measured on control samples at the interface between a noble metal (gold) and YBCO. Other oxygen migration mechanisms include electromigration caused by high current densities and thermomigration caused by high temperature gradients, as was introduced in the first part of this chapter (**Sect. 1.1.**).

Electromigration is a typical mechanism allowing for the control of the oxygen flow and was already reported in numerous papers [155,156,241,242,157,234–240]. It was shown in these

experiments that a sufficiently high current density of about $8\,MA.cm^{-2}$ will allow the oxygen to migrate in YBCO. [155–157] It was also shown that this phenomenon, if handled carefully, can lead to reversible superconducting-to-insulating phase transitions in nanobridges [156,157]. The maximum current density flowing through the superconducting YBCO channel during a writing cycle in the present experiments can be calculated as:

$$J_G(V_{write}) = \frac{I_G(V_{write})}{A_2} = \frac{I_G(V_{write})}{10^{-4}.t_{YBCO}} \tag{4.6}$$

with $I_G(V_{write})$ the maximum value of the current measured while applying a V_{write} writing cycle and $A_2 = 10^{-4} \times t_{YBCO}$ is the surface through which the current is flowing as indicated in **Fig. 4.24(a)**.

The calculated $J_G(V_{write})$ for different devices with varying thicknesses are plotted in **Fig. 4.24(b)**. As can be seen from this figure, the values of the current densities vary between $\sim 0.2\ kA.cm^{-2}$ and $\sim 138\ kA.cm^{-2}$, a much smaller current density compared to the threshold value of $8\,MA.cm^{-2}$ reported in the aformentionned papers and required to launch the electromigration process. Even considering much smaller effective areas while carrying out the calculation, it is difficult to imagine electromigration to play a key role in the observed phenomena.

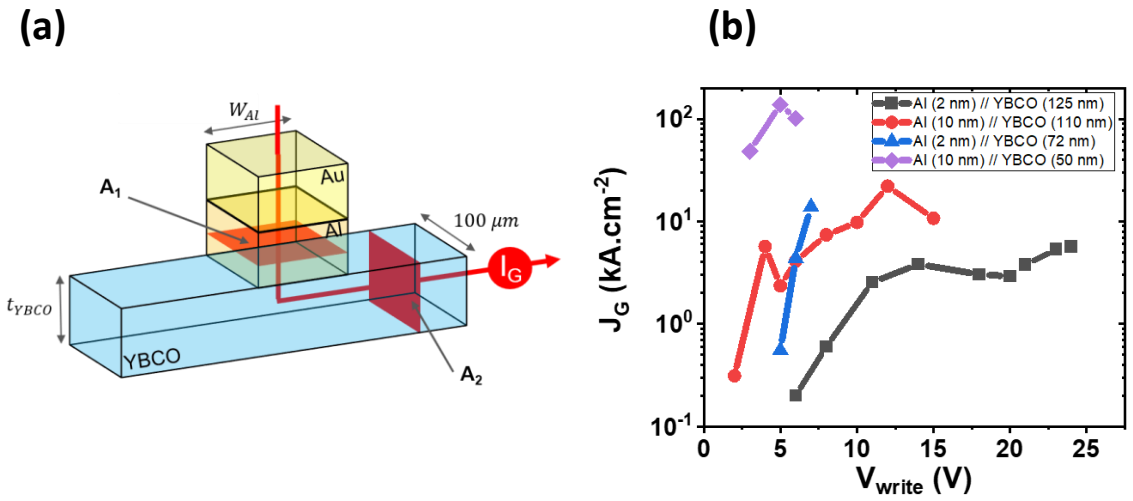

Fig. 4.24: (a) Schematic 3-dimension representation of the device, displaying the important geometric parameters, particularly the areas A_1 and A_2 through which the current is flowing while applying V_{write}. (b) Calculated J_G as a function of V_{write} for different devices with varying thicknesses. We observe that, as the voltage V_{write} is increased, the current densities increase to values between approximately $10\ kA.cm^{-2}$ to $100\ kA.cm^{-2}$. These values are much lower than the expected minimum J_G required to launch the electromigration process as measured in the litterature.

Therefore, electromigration can not account for the non-reversible modulation of YBCO's conducting and superconducting properties. Another possible explanation is the thermomigration of oxygen ions triggered by Joule heating. In fact, oxygen ions are the lighter elements within the YBCO structure and are expected to migrate first when exposed to external stimuli, although at very high voltages and temperature gradients, it is difficult to discard the possibility that other elements (copper, yttrium and barium) may be affected. However, the smooth decrease of T_C^* and the zero-resistance state observed in the $R(T)$ curves of **Fig. 4.19** for low-applied voltages, even after multiple writing cycles, indicates that oxygen might be the only migrating specie for low voltages. The thermomigration scenario is supported by the experiments concerning the dissipated power and dissipated energy of **Sect. 3.3.2.**, showing a clear correlation between the peaks of high dissipated power and the irreversible increase of R_{SD} (see **Fig. 4.20** and **Fig. 4.21**). Moreover, thermal effects are expected to be cumulative, and the application of high temperature gradients during longer times are expected to

lead to faster and more powerfull consequences on R_{SD}. This effect is illustrated in **Fig. 4.22**, demonstrating a faster degradation of the channel's resistance for longer t_G, showing that the R_{SD} increase is ultimately triggered by a dissipated energy of approximately $E_C \approx 10\ mJ$.

Let's now discuss the differences observed while measuring devices with different values of the gate contact's width W_{Al} (see **Fig. 4.11**). As was presented at the beginning of this chapter, devices with $W_{Al} = 60\ \mu m$ and $W_{Al} = 5\ \mu m$ were fabricated to study the scalability of the proof-of-concept device. First, the reversible memristive effects were invariably seen and presented similar shapes and amplitudes indiferently of W_{Al}. Second, the superconducting properties of the YBCO channel were more robust and could withstand higher values of V_{write} in the case of $W_{Al} = 5\ \mu m$. This last observation further support the Joule heating scenario: a larger YBCO/Al interface (a larger W_{Al}) implies a higher number of impurities at the interface and should lead to a higher sensibility to thermal effects and thermal runaways.

Finally, the origin of the T_C^* depression of the YBCO channel can be explained either through a change in the doping level (see the temperature-doping phase diagram of **Fig. 4.1**) or through the formation of structural disorder. In order to differentiate between both mechanisms, the 2-probe $R(T)$ measurements of a YBCO channel after applying writing cycles of increasing amplitudes are plotted in **Fig. 4.25(a)** for $30\ K < T < \sim 300\ K$. The resistivity ρ_{100K} at $T = 100\ K$ is displayed in the inset of **Fig. 4.25(a)**, calculated by considering the volume of the YBCO channel, although this value of the resistivity might be slightly off due to the 2-probe measuring method. The shape of the $R(T)$ curves above T_C point toward a disorder-induced phenomenon. This conclusion is supported by two key observations:

(i) Arpaia *et al.* [250] demonstrated in 2018 that in strongly underdoped YBCO thin films, the low doping concentration leads to the appearance of a downward bending of the $R(T)$ just above T_C. This feature is not observed in the $R(T)$ curves of **Fig. 4.25(a)**.

(ii) The value of the doping can be assessed through the pseudogap temperature T^*. The calculation method for T^* is presented in **Fig. 4.25(b)**. First, a linear fit of the curve for high-temperature is performed, and the departure (defined with a 1 % criteria) between the measured resistance and the fitting allows to determine T^*, yielding $T^* \approx 152\ K$ for a

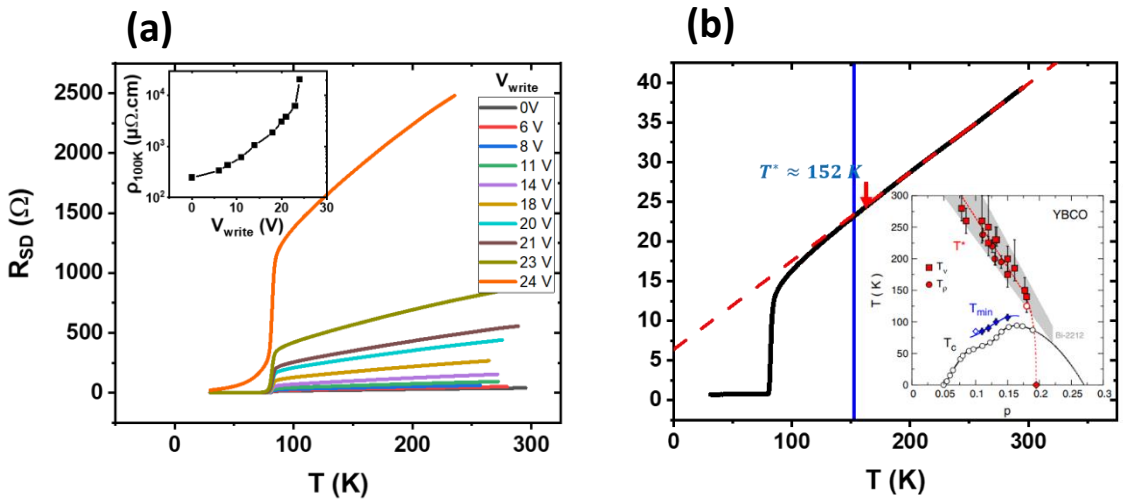

*Fig. 4.25: Measurements done on a device with $t_{Al} = 10\ nm$ and $t_{YBCO} = 125\ nm$ (X3A). (a) $R_{SD}(T)$ for increasing values of V_{write} from $0\ V$ to $24\ V$. The resistivity at $100\ K$ as a function of V_{write} is shown in the inset. (b) Example of calculation of T^* in the case of the 0 V curve of **Fig. 4.25(a)**, showing the linear fit (red dotted line) for high temperature. The value of T^* is determined by taking the value of the temperature for which R_{SD} decreases by $1\ \%$ compared to the linear fit. In the inset, the temperature-doping phase diagram shows the behaviour of T^* as a function of the hole doping. Figure taken from Cyr-Choinière et al., Phys. Rev. B (2018) [251].*

sample prior to the application of any V_{write} [**Fig. 4.25 (b)**] and $T^* \approx 178\ K$ after aplying $V_{write} = 23\ V$ [orange curve in **Fig. 4.25(a)**]. A strong reduction of the doping concentration should lead to an increase of T^* [250,251]. However, the small change of $26\ K$ between both temperatures does not amount for a major change of the doping content, as shown in the inset of **Fig. 4.25(b)** [251]. In fact, these values of T^* translate to values of the doping: $p \approx 0.175$ after applying $V_{write} = 0\ V$ and $p \approx 0.155$ after applying $V_{write} = 23\ V$. This change of the doping concentration cannot amount for the abrupt change in T_C^*. However, although yielding interesting key observations, this analysis might not hold true as a consequence of the 2-point configuration which probes in series part of the YBCO region untouched by the thermomigration process.

Consequently, the non-reversible modulation of the superconducting properties of the YBCO channel is likely to be caused by the generation of structural disorder mediated by Joule heating (*i.e.* the local rise of the temperature of the device). This conclusion is consistent with the already mentioned (**Sect. 1.1.3**) paper from Marinkovic *et al.* [243], in which the authors demonstrate that the oxygen vacancy migration in YBCO microbridges is ultimately triggered by the dissipated power.

4.2. Limits of the device

We now understand that two concomitant effects are taking place simultaneously during the electrical characterizations of the devices: on one hand, a reversible redox chemical reaction at the Al/YBCO interface; on the other hand, a non-reversible degradation of YBCO's superconducting properties produced by Joule heating. This section is aimed at discussing how these two mechanisms can be utilized to explain the behaviour of the devices under application of higher voltages and current densities.

4.2.1. Intermediate regime: concomitant reversible and non-reversible effects

Evolution of the switching with consecutive increasing voltage cycles

The gate-drain's memristive effects were also investigated for writing cycles of increasing amplitudes, as illustrated in **Fig. 4.26(a)**, showing consecutive $G_G(V_{write})$ loops for a device with $t_{Al} = 10\ nm$ and $t_{YBCO} = 53\ nm$ at $87\ K$. The black curve corresponds to a $-5\ V < V_{write} < 5\ V$ writing process and shows no sign of switching, indicating that applying $5\ V$ is not enough to launch the redox reactions for this particular device. For cycles with V_{write} higher than $7\ V$, G_G switches between non-volatile ON and OFF states. The loops become broader and broader as the maximum V_{write} is increased. Furthermore, the levels of the ON and OFF states seem to be shifting to higher values. These two effects are summarized in **Fig. 4.26(b)** and **Fig. 4.26(c)**, showing, respectively, the value of the differential conductance in the ON and OFF states and the switching voltages as a function of V_{write} for the same device as in **Fig. 4.26(a)**.

Fig. 4.26(b) can be divided into 3 distinct regimes as a function of V_{write}:

(i) For $V_{write} < 7\ V$, no clear signs of redox reactions are observed.

(ii) For $7\ V < V_{write} < 40\ V$, we can see a clear switching behaviour of G_G between an ON

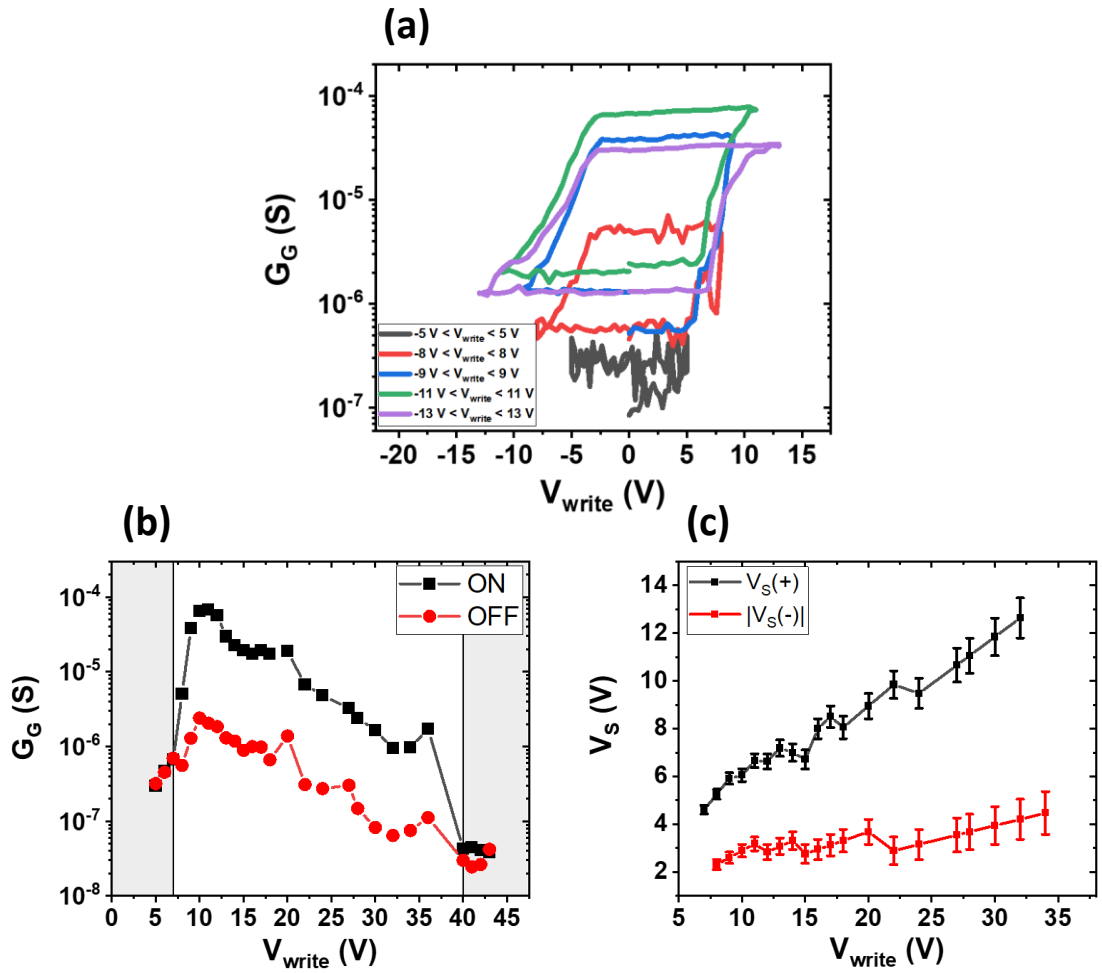

*Fig. 4.26: Measurements done on a device with $t_{Al} = 10\ nm$ and $t_{YBCO} = 53\ nm$ at 87 K (X4C). (a) G_G as a function of V_{write} for consecutive switchings from $-5\ V < V_{write} < 5\ V$ (black curve) to $-13\ V < V_{write} < 13\ V$ (purple curve). For $-5\ V < V_{write} < 5\ V$ (black curve), no switching of the differential conductance is observed. For $V_{write} > 7\ V$, the curves display a clear switching between ON and OFF states that evolve as the voltage is ramped up. (b) G_G in the ON and OFF states as a function of V_{write} calculated from the $G_G(V_{write})$ loops of **Fig. 4.26(a)**. We can distinguish three voltage regimes, represented by the grey and white regions. (c) $V_S(+)$ and $|V_S(-)|$ as a function of V_{write} calculated from the $G_G(V_{write})$ loops of **Fig. 4.26(a)**. $V_S(+)$ is always larger than its negative counterpart. Moreover, both switching voltages are getting larger with increasing values of V_{write}, i.e. with consecutive switchings.*

and an OFF state. At first, for voltages lower than $10\ V$, the loops shift to higher values upon cycling. This "training effect" is a common feature of the studied devices: the amplitude and the conducting levels of the cycles are gradually getting enlarged up until a given (device-dependent) voltage threshold. From there, the ON and OFF conductance levels diminish, although the amplitude of the switching remains constant.

(iii) For $V_{write} > 40\ V$ (this value depends largely on the studied device, as well as the geometry of the transistor-like structure), the cycles collapse.

Another phenomenon arising in the transport properties of the gate-drain junction is depicted in **Fig. 4.26(c)**: the switching voltages $V_S(+)$ and $V_S(-)$ are enhanced with consecutive cycles of increasing V_{write}. In the example shown in **Fig. 4.26(c)**, the positive switching voltage increases to $12\ V$ after applying a voltage cycle with a writing voltage gate of $34\ V$. It is important to mention that the measurements presented in **Fig. 4.26** belong to a particularly sturdy device: the transistor was able to withstand cycles with amplitudes up to 40 V before collapsing, while typical gate-drain junctions could not endure voltages higher than $\sim 15 - 20\ V$. Note that this device was made with $W_{Al} = 5\ \mu m$. The enhancement of $V_S(+)$ and $V_S(-)$ is a consequence of the non-reversible modulation of the channel

that causes a voltage divider configuration, as demonstrated in the next sub-section.

Resistive model: voltage divider

Fig. 4.26(c) illustrated a recurring feature of the $V_S(V_{write})$ measurements: $V_S(+)$ and $|V_S(-)|$ are steadily increasing as the V_{write} excursions are increasing. As was pointed out while describing the geometry of the transistors, and because of the 2-probe measurement setup, applying a voltage between the gate and drain contacts probes not only the resistance of the Al/YBCO interface, but also part of the superconducting channel in series. We now understand that the channel is non-reversibly affected by V_{write}, and consequently, the voltage V_G that is applied is not falling exclusively on the Al/YBCO interface. **Fig. 4.27** depicts a schematic picture of the device, with V_G being divided into two different voltages, as a first approximation: V_{int} is the voltage falling onto the interface of resistance R_{int}while V_{SD} is the voltage falling onto the superconducting channel of resistance R_{SD}. This setup simply describes a voltage divider, and therefore yields the following set of equations:

$$R_G \approx R_{int} + R_{SD} \tag{4.7}$$

$$V_{SD}(V_G) \approx V_G \frac{R_{SD}}{R_{SD} + R_{int}} \tag{4.8}$$

with R_G the measured gate-drain resistance, R_{SD} the measured source-drain resistance of the transistor channel and V_G the applied voltage during a cycle.

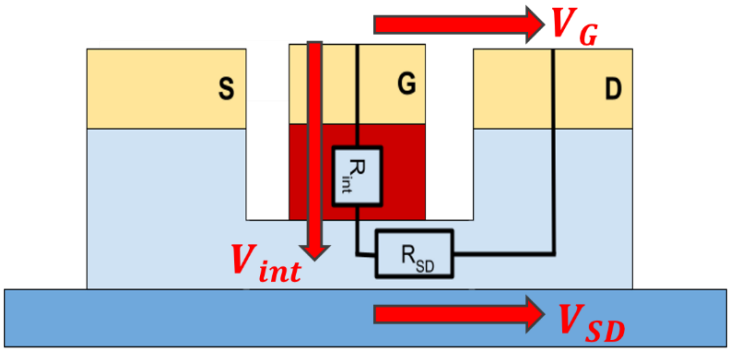

Fig. 4.27: Voltage divider resistive model. R_{int} represents the resistance of the interface between Al and YBCO while R_{SD} is the resistance of the channel, approximated to be the same resistance as the resistance measured between the source and drain contacts.

With **Eq. 4.8**, and knowing the values of the involved resistances in real time as the writing cycles are applied [from plots similar to **Fig. 4.20(b)**], it is possible to calculate the voltage falling onto the channel at the exact moment of the switching process, *i.e.* for a specific value of the voltage equal to $V_S(\pm)$, yielding the final equation:

$$V_{SD}\big(V_S(\pm)\big) = V_S(\pm)\frac{R_{SD}(V_S(\pm))}{R_{SD}(V_S(\pm)) + R_{int}(V_S(\pm))} \tag{4.9}$$

As a conclusion, **Eq. 4.9** gives the additional voltage required to start the redox reaction due to the voltage divider configuration. **Fig. 4.28** shows an example of a calculation based on the presented model. **Fig. 4.28(a)** shows the consecutive $G_G(V_{write})$ conducting loops for a device with $t_{Al} = 10\ nm$

and $t_{YBCO} = 87\ K$ at $87\ K$. The switching voltages extracted from **Fig. 4.28(a)** are plotted in **Fig. 4.28(b)** as solid square dots, while $V_S(+)$ and $V_S(-)$ calculated from the voltage divider resistive model are plotted as dashed lines. The model seems to describe very well the observed phenomena: the gradual and monotonic increase of $V_S(+)$ and $V_S(-)$ can therefore be explained by the non-reversible degradation of the superconducting channel and the 2-probe measurement setup. Moreover, this model also illustrates another recurring effect: $V_S(+)$ increases more rapidly than its negative counterpart $V_S(-)$. This behaviour can be seen both in **Fig. 4.26(c)** and **Fig. 4.28(b)**, and is another consequence of the 2-probe configuration: while R_{SD} is steadily increasing with consecutive cycles, R_{int} is much larger in the OFF state than in the ON state (more than two orders of magnitude higher), meaning that the voltage falling onto the channel is much lower while performing a gate switching from the ON to the OFF state as compared to the opposite switching.

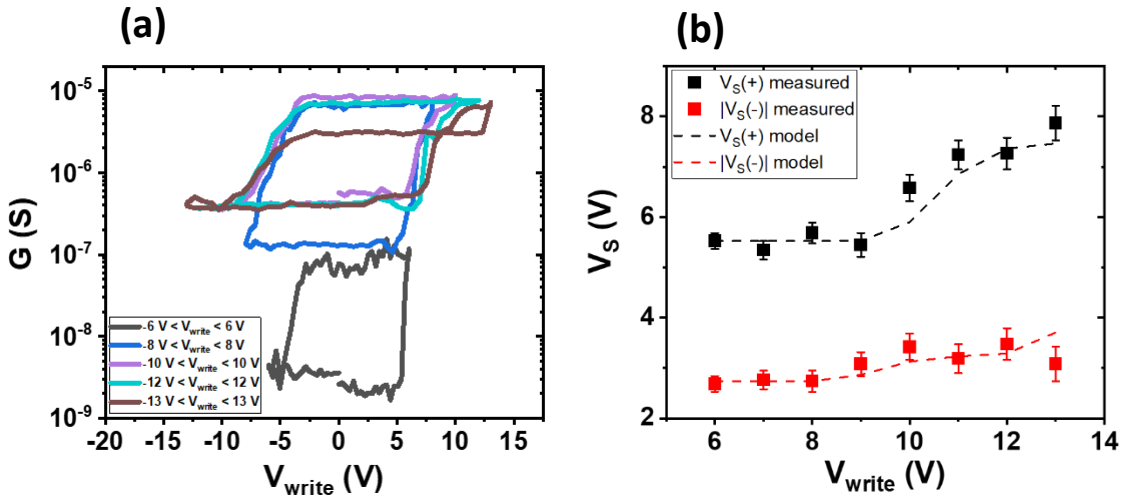

*Fig. 4.28: Measurements done on a device with $t_{Al} = 10\ nm$ and $t_{YBCO} = 87\ nm$ at $87\ K$ (X4B). (a) G_G as a function of V_{write} for consecutive switchings from $-6\ V < V_{write} < 6\ V$ (black curve) to $-13\ V < V_{write} < 13\ V$ (brown curve). (b) $V_S(+)$ and $|V_S(-)|$ as a function of V_{write}. The solid square dots represent the measured values extracted from the $G_G(V_{write})$ loops of **Fig. 4.28(a)** while the dashed lines show the calculated values based on the voltage divider resistive model (**Eq. 4.9**).*

4.2.2. High bias regime: reversible switching of the YBCO channel

An additional consequence of the irreversible increase of R_{SD} as V_{write} is ramped up is that, after enough voltage cycles, the resistances R_{SD} and R_G become of comparable magnitudes [see **Fig. 4.21(b)**]. As a result, I_{SD} is shorted by the Al/YBCO interface's resistance, and part of the current can flow through the gate. This is depicted in **Fig. 4.29(a)**, showing a schematic picture of a device with R_{Al} and $R_{channel}$ representing the resistance of the Al/YBCO interface and the resistance of the YBCO channel, respectively. Because of the different experimental setup compared to the one of **Fig. 4.27**, R_{Al} and $R_{channel}$ must be close but not strictly identical to the previously mentioned resistances R_{int} and R_{SD}, motivating the different denominations. **Fig. 4.29(b)** is a graph of the resistance R_{SD} measured between the source and drain contacts while applying writing cycles with very high $-70\ V < V_{write} < 50\ V$. For this range of voltages, R_{SD} has become comparable to R_G and is of the order of magnitude of a few tens of $M\Omega$. Furthermore, R_{SD} now shows a clear reversible and non-volatile memristive behaviour. This reversible feature is a consequence of the current flowing through the gate, and therefore retrieving part of the switching due to the redox chemical reactions occurring at the Al/YBCO interface.

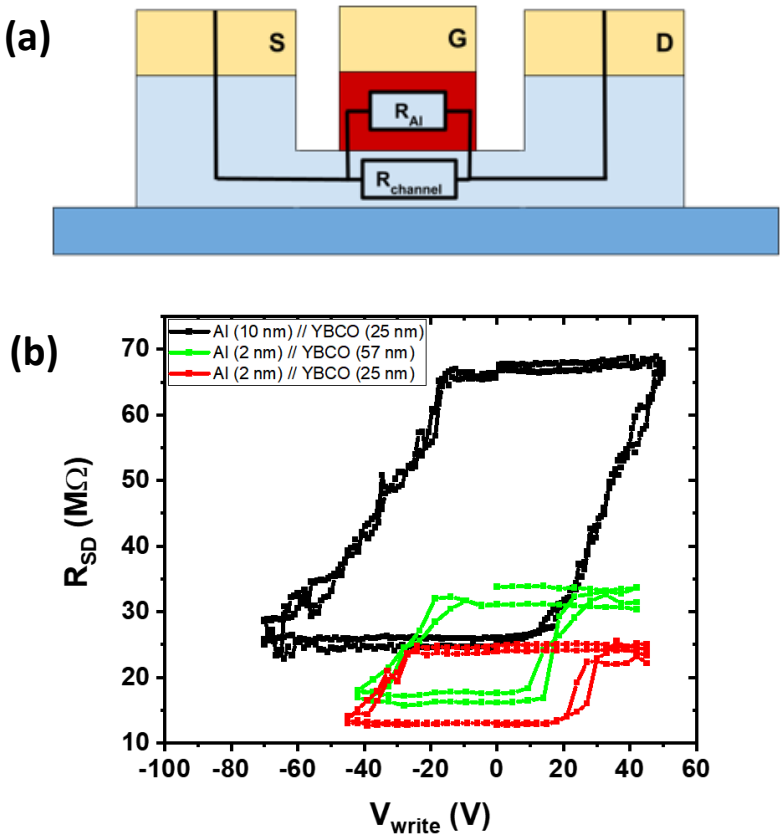

Fig. 4.29 : (a) Schematic picture of a device representing the resistances R_{Al} of the Al/YBCO interface and the resistance $R_{channel}$ in parallel. When the resistances R_{Al} and R_{SD} become comparable, the current injected between the source and drain contacts can split between the two parallel paths. (b) R_{SD} measured in a 2-probe configuration as a function of V_{write} for various devices with varying geometries. The resistances are reversibly switching between two non-volatile ON and OFF states. Measurements done on samples X1E, X3E and X3C.

This hypothesis is further demonstrated in **Fig. 4.30**, showing the measured R_{SD} and R_G resistances for a writing cycle between $+9\,V$ and $-9\,V$, for a device with $t_{Al} = 10\,nm$ and $t_{YBCO} = 53\,nm$ at $87\,K$. For this device, $R_{SD}$is, after applying voltage cycles of $8\,V$, already close to the value of $1\,M\Omega$, similar to R_G. We observe, in these conditions, a reversible switching of R_{SD}, although smaller in size compared to the gate's resistance switching. Moreover, the two cycles are perfectly synced in time, emphasizing the relation between both. This conclusion is supported by the microscope pictures presented in **Annexes, Sect. 1.3.**

5. Conclusions and perspectives

In this chapter, I have realized and characterized transistor-like superconducting devices made of YBCO and Al. The interface between YBCO and Al display strong memristive effects: the large and reversible switching of the differential conductance within a continuum of states depending on the history of applied voltages. This switching, mediated by redox chemical reactions, is non-volatile within a timescale of a few hours for temperatures lower than $150\,K$ and spontaneously relaxes to the OFF

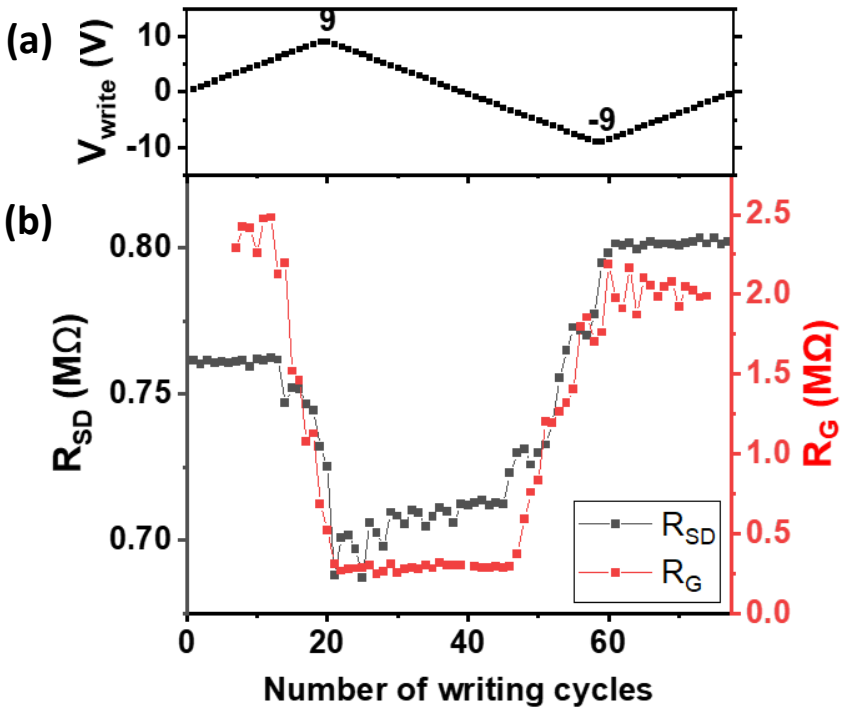

Fig. 4.30: Measurements done on a device with $t_{Al} = 10\ nm$ and $t_{YBCO} = 53\ nm$ at 87 K (X4C). (a) V_{write} as a function of the number of writing cycles for $-9\ V < V_{write} < 9\ V$. (b) Evolution of R_{SD} (black curve, left y-axis) and R_G (red curve, right y-axis) as a function of the number of writing cycles. Both resistances show a synchronized reversible switching between an OFF and ON states exacerbating the direct relation between both phenomena.

state for temperatures above $200\ K$. Simultaneously, the YBCO superconducting channel exhibits a controllable superconductor-to-insulator phase transition triggered by the dissipated powers and energies. This thermomigration process exhibits an interesting feature: the dissipated power required to induce a resistance increase in the channel is self-limiting; after a few training cycles, this dissipated power is stabilizing towards a limiting value of approximately $5\ mW$ in the case of **Fig. 4.21(c)**. This property can allow exploiting the memristive behaviour of the gate-drain interface while keeping the resistance of the channel unchanged. On the other hand, by increasing the dissipated power, one can tune the properties of the channel without affecting the memristive functions. This ability can be used for current-limiting applications and for the protection of superconducting circuitry. Additionally, if the control of the YBCO depleted volume can be accurately controlled, such a device can allow the fabrication of reconfigurable Josephson junctions for magnetic sensing applications.

The studied devices also show high voltage limitations due to very high current densities and temperature gradients. Three distinct regimes can be separated as a function of the applied writing voltages:

(i) **Low bias regime** $(\boldsymbol{V_{write} < 4\ V})$: the writing voltage is not high enough to trigger the redox processes that leads to the memristive behaviour.

(ii) **Intermediate regime** $(\boldsymbol{4\ V < V_{write} < 15 - 30\ V})$: both reversible and non-reversible effects take place simultaneously; the resistance R_{SD} depends on the history of applied dissipated powers and energies.

(iii) **High bias regime** $(\boldsymbol{15 - 30\ V\ < V_{write}})$: a strong degradation of the channel is observed, leading to the creation of additional current paths inside the device's structure due to globally high resistances. In this regime, the resistance R_{SD} becomes reversible as part of the Al/YBCO gate is measured in parallel.

Memristive systems are very promising candidates for multiple applications, for example for logic circuits [252], signal processing [90,91], digital memories [89] and in the emerging field of neuromorphic computing [92,94,253]. In particular, in reconfigurable computing, it has been demonstrated that memristors can mimic the working principle of neurons and synapses. In our case, by varying the working temperature of the device, the YBCO/Al interface can be switched from a volatile to a non-volatile memristor. This, in turn, can give rise to novel applications: at low-temperature, the non-volatile property can be used to accurately store a specific resistance, simulating the state of the synapse. At room temperature, relaxation of the resistive state over time can give rise to novel functionalities, such as stochastic switching, a property that can be used to emulate the inherent stochastic dynamics of the biological neurons [97,254–256] .

To broaden the range of applications and add functionalities to these superconducting transistor-like structures, a few approaches can be considered for future investigations. The initial goal of this chapter was to design an active element for a cryogenic RF switch in the form of a SCPW (see **Sect. 1.2.**) that we can reversibly switched between insulating and superconducting states by application of a gate voltage. The transistor-like device studied in this chapter doesn't display the desired functionality: the superconductor-to-insulator phase transition is governed by the non-reversible process of thermomigration. However, a reversible switching of the channel's conductance by chemical redox reactions is achievable by modifying the geometry and the involved materials. This reversible modulation can be realized through: (i) a reduction of t_{YBCO} between 5 and $15\ nm$; and (ii) a reduction of the thermal gradients and high current densities that lead to the thermomigration and electromigration of oxygen ions.

(i) Drastically reducing the thickness of YBCO can simplify the control of the oxygen depleted volume of the superconducting channel. However, this approach involves changing the fabrication process. In fact, etching the YBCO layer down to a thickness of $15\ nm$ while keeping a non-zero T_C might reveal impossible with IBE and therefore, the YBCO layer must be deposited to ensure an optimal quality of the superconducting properties. The deposition can be done by PLD or magnetron sputtering, for example.

(ii) The reduction of the thermal gradients can be achieved by injecting lower writing voltages in order to reduce to a minimum the current densities and the heating of the device. However, the devices studied in this chapter require a switching voltage of $4\ V$ to trigger the redox reaction. Changing the oxidizing material (for instance with MoSi, Gd, Ag etc…) can greatly affect the amplitude of the switching for specific applications. In fact, by changing the reduction potentials of the involved materials, it is possible to engineer memristive devices with lower and higher $V_S(\pm)$. As an example, the MoSi/YBCO interface mentioned in **Sect. 1.1.1.** and studied by Rouco *et al.* [154] in 2020 displayed a switching field of $V_S(+) \approx 2\ V$, as compared to $V_S(+) = 4.1\ V$ in the present experiments.

Chapter 5: Magnetic switching in superconducting spin valve structures

1. Introduction

Spin valve structures, made of two magnetically active conducting electrodes sandwiching a non-magnetic thin layer (often referred to as the spacer), are devices whose resistance can be tuned between a high-resistive state and a low-resistive state by changing the relative orientations of the magnetizations of the magnetic layers, as depicted in **Fig. 5.1**. Typically, ferromagnets (FMs) are used as magnetic layers for their ability to keep a permanent magnetization even after the removal of the external magnetic field (see **Chapter 2, Sect. 3.**).

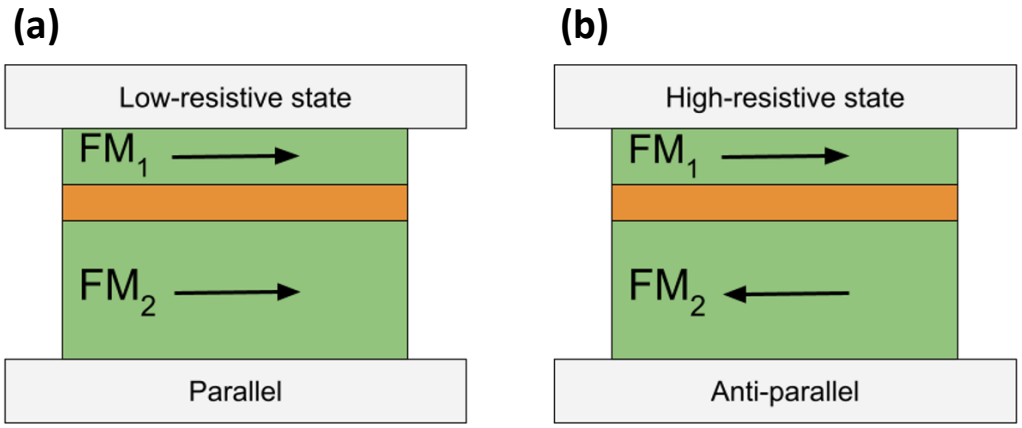

Fig. 5.1: Representation of a spin valve structure with two ferromagnetic layers (FM_1 and FM_2) on both sides of a non-magnetic thin spacer in the (left) parallel and (right) anti-parallel configurations. The resistance of the junction can switch between the low-resistive state and the high-resistive state by application of an external magnetic field, owing to the different coercive fields of the two ferromagnetic layers.

The case of a metallic spacer was investigated independently in the 80s by Albert Fert [12] and Peter Grunberg [13] when they observed a giant modulation of the electrical resistance of $[Fe/Cr]_n$ superlattices while applying an external magnetic field, now known as the giant magnetoresistance (GMR) effect. This effect is illustrated in **Fig. 5.2(a)**, showing a famous graph from the original paper of Baibich *et al.* [12]. The change in resistance is a consequence of the spin-dependent scattering of s-d conduction electrons and can be understood through the so-called Mott model [257]. In this model, spin up and spin down electrons are described in terms of two parallel conducting channels. The diffusion of electrons from a classical point of view is described by the Drude model [258], yielding the well-known conduction for a system of n electrons:

$$\sigma = \frac{ne^2\tau}{m_e} \tag{5.1}$$

where e is the charge of an electron, m_e is the mass of an electron and $\tau \propto 1/N(E_F)$ [259]is the mean time between electrons collisions and is inversely proportional to the density of states N at the Fermi energy E_F. In a metal, the density of states is symmetric at E_F for both spin populations $N_\uparrow(E_F) = N_\downarrow(E_F)$ (see **Chapter 2, Sect. 3.1.**), and therefore spin-flip scattering processes are equally probable for both spins' directions, leading to an equal resistance in the two channels. However, the splitting of the density of states for spin up and spin down electrons at the Fermi energy in a FM $N_\uparrow(E_F) \neq N_\downarrow(E_F)$, arising from the exchange coupling mechanism (see **Chapter 2, Sect. 3.1.**), leads to an imbalance in the channels' resistance in a spin valve device. This effect is summarized in **Fig. 5.2(b)** [260]:

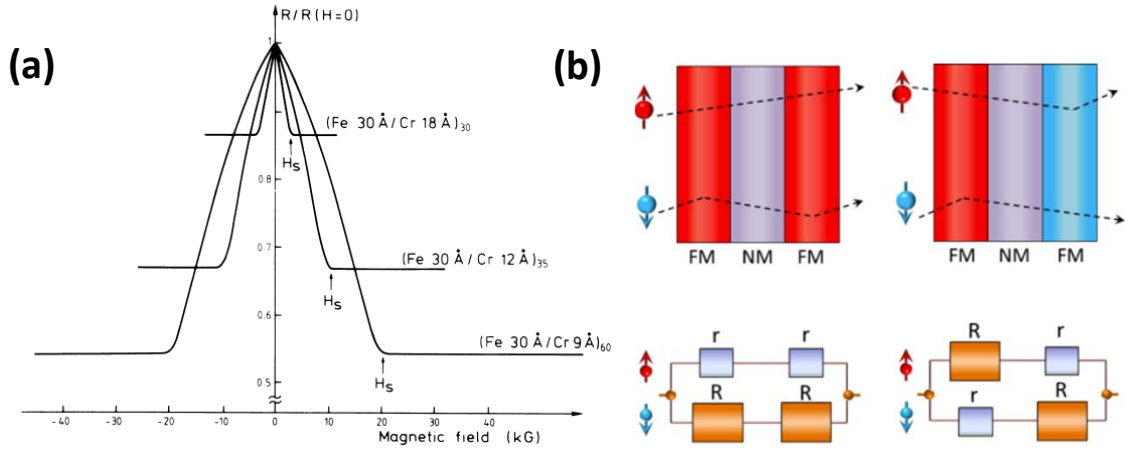

Fig. 5.2: (a) Resistance vs magnetic field of $[Fe/Cr]_n$ $(n = 30, 35\ and\ 60)$ superlattices showing the so-called giant magnetoresistance (GMR) effect. Figure taken from Baibich et al. (1988) [12]. (b) Resistor model of a spin valve structure showing the two conducting channels for spin up and spin down electrons in parallel in the (left) P and (right) AP configurations. Figure taken from Ullah, PhD thesis (2017) [260].

- In the parallel (P) configuration [**Fig. 5.2(b)**, left], spin up electrons experience a lower global resistance $2r$ compared to spin down electrons who see a large resistance $2R$ due to a lower spin-dependent scattering probability, leading to a low-resistive state.
- In the anti-parallel (AP) configuration [**Fig. 5.2(b)**, right], both electron spin populations are scattered equally (r+R) so that the spin valve displays a higher resistance.

When the metallic spacer is replaced by an insulating material, the spin valve device is known as a magnetic tunnel junction (MTJ) [100]; if the barrier is thin enough (a few nanometres), electrons can tunnel through the barrier, and the tunnelling rate depends on the relative orientation of the magnetization in the FMs layers, an effect known as tunnelling magnetoresistance (TMR). This effect was first studied by Juliere *et al.* [100] in 1975 by studying Fe/Ge/Pb and Fe/Ge/Co spin valve structures.

In order to obtain a stable AP state using external magnetic fields, the coercive fields of both ferromagnetic layers have to be different to prevent simultaneous reversal of the magnetizations. One possible way to achieve this AP state is to pin one of the FMs' magnetization by adding an anti-ferromagnetic (AF) layer to produce exchange bias: the magnetization of the FM in contact with the AF will be "pinned" and remain constant in a range of fields in which the other ferromagnetic layer's magnetization is reversed by the external field [261,262]. Another possibility is to take advantage of the thickness dependence of the coercive field: the thinner the FM, the stronger the coercive field [17,18]. Therefore, an asymmetric spin valve structure with ferromagnetic layers having different thicknesses will allow the appearance of an AP alignment within a certain range of applied fields. Finally, it is possible to engineer spin valve structures with ferromagnetic layers made from different materials [263].

Superconducting spin valves (SSVs) represent a specific kind of spin valve devices in which the spacer is a superconductor. This chapter is dedicated to the study of SSVs made with the high-critical temperature superconductor $YBa_2Cu_3O_{7-x}$ (YBCO) and half-metallic materials, namely $La_{1-x}Ca_xMnO_3$ (LCMO) and $La_{1-x}Sr_xMnO_3$ (LSMO). Half-metals are very promising materials for their unique property of being metallic for only one spin direction, *i.e.,* they correspond to the extreme case of a 100 % spin-polarized ferromagnetic material with a net spin polarization $P = 1$ and a large exchange energy E_{ex} (see **Chapter 2, Sect. 3.**). The first part of this chapter will be dedicated to an introduction of the basics

of this structure as well as the state of the art, principally from the viewpoint of cuprate/manganite heterostructures. Then, a description of the studied junctions with their corresponding fabrication process will be given and will be used for the global definition of the important geometric parameters. Finally, the results of the transport and magneto-transport experiments of the SSVs will be presented before discussing the origins and applications of the observed phenomena.

1.1. Superconducting spin valve effect: first predictions based on superconducting exchange coupling

The SSV structure was first introduced in 1966 by Pierre-Gilles de Gennes, who theoretically studied the properties of a thin s-wave superconductor (thinner than its coherence length) placed between two ferromagnetic layers [14]. Interestingly, this paper was released more than 20 years prior to the discovery of the giant magnetoresistance (GMR) effect by Albert Fert and Peter Grünberg in 1988 [12,13]. De Gennes concludes his visionary paper by indicating that $FM_1/S/FM_2$ multi-layers (with S a superconductor) might be of interest in shedding light on the relationship between superconductivity and ferromagnetism and could lead to potential applications in information storage, although de Gennes concludes that this system "does not look very promising on the theoretical side".

The next important step in the development of SSV devices was taken in 1999, when Tagirov [15] and Buzdin [16] derived concurrently and independently the theoretical equations describing the reduced critical temperatures (divided by T_C), t_C^P and t_C^{AP} in P and AP configurations respectively, of a superconducting spin valve using Usadel's anomalous Green functions and the linear Gor'kov equation:

$$\ln(t_c^P) = \Psi\left(\frac{1}{2}\right) - Re\Psi\left(\frac{1}{2} + j\frac{2R''}{\left(t_{spacer}/\xi_{spacer}\right)^2 t_C^P}\right) \tag{5.2}$$

$$\ln(t_c^{AP}) = \Psi\left(\frac{1}{2}\right) - \Psi\left(\frac{1}{2} + \frac{2(R'')^2}{\left(t_{spacer}/\xi_{spacer}\right)^2 t_C^{AP}}\right) \tag{5.3}$$

where Ψ is the digamma function, t_{spacer} is the S layer's thickness, ξ_{spacer} is the S layer's coherence length, R'' is the pair-breaking parameter.

The solutions of **Eq. 5.2** and **Eq. 5.3** are displayed in **Fig. 5.3**, taken from Tagirov's paper [15]. As the figure shows, there exists a large range of the pair-breaking parameter R'' for which t_c is completely suppressed in the P case but not in the AP configuration. This effect is thus opposite to the conventional GMR effect: in the P configuration, superconductivity in the spacer is suppressed and the resistance is higher than in the AP configuration. In the P state, the spin-polarized perturbations of the pairing functions for both ferromagnetic layers couple and reinforce each other (or in other words, the ferromagnetic exchange fields), effectively breaking apart the Cooper pairs and quenching superconductivity. This mechanism is called the superconducting exchange coupling. It is important to note that the previous calculations have been conducted in the case of an s-wave superconductor with singlet Cooper pair pairing. However, Kulić *et al.* [264] demonstrated theoretically that, in the case of ferromagnetic insulator (FI) based spin valves FI/S/FI, the calculations yield very similar solutions in the

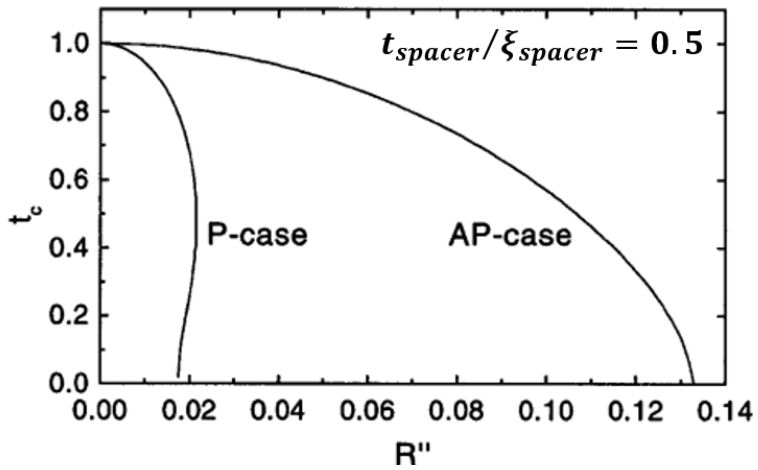

Fig. 5.3: Dependence of t_c as a function of R'' in the P and AP states for a SSV structure $FM_1/S/FM_2$, with $t_{spacer}/\xi_{spacer} = 0.5$. We observe that superconductivity is more robust in the AP configuration compared to the P configuration. Figure adapted from Tagirov, Phys. Rev. Lett. (1998) [15].

case of singlet or triplet Cooper pairs, with $t_c^P < t_c^{AP}$ (see **Fig. 5.3**). Thus, the observed effect is not expected to vary depending on the presence or absence of equal-spin pairing in the ferromagnetic layers.

There exist two main parameters commonly investigated in the literature to characterize SSVs, namely the critical temperature shift ΔT_C and the resistance difference ΔR between the P and AP configurations, defined as:

$$\Delta \mathrm{T}_C = T_C^P - T_C^{AP} \tag{5.4}$$

$$\Delta \mathrm{R} = R_{AP} - R_P \tag{5.5}$$

where T_C^P and T_C^{AP} are the critical temperatures and R_P and R_{AP} are the resistances (for a given temperature) in the P and AP configurations, respectively.

Of crucial importance for the rest of this chapter, two types of spin valve effects (SVE) can be defined depending on the sign of ΔT_C and ΔR:

- The negative SVE (also called standard SVE) corresponds to a device exhibiting $\Delta T_C < 0$ and $\Delta R < 0$ and is illustrated in **Fig. 5.4(a)**, summarizing the relation between both parameters, calculated from typical transport measurements: $R(T)$ in the P and AP states [**Fig. 5.4(b)**, left] and $R(B)$ at a given temperature [**Fig. 5.4(a)**, right] . For the negative SVE, the $R(T)$ in the AP state is shifted to higher temperatures as compared to the $R(T)$ in the P state, leading to an increased value of T_C in the AP configuration. $R(B)$ displays a characteristic hysteretic behaviour with two minima in the AP configurations that depends on the sweeping direction of the magnetic field.
- The positive SVE (also called inverse SVE) corresponds to a device exhibiting $\Delta T_C > 0$ and $\Delta R > 0$ and is illustrated in **Fig. 5.4(b)**. In this case, the $R(T)$ in the AP state is shifted to lower temperatures as compared to the $R(T)$ in the P state and $R(B)$ displays two maxima in the AP configurations.

The SVE based on superconducting exchange coupling as theorized by Tagirov and Buzdin in **Eq. 5.2** and **Eq. 5.3** leads to $\Delta T_C < 0$ and $\Delta R < 0$, and therefore corresponds to a negative SVE.

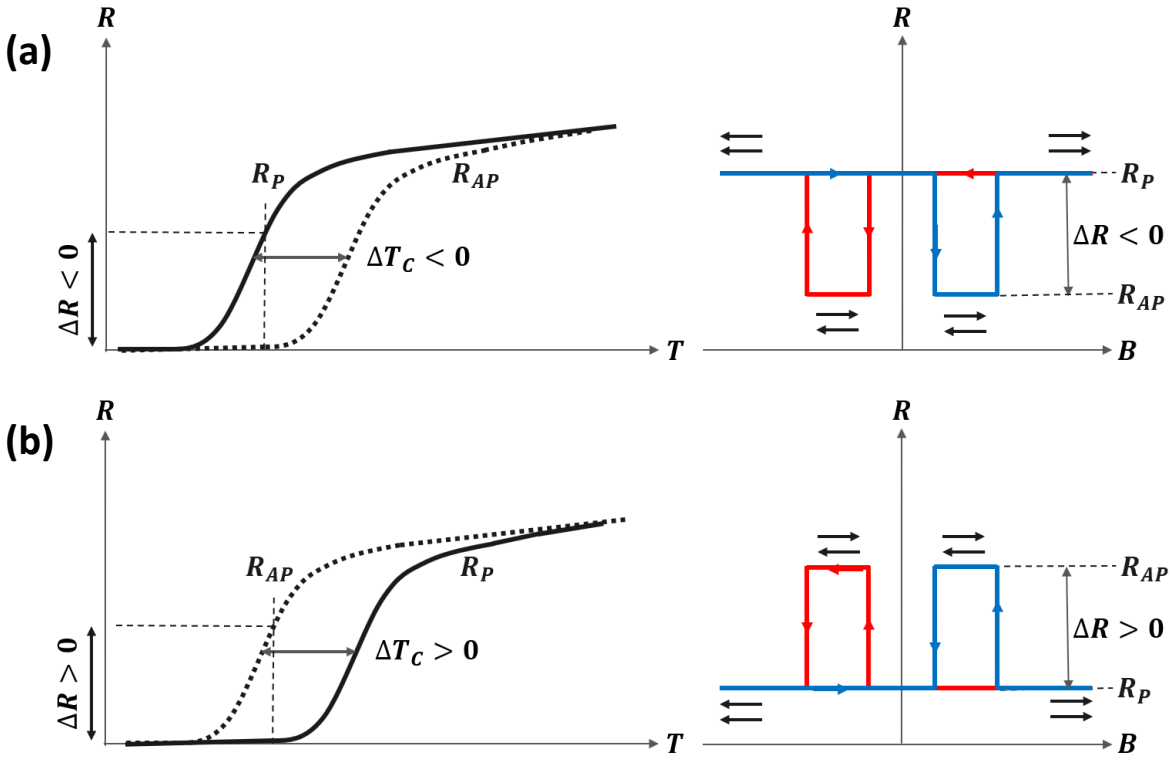

Fig. 5.4: (a) Illustration of the negative SVE with (left) a schematic of the $R(T)$ in the P and AP configurations. ΔT_C represents the shift of the critical temperatures induced by the SVE, and ΔR is the difference between R_{AP} and R_P for a given temperature and (right) a schematic of the $R(B)$ with a typical hysteretic behaviour with two dips in the AP configurations. The red curve corresponds to the resistance of the SSV while decreasing B whereas the blue curve corresponds to increasing B. (b) Illustration of the positive SVE with $\Delta T_C > 0$ and $\Delta R > 0$.

Theoretically, having a large enough value of ΔT_C will allow to induce an infinite magnetoresistance switch of the SSV device as, for a well-chosen temperature, $R_{AP} = 0$ while the resistance is finite in the P configuration, a property of paramount importance for technological applications.

Following the papers of Tagirov and Buzdin, the discovery of GMR and the development of spintronics, a lot of attention has been brought to the design and characterization of SSV devices, mainly using s-wave superconductors coupled with transition metals and rare-earth ferromagnets. The next sub-chapter will review the main advancements in the field of SSVs.

1.2. State of the art: spin valve effects mechanisms

SSVs have been investigated since the beginning of the 21st century under various geometries and with different materials. They can be designed with a current-in-plane (CIP) or current-perpendicular-to-plane (CPP) configurations. These two geometries are schematically summarized in **Fig. 5.5** [99]. CIP spin valves [**Fig. 5.5(a)**] correspond to planar junctions with the current circulating in-plane with respect to the stack of FMs and S layers (that is, parallel to the interface), whereas CPP spin valves [**Fig. 5.5(b)**] are vertical junctions with a current flowing perpendicular to the FMs and S interfaces. In this work, the CPP geometry has been chosen for the design of the SSVs and the structure as well as the fabrication process will be presented later in the chapter (see **Sect. 1.3.**). Although typical structures $FM_1/S/FM_2$ correspond to the most studied type of SSV, other spin valve structures such as $S/FM_1/(N)/FM_2$ have unveiled interesting effects and will be discussed below as well.

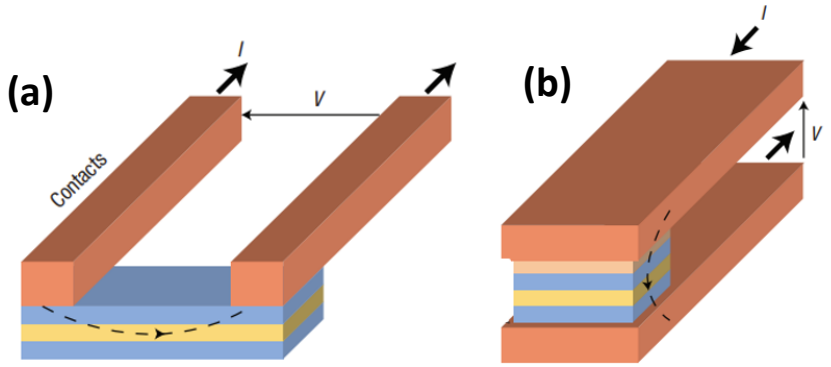

Fig. 5.5: Schematic of the two typical measuring geometries of a spin valve structure :(a) Current-in-plane (CIP) and (b) current perpendicular-to-plane (CPP). In this thesis, the SSVs will be measured in a CPP geometry using a 4-probe measuring configuration. Figure adapted from Chappert et al., Nature Materials (2007) [99].

1.2.1. Current-in-plane (CIP) superconducting spin valve junctions

Historically, the first SSV structures that were experimentally studied were current-in-plane (CIP) planar $FM_1/S/FM_2$ trilayers made from conventional s-wave superconductors and transition metal FMs owing to their easier fabrication processes [265–274]. More recently, novel experiments have been conducted with rare earth FMs and ferromagnetic insulators such as europium sulfide (EuS) and gadolinium nitride (GdN), exhibiting higher values of ΔT_C [275–277]. **Fig. 5.6** shows a summary of the typical values of ΔT_C for various systems with different materials [278]. The left part of the graph consists of structures made from s-wave superconductors, while the right part shows ΔT_C values obtained with SSVs made with cuprate d-wave superconductors. SSVs made from d-wave superconductors started to emerge in the second half of the 2000s, mainly centred around the cuprate superconductor YBCO and manganite ferromagnets [278–282], due to their matching crystalline structures related to the perovskite family (see **Chapter 2, Sect. 2.2.** and **Sect. 3.5.**). As can be seen from **Fig. 5.6**, the origins of the polarity and amplitude of ΔT_C have many interpretations depending on the studied system and materials. The next sub-sections are dedicated to the description of the

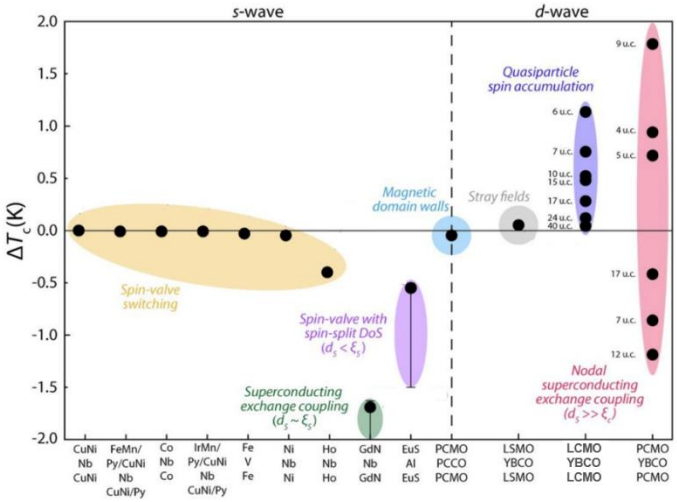

Fig. 5.6: ΔT_C for a large diversity of SSVs made from various FMs (transition metals, ferromagnetic insulators, oxides…) and various superconductors, including s-wave and d-wave superconductors. As can be seen from this figure, there exist a large panel of attributed origins to explain the positive and/or negative SVEs in these junctions. Figure adapted from Di Bernardo, Nature materials (2019) [278].

main physical explanations for the positive and negative SVEs in SSV structures, namely quasiparticle spin accumulation, stray fields and crossed Andreev reflections.

1.2.1.1. Quasiparticle spin accumulation: positive spin valve effect

In 2005 and 2008, respectively, Peña *et al.* [281] and Nemes *et al.* [282] measured the magnetoresistance of LCMO/YBCO/LCMO trilayers and obtained only positive values of ΔT_C between a few mK [**Fig. 5.7(b)**] to $\sim 1\ K$ [**Fig. 5.7(a)**], depending on the thickness t_{YBCO} of the YBCO spacer. This positive SVE was attributed to a different density of quasiparticles depending on the relative orientations of the half-metals' magnetizations [282]. While the magnetizations are AP, assuming that the superconductor is thinner than the spin-diffusion length, an incoming polarized electron from one ferromagnetic electrode will be reflected at the opposite interface, due to the $100\ \%$ spin-polarized property of half-metallic materials (see **Chapter 2, Sect. 3.5.**), causing an excess of quasiparticles in the superconducting spacer. This quasiparticle accumulation effectively suppresses the spacer's critical temperature in the AP state, leading to positive values of ΔT_C and ΔR, *i.e.* a positive SVE.

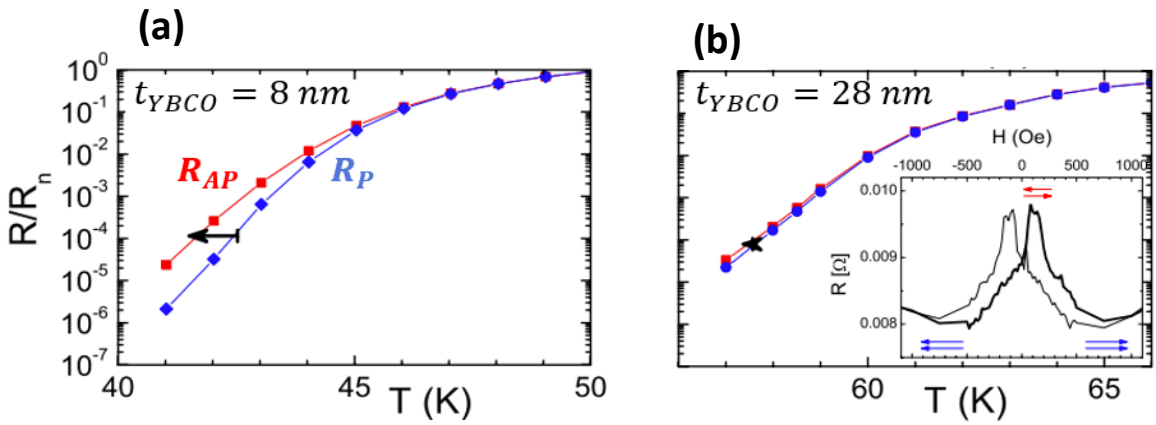

Fig. 5.7: (a) Normalized resistance vs. temperature of a LCMO/YBCO/LCMO trilayer with $t_{YBCO} = 8\ nm$ in the AP (red points) and P (blue points) configurations, showing a positive ΔT_C shift of $\sim 1\ K$, characterizing a positive SVE. (b) $R(T)$ measurements of a similar trilayer with $t_{YBCO} = 28\ nm$ showing a positive SVE with a lower ΔT_C shift. The magnetoresistance at $58\ K$ is displayed in the inset, showing a positive ΔR, consistent with the $R(T)$ curve. Figure adapted from Nemes et al., Phys. Rev. B (2008) [282].

1.2.1.2. Stray fields and motion of superconducting vortices: positive spin valve effect

In a SSV, the reversal of the magnetization of the magnetic domains within the FMs can lead to the generation of magnetic stray fields that modulate the superconducting properties of the spacer [270,280,283–289]. This phenomenon was first discussed in 2006 by Steiner and Ziemann [283] while experimentally investigating the magneto-transport properties of Co/Nb/Fe trilayers below the T_C of the Nb spacer. The authors observed two magnetoresistance peaks (positive SVE) located at the coercive fields of both FMs, as illustrated in **Fig. 5.8** [283]. In fact, the stray field generation is expected to be maximum in the vicinity of the coercive fields as it corresponds to the state with a larger density of domain walls and magnetic domains. The increase of the resistance is a consequence of the stray fields penetrating the superconducting spacer and quenching the superconducting properties.

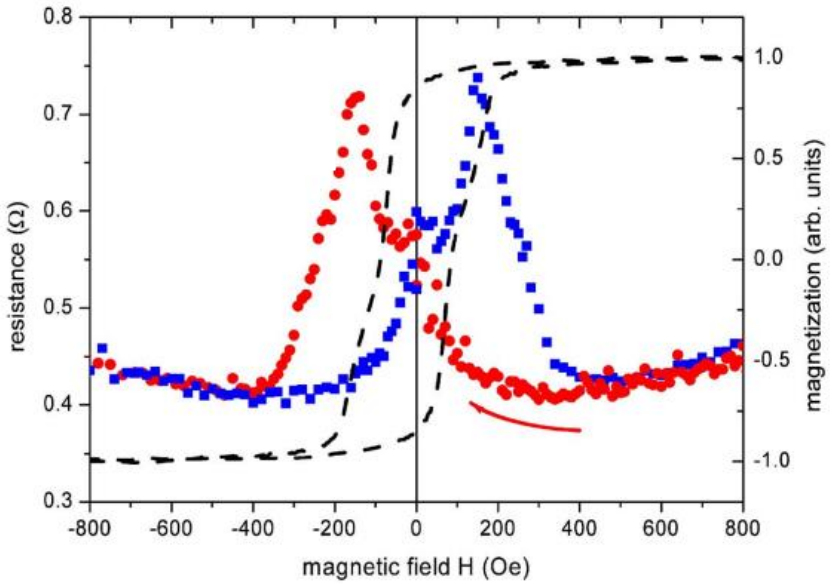

Fig. 5.8: Resistance vs. magnetic field of a Co/Nb/Fe trilayer at $3.4\ K$ for sweeping down fields (red line) and sweeping up fields (blue line), showing two distinct peaks for magnetic fields close to the coercive fields, as indicated by the $M(B)$ hysteresis loop (black dashed line). Figure taken from Steiner et al., Phys. Rev. B (2006) [283].

In the case of type-II superconductors, the upper critical magnetic field H_{c2} is substantially higher (approximately $20\ T$ at $0\ K$ in the case of YBCO [132]) than the critical field in the case of type-I superconductors and therefore, stray fields have a lower impact on the stability of Cooper pairs. However, out-of-plane stray fields can generate vortices, leading to strong dissipation, *i.e.* an increase of the global resistance of the SSV junction in the AP configuration. In 2006, Bell *et al.* [286] experimentally investigated GdNi/MoGe/GdNi trilayers and observed the signatures of a positive SVE in the magnetoresistance experiments, with $\Delta R > 0$. The authors attributed this effect to the generation of a flow of vortices caused by stray fields. Then, Zalk *et al.* [280] studied in 2009 a LSMO/YBCO/LSMO all-oxide SSV and found a positive value of ΔT_C, also attributed to the generation of stray fields within the YBCO spacer. Magnetic stray fields have been known to give rise to this type of behaviours in $FM_1/S/FM_2$ junctions, particularly for SSVs with no preferentially pinned ferromagnetic layer, *i.e.* without using an AF pinning layer [270,289], which will be the case of the spin valves studied in this chapter.

1.2.1.3. Crossed Andreev reflections: negative spin valve effect

Many scientific reports also consider the occurrence of non-local Andreev processes (also called crossed Andreev reflections or CARs) as a possible mechanism that can explain a negative SVE in N/S/N and $FM_1/S/FM_2$ trilayers [290–296]. Contrarily to conventional Andreev reflections (refer to **Chapter 2, Sect. 4.1** for more details), this phenomenon necessitates two distinct interfaces on both sides of a very thin superconducting layer (thinner than the superconducting coherence length) and is schematically illustrated in **Fig. 5.9** [102] in the particular case of a $FM_1/S/FM_2$ system. Through this process, an incoming electron (hole) from one electrode (for example FM_1 in **Fig. 5.9**) can generate a Cooper pair within the superconducting layer by retroreflecting a hole (electron) of opposite spin in the opposite electrode (FM_2 in this case). Therefore, the Andreev process occurs at both electrodes at the same time, requiring that electrons of opposite spins can be found in both materials simultaneously. In the case of a $FM_1/S/FM_2$ junction, CARs are therefore non-compatible with the P

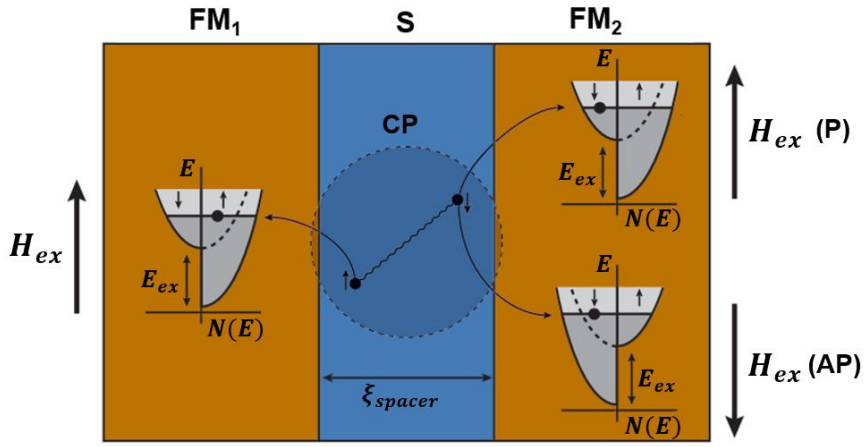

Fig. 5.9: Schematic of the CARs process which describes the non-local generation of a Cooper pair in a superconductor thinner than ξ_{GL}. In the case of two ferromagnetic electrodes, CARs are not compatible with the P configuration of the spin valve, leading to a lower T_C in the P state, i.e. a shift $\Delta T_C < 0$. Figure adapted from Flokstra, PhD thesis (2010) [102].

configuration of the spin valve, yielding reduced superconducting properties in the P state. CAR processes have been theorized to be the origin of the long-range proximity effects [297] observed at FM/S interfaces in bilayers such as YBCO/LCMO [298] and YBCO/$SrRuO_3$ [291], caused by the typical geometry of the magnetic domains in the ferromagnetic layers, with domain wall thicknesses of approximately $\sim 3\ nm$ (as compared to YBCO's coherence length of $\sim 2.41\ nm$ in the ab-plane) for SRO [291], for example.

1.2.2. Current-perpendicular-to-plane (CPP) superconducting spin valve junctions

A well-known property of magnetic spin valves in spintronics is the possibility to enhance the amplitude of the GMR and TMR effects in CPP devices compared to CIP devices [299,300]. Following the same logic, superconducting spin valves having a CPP vertical geometry are promising candidates for future investigations. Because of the enhanced difficulty for the fabrication of such devices (with a large number of clean-room deposition and etching steps), studies of this kind of structures have been relatively limited to this day [290,301]. In 2022, Stoddart-Stones *et al.* [290] fabricated and characterized a current-perpendicular-to-plane SSV made of niobium and permalloy, demonstrating a crossover between positive and negative SVEs. In particular, the authors showed that a reversal from a positive to negative spin valve behaviour can be induced by reducing the thickness of the superconducting spacer below its superconducting coherence length. The authors attributed the positive SVE to quasiparticle spin accumulation (**Sect. 1.2.1.1.**) and the negative SVE to superconducting exchange coupling (**Sect. 1.1.**). In the present work, all the measured SSVs were designed with a CPP configuration following a multi-steps microfabrication process that will be detailed later on.

1.2.3. Triplet spin valves

Some authors (including Tagirov [302]) proposed S/FM_1/(N)/FM_2 structures (sometimes referred to as triplet spin valves) as potential devices that can be used for the generation of equal-spin triplet Cooper pairs [302,303]. A schematic representation of a triplet spin valve is given in **Fig. 5.10(a)** [112].

The normal metal between FM_1 and FM_2 is not mandatory but can be needed as a de-coupling layer to prevent the two ferromagnets to act as a unique entity and reverse their magnetizations simultaneously. Spin triplet generation is accomplished through spin mixing (induced by the thin mixing layer FM_1) and spin rotation (induced by the drainage layer FM_2) mechanisms, as was described in more details in **Chapter 2, Sect. 4.3.** It was shown, both theoretically [28,304–306] (including some studies with half-metallic materials [307]) and experimentally [112,273,283,308,309] that these structures can generate equal-spin triplets when the magnetizations are in a perpendicular configuration, *i.e.* while the magnetic inhomogeneities are maximum in the system. This leads to a leakage of triplet Cooper pairs from the superconductor to the drainage layer FM_2, which decreases the T_C of the superconducting layer. This layer needs to be thin enough (a few nanometres) in order to generate an observable change of the T_C, as a very thick YBCO layer will not be affected by the leakage of equal-spin Cooper pairs. In 2015, Singh *et al.* [112] investigated the triplet supercurrent leakage in a multi-layered triplet spin valve $S/FM_1/N/FM_2$ made of MoGe, Ni, Cu and the half-metallic ferromagnet CrO_2. The authors observed a modulation of the value of ΔT_C of $\sim 1\ K$ by varying the angle of the external magnetic field between an in-plane and an out-of-plane configuration. They demonstrated that ΔT_C (and therefore the triplet generation) is maximum while the magnetic field is applied out-of-plane and the magnetizations are in a perpendicular configuration. This effect is illustrated in **Fig. 5.10(b)**, showing $R(T)$ measurements and ΔT_C for different incident angles θ of the external applied field ($\theta = 90\,°$ corresponds to the direction perpendicular to the FMs and S interfaces). The triplet generation thus leads to the global decrease of the resistance in the P configuration, *i.e.,* a positive SVE.

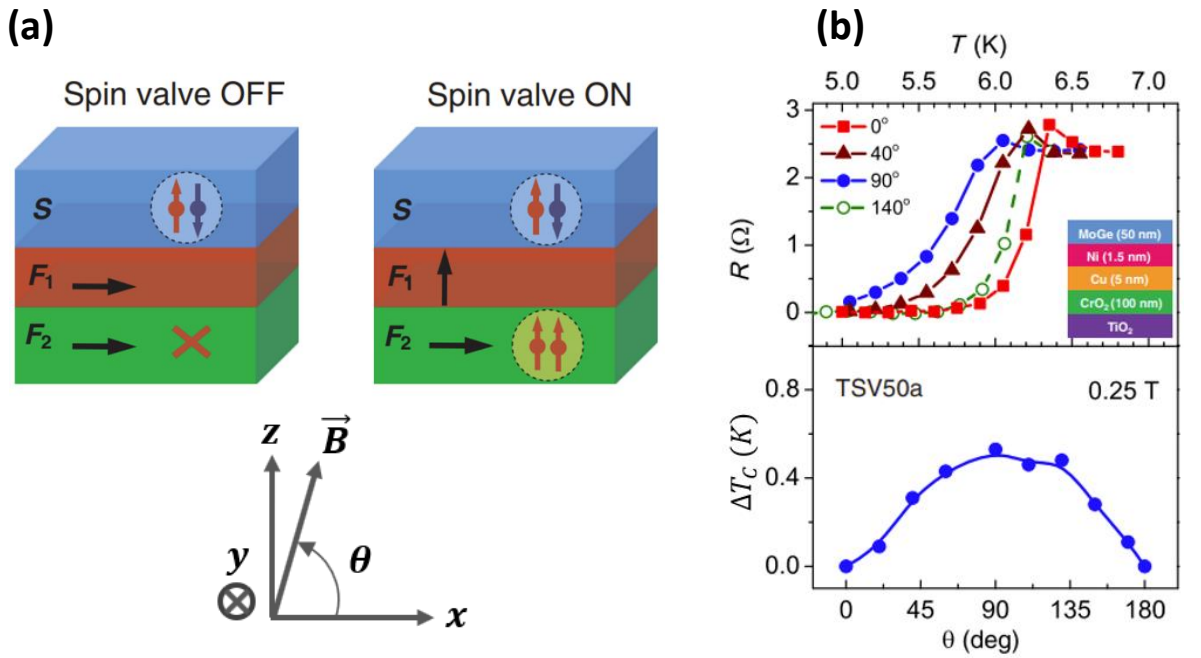

Fig. 5.10: (a) Schematic representation of a triplet spin valve structure $S/F_1/F_2$. (left) While the magnetizations are parallel, there is no triplet generation, and the T_C of the S layer is maximum. (right) When the magnetizations of the ferromagnetic layers are perpendicular, a leakage of triplet cooper pairs in the F_2 layer reduces the T_C of the S layer, therefore yielding a higher global resistance. (b) $R(T)$ experiments carried on MoGe ($50\ nm$)/ Ni ($1.5\ nm$)/ Co ($5\ nm$)/ CrO_2 ($100\ nm$) multilayers with $B = 0.25\ T$, with a clear maximum of ΔT_C for $\theta = 90\,°$, i.e. for the perpendicular configuration. Figures adapted from Singh et al., Phys. Rev. X (2015) [112].

1.3. Description of the multilayer SSV studied in this thesis

The SSVs studied in this chapter are multilayers S/FM_1/S/FM_2/S vertical junctions made from the cuprate high-temperature superconductor YBCO and half-metallic FMs, either LCMO or LSMO (in all the SSVs in this chapter, the structure is symmetrical, *i.e.* FM_1 and FM_2 are made of the same half-metal). Interfaces between superconductors and half-metals have gained a lot of attention is the past two decades as promising systems that can give rise to long-range triplet correlations [105,310–313]. The multilayer structure is depicted in **Fig. 5.11(a)** and consists in a micrometric squared vertical pillar with $W = 10\ \mu m$ or $W = 20\ \mu m$. The two outer superconducting layers both have the same thickness of $30\ nm$, whereas the superconducting spacer has a thickness t_{YBCO} between 3 and $10\ nm$. The thicknesses of the ferromagnetic layers were chosen to be different ($5\ nm$ and $15\ nm$) in order to define two distinct coercive fields: the thicker ferromagnetic layer should exhibit a lower coercive field [17,18]. In 2012, Visani *et al.* [310] demonstrated that YBCO's superconducting correlations can propagate through an LCMO thin layer over a distance at least equal to $\xi \sim 30\ nm$, which motivates the choice of the ferromagnetic layers' thicknesses.

For comparison purposes, control samples with a $PrBa_2Co_3O_{7-x}$ (PBCO) spacer will also be investigated to help identifying the origins of the various spin valve phenomena. PBCO is a wide-gap semiconductor [140] that is commonly used in conjunction with cuprate superconductors and manganite ferromagnets for its small lattice parameter mismatch, yielding optimal epitaxial interface transparency [314–316].

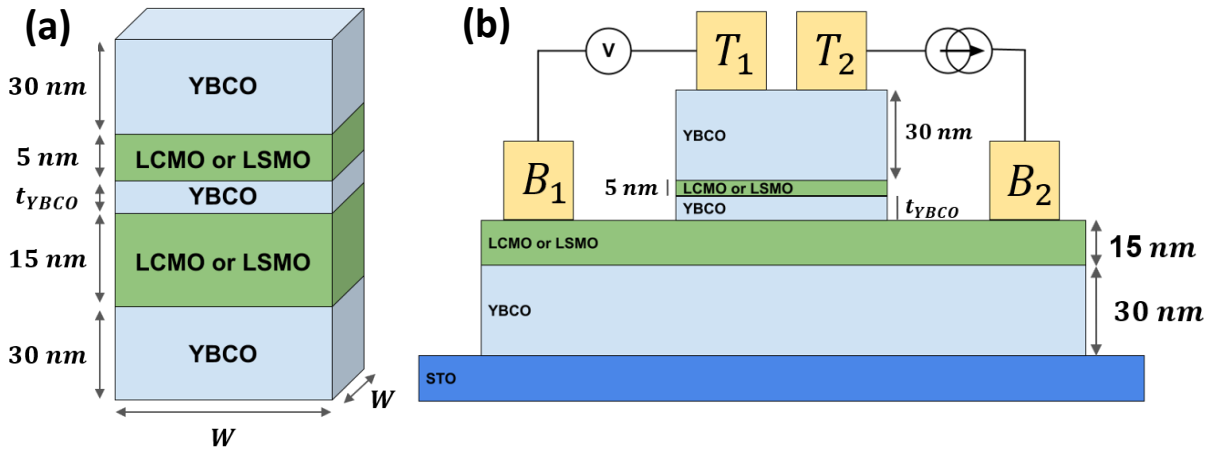

Fig. 5.11: (a) Structure of the multilayers S/FM_1/S/FM_2/S studied in this chapter patterned into squared vertical pillar of cross-section $W \times W$. (b) Schematic representation of a typical device and the 4-probe measuring setup. The current is applied between T_2 and B_2 while the voltage is measured between T_1 and B_1.

The aim of this chapter is to study the transport and magneto-transport properties of the SSV structure displayed in **Fig. 5.11(a)** in a particular geometry that allows for a 4-probe measurement, as illustrated in **Fig. 5.11(b)**. The current will be applied perpendicular to the various interfaces (CPP geometry) between the T_2 and B_2 gold contact pads, and the voltage will be measured between T_1 and B_1. The next section is focused on the description of the clean-room fabrication process of these vertical junctions (lithography, deposition, etc…).

2. Samples fabrication and description

2.1. Fabrication process

The junctions were fabricated through two different methods. The first method (denoted as method 1 in **Fig. 5.12**) was used for the fabrication of the first SSVs that were measured within the frame of this project. For reasons that will become clear later while presenting the experimental results from these SSVs, the fabrication process was modified and evolved into a second method (denoted as method 2 in **Fig. 5.12**). In both cases, the fabrication is performed on $5 \times 5\ mm^2$ multi-layered samples STO (001)// S ($30\ nm$)/ FM_1 ($15\ nm$)/ spacer (t_{spacer})/ FM_2 ($5\ nm$)/ S ($30\ nm$), where S is a superconductor (YBCO for all the samples studied in this chapter), FM_1 and FM_2 are the same half-metallic ferromagnets (either LSMO or LCMO) and the spacer can be a superconductor (YBCO) or an insulator (PBCO) for the control samples. t_{spacer} represents the thickness of the spacer and will be rewritten as t_{YBCO} and t_{PBCO} for spin valves with a YBCO and PBCO spacer, respectively.

Of crucial importance for the fabrication process, the multi-layered samples can be covered or not by a gold capping layer of $30\ nm$. This gold capping will define the method used for the fabrication: for the samples with no gold capping, method 1 was used, whereas for the other samples, method 2 was used. In the rest of the thesis, the denomination "*in-situ*" and "*ex-situ*" will be used to describe the deposition technique that was employed for the capping layer. On the one hand, "*in-situ* " indicates that the gold layer was deposited by PLD during the same deposition process as the other layers, without breaking the chamber's vacuum to prevent the degradation of the top YBCO layer's surface. On the other hand, "*ex-situ*" indicates that the gold layer was deposited via magnetron sputtering in a separate apparatus.

For every step, laser lithography (see **Chapter3, Sect. 4.1.2.**) was performed before etching or depositing materials for the patterning, and the masks were prepared using the software KLayout. **Fig. 5.12** describes the various steps involved in the fabrication of the SSVs. For each step, the left picture shows a schematic representation of the stack while the right picture displays a microscope picture corresponding to the state of the junction right after the corresponding step.

Step 1: The first step [**Fig. 5.12(a)**] consists of the etching of the upper half of the vertical junctions (down to the second FMs) as well as the definition of the alignment marks to allow for the precise alignment of future lithography masks. The width W of the vertical junctions is equal to either $10\ \mu m$ or $20\ \mu m$ and the cross-section of the junctions is a square. The etching is performed using ion beam etching (IBE), monitored with a secondary ion mass spectrometer (SIMS), as described in **Chapter 3, Sect. 4.2.** The typical SIMS signals obtained during step 1 can be seen in **Fig. 5.13(a)** showing the etching, in chronological order, of gold (monitored via Au), YBCO (monitored via Ba), LSMO (monitored via La), YBCO and LSMO again. The etching was stopped by looking at the barium (lanthanum) signal: when the count starts to go down (up) a second time, the second ferromagnetic layer is starting to be etched. In fact, the second FM is kept as a protection for the bottom YBCO layer to prevent degradation during the subsequent fabrication steps due to the developing chemicals and/or oxygen exchanges with air.

Step 2: The second step [**Fig. 5.12(b)**] is the etching of the FM_2 and bottom YBCO layers down to the STO substrate to define the measuring bars. Again, the etching time is monitored using a SIMS, and the typical signal observed during this step can be seen in **Fig. 5.13(b)**. This time, the etching was halted by looking at the increase of titanium's signal, indicating that the substrate is being etched.

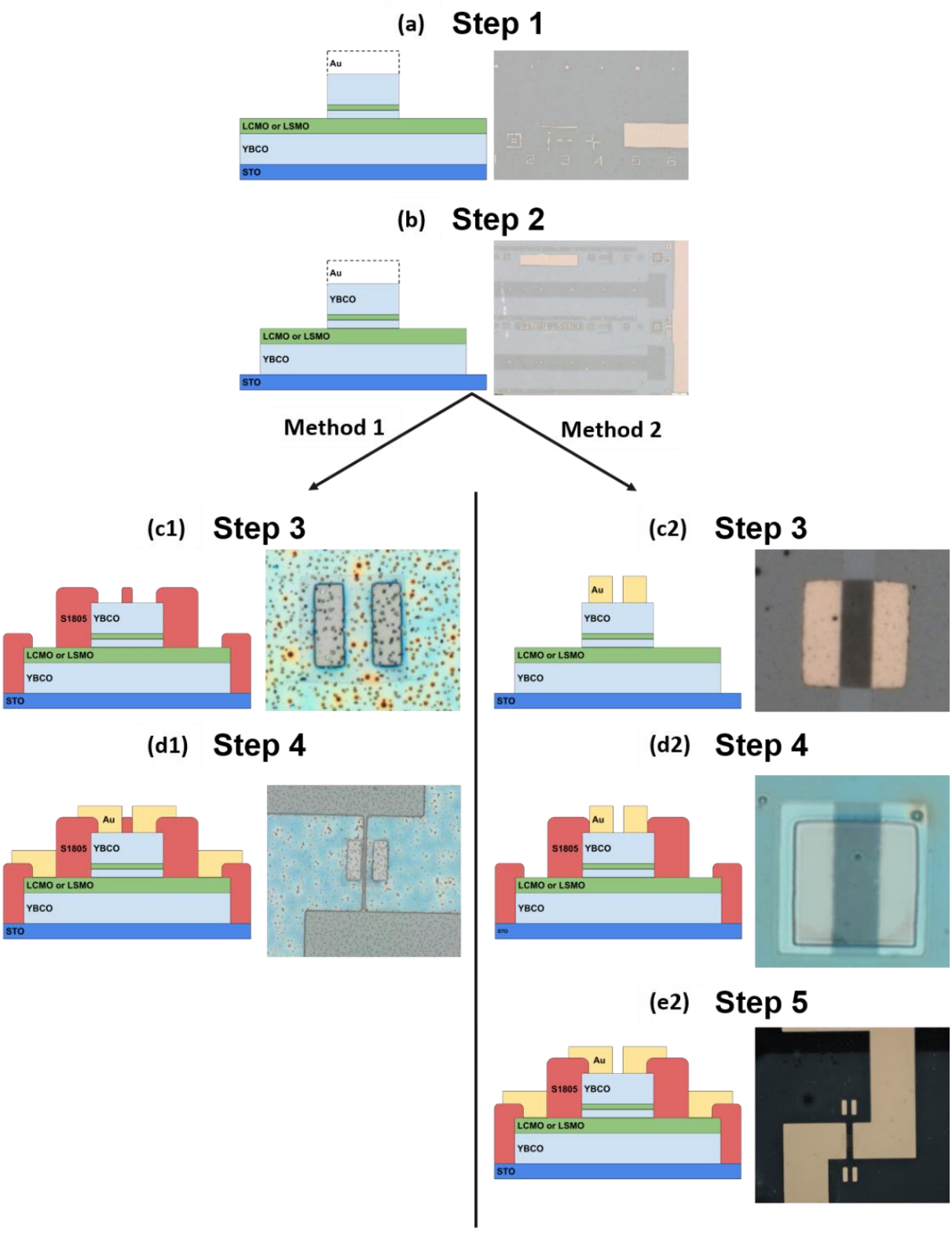

Fig. 5.12: Fabrication process of the SSV vertical junctions. The fabrication recipe is described in full details in ***Annexes, Sect. 2.1.*** *(a) Step 1: etching of the upper half of the vertical pillars and the alignment marks for future lithography steps. Junctions have a square cross-section of area* $10 \times 10\ \mu m^2$ *or* $20 \times 20\ \mu m^2$*. (b) Step 2: etching of the measuring bars that will be used for the 4-probe measurement of the SSVs. Each bar contains twelve junctions. (c), (d) and (e) describe the last fabrication steps relative to the contacts deposition and differ depending on whether or not a gold capping layer was deposited prior to the patterning process (methods 1 and 2).*

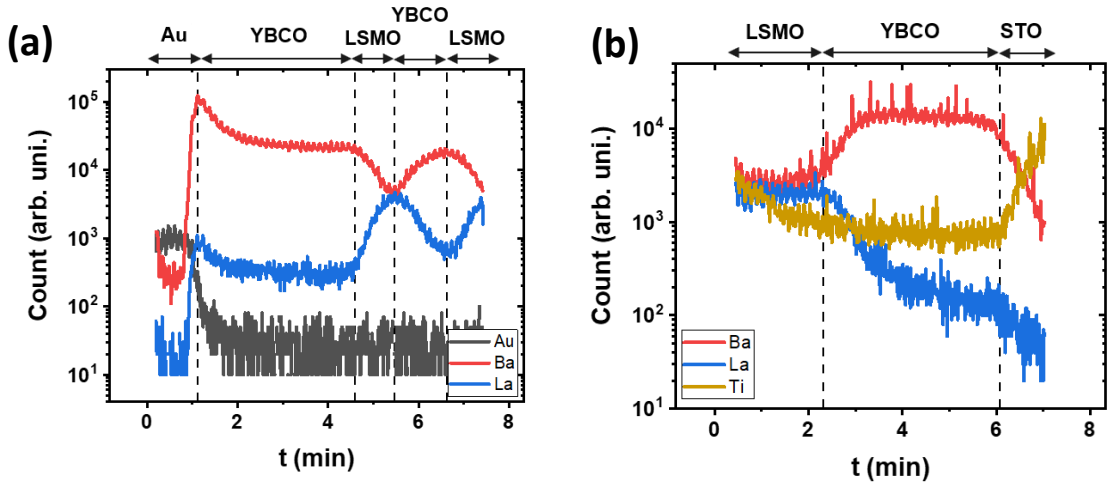

Fig. 5.13: Typical SIMS signal during (a) step 1 and (b) step 2 of the etching process. (a) Etching of gold (30 nm), YBCO (30 nm), LSMO (5 nm) and YBCO (t_{YBCO}). The etching was stopped when the lanthanum (barium) signal was starting to go up (down) again, signalling that the second LSMO layer is being etched. (b) Etching of LSMO (15 nm) and the last layer of YBCO (30 nm). In that case, the etching was halted when the titanium signal was starting to rise, indicating that the STO substrate is being etched.

Steps 3,4 and 5: The following fabrication steps differ depending on whether or not a gold capping was deposited prior to the clean-room patterning of the samples:

(i) **Method 1, without a gold capping layer:** in the case of method 1, two small apertures are lithographed on top of the vertical junctions during step 3 [**Fig. 5.12(c1)**] to allow for the subsequent gold deposition and the definition of the 4-probe measurement setup. S1805 was used as a resist during this fabrication step as it is possible to make it part of the structure by heating up the sample for one minute at 170 °C. Thus, the resist is aimed at preventing short-circuits to occur while depositing gold contacts via evaporation in step 4 [**Fig. 5.12(d1)**]. The evaporation deposition was done with a PLASSYS MEB5050 ($E = 200\ eV, I = 110\ mA$ and $t = 15\ min$) by a third party in Thales.

(ii) **Method 2, with a gold capping layer:** in the case of method 2, step 3 [**Fig. 5.12(c2)**] corresponds to the etching of part of the top gold layer. This step is aimed at dissociating the top two contacts of the vertical spin valve junctions to allow for 4-probe measurements. Then, step 4 [**Fig. 5.12(d2)**] is designed at opening the top part of the vertical spin valve structures to allow for the deposition of the deported gold contacts. Again, the resist S1805 is used and permanently harden by a heating step to protect the measuring bars and prevent short-circuits. Finally, step 5 [**Fig. 5.12(e2)**] consists in the deposition via evaporation of the deported contacts' gold layer.

The full description of the fabrication process with all clean-room parameters is given in **Annexes, Sect. 2.1.** in the case of method 2, which corresponds to the final and optimal fabrication method yielding the most reproducible and reliable measurements.

2.2. Samples summary

For this chapter, the presented data was obtained while measuring four batches of samples, made from different materials and with varying geometries. **Tab. 5.1** gives a summary of all of them with their respective materials, t_{spacer}, nature of the gold capping deposition (*in-situ* and *ex-situ*) and

names. While describing and discussing the results in the next sections, the name of the presented samples will be given in the figures' caption and the reader may refer back to **Tab. 5.1** for further information about the sample's geometry and composition.

	Ferromagnet	Spacer	t_{spacer} [nm]	Gold capping	Sample's name
Batch 1 Method 1	LCMO	YBCO	3	-	SY1
			5	-	SY2
			7	-	SY3
			10	-	SY4
Batch 2 Method 1	LCMO	PBCO	3	-	SP1
			2	-	SP2
			1	-	SP3
Batch 3 Method 2	LSMO	YBCO	3	*Ex-situ* (Sput.)	REAL1
			5	*Ex-situ* (Sput.)	REAL2
			8	*Ex-situ* (Sput.)	REAL3
			10	*Ex-situ* (Sput.)	REAL4
Batch 4 Method 2	LSMO	YBCO	8	*In-situ* (PLD)	REAL5
			10	*In-situ* (PLD)	REAL6

Table 5.1: Summary of the various batches measured for this project, with a description of the important materials and parameters. The "gold capping" column indicates how it was deposited. In the case of the first two batches, the multi-layered samples were deposited without any gold capping. For batch 3, the gold capping was deposited ex-situ via magnetron sputtering, whereas for the last batch, it was deposited in-situ via PLD.

Each batch presented in **Tab. 5.1** has some specificities and will yield crucial information and results for the global understanding of the SSV:

(i) **Batch 1 (fabrication method 1):** the multi-layered samples of batch 1, STO (001)// YBCO ($30\ nm$)/ LCMO ($15\ nm$)/ YBCO (t_{YBCO})/ LCMO ($5\ nm$)/ YBCO ($30\ nm$), were deposited in Madrid by the team of Prof. Santamaria using magnetron sputtering for the deposition of all layers, without any gold capping [19,113]. As a consequence of the absence of a gold capping layer, method 1 was used for the spin valve patterning. As will be demonstrated further down, the contact resistances between gold and YBCO obtained from this method are considerably high (of the order of a few $M\Omega$) and can hinder the measurements of the spin valves and their superconducting properties, although the magneto-transport measurements of some SSVs yielded very promising results (see **Sect. 3.2.**).

(ii) **Batch 2 (fabrication method 1):** batch 2 is made of three control samples with spin valve structures having a non-superconducting spacer (PBCO). These samples will help for the discussion of the origins of the observed effects. Like batch 1, the multi-layered samples, STO (001)// YBCO ($30\ nm$)/ LCMO ($15\ nm$)/ PBCO (t_{PBCO})/ LCMO ($5\ nm$)/ YBCO ($30\ nm$), were deposited in Spain with identical deposition techniques and the spin valves were fabricated using method 1.

(iii) **Batch 3 (fabrication method 2):** this batch consists of 4 samples that were fully prepared at the UMR CNRS/Thales using pulsed laser deposition (PLD) and magnetron sputtering. For this batch (and the next), LSMO was chosen as the spin valve's FMs as opposed to LCMO for the two previous batches. The samples were prepared with a gold capping layer of $30\ nm$ prior to the clean-room patterning, deposited by magnetron sputtering, and the spin valves were fabricated following method 2.

(iv) **Batch 4 (fabrication method 2):** for this last batch, the whole multi-layered stacks were deposited *in-situ* at the UMR CNRS/Thales via PLD, including the gold capping layer,

meaning that method 2 was chosen for the micro-patterning of the SSVs. The denomination *in-situ* indicates that the gold layer has been deposited in the PLD chamber in the same deposition process as the other layers, without breaking the vacuum to prevent the degradation of the top YBCO layer's surface.

Fig. 5.14(a) shows the 4-probe measurement setup that was used for the characterization of all the SSVs as well as a summary of the important geometric parameters and thicknesses. The data is acquired by biasing in current with a Keithley 2400 sourcemeter and measuring a voltage with a Keithley 2182A nanovoltmeter. The top contacts of the vertical spin valves are denoted with the letter T (T_1 and T_2) and the bottom contacts are denoted with the letter B (B_1 and B_2). **Fig. 5.14(b)** is a microscope picture of a typical measuring bar (highlighted with a green dashed line as a guide to the eye) after the fabrication process is over. Each sample is made of four measuring bars, while each bar has a total of twelve spin valves that can be measured in 4-probe independently. The cryocooling system (Janis refrigerator, see **Chapter 3, Sect. 5.2.**) was equipped with a motor to allow for the rotation of the rod and therefore the rotation of the sample. As the electromagnet and the direction of the external magnetic field is fixed, rotating the sample is equivalent to a rotation of the in-plane magnetic field. **Fig. 5.14(c)** is a schematic view of a measuring bar from above showing how the in-

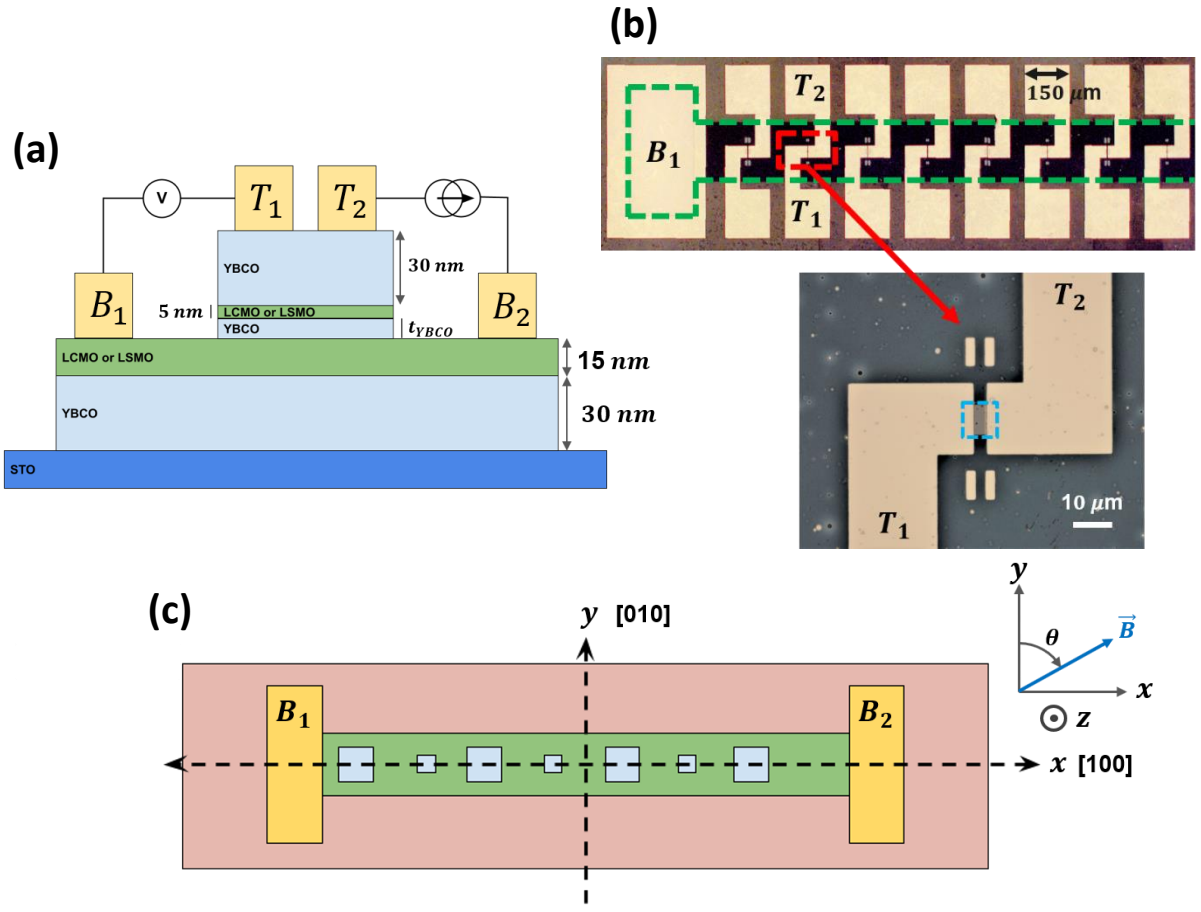

Fig. 5.14: (a) Schematic representation of a typical CPP spin valve and the 4-probe measuring setup. The current is applied between T_2 and B_2 while the voltage is measured between T_1 and B_1. (b) (top) Microscope picture of a sample after the whole fabrication process, showing a measuring bar and a few junctions with their respective gold contacts for the 4-ptobe measurement. The green dashed line represents the shape of the measuring bar as a guide to the eye. (bottom) Close-up of the top part of a spin valve with T_1 and T_2. The blue dashed square represents the top part of the junction ($10 \times 10\ \mu m^2$). (c) Schematic representation of a measuring bar from above. The external magnetic field is applied in plane and can be rotated around the z-axis. θ represents the angle between the y-axis and the direction of the applied field.

plane magnetic field is applied with an angle θ between $\vec{B}$ and the y-axis: $\theta = 0\,°$ corresponds to a magnetic field perpendicular to the bar in the [010] crystallographic direction and $\theta = 90\,°$ corresponds to a magnetic field along the measuring bar in the [100] crystallographic direction. Therefore, $\theta = 45\,°$ coincides with the [110] crystallographic direction.

3. Preliminary characterizations and optimization of the fabrication process

In this section, the results of the transport measurements that were acquired on the spin valves from the first two batches are presented. These two batches were deposited in Madrid by the group of Prof. Santamaria by magnetron sputtering and are made of multi-layered samples STO (001)// YBCO ($30\ nm$)/ LCMO ($15\ nm$)/ spacer (t_{spacer})/ LCMO ($5\ nm$)/ YBCO ($30\ nm$). In batch 1, the spacer is a thin layer of YBCO with a thickness $t_{YBCO} = 3, 5, 7 \text{ or } 10\ nm$ whereas batch 2 is made of three control samples with a spacer layer of PBCO with a thickness $t_{PBCO} = 1, 2 \text{ or } 3\ nm$ (see **Tab. 5.1** for a summary of the various samples). Importantly, no gold layer was deposited on top of the samples before the clean-room patterning of the spin valve structures. As a consequence, the top gold contacts have been deposited as a last microfabrication's step via evaporation, and method 1 was used for the fabrication process.

The electrical and magnetic characterization was carried with an identical method for each spin valve junction, and consists in a set of curves (which can be measured using a 4-probe or a 2-probe configuration) as follows:

(i) Resistance *vs*. temperature $R(T)$ of the bottom YBCO layer.
(ii) Voltage *vs.* current $V(I)$ characteristics of the junction.
(iii) Resistance *vs.* temperature $R(T)$ of the junction.
(iv) Resistance *vs.* magnetic field $R(B)$ magnetoresistance measurements of the junction.

The magneto-transport experiments of SSVs from these two batches, as will be shown later, exhibit very interesting features: the reversal of the SVE from positive to negative while decreasing the temperature and the injected current, as well as a giant enhancement of the switching magnetic fields at low temperatures. However, the measurements also unveiled experimental issues that hindered the reproducibility of the observed phenomena. These problems led to the optimization of the fabrication process that will be applied for the fabrication of subsequent batches (batches 3 and 4).

3.1. Superconducting properties of the bottom YBCO layer

An important preliminary experiment that was systematically performed before the measurements of the SSVs' transport properties consists in an $R(T)$ of the bottom YBCO electrode ($30\ nm$) to verify and quantify its superconducting properties. It also gives important clues regarding the quality of the superconducting phase of the bottom and top YBCO layers (as they share the same thickness of $30\ nm$). The resistance is measured in a 4-probe geometry by injecting a current $I = 1\ \mu A$ between contacts B_1 and B_2 while measuring the voltage between the top contacts of two different junctions (see **Fig. 5.14** for the schematic and microscope pictures). A typical example of such

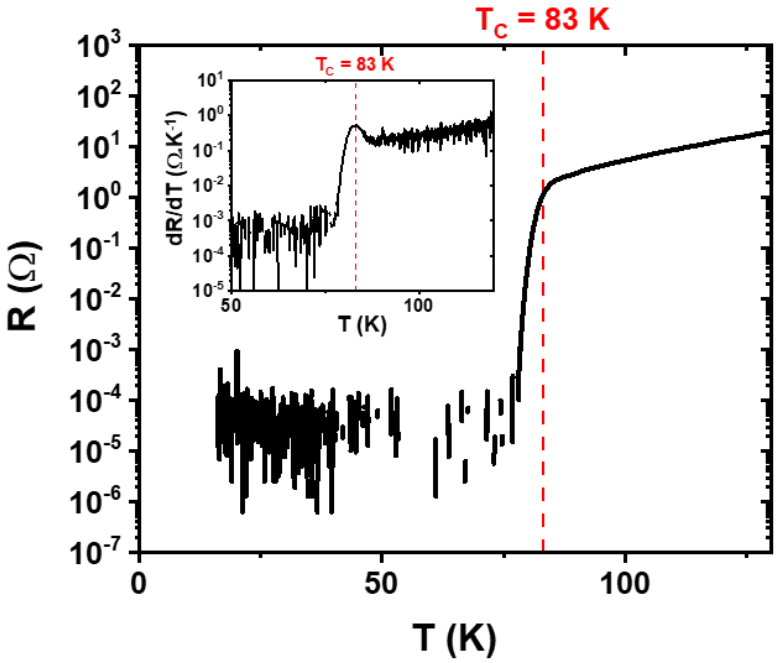

Fig. 5.15: Measurements done on a measuring bar from sample SY1 (batch 1) showing the 4-probe resistance in a semi-log scale of the YBCO bottom layer (30 nm). We can observe a clear superconducting transition arising at about 83 K. T_C was determined by retrieving the abscissa for which the first derivative reaches its maximum, as depicted by the inset.

measurement is given in **Fig. 5.15**, with a clear superconducting transition at $T_C = 83\ K$ below which the resistance abruptly drops to zero (indicated by the noise level). T_C was calculated by performing the first derivative dR/dT of the $R(T)$ and finding the abscissa of the derivative's maximum, as depicted in the inset.

3.2. Magnetic characterization of the superconducting spin valves

3.2.1. Magnetization *vs.* in-plane magnetic field hysteresis loop

A magnetization *vs.* in-plane magnetic field $M(B)$ hysteresis loop was measured prior to the clean-room microfabrication on the unpatterned sample SY4 ($t_{YBCO} = 10\ nm$) from batch 1. The data was acquired with a SQUID magnetometer at $100\ K$ with an in-plane magnetic field along the [100] crystallographic direction [see **Fig. 5.14(c)**]. The result is plotted in **Fig. 5.16(a)**, showing a typical ferromagnetic $M(B)$ loop (see **Chapter 2, Sect. 3.4.**) with saturation for high magnetic field (depicted by the black parallel arrows) and a reversal of the magnetization at low magnetic fields. The negative linear diamagnetic background caused by the STO substrate was subtracted to isolate the signal coming from the LCMO layers. The red curve (blue curve) corresponds to the magnetization measured while sweeping down (sweeping up) the magnetic field and the sweeping directions are indicated by the coloured red and blue arrows. The first derivative dM/dB of the hysteresis loop is displayed in **Fig. 5.16(b)**. One can distinguish two peaks in the derivative (represented by the red and blue vertical dashed lines), corresponding to the coercive fields of the two ferromagnetic layers: $B_C \approx 16\ mT$ for the thicker LCMO layer ($30\ nm$) and $B_C \approx 36\ mT$ for the thinner LCMO layer ($5\ nm$). Although the peak corresponding to $B_C \approx 36\ mT$ is hardly distinguishable, a later similar experiment performed on an unpatterned sample from batch 3 will show a similar behaviour with more clearly defined features

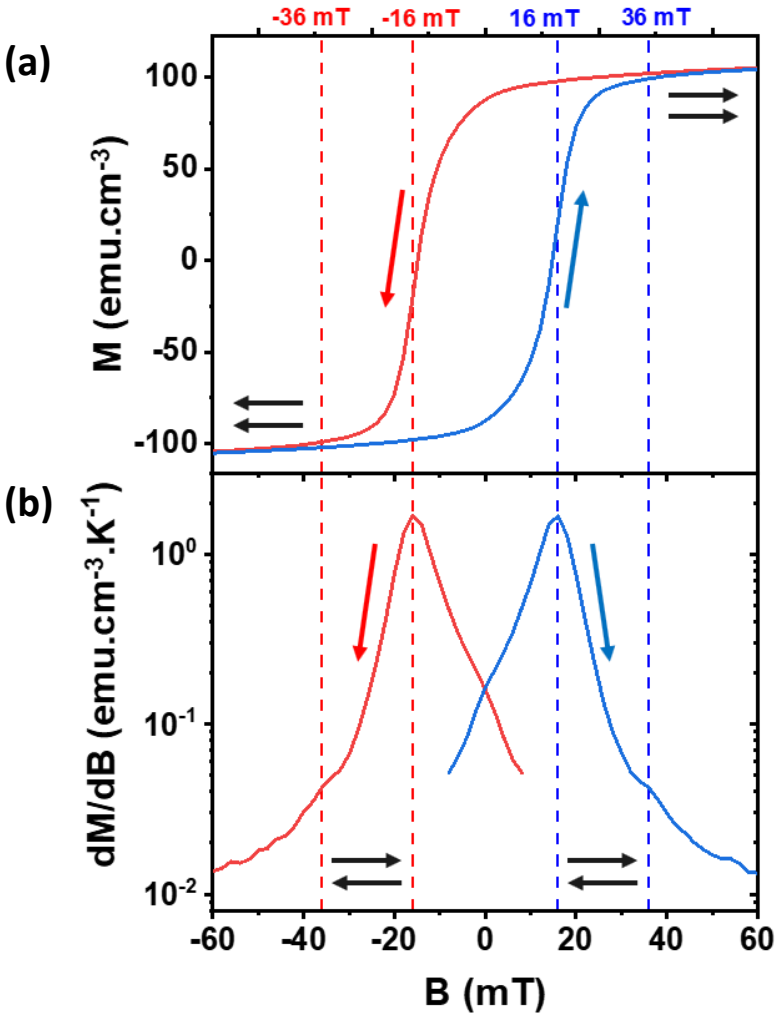

*Fig. 5.16: Measurement done on the unpatterned sample SY1 from batch 1. (a) $M(B)$ hysteresis loop measured at $100\ K$ along the [100] crystallographic direction [see **Fig. 5.14(c)**]. One can observe a typical ferromagnetic behaviour after subtraction of the background induced by the diamagnetic response from the STO substrate. (b) First derivative of the top figure as a function of B. One can distinguish two peaks from the derivative curve, corresponding to the coercive fields of the two ferromagnet: $B_C \approx 16\ mT$ for the thicker LCMO layer and $B_C \approx 36\ mT$ for the thinner LCMO layer.*

(see **Fig. 5.24**). Note that the peak for $B_C \approx 36\ mT$ corresponds to the upper LCMO layer, which is smaller in volume compared to the lower LCMO layer (three times smaller, with a thickness of $5\ nm$ instead of $15\ nm$), which explains the relatively faint signal in the SQUID measurement.

This value of B_C is similar to previously reported values in the litterature [285,317,318]: in 2018, Wang *et al.* [318] reported values of $B_C = 16.1\ mT$ and $B_C = 11.5\ mT$ at $T = 5\ K$ and $T = 100\ K$, respectively, measured on polycrystalline bulk $La_{1-x}Ca_xMnO_3$ $(x = 0.5)$ synthesized via solid-state reaction with a thickness of $10\ nm$. Although the coercive field depends on the doping level, thickness and temperature, LCMO's coercive field is expected to stay within the range of a few mT to a few tens of mT at this temperature.

We can conclude from this experiment that the coercive fields of the two LCMO layers are distinct, which allows to define an AP state [indicated by the black arrows in **Fig. 5.16(b)**] of the spin valve for the range of magnetic fields between the two coercive fields, *i.e.* for $16\ mT < B < 36\ mT$ at $100\ K$.

3.2.2. Magnetoresistance reversal with temperature

An important experiment performed on the spin valves to study their magnetic properties consists in measuring the change of the electrical resistance with respect to an external magnetic field, also called magnetoresistance (MR). For these experiments, an in-plane magnetic field B was applied via an electromagnet, producing fields as high as $B = \pm 1\ T$.

MR in percentage is defined (see **Chapter 3, 6.4.**) as:

$$MR = 100 \times \frac{R_{AP} - R_P}{R_P} = \frac{\Delta R}{R_P} \tag{5.6}$$

with R_{AP} and R_P the resistance of the junction in the anti-parallel and parallel configuration, respectively. Note that MR exhibits the same sign as ΔR (as defined in **Sect. 1.1.**) and therefore the polarity of the SVE can also be assessed from the sign of MR: a positive SVE corresponds to $\mathrm{MR} > 0$ whereas a negative SVE corresponds to $\mathrm{MR} < 0$.

Fig. 5.17 is an example of $R(B)$ plots measured for various currents and temperatures on a SSV from sample SY2 with $t_{YBCO} = 5\ nm$. As was the case for the $M(B)$ hysteresis loops of **Fig. 5.16(a)**, in all the magnetoresistance measurements presented in this chapter, the red curve (blue curve) corresponds to the resistance measured while sweeping down (sweeping up) the magnetic field and the sweeping direction are indicated by the coloured red and blue arrows.

The switching magnetic fields B_S^- and B_S^+ are defined as the value of the magnetic field for which the magnetoresistance reaches an extremum for decreasing magnetic fields and for increasing magnetic fields, respectively (see **Chapter 3, 6.4.**). For example, in the case of **Fig. 5.17(b)**, the switching fields observed are $B_S^- = -0.2\ T$ and $B_S^+ = 0.19\ T$, illustrated by the vertical red and blue dashed lines. The behaviour of the magnetoresistance for different temperatures and currents can be split into three consecutive regimes:

(i) For high temperatures and/or high currents [**Fig. 5.17(a)**], the typical shape of the magnetoresistance is characterized by a linear background with a decreasing R for increasing B, that is a signature of the colossal magnetoresistance (CMR) of the manganite ferromagnets [19–22]. CMR was defined in **Chapter2, Sect. 5.5.3.** The negative and positive switching magnetic fields are $B_S^- = -25\ mT$ and $B_S^+ = 25\ mT$, respectively. These values of $B_S^\pm$ appear to be exactly within the range of magnetic fields that defines the AP configuration as calculated from the $M(B)$ curve in **Fig. 5.17**. This feature highlights the clear relation between $B_S^\pm$ and B_C, although B_C was measured at $100\ K$ in **Fig. 5.16** and the coercive field of a FM is expected to rise at low temperatures [17,319]. The calculated MR was found to be equal to $0.77\ \%$.

(ii) While decreasing the temperature from $50\ K$ to $45\ K$, the magnetoresistance is modified: the background resistance decreases while the switching fields increase by a factor of ten: at this temperature, we observe $B_S^- = -0.2\ T$ and $B_S^+ = 0.19\ T$. The magnetoresistance exhibits maxima at B_S^- and B_S^+ and the background is no longer linear. Moreover, the value of the MR increases from $0.77\ \%$ to $3.41\ \%$.

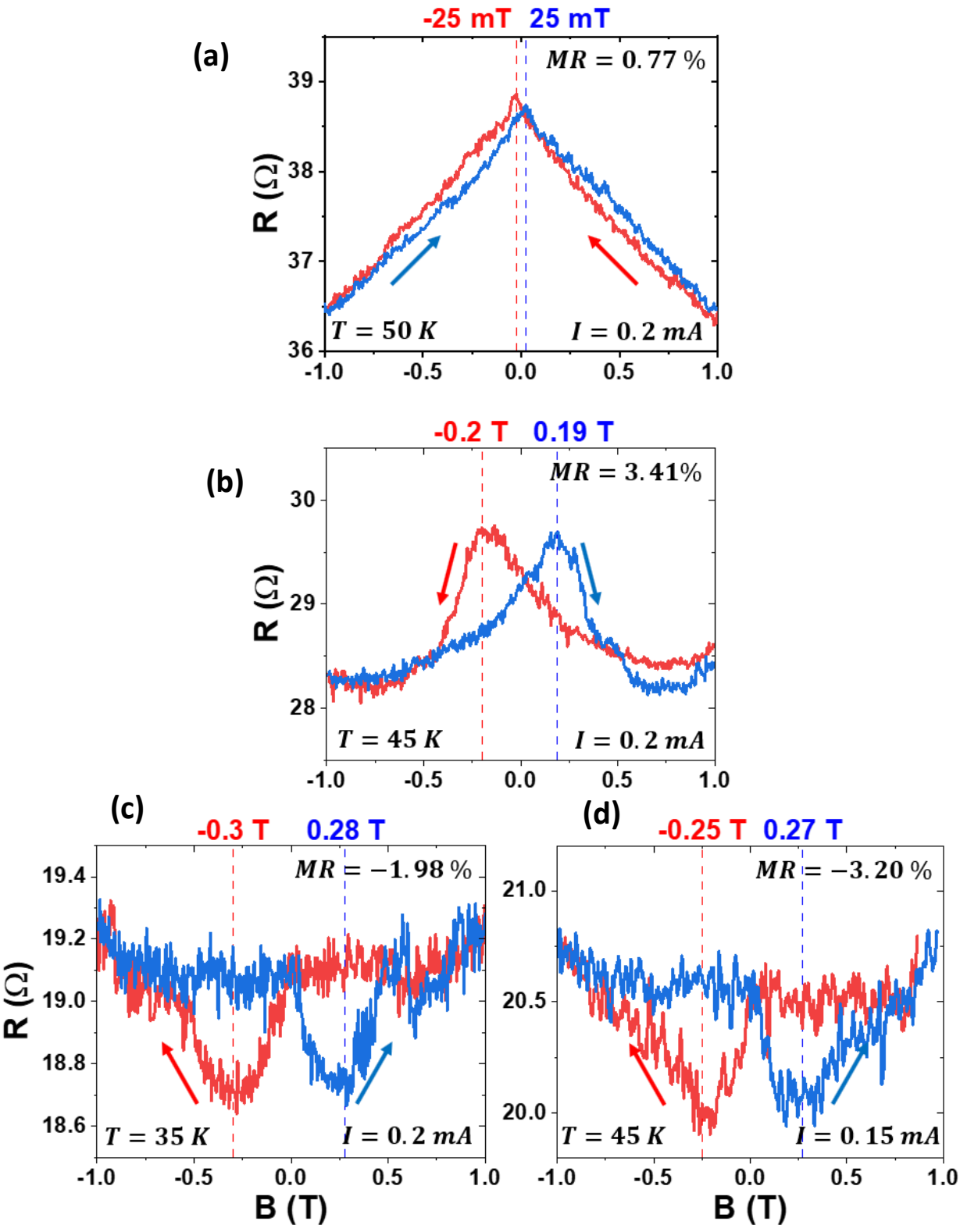

Fig. 5.17: Measurements done on a SSV from sample SY2 with $t_{YBCO} = 5\ nm$ for different sets of temperatures and currents. (a) Magnetoresistance at $50\ K$ for $I = 0.2\ mA$ with a linear background caused by the CMR effect exhibiting a very small positive SVE with $MR \approx 0.8\ \%$. (b) Positive SVE for $T = 45\ K$ and a reading current of $0.2\ mA$, displaying two hysteretic maxima for $B_C^- = -0.2\ T$ and $B_C^+ = 0.19\ T$ as well as a large $MR \approx 3.4\ \%$. The sign of the effect (i.e. the sign of MR) can be reversed from positive to negative either by decreasing (c) the temperature from $45\ K$ to $35\ K$ or (d) the reading current from $0.2\ mA$ to $0.15\ mA$.

(iii) From regime (ii), a reversal of the magnetoresistance features (R is maximum for $B = B_S^-$ and $B = B_S^+$) to negative (R is minimum for $B = B_S^-$ and $B = B_S^+$) is observed by either reducing the temperature while keeping a constant current or reducing the current while keeping a constant temperature. The reversal can be seen from the sign reversal of the MR in percentage, going from $3.41\ \%$ in **Fig. 5.17(b)** to $-1.98\ \%$ and $-3.20\ \%$ in **Fig. 5.17(d)**.

Fig. 5.17 only shows a selected subset of magnetoresistance plots that illustrate the three different regimes observed during the characterizations of the SSVs. In **Annexes, Sect. 2.2.**, all the plots for temperatures ranging from $15\ K$ to $50\ K$ and reading currents of $0.15\ mA$ and $0.2\ mA$ are displayed, and the reader may refer to them for a more complete view of the reversal phenomenon.

3.2.3. Giant enhancement of the resistive switching fields with decreasing temperature

This section focusses on the evolution of $B_S^{\pm}$ for varying temperatures. **Fig. 5.18(a)** shows the behaviour of B_S^+ (B_S^- displays identical behaviours) as a function of the temperature, calculated from the magnetoresistance plots presented in **Annexes, Sect. 2.2.:** the blue points (red points) correspond to B_S^+ calculated while applying $I = 0.15\ mA$ ($I = 0.2\ mA$). The lower coercive field $B_C = 16\ mT$ obtained at $100\ K$ from the $M(B)$ hysteresis loop presented in **Fig. 5.16** is reported in **Fig. 5.18(a)** by a black star for comparison purposes. Moreover, the polarity of the magnetoresistance is also reported in this figure: hollow points refer to $MR > 0$ (positive SVE) whereas full points refer to $MR < 0$ (negative SVE). Strikingly, the abrupt increase of B_S^+, as well as the reversal between positive and negative MR seem to arise for temperatures between $45\ K$ and $50\ K$, illustrated by the black vertical dashed line (for $T = 47\ K$) in **Fig. 5.18(a)**.

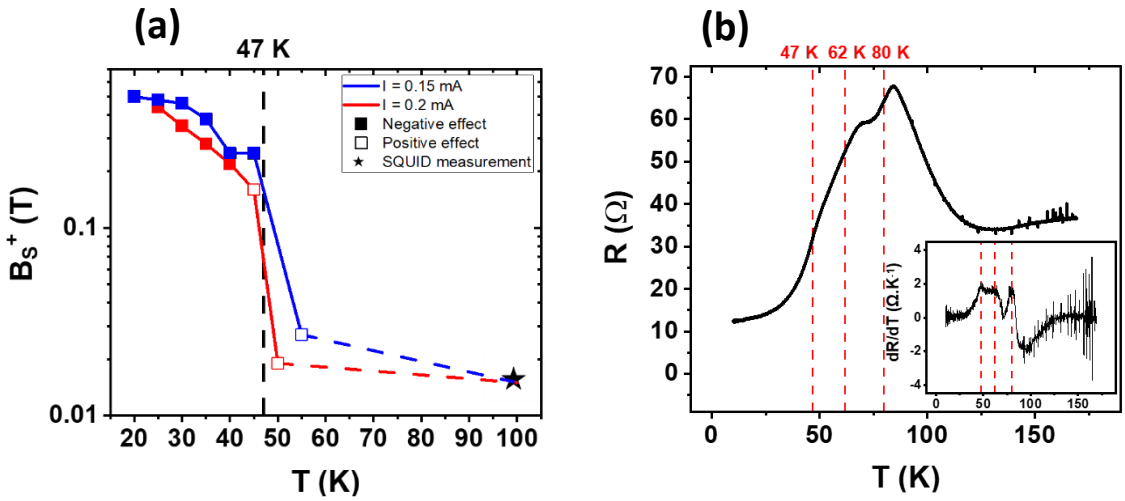

*Fig. 5.18: (a) Evolution of B_S^+ as a function of the temperature for $I = 0.15\ mA$ (blue line) and $I = 0.2\ mA$ (red line). Full points indicate a negative MR, whereas hollow points correspond to positive MR. The final point (depicted via a black star) corresponds to the lower value of $B_C = 16\ mT$ obtained via the SQUID measurement at $100\ K$ (**Fig. 5.16**) for comparison purposes. The vertical dashed line for $T = 47\ K$ corresponds to the lower T_C calculated from the $R(T)$ of **Fig. 5.18(b)**. (b) $R(T)$ of the junction for $I = 0.2\ mA$. The inset shows the first derivative as a function of the temperature, exhibiting three peaks that probably correspond to the three consecutive superconducting transitions. The lowest one ($T_C \approx 47\ K$) should correspond to T_C of the YBCO spacer.*

The 4-probe resistance as a function of temperature measured on the same SSV is plotted in **Fig. 5.18(b)** for a reading current of $0.2\ mA$. The first derivative $^{dR}/_{dT}$ is depicted in the inset and exhibits three distinct peaks, likely corresponding to the critical temperatures of the three distinct YBCO layers. The lowest T_C corresponds to the thinnest YBCO layer (in this case, the YBCO spacer with $t_{YBCO} = 5\ nm$) and is equal to $T_C \approx 47\ K$. This value corresponds to the onset temperature observed in **Fig. 5.18(a)** for the polarity reversal as well as the abrupt enhancement of the switching fields. Therefore, it seems that the superconducting properties of the spacer plays a crucial role in the appearance of the magnetoresistance reversal and the giant enhancement of the switching fields.

Note that the magnetoresistance curve of **Fig. 5.17(a)** at $T = 50\ K$ indicates that the resistive switching fields and the coercive fields of the two LCMO layers are closely related. This is indicated, as was already mentioned, by the fact that $B_S^{\pm}$ appears to be exactly within the range of magnetic fields between the coercive fields of the LCMO layers, *i.e.* in the AP configuration. However, the value of $B_S^{\pm}$ observed at low-temperatures and as high as $\sim 0.5\ T$ are more than one order of magnitude above the expected coercive field of LCMO for this temperature [318]. This giant enhancement is also observed in the magneto-transport experiments of the control samples, as discussed in the next section.

3.3. Control samples with an insulating PBCO spacer

3.3.1. Superconducting and tunnelling-like behaviours

Control samples with a non-superconducting PBCO spacer were fabricated following the exact same deposition recipe and fabrication process as the previous samples from batch 1. A preliminary $R(T)$ measurement of the superconducting bottom layer exhibits a clear normal-to-superconductor transition with $T_C = 64\ K$ [**Fig. 5.19(a)**]. **Fig. 5.19(b)** shows the typical shape of the I-V characteristics obtained while measuring spin valve structures from batch 2 in a 4-probe configuration. The I-Vs display a tunnelling-like behaviour, with resistances ranging between approximately $0.6\ M\Omega$ and $14\ M\Omega$, as can be seen from **Fig. 5.19(c),** which shows the resistance vs. current of the spin valve calculated from the I-V curves in semi-log scale. We can observe that a temperature-dependent voltage threshold is required to generate a sizable current within the junction, and this threshold varies from $\sim 22\ mV$ at $15\ K$ to $\sim 18\ mV$ at $90\ K$. The decrease of the voltage threshold with temperature is expected, as for higher temperatures, the thermal energy complements the electrical energy, leading to a lower voltage required to overcome the electron tunnelling barrier.

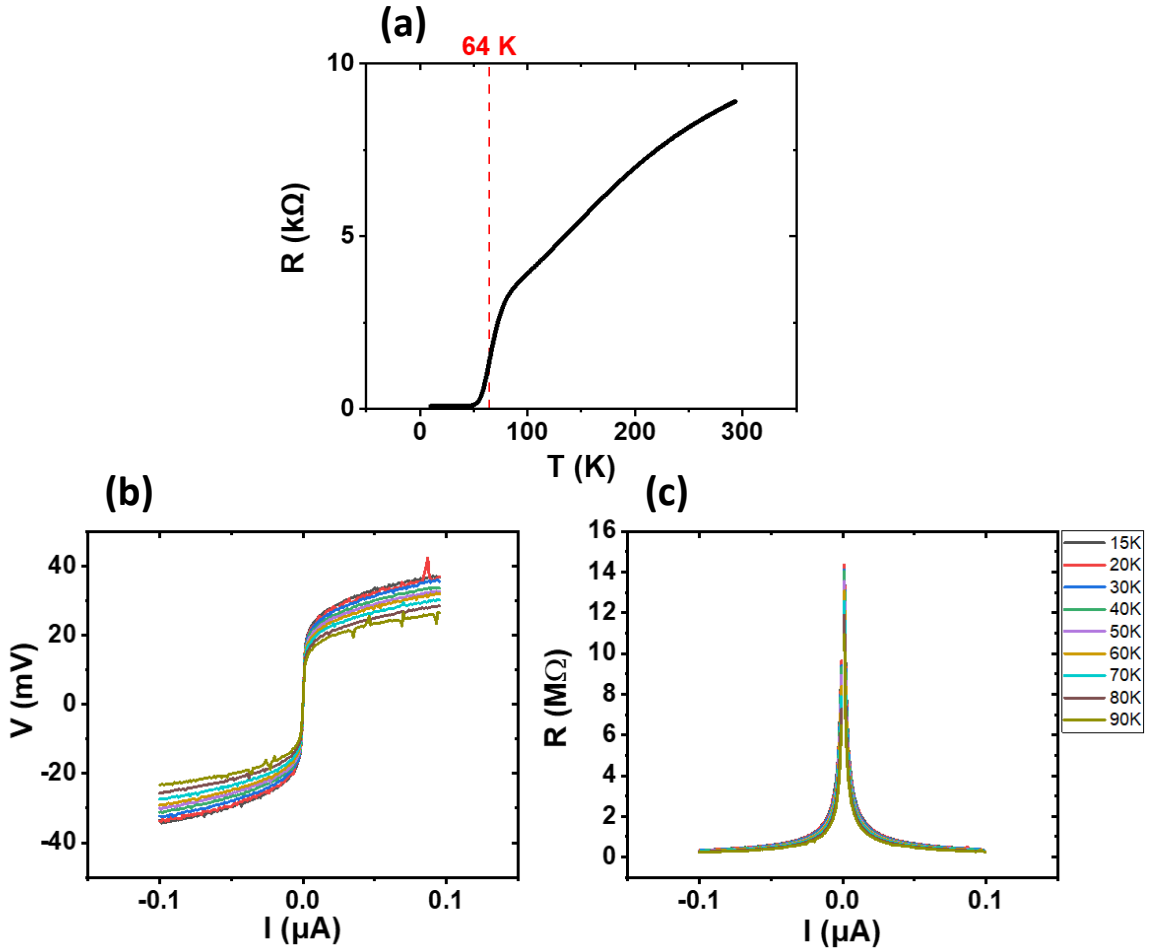

*Fig. 5.19: Measurements performed on a control spin valve from sample SP2 with $t_{PBCO} = 2\ nm$. (a) 2-probe R(T) of the superconducting bottom YBCO electrode ($30\ nm$) measured with $I = 1\ \mu A$ exhibiting a clear superconducting transition centred at $T_C \approx 64\ K$. (b) I-V characteristics for different temperatures showing a tunnelling-like behaviour. (c) $R(I)$ curves corresponding to the same set of data as in **Fig. 5.19(b)**.*

3.3.2. Tunnel magnetoresistance experiments

Magnetoresistance experiments similar to the ones described in the case of SSVs from batch 1 in **Sect. 3.2.2.** were performed on the control junctions and are displayed in **Fig. 5.20** for $T = 55, 65$ and $100\ K$. Note that in the case $T = 100\ K$, the magnetoresistance is plotted for $-1\ T < B < 1\ T$. This larger range allows to show the behaviour of the $R(B)$ background, which is also representative of the backgrounds at $T = 55\ K$ and $T = 65\ K$, although for these two temperatures only a close-up for low magnetic fields are displayed. In particular, the magnetoresistances of **Fig. 5.20(a)** and **Fig. 5.20(b)** exhibit a clear switching between two resistive levels with $\Delta R > 0$ (positive SVE) for different ranges of magnetic fields. For the sake of argument and discussion, these ranges of magnetic fields are supposed to correspond to the AP states of the spin valve, as indicated by the black arrows. Considering this hypothesis and taking the example of **Fig. 5.20(a)**, the magnetoresistance experiment can be split into four consecutive regimes:

(i) $\mathbf{+0.2\ T \rightarrow 0\ T}$**, red curve:** starting at a high value of the magnetic field ensures that both FMs are saturated and in a P configuration, indicated by the two parallel black arrows.

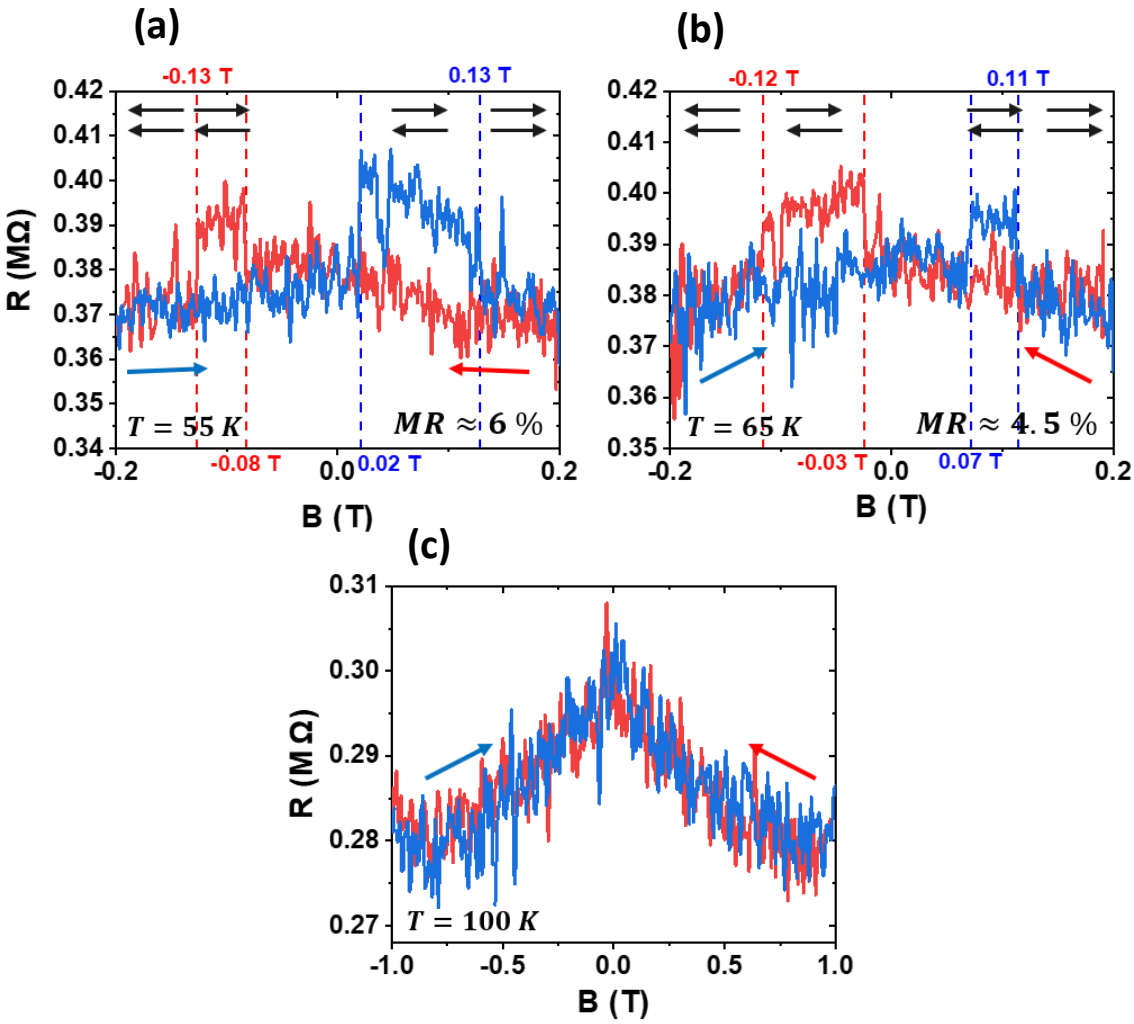

Fig. 5.20: Measurements done on a control spin valve from sample SP1 with $t_{PBCO} = 3\ nm$. The 4-probe magnetoresistance was measured with a current of $0.75\ \mu A$ for three different temperatures: (a) $55\ K$, (b) $65\ K$ and (c) $100\ K$. For (a) and (b), the curves exhibit a positive SVE ($MR > 0$) that disappears as the temperature increases. For the sake of argument and discussion, the black arrows represent the expected P and AP configurations of the spin valve for different ranges of magnetic fields.

While decreasing the magnetic field to $0\ T$, the resistance increases linearly (manifestation of the colossal magnetoresistance, as discussed in **Sect. 3.2.2.**) but does not switch as the magnetizations stay parallel.

(ii) $\mathbf{0\ T \rightarrow -0.2\ T}$**, red curve:** when the magnetic field is applied in the opposite direction, assuming that both FMs exhibit different B_C, one of the FMs' magnetization reverses first at $B_{C1} = -0.08\ T$, leading to the appearance of an AP state. This AP state is characterized by a higher value of the resistance and is depicted by the anti-parallel black arrows in **Fig. 5.20(a)**. While further increasing (in absolute values) the magnetic field, the spin valve will switch to a new P state at $B_{C2} = -0.13\ T$, yielding a decrease of the resistance.

(iii) $\mathbf{-0.2\ T \rightarrow 0\ T}$**, blue curve:** similar to regime (i), the junction is in a new stable P configuration as the magnetic field goes back to $0\ T$.

(iv) $\mathbf{0\ T \rightarrow +0.2\ T}$**, blue curve:** as the magnetic field becomes positive again, the switching between the low-resistive state and the high resistive state in the AP configuration is visible once more for $0.02\ T < B < 0.13\ T$.

The MR (**Eq. 5.6**) calculated from the magnetoresistance curve of **Fig. 5.20(a)** yields the value of $MR \approx 6\,\%$. As the temperature increases to $65\,K$, the positive SVE is still observed in **Fig. 5.20(b)**, but the MR decreases to $\sim 4\,\%$. Finally, for temperatures above $100\,K$, no spin valve behaviour was observed. The decrease of the relative magnetoresistance for increasing temperatures is as expected from previous studies on the GMR [320] and TMR [321,322] effects of spin valve structures made of various ferromagnets. In particular, Yoo *et al.* [321] investigated the temperature dependence of GMR in spin valve devices made of LSMO and an organic-based ferromagnet and attributed the decrease of the MR to the lowering of the surface spin polarization of the LSMO films with increasing temperatures.

Two main features are important to highlight in the experiments of this section:

(i) The control samples do not exhibit any signatures of a negative SVE, supporting the conclusion of the previous section: the superconducting nature of the spin valve's spacer is crucial to observe the reversal from positive to negative SVEs with decreasing temperatures and currents.

(ii) The coercive fields observed in **Fig. 5.20(a)** and **Fig. 5.20(b)** are much larger than the expected B_C of the LCMO ferromagnetic layers for these temperatures. This feature is reminiscent of the giant enhancement of B_S^+ observed in the SSV from batch 1 [see **Fig. 5.18(a)**] and will be addressed in the discussion section later in this chapter (**Sect. 5.**).

3.4. Spurious effects in the transport experiments

3.4.1. Current-voltage characteristics and resistance *vs.* temperature

Typical transport measurements that were performed on the SSVs with a YBCO spacer from batch 1 include I-V characteristics as well as $R(T)$ measurements in 4-probe and 2-probe configurations. Out of all the measured SSVs from this batch, two distinct behaviours for the I-V characteristics stand out:

- **Tunnelling-like behaviour [Fig. 5.21(a)]:** Many junctions showed a tunnelling-like behaviour, with characteristics similar to the ones presented in the main panel of **Fig. 5.21(a)**, measured in a 2-probe configuration. The typical resistances of such junctions were of the order of a few tens of $M\Omega$ at $40\,K$, as can be seen from the inset. These measurements indicate that the contact resistances between the top YBCO electrode and the gold contacts [T_1 and T_2 in **Fig. 5.14(a)**] deposited by sputtering are very high (in the $M\Omega$ range) and can prevent the measurement of the superconducting properties of the junction.
- **Superconducting behaviour [Fig. 5.21(b)]:** Another typical shape of the I-V characteristics (measured in 4-probe) that was observed while measuring junctions from batch 1 is displayed in **Fig. 5.21(b)**. Superconducting-like features can be seen, characterized by a current range in which the measured voltage is significantly lower. Notice however that the low-current resistance is not zero, as expected for a truly superconducting behaviour. Instead, we can observe a small "negative" ohmic resistance of $R = -6.25\,\Omega$ (pointed out by the dashed line). This low-dissipation regime appears below the effective critical current I_C^* (see the definition in **Chapter 3, Sect. 6.3.)** that increases with decreasing temperatures, similarly as expected for the critical current I_C of a superconductor. This is shown in the inset of **Fig. 5.21(b)**, which shows $I_C^*(T)$, calculated by retrieving the first value of the current for which the voltage is higher than $1\,mV$ after subtraction of the negative

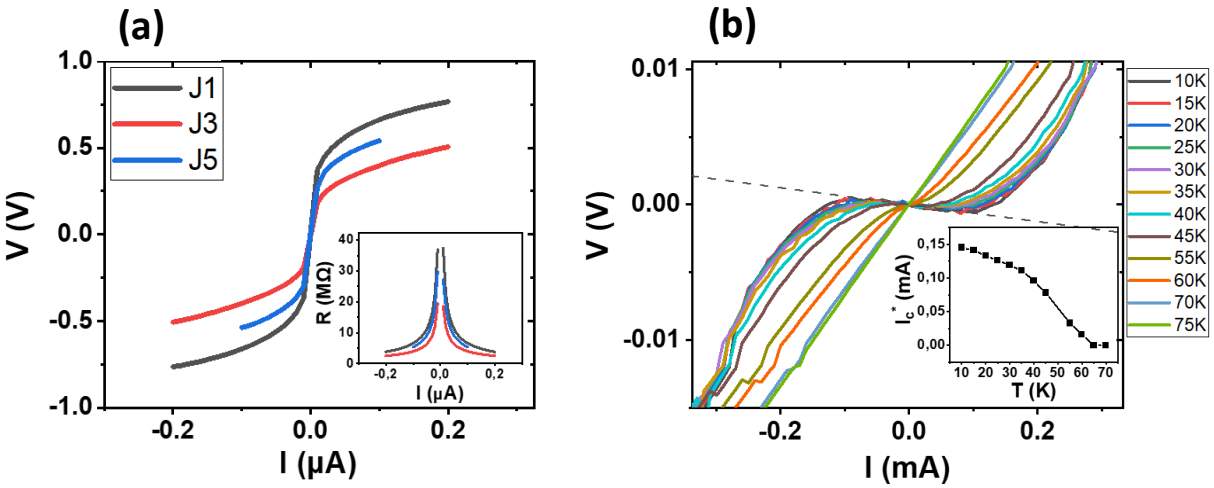

Fig. 5.21: I-V characteristics measured on SSVs from batch 1. Two typical behaviours stand out: (a) Tunnelling-like behaviour at $40\ K$ for three distinct junctions from sample PY3 with $t_{YBCO} = 7\ nm$ in a 2-probe configuration. The inset displays the resistance as a function of the current for the same set of data and junctions. (b) I-V curves of a junction from sample SY2 with $t_{YBCO} = 5\ nm$ for $10\ K < T < 75\ K$ showing a superconducting-like behaviour with $I_C^* = 0.15\ mA$ at $10\ K$, reducing to $0\ mA$ for $T > 65\ K$, as shown by the inset. I_C^* was calculated by taking the first value of the current for which the measured voltage is higher than $1\ mV$ after correction of the negative resistance background. For temperatures above $65\ K$, the I-V curves become perfectly ohmic. The black dashed line represents the linear negative slope observed for low current bias and low temperatures.

background. I_C^* monotonically decreases until completely disappearing for $T > 65\ K$. In summary, these junctions' I-V curves show features reminiscent of superconducting behaviours but, instead of a zero-resistance state for low currents, often a negative ohmic resistance is found. This negative resistance also appeared randomly in other transport measurements of SSVs from batches 1 and 2 [such as in $R(T)$ measurements] and points towards a fabrication problem that reduces the number of exploitable devices and eventually led to the modification of the fabrication steps for the fabrication of batches 3 and 4.

3.4.2. Negative resistance: high contact resistances and conducting substrate

The spin valves studied in this section displayed interesting and promising features, namely:

(i) A magnetoresistance reversal arising while decreasing the temperature and the injected current (see **Fig. 5.17**). This feature was not observed on the control samples with a non-superconducting spacer and arises below the T_C of the YBCO spacer (**Fig. 5.18**), pointing toward a mechanism that is governed by the superconducting properties of the spacer.

(ii) A giant enhancement of $B_S^{\pm}$ at low-temperatures (**Fig. 5.18** and **Fig. 5.20**), seen both in the magneto-transport measurements of the spin valves from batch 1 and batch 2.

However, the negative resistances found in the transport measurements of most junctions at low injected currents and low temperatures [see **Fig. 5.21(b)**] are a major hindrance for the understanding and reproducibility of the measurements presented above. The origin of the negative resistances is attributed to two concomitant causes:

- Upon etching the STO layer during step 2 of the fabrication process [**Fig. 5.12(b)**], it is possible that the substrate becomes conducting rather than insulating, via charge carrier doping [323]. As a consequence, it is likely that the measuring bars are shorted and that

the current is flowing through the substrate rather than inside the vertical junctions at high temperatures.

- As hinted by **Fig. 5.21(a)**, the contact resistance between the top YBCO layer and the gold contacts deposited via evaporation as a last technological step after processing the vertical junctions is of the order of a few tens of $M\Omega$, greatly altering the 4-probe measurements of the junctions and sometimes leading to tunnelling effects.

Combining these two conditions can lead the current to flow in the substrate or in the spin valve depending on the relative resistances of the two channels at a given temperature. At very low temperatures, it is expected that the superconducting electrodes have turned completely superconducting, and the current must be flowing for the most part through the junctions and through the measuring bar due to very low resistances. At higher temperatures, the current might redistribute through multiple parallel channels. Moreover, while contacting the samples and junctions with gold wires on the deported contacts [see **Fig. 5.14(b)**], the wires might contact the STO substrate through the permanently baked S1805 resist layer (the thickness of the resist layer is expected to be less than $0.5\ \mu m$ after a spin coating at 4000 rotation-per-minute for 30 seconds [324], due to the prior 1:1 dilution of the resist). Consequently, the redistribution of the current between the substrate and the spin valve structure can lead to negative resistances.

To circumvent these fabrication issues, multiple changes were brought to the fabrication process, yielding the optimal fabrication process (method 2) as described previously in **Sect. 2.1.** and in **Annexes, Sect. 2.1.** First, more attention is required during step 2 of the fabrication process to prevent the STO layer to become conducting upon etching; the etching needs to be stopped immediately as the titanium signal starts to rise in the SIMS' signal. Second, one can deposit a gold capping layer on top of the upper YBCO layer prior to the clean-room patterning to help reduce to a minimum the contact resistance between Au and YBCO. In fact, the surface of the top YBCO electrode can be damaged from the consecutive developing steps during the fabrication process (following method 1) and adding a capping layer help reduce the degradation to a minimum.

4. Study of the superconducting spin valve effects

Batches 3 and 4 have been prepared following method 2 as described in **Fig. 5.12**. The key difference with batches 1 and 2 is that an Au capping was deposited on the top YBCO layer prior to the patterning process of the SSVs. In particular, in the case of batch 3, a gold capping layer of $30\ nm$ was deposited *ex-situ* with magnetron sputtering, whereas in the case of batch 4, it was deposited *in-situ* with PLD. In the following paragraphs, samples from batch 3 will be referred as "*ex-situ* samples" while samples from batch 4 will be referred as "*in-situ* samples" for clarity. In all cases, the multilayers STO// YBCO ($30\ nm$)/ LSMO ($15\ nm$)/ YBCO (t_{YBCO})/ LSMO ($5\ nm$)/ YBCO ($30\ nm$) were deposited by PLD at the UMR CNRS/Thales laboratory with deposition parameters as described in **Chapter 3, Sect. 1.** Note in particular that LSMO was used in these batches instead of LCMO, at contrary to the SSVs studied in the previous sections.

4.1. Superconducting properties of the bottom YBCO layer

As was stated before, a preliminary measurement that was carried before the magneto-transport experiments of the SSVs is an $R(T)$ of the bottom YBCO layer to study its superconducting properties. The result of this experiment, carried on a measuring bar from sample REAL5 ($t_{YBCO} = 8\,nm$) with $I = 1\,\mu A$, is shown in **Fig. 5.22** and displays a clear superconducting transition at $T = 61\,K$, measured from the first derivative method as plotted in the inset. The typical T_C of the bottom YBCO electrode measured on bars from batches 3 and 4 was typically found to be between $50\,K$ and $60\,K$.

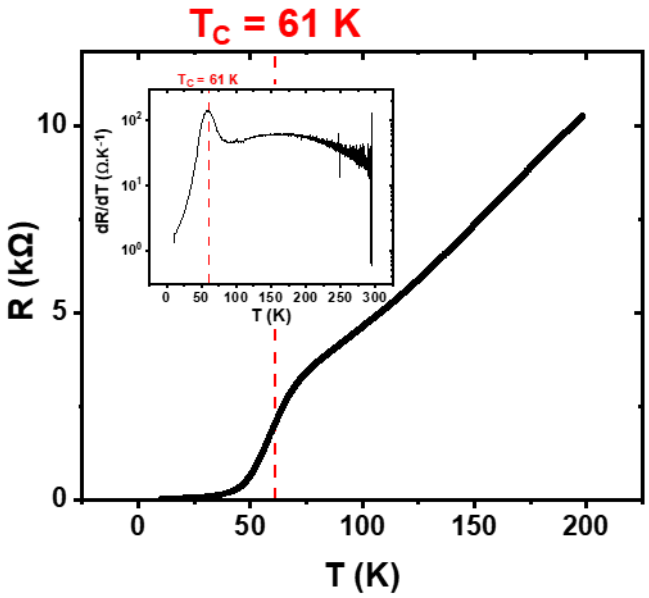

Fig. 5.22: 2-probe $R(T)$ of a measuring bar from the in-situ sample REAL5 ($t_{YBCO} = 8\,nm$) with $I = 1\,\mu A$ with a clear superconducting transition at $T = 61\,K$ calculated via the first derivative method, as illustrated in the inset.

4.2. Resistance *vs.* temperature and current-voltage characteristics of the superconducting spin valves

The typical results of the 4-probe I-V characteristics measurements for SSVs from the *in-situ* samples of batch 4 are displayed in **Fig. 5.23(a)** for temperatures between $10\,K$ and $60\,K$, showing evident superconducting features characterized by a vanishing resistance for $|I| < |I_C|$, with $I_C(T)$ plotted in the inset of **Fig. 5.23(a)**. I_C is defined in this experiment by calculating the second derivative of the I-V curve and retrieving the abscissas of the extrema, and an example of such calculation is given in **Chapter 3, Sect. 6.3.** The superconducting features and the superconducting-to-normal transition are further illustrated by the evolution of the differential resistance $dR = dV/dI$ in log-log scale as a function of the current calculated from **Fig. 5.23(a)** and showed in **Fig. 5.23(b)**. One can see that the resistance varies on more than two orders of magnitude for a fixed current of $10\,\mu A$ (vertical dashed line), increasing from $\sim 0.25\,\Omega$ at $T = 10\,K$ to $\sim 48\,\Omega$ at $T = 60\,K$. All of these observations are consistent with the measured 4-probe $R(T)$ [**Fig. 5.23(c)**], showing a clear $T_C \approx 49\,K$, calculated via the first derivative method, as shown in the inset of **Fig. 5.23(c)**. Note that the negative resistances that were observed at low currents and low temperatures in the I-V characteristics of the previous two

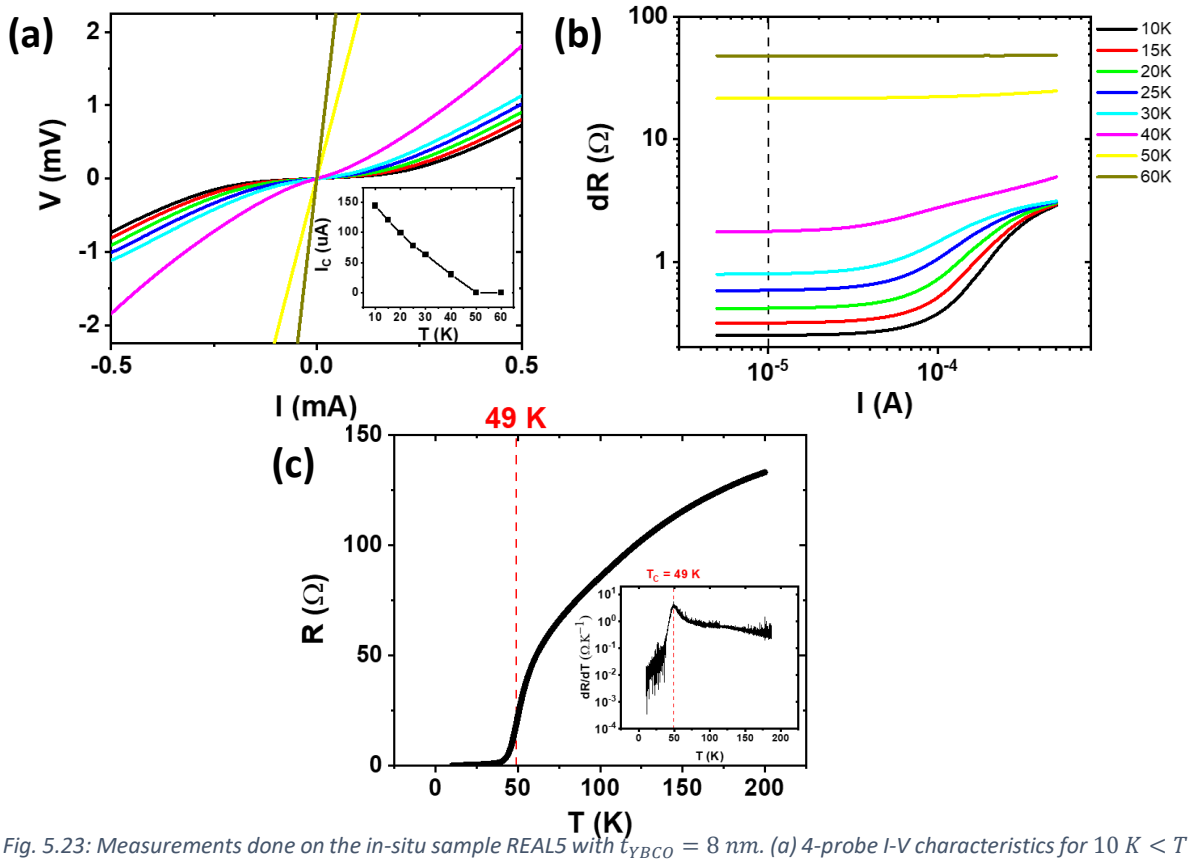

*Fig. 5.23: Measurements done on the in-situ sample REAL5 with $t_{YBCO} = 8\ nm$. (a) 4-probe I-V characteristics for $10\ K < T < 60\ K$. The curves display clear superconducting features, with a I_C decreasing from $\sim 150\ \mu A$ to 0 between $10\ K$ and $50\ K$, as displayed by the inset figure. (b) $dR(I)$ in log-log scale calculated from **Fig. 5.23(a)**. The superconducting features disappear for temperatures above $50\ K$. (c) 4-probe $R(T)$ of the same junction showing a clear superconducting transition at $T_C = 49\ K$, calculated by the first derivative method as illustrated by the inset.*

batches [see **Fig. 5.21(b)**] are not observed after modification of the fabrication process, yielding much more reliable and reproducible results.

4.3. Magnetic characterization of the superconducting spin valves

In this paragraph, the results of the magneto-transport characterisation of the SSV junctions from batches 3 and 4 are presented, exhibiting a reproducible and reversible crossover between positive and negative SVEs while reducing the temperature, reminiscent of the MR reversal that was observed on the SSVs from batch 1 (see **Fig. 5.17**).

4.3.1. Magnetization vs. in-plane magnetic field hysteresis loops

Prior to the clean-room patterning of the SSVs , $M(B)$ hysteresis loops were measured with a SQUID magnetometer at $100\ K$ [**Fig. 5.24(a)**, top panel] and $15\ K$ [**Fig. 5.24(b)**, top panel] on the *ex-situ* sample REAL3 with $t_{YBCO} = 8\ nm$ for an in-plane magnetic field. The negative linear background induced by the diamagnetic response of the STO substrate is subtracted from the data to isolate the

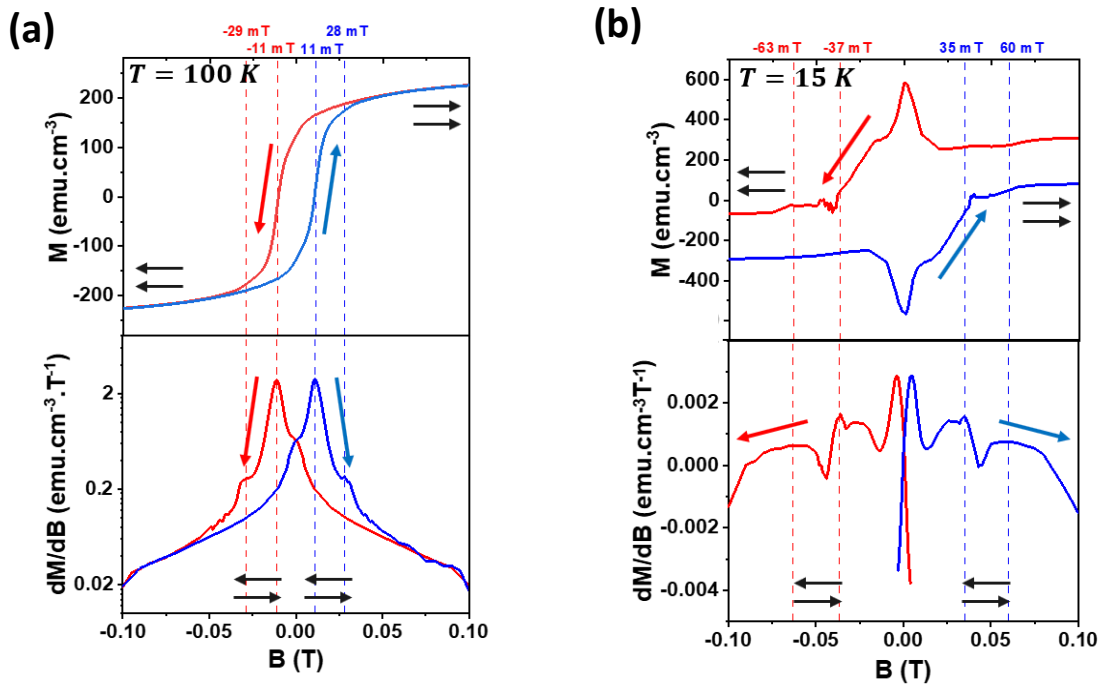

Fig. 5.24: Measurements done on the unpatterned ex-situ sample REAL3 from batch 3 with $t_{YBCO} = 8\ nm$. (a) (top) $M(B)$ at $100\ K$ along the [100] direction after subtraction of the background caused by the diamagnetic response of the STO substrate, showing a clear hysteretic behaviour between descending (red line) and ascending (blue line) sweeping directions. (bottom) first derivative of the top figure as a function of B. The two peaks correspond to the coercive fields of the two FMs: $B_C \approx 11\ mT$ for the thicker LSMO layer and $B_C \approx 28\ mT$ for the thinner LSMO layer. (b) Identical set of measurements for $T = 15\ K$ after cooling from $100\ K$ to $15\ K$ in a $10\ T$ field cooled chamber. (top) M exhibits a strong superconducting background characterized by the peaks at low fields corresponding to the lower critical field of YBCO at around $H_{c1} \approx \pm 3\ mT$. (bottom) first derivative of the magnetization as a function of B. Once more, B_C can be estimated from the apparent peaks in the derivative, showing enhanced values compared to the ones obtained at $100\ K$.

magnetic response of the SSV. The magnetic field was applied along the [100] crystallographic direction corresponding to the expected hard axis of the LSMO ferromagnetic layers [325,326].

At $100\ K$, above the T_C of YBCO, the hysteretic behaviour is typical of ferromagnetic systems [25]. By taking the first derivative of the $M(B)$ curve [**Fig. 5.24(a)**, bottom panel] we observe two distinct peaks, corresponding to the switching of both ferromagnetic layers independently, caused by their different thicknesses [17,18]. The values of the coercive fields are consistent with previously measured coercive fields for LSMO thin films [17,319], and the thinnest LSMO layer is expected to have a greater coercive field. Therefore, the thinner LSMO layer ($5\ nm$) exhibits a coercive field of $B_C \approx 28\ mT$, while for the thicker LSMO layer ($15\ nm$), we observe $B_C \approx 11\ mT$. We can thus conclude that the range of magnetic fields $11\ mT < B < 28\ mT$ between both coercive fields corresponds to the magnetic state closest to a fully AP alignment of the magnetizations at this temperature.

At $15\ K$, well below the superconducting transition, the $M(B)$ curve displays signatures of both ferromagnetism and superconductivity [**Fig. 5.24(b)**, top panel]. The superconducting features appear stronger for low values of B, exhibiting a pronounced peak for $B = \pm 3\ mT$. This field corresponds to the lower critical field H_{c1} of YBCO and corresponds to the onset magnetic field for the appearance of vortices [26]. Importantly, the $M(B)$ hysteresis loop at $15\ K$ was measured after cooling the SQUID magnetometer from $100\ K$ to $15\ K$ with an applied magnetic field of $B = -10\ T$. Therefore, field trapping can have an impact on the shape of the $M(B)$ curve [327] but should not affect the global conclusions that one can deduct from the figure. A fitting of the $M(B)$ hysteresis curve of **Fig. 5.24(b)** is given in **Annexes, Sect. 2.3.** by considering that the magnetization is equal to the sum of

ferromagnetic and superconducting contributions, yielding a rough approximation of the unusual shape of the magnetization. The values of the coercive fields deduced from the first derivative [**Fig. 5.24(b)**, bottom panel] are enhanced compared to the values at $100\ K$: $B_C \approx 61\ mT$ for the $15\ nm$-thick LSMO layer and $B_C \approx 36\ mT$ for the $5\ nm$-thick LSMO layer.

We can conclude from this experiment that the coercive fields for the two LSMO layers are different, allowing for an AP configuration of the SSV to arise for a magnetic field within the range between both coercive fields, *i.e.* $11\ mT < B < 28\ mT$ at $T = 100\ K$ and $37\ mT < B < 63\ mT$ at $T = 15\ K$.

4.3.2. Magnetic properties for temperatures above T_C

MR measurements (using a 4-probe configuration) were carried for a temperature above T_C to study the magnetic properties of the SSVs in the absence of superconductivity. **Fig. 5.25(a)** shows the MR at $T = 120\ K$ for two different angles of the in-plane magnetic field: $\theta = 45\ °$ [**Fig. 5.25(a)**, left] and $\theta = 90\ °$ [**Fig. 5.25(a)**, right]. The shape of the curves is reminiscent of the one of the already discussed MR of the SSVs from batch 1 for high temperatures in **Fig. 5.17(a)**: the linear background is a consequence of the colossal magnetoresistance of the LSMO layers. B_S^- and B_S^+ are reported in the figure through the red and blue vertical dashed lines and one can observe an increase of the switching fields while varying θ from $45\ °$ to $90\ °$. This property is more accurately illustrated by the 2d-colorplot of the normalized resistance displayed in **Fig. 5.25(b)** as a function of θ (y-axis) and B (x-axis). The linear CMR background was subtracted to allow for a direct comparison of the hysteretic features. Then, the resistance was normalized between -1 and 1 via the relation:

$$R_N = \frac{2(R - R_{min})}{R_{max} - R_{min}} - 1 \qquad (5.7)$$

where R_{max} and R_{min} represent the maximum and minimum resistances measured during the magnetoresistance experiments.

Furthermore, the values of $B_S^{\pm}$ are calculated from the magnetoresistance curves and plotted in **Fig. 5.25(c)** in the form of a 2d-polar plot to follow the evolution of B_S^+ and $|B_S^-|$ as a function of θ. The easy axes of the LSMO layers $\theta = 45\ °, \theta = 135\ °, \theta = 225\ °$ and $\theta = 315\ °$ are reported in **Fig. 5.25(c)** as black dotted lines, as expected from various studies in the literature on LSMO and LCMO thin films, measured through ferromagnetic resonance experiments [325,326]. It is clear that the minima of $|B_S^-|$ and B_S^+ correlate with the easy axes while the maxima are aligned with the expected hard axes. The magnetoresistance is expected to switch for a lower magnetic field while applying $\vec{B}$ along the easy axis compared to the hard axis. The domains of YBCO/LSMO bilayers have been shown to exhibit a filamentary structure along the easy axis (that is, along the [110] crystallographic direction) as was illustrated in **Chapter 2, Sect. 3.5.5.** [19]**.** Consequently, reversing the magnetization of the ferromagnets while applying a magnetic field along the hard axis requires a rotation of the magnetic domains' magnetizations, which in turn leads to higher switching fields.

Finally, one can observe an asymmetric behaviour $|B_S^-| > B_S^+$ with a constant difference $|B_S^-| - B_S^+ \approx 6\ mT$ for all angles. This feature is reminiscent of exchange bias mechanisms that can lead to a shift of the $M(B)$ magnetization hysteresis loops, yielding a similar asymmetry of the magnetic

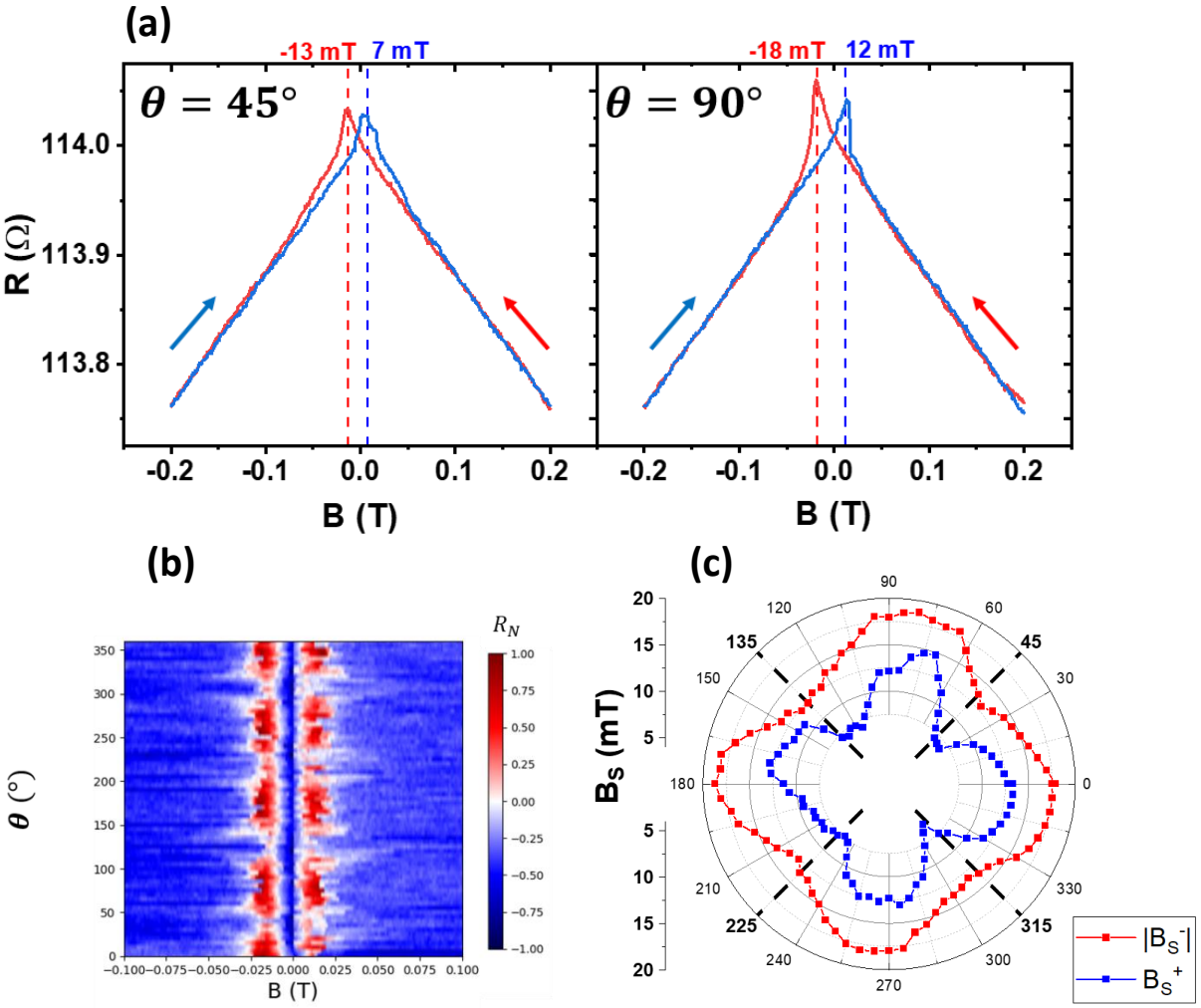

Fig. 5.25: Measurements done on the in-situ sample REAL5 with $t_{YBCO} = 8\ nm$. (a) 4-probe magnetoresistance for an in-plane magnetic field $-0.2\ T < B < 0.2\ T$ for: (left) $\theta = 45\ °$ and (right) $\theta = 90\ °$. The linear background is a signature of the CMR effect of the manganites. (b) 2d-colorplot of the normalized 4-probe resistance (z-axis) as a function of θ (y-axis) and B (x-axis). The linear background was subtracted to ease the comparison of the hysteretic behaviours. (c) 2d-polar plot of the positive (blue) and negative (black) switching fields for $0\ ° < \theta < 360\ °$.

anisotropy in AF/FM heterostructures. In fact, it has been shown experimentally that LSMO/YBCO [328] bilayers and LSMO/YBCO/LSMO [329] trilayers have displayed signatures of exchange bias. However, the constant difference $\sim 6\ mT$ is relatively small and could also originate from an experimental shift induced by the measuring setup.

4.3.3. Magnetoresistance reversal with temperature

The magnetoresistance measurements of a junction from the *ex-situ* sample REAL3 ($t_{YBCO} = 8\ nm$) with $I = 40\ \mu A$ for decreasing temperatures from $60\ K$ to $10\ K$ are displayed in **Fig. 5.26**. For $T = 60\ K$, the usual shape of the magnetoresistance is observed, with the already discussed linear background induced by CMR. While decreasing the temperature to $T = 25\ K$, a reversal of the polarity of the SVE is observed as the maxima of the magnetoresistance gradually become minima for and the MR ratio becomes negative ($MR = -0.08\ \%$ at $25\ K$). I define the reversal temperature T_R as the temperature at which the reversal of the SVE between positive to negative arises. For the junction presented in **Fig. 5.26**, T_R was found to be approximately $30\ K$.

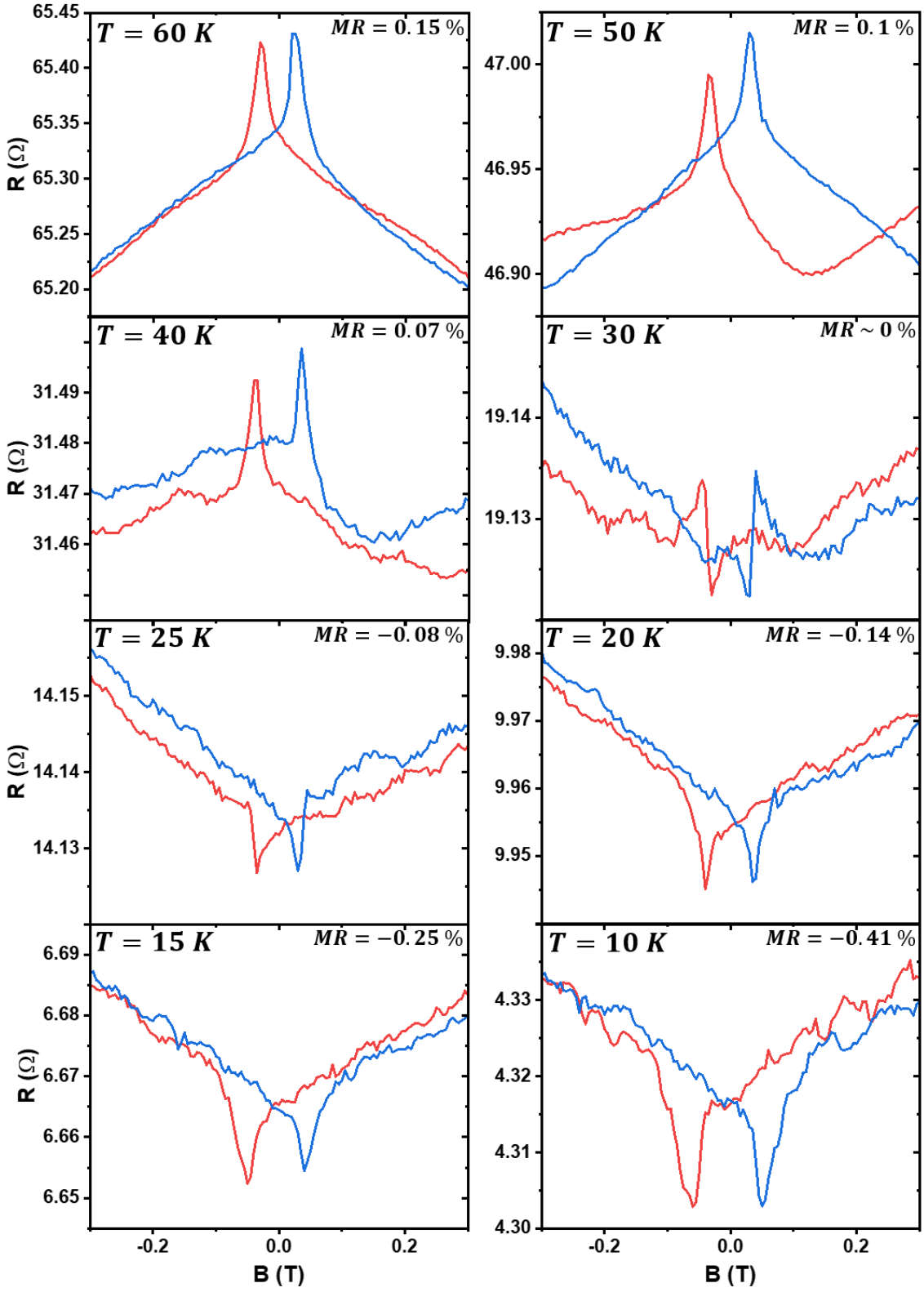

Fig. 5.26: Magnetoresistance measurements done on the ex-situ sample REAL3 ($t_{YBCO} = 8\,nm$) with $I = 40\,\mu A$ for decreasing temperatures from $60\,K$ to $10\,K$. A crossover between positive and negative SVEs arises at the reversal temperature $T_R \approx 30\,K$.

The crossover between positive and negative SVEs is further demonstrated in **Fig. 5.27,** showing a colorplot of the normalized resistance between 1 and -1 (z-axis) as a function of the temperature (y-axis) and the magnetic field (x-axis). The resistance was normalized using **Eq. 5.7** to allow for a direct comparison of the magnetoresistance curves. In fact, the 4-probe resistance of a junction typically varies from more than $100\ \Omega$ at $100\ K$ to approximately $1\ \Omega$ at $10\ K$, making it impossible to compare on the same figure the switching profiles without prior normalization. Three regimes can be observed from **Fig. 5.27** above and below $T_R = 30\ K$:

(i) For $T > T_R$, the magnetoresistance exhibits a clear positive SVE (indicated by the red areas that correspond to a high R_N) with relatively constant $B_S^{\pm} = \pm 25\ mT$. Moreover, the magnetoresistance linear background is governed by CMR.

(ii) For $T = T_R$, a mixed state between positive and negative SVEs arises. This effect can be seen in **Fig. 5.26** as both peaks and dips are visible for the same temperature. Additionally, this feature is also noticeable in **Fig. 5.27** where one can see a crossing-like behaviour with red and blue features arising simultaneously at $T_R = 30\ K$.

(iii) For $T < T_R$, we observe the reversal from a positive SVE to a negative SVE accompanied by the reversal of the background from a CMR-like behaviour to a superconducting behaviour. In fact, the magnetic field acts as a de-pairing force on the superconducting ground state, leading to an increase of the resistance for increasing fields. Note that all the studied SSVs that displayed a reversal of the SVE (as the one illustrated in **Fig. 5.26** and **Fig. 5.27**) also exhibited a reversal of the MR background for the same range of temperatures. Moreover, as was already discussed in **Sect. 4.2.**

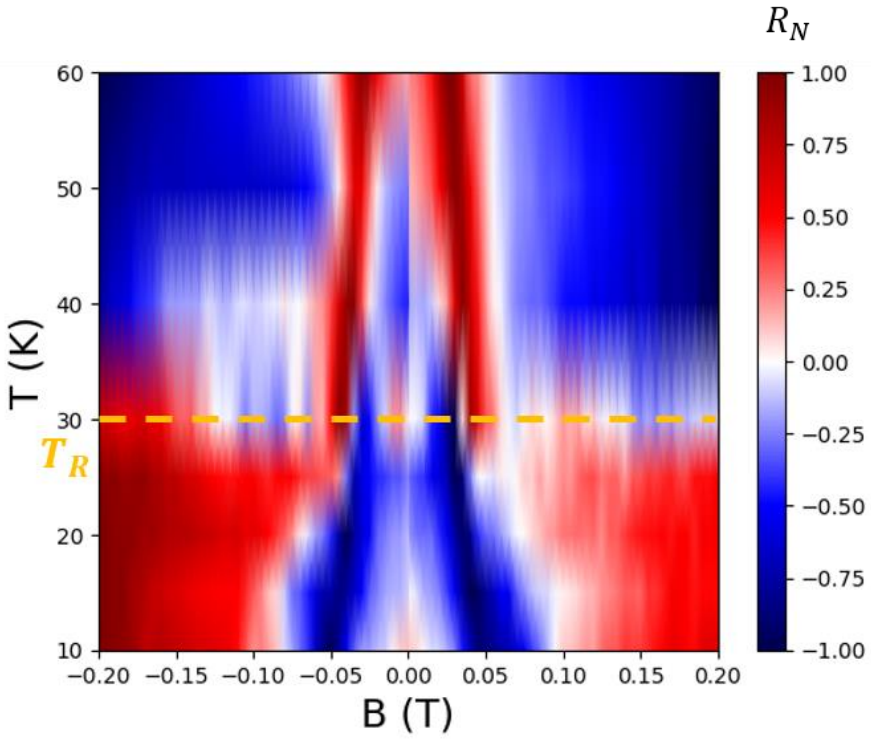

*Fig. 5.27: Measurements done on the ex-situ sample REAL3 ($t_{YBCO} = 8\ nm$) with $I = 40\ \mu A$ showing a 2d colorplot of the normalized resistance of a SSV (z-axis) between 1 and -1 as a function of the temperature (y-axis) and magnetic field (x-axis). For temperatures above $T_R \approx 30\ K$, the magnetoresistance curves show a positive SVE, while for temperatures lower than 30 K, the curves display a negative SVE as can be seen from the diverging blue lines. For $T = 30\ K$, there seems to be a crossing between both effects. The diverging behaviour of the switching fields is expected from the SQUID measurements of **Fig. 5.24** and is characteristic of FM materials.*

while presenting the $M(B)$ hysteresis loops, the switching fields are getting enlarged as the temperature decreases, as can be seen by the diverging blue traces in **Fig. 5.27**.

Fig. 5.28 demonstrates that the magnetoresistance peaks observed in **Fig. 5.26** and **Fig. 5.27** arise within the field range in which the relative magnetizations of the LSMO layers are anti-parallel (AP). The figure shows the magnetoresistance for a SSV from the *ex-situ* sample REAL3 ($t_{YBCO} = 8\,nm$) at $T = 100\,K$ [**Fig. 5.28(a)**, bottom] and $T = 15\,K$ [**Fig. 5.28(b)**, bottom]. In this SSV, one can observe the same reversal from positive to negative magnetoresistance as in **Fig. 5.26**. The magnetization loops (top panels in **Fig. 5.28**) and their derivatives (middle panels) are also shown to allow for a direct comparison between $B_S^{\pm}$ (extrema of the magnetoresistance) and B_C (represented by the red and blue vertical dotted lines). One can see that the magnetoresistance maxima [**Fig. 5.28(a)**, bottom] and minima [**Fig. 5.28(b)**, bottom] arise within the magnetic field range indicated by the vertical red and blue dashed lines.

A similar reversal from positive to negative SVEs was also observed by reducing the injected current while keeping the temperature constant. However, it is demonstrated in **Annexes, Sect. 2.5.**

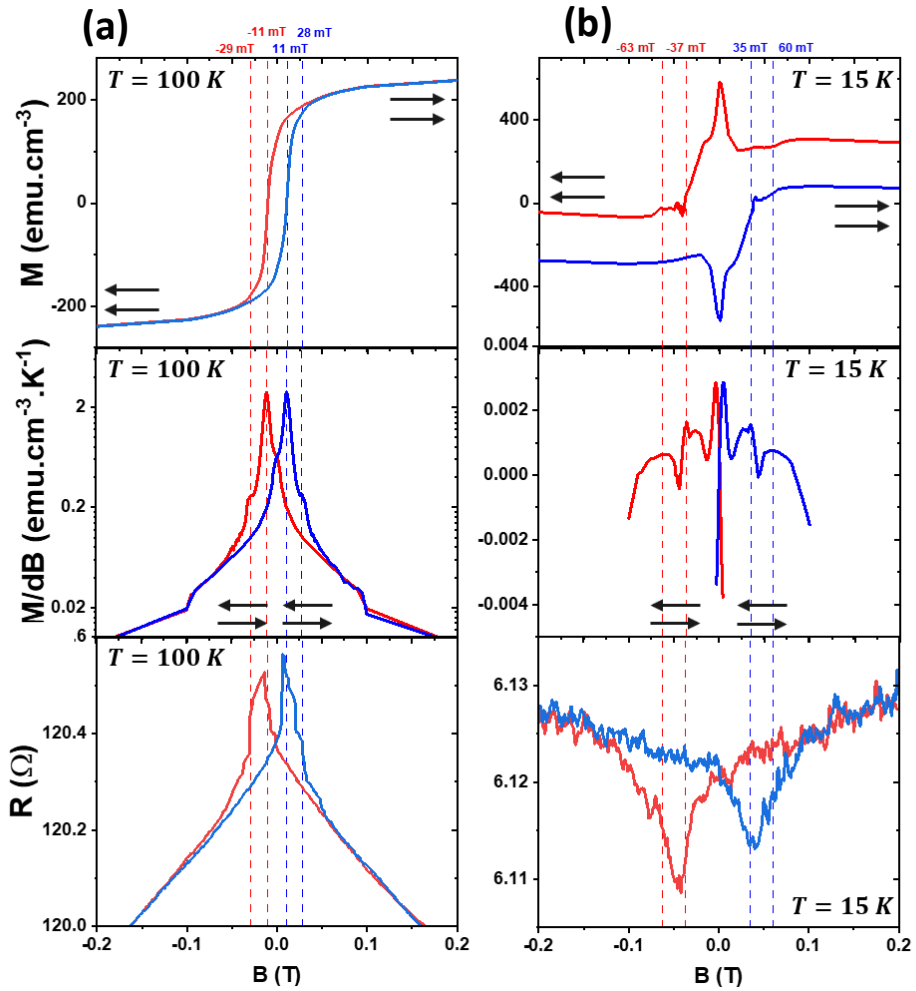

Fig. 5.28: Set of measurements for a temperature of (a) $100\,K$ and (b) $15\,K$, displaying from top to bottom: (top) $M(B)$ hysteresis loop of the unpatterned ex-situ sample REAL3 measured with a SQUID magnetometer (middle) first derivative dM/dB of the top graph as a function of B showing a two-step switching of the magnetization as indicated by the two maxima (coercive fields) and (bottom) the magnetoresistance of a SSV junction from the ex-situ sample REAL3 showing a positive SVE at $100\,K$ and a negative SVE at $15\,K$. The switching fields B_S^+ and B_S^- are located between the two coercive fields of the LSMO layers, i.e. in the AP configuration.

that this effect can be explained through Joule heating caused by a diode-like behaviour at the YBCO/Au interface as discussed in **Annexes, Sect. 2.4.**

4.3.4. Dependence of the reversal temperature on the spacer's thickness

Fig. 5.29 displays the reversal temperature T_R as a function of the intermediate YBCO layer thickness t_{YBCO} measured for various SSVs from different wafers and for different injected current densities. For clarity purposes, in particular to avoid the overlapping of data points, the thickness has been randomized within $[t_{YBCO}, t_{YBCO}+1]\ nm$ (that is, all the data points for $5\ nm < t_{YBCO} < 6\ nm$ actually correspond to $t_{YBCO} = 5\ nm$). The current density $J = I/S$ (with S the cross-section of the SSV) used for the measurement of the magnetoresistance curves from which T_R is deduced is indicated via the symbols' colours (see the legend). Moreover, T_R measured on the same SSV are plotted with the same symbol. As an example, we can see that one SSV from sample REAL3 (represented by a star) exhibited values of: $T_R = 15 \pm 5\ K$ for $J = 0.125\ \mu A.\mu m^{-2}$ and $T_R = 20 \pm 10\ K$ for $J = 0.025\ \mu A.\mu m^{-2}$. A value of $T_R = 0\ K$ indicates that for this particular current density, no signatures of the negative SVE could be observed for temperatures of down to $5\ K$ (minimum temperature of the cryocooling system) and above. In particular, **Annexes, Sect. 2.6.** illustrates the magnetoresistance of a junction that only displayed a positive SVE for $10\ K < T < 90\ K$ and this junction is used as an example to discuss the evolution of B_S^- and B_S^+ as a function of temperature.

For sample REAL1 with $t_{YBCO} = 3\ nm$, no negative SVE was observed throughout the magnetic measurements of more than ten junctions, although only three of them are presented in **Fig. 5.29** to prevent overcrowding the figure. The typical behaviour of the magnetoresistance for junctions from

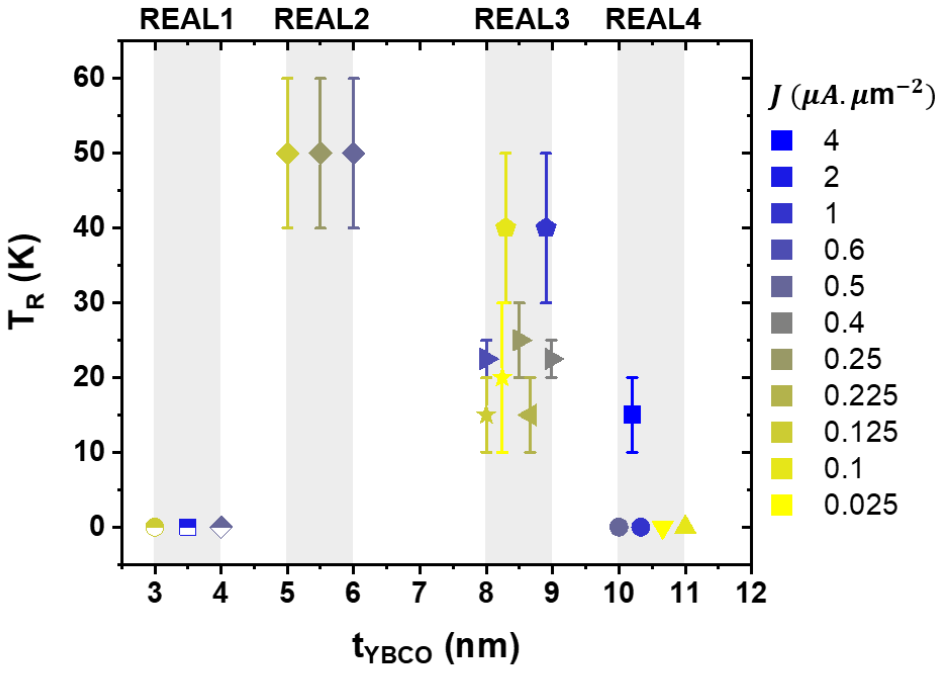

Fig. 5.29: T_R as a function of t_{YBCO} for different biasing current densities. The value of the thickness has been randomized between $[t_{YBCO}, t_{YBCO}+1]$ for clarity. The points' colour is representative of the injected current density as described by the legend. Identical symbols represent T_R that have been measured on the same SSV.

this sample is presented in **Fig. 5.30** for increasing temperature from $15\ K$ to $60\ K$. For the lowest temperature [**Fig. 5.30(a)**], the magnetoresistance exhibits a superconducting background: as the magnetic field intensity is increased, the resistance of the SSV increases. As the temperature is ramped up from $15\ K$ to $35\ K$ [**Fig. 5.30(b)**], we see appearing positive hysteretic peaks in the magnetoresistance, while the background stays the same. Finally, for $T = 60\ K$ [**Fig. 5.30(c)**], the background reverses to a manganite CMR-like shape, as already observed in **Fig. 5.25(a)**. The behaviour described here is invariably seen on all the junctions of sample REAL1. Moreover, sample REAL4 with $t_{YBCO} = 10\ nm$ also shows the same behaviour, at the exception of one junction that showed a negative SVE, as can be seen from the black square point in **Fig. 5.29** for $J = 4\ \mu A.\mu m^{-2}$. Although **Fig. 5.30** only shows three magnetoresistance measurements, all the measured curves corresponding to this particular junction are available in **Annexes, Sect. 2.7.** for temperatures between $10\ K$ and $70\ K$.

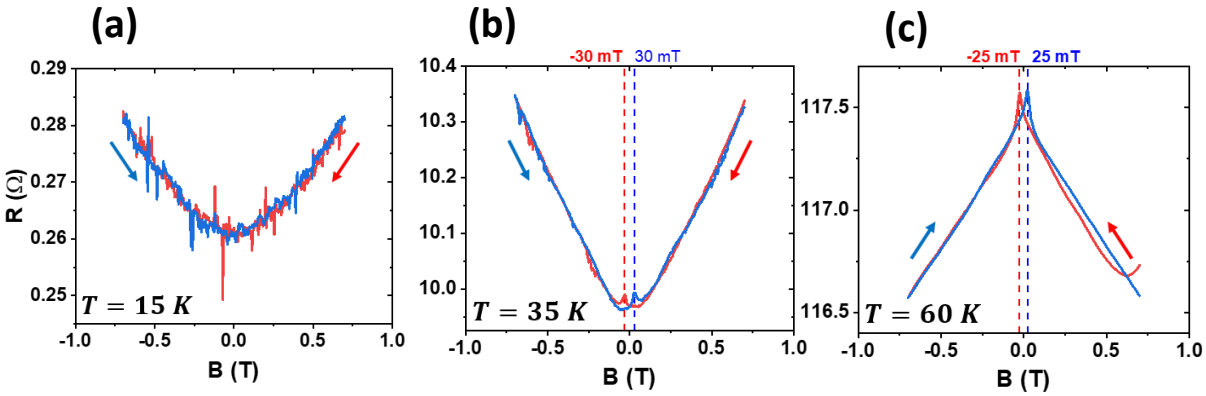

Fig. 5.30: Measurements done on a SSV from the ex-situ sample REAL1 with $t_{YBCO} = 3\ nm$, showing the magnetoresistance for a biasing current of $100\ \mu A$ and for three different temperatures (a) $15\ K$, (b) $35\ K$ and (c) $60\ K$. Even at the lowest temperature, no sign of negative SVE was observed in this particular set of measurements.

To conclude, SSVs that displayed a reproducible reversal of the magnetoresistance between positive and negative SVEs were observed for $5\ nm < t_{YBCO} < 10\ nm$, with most of them from sample REAL3 with $t_{YBCO} = 8\ nm$ (for which $100\ \%$ of the measured junctions show the reversal), whereas only one SSV from sample REAL2 (represented as a diamond in **Fig. 5.29**) and one SSV from sample REAL4 (represented as a square in **Fig. 5.29**) exhibited a negative SVE. This illustrates the crucial importance of the spacer's thickness to explain the origin of this phenomenon. *In-situ* samples (REAL5 and REAL6 as introduced in **Tab. 5.1**), with nominal $t_{YBCO} \geq 8\ nm$, only exhibited positive SVEs similar to samples REAL1 (**Fig. 5.30**) and REAL4.

4.3.5. Evolution of the magnetoresistance with temperature

This section focuses on the evolution of the magnetoresistance in percentage as a function of the temperature for various junctions from different samples. The MR is calculated from **Eq. 5.6** and corresponds to the relative height of the magnetoresistance peaks and dips characteristic of the positive and negative SVEs, as defined in **Chapter 3, Sect. 6.4**. The results are displayed in **Fig. 5.31**, showing $MR(T)$ curves for six SSVs from four samples (REAL1, REAL3, REAL5 and REAL6). From this figure, one can distinguish between two distinct behaviours, depending on the presence or absence of the magnetoresistance reversal.

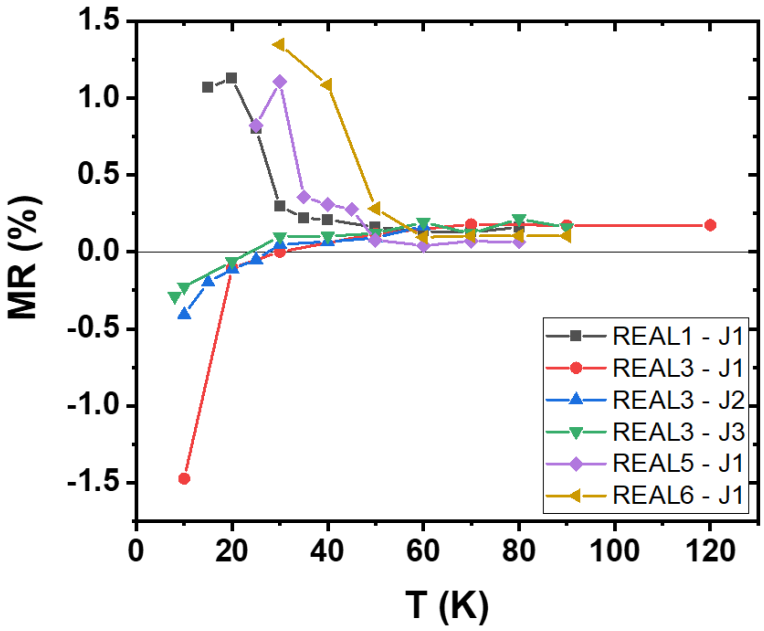

Fig. 5.31: MR in percentage as a function of the temperature for various SSVs from samples REAL1 ($t_{YBCO} = 3\ nm$), REAL3 ($t_{YBCO} = 8\ nm$), REAL5 ($t_{YBCO} = 8\ nm$) and REAL6 ($t_{YBCO} = 10\ nm$). One can observe two different behaviours of the $MR(T)$ curves: for SSVs that do not exhibit a negative SVE, MR diverges to $+\infty$, whereas for SSVs showing a negative SVE, MR diverges to $-\infty$. Only a selected subset of $MR(T)$ is displayed in this figure to avoid overcrowding the figure.

(i) **No magnetoresistance reversal:** In this case, MR is positive for all temperatures (examples of such junctions are discussed in **Fig. 5.30** and in **Annexes, Sect. 2.6.**) and diverges to high positive values as the temperature decreases.

(ii) **With magnetoresistance reversal:** In this case, MR is positive at high temperatures and becomes negative below T_R, as already studied in **Sect. 4.3.3.** and **Sect. 4.3.4.**, signalling the reversal between positive and negative SVEs. Moreover, MR diverges to high negative values as the temperature decreases.

Note that for $T > 60\ K$, MR ranges from $0.07\ \%$ to $0.17\ \%$ for all SSVs and is relatively constant with temperature. Then, the onset of the MR increase and decrease arises within a similar range of temperature for all junctions ($50\ K < T < 60\ K$), which corresponds to the typical T_C of the bottom YBCO layer as determined by the preliminary $R(T)$ experiments (see **Sect. 4.1.**). Thus, one can conclude that the diverging behaviour of $MR(T)$ is concomitant with the abrupt lowering of the junction's resistance across the normal to superconducting transition, which leads to higher relative change in percentage. This feature highlights one of the most compelling aspect of superconducting spin valve devices as compared to typical MTJs: the possibility to drastically increase MR upon cooling, a property of paramount importance for practical applications.

5. Discussion

The SSVs presented in this chapter show a characteristic and reproducible reversal of the magnetoresistance between positive and negative values while decreasing the temperature below T_R (**Fig. 5.17** and **Fig. 5.26**). The reversal process can be split into three consecutive regimes for different ranges of temperature: the non-superconducting regime above the T_C of the bottom YBCO layer (T_C is

estimated to be $\sim 50\,K - 60\,K$ according to the $R(T)$ measurements shown in **Fig. 5.22**), an intermediate regime for $T_C < T < T_R$ and finally a low-temperature regime $T < T_R$ for which the negative SVE is observed for specific t_{YBCO} (see **Fig. 5.29**).

5.1. Non-superconducting regime for $T > T_C$

We first discuss the behaviour and magneto-transport properties of the SSVs for temperatures well above the T_C of YBCO, as illustrated in **Fig. 5.25(a)**. For these temperatures, superconductivity does not play a role in the observed phenomena.

The linear background can be attributed to CMR, already observed in multiple experiments involving FM manganites [19–24]. In fact, CMR represents a drastic decrease of the resistance at high injected magnetic field (see **Chapter 2, Sect. 3.5.3.**) and the linear background is attributed to the suppression of spin fluctuations [20,23,24]. On the other hand, the hysteretic behaviour of the magnetoresistance for low magnetic field is typical of the GMR effect. This conclusion is supported by the SQUID $M(B)$ hysteresis loops [**Fig. 5.24(b)**] measured on the unpatterned sample REAL3 at $100\,K$ and $15\,K$ showing two distinct coercive fields for the two ferromagnetic layers that allows for an AP configuration of the SSV. Then, it was shown in **Fig. 5.28** that the maxima ($B_S^{\pm}$) of the MR fall in these particular ranges of magnetic field, indicating that the switching occurs in the AP configuration, characteristic of GMR effects. A schematic representation of the spin valve is shown in **Fig. 5.32**: for this range of temperature, the three superconducting layers are in a metallic normal state (N) and the resistance of the junction is lower in the P state [**Fig. 5.32(a)**] compared to the AP state [**Fig. 5.32(b)**] via the GMR effect (see **Sect. 1.**), leading to a positive SVE.

Note that we can completely rule out that the hysteretic MR observed at low fields can be linked to anisotropic magnetoresistance (AMR), another phenomenon that has been thoroughly studied in the literature and that can give rise to MR patterns in manganites, notably in LSMO [20,22,330–332] and in LCMO [333]. AMR corresponds to a change of the MR of a ferromagnetic layer while varying the angle between the external magnetic field and the direction of the injected current and originates from

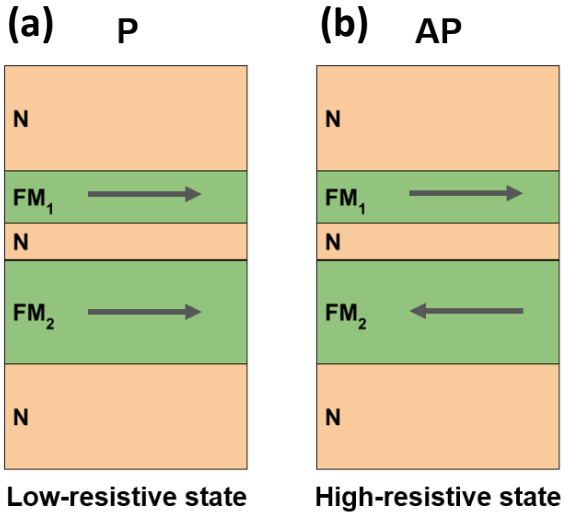

*Fig. 5.32: Schematic representation of the spin valve for $T > T_C$. At this temperature, the three superconducting layers are in a normal state (N), and the magnetic response is typical of GMR as already discussed in the introduction (**Sect. 1.**), leading to (a) a low-resistive state while the magnetizations are in the P configuration and (b) a high-resistive state in the AP configuration, i.e. a positive SVE with $\Delta R > 0$.*

the interplay between the splitting of the spin up and spin down populations of a ferromagnet at the Fermi energy and spin-orbit coupling [334]. However, in the case of the present experiments, the magnetic field is rotated in-plane while the current is flowing perpendicular to the interfaces, *i.e.* in the out-of-plane direction. Therefore, the angle between I and B remains constant throughout the magneto-transport measurements. Additionally, the extrema of the magnetoresistance are located within ranges of magnetic fields that correspond to the expected AP configuration of the SSV, as was demonstrated by the SQUID measurements in **Fig. 5.28**. In fact, AMR is expected to have an impactful contribution to the $R(B)$ signal in the vicinity of $B = B_C$ [22,331,332], and in the case of the SSVs, one should expect the appearance of two distinct peaks or dips at the coercive fields of the two ferromagnets instead of a unique peak in between.

In summary, one can rule out AMR from playing a major role in the MR switching and conclude that the MR curves at high temperatures are governed by CMR and GMR effects.

5.2. Intermediate regime for $T_C > T > T_R$

The typical critical temperature of the bottom YBCO layer was found to be between $50\ K$ and $60\ K$ as calculated from the $R(T)$ preliminary measurements, illustrated for example in **Fig. 5.22**. Furthermore, the negative spin valve effect was shown to arise below T_R, typically varying between $15\ K$ and $50\ K$, implying the existence of an intermediate range of temperatures for which the bottom and top YBCO layers (both having a thickness of $30\ nm$) have transitioned to the superconducting state whereas the middle spacer is still in a metallic normal state, due to its reduced thickness.

Interfaces between half-metallic manganites and cuprates are suitable for the generation of equal-spin triplets, and it was demonstrated in numerous experiments that long-range supercurrents can be induced within the FM layer at carefully engineered YBCO/LSMO [106,335,336] and YBCO/LCMO [298,310,337] interfaces. The generation of triplet Cooper pairs $\Psi_{S_Z=1}^{triplet} = \uparrow\uparrow \text{ or } \downarrow\downarrow$ (with a net spin component $S_Z = \pm 1$) can be understood through the mechanisms of spin mixing and spin rotation at the interface between FMs and superconductors [104] (see **Chapter 2, Sect. 4.3.**).

In the present experiments, according to the studies mentioned in the previous paragraph, equal-spin triplets are expected to be generated within the structure at low enough temperature via proximity effect at the various S/FM interfaces. In this regard, a key observation is the reversal between a linear background caused by the CMR effect at high temperatures and an opposite curvature-background consistent with superconducting behaviour (resistance increase with magnetic field) at low temperatures, as illustrated in **Fig. 5.26**, **Fig. 5.28** and **Fig. 5.30**. This background reversal was systematically observed for all SSVs from batches 3 and 4. One can speculate from the disappearance of the CMR background that with decreasing temperatures, the superconducting correlations from the bottom and top electrodes $(30\ nm)$ penetrate the manganite FMs to give rise to equal-spin triplet Cooper pairs through proximity effects. A schematic of the SSV for this range of temperature is displayed in **Fig. 5.33**: the two outer YBCO layers have become superconducting and the FMs can be considered as triplet generators (depicted by the red parallel arrows). Note that the half-metallic property of LSMO and LCMO insures that the equal-spin triplets are polarized alongside a unique direction due to the $100\ \%$ spin-polarized feature of manganites.

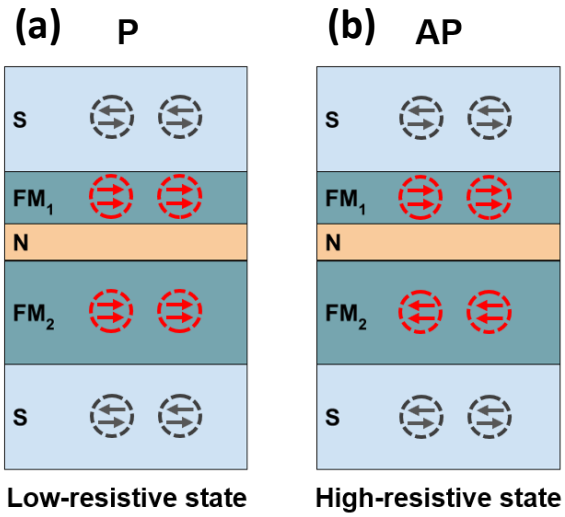

Fig. 5.33: Schematic representation of the spin valve for $T_C > T > T_R$. At this temperature, the two outer YBCO layers have become superconducting and the FMs can be considered as equal-spin triplet generators caused by proximity effects. The magnetoresistance is expected to display a positive SVE with $\Delta R > 0$ via a mechanism analogous to the GMR effect, yielding (a) a low-resistive state in the P configuration and (b) a high resistive state in the AP configuration.

In this scenario, the magnetoresistance of the SSV is expected to display an increase in the resistance in the AP configuration, analogous to the GMR effect in **Fig. 5.32.** In particular, because the YBCO spacer is in a metallic state, the propagation of the $100\ \%$ spin-polarized superconducting correlations from FM_1 to FM_2 will be possible only if both FMs have parallel magnetizations because equal-spin triplet correlations aligned anti-parallel to the local magnetization are expected to die off. Thus, the P configuration expectedly leads to the full propagation of superconducting correlations across the stack, yielding a lower resistance compared to the AP configuration, which explains the positive SVE for $T_C < T < T_R$.

5.3. Negative spin valve effect for $T < T_R$

Let's now turn to the explanation of the negative SVE that is observed while decreasing the temperature below T_R (for example in **Fig. 5.17** and **Fig. 5.26**). A key ingredient for its understanding is that the YBCO spacer is required to be intrinsically superconducting (*i.e.* not induced by proximity effect from the top and bottom YBCO layers) for the negative SVE to arise. A first piece of supporting evidence is found in **Fig. 5.18(a)**: the crossover from positive to negative SVEs occurs for a temperature close to the $T_C \approx 47\ K$ of the YBCO spacer, calculated from the first derivative of the $R(T)$ curve. Second, no evidence of a negative SVE was observed on the control samples with a non-superconducting PBCO spacer. Finally, MR measurements from SSVs from sample REAL1 with $t_{YBCO} = 3\ nm$ also show no signatures of the negative SVE (see **Fig. 5.30**). In fact, it has been shown in previous experiments on YBCO/LCMO bilayers (Sefrioui *et al.* in 2003 [27]) that the T_C of YBCO is reduced to zero for $t_{YBCO} < 3\ nm$. In the present work, although LSMO was used for batches 3 and 4 instead of LCMO, it is likely that the YBCO spacer is not intrinsically superconducting in the case of sample REAL1. Thus, the SSV's spacer must display superconducting properties in order to allow for the appearance of the negative SVE.

In the literature, positive and negative spin valve effects in SSVs are explained through a wide variety of physical phenomena, discussed in the introduction (**Sect. 1.2.**), including:

(i) **Quasiparticle spin accumulation (Sect. 1.2.1.1.)** [282,298]**:** Quasiparticle spin accumulation effectively suppresses the T_C of the superconducting spacer in the AP configuration as a consequence of the retroreflection of one spin population due to the $100\ \%$ spin-polarized property of the manganites**.** In turn, the global resistance of the junction rises, leading to a positive SVE. Thus, this effect cannot account for the observed negative spin valve effect.

(ii) **Vortices dynamic (Sect. 1.2.1.2.)** [270,280,283–289]**:** The motion of superconducting vortices [338,339] in a type-II superconductor is a well-known mechanism that can lead to strong dissipation in high-T_C superconductors. In fact, in the presence of applied electrical currents, vortices will feel a Lorentz force that generate an electric field $\vec{E}$ which is parallel to the flow direction, leading to an increase of the dissipated power.
In the present experiments, the magnetic field was applied in-plane and should not be responsible for the generation of vortices due to the high anisotropy of YBCO, which makes it nearly transparent to moderate magnetic fields [340]. However, out-of-plane stray fields can be generated across the magnetization reversal, when magnetic domains are present within the ferromagnetic layers. In this case, the motion of vortices should lead to an increase of resistance of the SSV junction in the vicinity of the coercive fields of the FMs, and therefore to a positive SVE. Therefore, the negative SVE cannot be explained through stray fields and vortices dynamics.

(iii) **Crossed Andreev reflections (CARs) (Sect. 1.2.1.3.)** [291–296]**:** This phenomenon can only occur if the superconducting layer is thinner than its superconducting coherence length**.** In the case of YBCO, ξ is anisotropic and depends on the crystallographic direction: values of $\xi^c(T = 0\ K) \approx 0.7\ nm$ were reported along the c-axis, whereas values of $\xi^{ab}(T = 0\ K) \approx\ 2.4\ nm$ were reported along the ab-planes [123]. In the case of the SSVs studied in this chapter, t_{YBCO} ranged between 3 and $10\ nm$. Although ξ is known to diverge as $T \to T_C$ (see **Eq. 2.6**, **Chapter 2, Sect. 1.2.**), the negative SVE was observed at very low temperatures ($T = 10\ K$ in **Fig. 5.26** for instance) that is, not for temperatures close to T_C. Therefore, it seems unlikely that CARs can be responsible for the observed negative SVE.

Having ruled out quasiparticle spin accumulation, stray fields, vortices dynamics and CARs from being responsible for the negative SVE, one can consider the implication of ferromagnetic exchange coupling on superconductivity, as was first theorized by Tagirov [15] and Buzdin [16] and introduced in **Sect. 1.1.** [28,276]. The average exchange field h acting on the spin of the conduction electrons is maximum while the spin valve is in a P configuration as the exchange fields from both ferromagnetic layers couple and reinforce each other's, effectively quenching superconductivity in the spacer layer and raising the global resistance of the junction. The average exchange field seen by the superconducting spacer is proportional to $\propto \frac{\cos(\delta/2)}{t_{YBCO}}$, where δ represents the angle between the magnetizations of both ferromagnetic layers [14,28]. Moreover, this explanation is consistent with the following:

- For SSVs with $t_{YBCO} = 3\ nm$ (**Fig. 5.29**, REAL1), the middle YBCO spacer is likely not superconducting [27]. Therefore, no evidence of negative SVE is observed.
- For SSVs with $t_{YBCO} = 10\ nm$ (**Fig. 5.29**, REAL4), the average exchange field h is probably not large enough to quench superconductivity in the P state, therefore yielding a positive SVE.

Note that this explanation is compatible with the presence of equal-spin triplets within the structure. In fact, it has been theoretically demonstrated that in the case of FM/S/FM spin valves (with

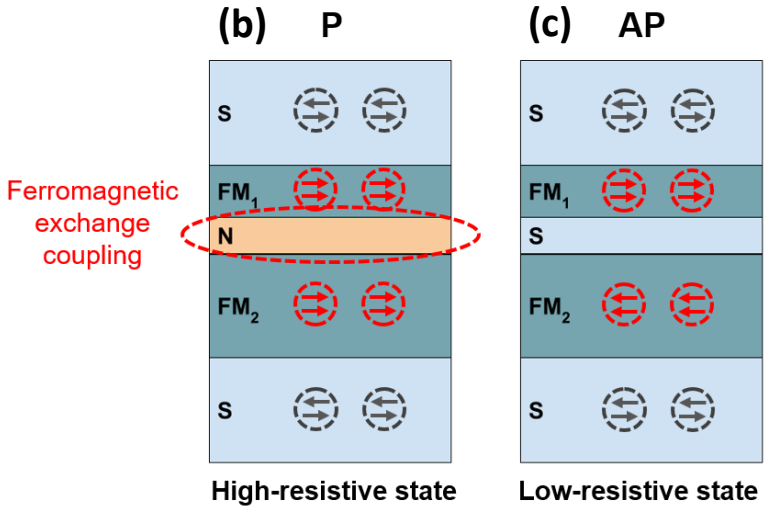

Fig. 5.34: Schematic representation of the spin valve for $T < T_R$. At this temperature, the YBCO spacer has become intrinsically superconducting. In the P configuration, the ferromagnetic exchange fields from both FMs couple and reinforce each other's, leading to a depression of the T_C and a higher resistance.

FM a ferromagnetic insulator), the phenomenology related to exchange effects is expectedly the same in the case of triplet and singlet Cooper pairing [264]. Therefore, the negative SVE of the SSVs studied in this chapter is likely to be the manifestation of the exchange coupling from the FMs' through the superconducting spacer, effectively quenching superconductivity in the P configuration for an intermediate range of t_{YBCO}. This effect is summarized in **Fig. 5.34**, showing the state of the junction in the P and AP configurations corresponding to the high and low-resistive states, respectively.

On a final note, I would like to point to results shown in the Annexes, that show that the reversal of the magnetoresistance sign can be observed while varying the injected current (**Annexes, Sect. 2.5.**). However, as demonstrated in **Annexes, Sect. 2.5.**, this reversal results from current heating effects and thus, *in fine*, from temperature variations, in full consistence with the above discussion. Furthermore, a different type of magnetoresistance sign reversal is observed as a function of the magnetic field direction (see **Annexes, Sect. 2.8.**), which is not related to superconductivity (as it is observed above T_C) and is explained through a ste-by-step reversal process of the FMs' magnetizations.

6. Conclusions and perspectives

In this chapter, the results of the transport and magneto-transport measurements of a multilayer SSV device made of alternating layers of YBCO and half-metallic materials, LCMO and LSMO, were presented. These devices display a reproducible reversal between a positive SVE (with $\Delta R > 0$) and a negative SVE (with $\Delta R > 0$) while decreasing the temperature below a threshold that is device-dependent. This reversal can be explained by the effects of exchange coupling on the superconducting state for intermediate t_{YBCO} thicknesses, and disappears in the case of a very thin or very thick non-superconducting YBCO spacer.

Another key result of this study is the unusual high values of $B_S^{\pm}$ observed from the MR experiments of SSVs from batches 1 and 2. Note that these batches have been deposited in Madrid by magnetron sputtering and are made of YBCO and LCMO (instead of LSMO). This giant enhancement is

illustrated in **Fig. 5.18**, showing switching fields as high as $0.5\ T$ at $T\ =\ 20\ K$, more than one order of magnitude above the expected coercive field of LCMO for this range of temperatures [285,317,318]. Similar effects have been observed previously for non-oxide materials, for example at the interface between the strong type-II superconductor NbN ($35\ nm$) and the ferromagnet Co_2FeSi ($35\ nm$), with a change of B_S from $5\ mT$ at $T = 6\ K$ to $100\ mT$ at $T = 2\ K$, measured from $M(B)$ magnetization hysteresis loops [341].

This feature could originate from "inverse proximity effect" [342] (the leakage of the ferromagnetic phase in the superconductor), inducing a magnetization within the superconducting layer. In turn, the presence of strongly pinned superconducting vortices at the YBCO/LCMO interfaces [343–345] can generate a delay in the magnetization's reversal of the induced ferromagnetic layer, *i.e.* higher values of the apparent switching fields. Furthermore, an alternative explanation could be that the bottom and top superconducting electrodes generate a screening magnetic field that eventually enhances the magnetic field needed to start the magnetization reversal [346]. Yet, the giant enhancement of $B_S^{\pm}$ was not observed while measuring SSVs from batches 3 and 4, pointing toward a mechanism that is unique to YBCO/LCMO interfaces or related to the deposition techniques (magnetron sputtering instead of PLD) and fabrication methods (methods 1 and 2 as described in **Fig. 5.12**).

Beyond the scientific case and the possibilities for further research, the obtained behaviours are interesting from a technological point of view. As introduced in **Chapter 1**, superconducting electronics [44] represents a very promising field of research owing to the high energy efficiency and fast operation inherent to superconducting materials [347,348]. However, conventional CMOS technologies are usually not compatible with superconducting components as semiconducting transistors are subject to Joule heating, especially on high-density chips, hindering the properties of adjacent superconducting devices. Thus, to broaden the range of applications of superconducting electronics, it is crucial to design and characterize novel types of devices that can perform all kind of electrical operations (such as superconducting transistors, memories, diodes etc…). The SSV device presented in this chapter displays interesting functionalities that can be implemented in a plethora of applications.

Nowadays, cryogenic magnetic memories based on superconducting materials represent an active field of study for the engineering of fast, non-volatile and high density components that can be used for data storage [349–354]. The possibility to control the resistance of the SSV through the relative orientations of the magnetizations allows the design of reconfigurable resistive switching devices that can keep a memory of the applied magnetic pulses. Additionally, the crossover between positive and negative SVEs can lead to novel functionalities: inducing a switch between the two regimes allows to write and read different information. Moreover, as shown in **Fig. 5.31**, the MR can be increased from $\sim 0.2\ \%$ in the positive SVE regime to $\sim 2\ \%$ in the negative SVE regime, an important feature that can prove crucial to differentiate the P and AP configurations and perform reading operations, and the MR is expected to diverge close to $0\ K$ due to enhanced superconducting properties and vanishing resistances.

SSVs can also have potential applications in quantum sensing and quantum computing, for example through the design of switchable Josephson spin valve devices $S/F_1/N/F_2/S$ [355–358]. Such devices have been shown to exhibit signatures of π-Josephson effects by Gingrich *et al.* [357] in 2016; the phase φ of the junction is equal to π in the ground state in the absence of external magnetic fields. It was demonstrated that π-Josephson junctions are promising building blocks for specific kinds of qubits [359] that can be implemented for quantum computing applications.

One of the key issues for all the above applications is scalability, which will certainly require a more thorough analysis. Varying the cross-section and the thicknesses of the involved layers can lead to a more complete understanding of the working principle of the multilayer. In particular, reducing further the cross-section of the junction may lead to increased values of the MR as the global resistance of the SSV is expected to rise in the normal state while being zero below T_C, yielding a higher (infinite in the ideal case) relative change in percentage. Reducing the structure to the nanometre-size (of the same order of magnitude of the coherence length) may also yield novel phenomena such as interference and oscillating behaviours. Additionally, reducing the typical dimensions allows for higher device densities for miniaturization purposes.

All in all, this work brings us one step closer toward the general understanding of the interplay between ferromagnetism and superconductivity at cuprate/manganite interfaces, and opens the path for the design of high-temperature devices for superconducting spintronics, for a vast number of applications [94,360].

Chapter 6: General conclusions and perspectives

With the approaching end of Moore's law, and the constant need for smaller and faster devices, superconducting alternatives to conventional electrical components are becoming of increasing interest. In fact, the main problem underlying CMOS technologies at cryogenic temperatures is Joule heating, making superconductors perfect candidates owing to their inherent zero-resistance state below the critical temperature and ultra-fast operating frequencies [347,348]. This thesis has been dedicated to the fabrication, optimization and characterization of two types of devices made from the archetypal high-temperature cuprate superconductor $YBa_2Cu_3O_{7-x}$ (YBCO) in which a switch of the superconducting properties can be achieved by application of electrical and magnetic fields. The obtained results pave the way for novel resistive-switching electrical components with potential applications for magnetic memories [350–352,354], neuromorphic [361,362] and quantum computing and highly-sensitive sensors for superconducting electronics operating at temperatures above the boiling point of liquid nitrogen.

1. Electrical tuning in transistor-like structures

In the first part of this thesis, the superconducting ground state of a cuprate superconductor can be modulated through a change in the hole doping concentration, revealing the possibility to engineer resistive-switching devices based on a reversible superconductor-to-insulator phase transition.

One possible way to alter the hole doping content is to induce a reversible motion of oxygen ions within the crystal structure, locally modifying the charge carrier concentration. We have taken advantage of this mechanism in a transistor-like structure made from an aluminium (Al) gate on top of a YBCO thin film. This device exhibits two concomitant effects: a large reversible memristive switching of the YBCO/Al interface's conductance accross a continuum of states (non-volatile below $200\ K$), as well as the non-reversible and monotonic depression of the superconducting properties of the YBCO channel. The first behaviour is attributed to interfacial chemical redox reactions that induce a back-and-forth motion of oxygen across the interface, generating an electron tunnelling barrier with a thickness that can be controlled through the application gate voltages. simultaneously, the non-reversible decrease of the channel's T_C originate from structural disorder induced by high dissipated powers and subsequent Joule heating. In fact, YBCO is known to be extremely sensitive to disorder as a consequence of the d-wave pairing mechanism characteristic of cuprate superconductors. The observed effects were highly reproducible and all the studied devices displayed identical behaviours for both the YBCO/Al interface and the transistor's channel. Moreover, scalability was also investigated, yielding similar results by varying the involved thicknesses and the gate's width.

The memristive properties of the YBCO/Al interface, with an absolute change of the conductance on more than 2-3 orders of magnitude, are very promising for a number of technological applications. In particular, memristors have acquired a great deal of attention lately for their potential utility in

neuromorphic computing: memristors are ideal components for simulating the working principle of biological neurons and synapses. For temperatures below $200\ K$, the non-volatile conductance can be used to accurately store information, effectively simulating a synapse [363]. Additionally, for temperatures above $200\ K$, the natural relaxation of the conducting state may be attractive to mimic the stochastic behaviour of neurons, particularly suited for the leaky integrate-and-fire model [97,254–256].

Furthermore, the dissipated power required to induce a resistance increase in the channel is self-limiting; after a few training cycles, this dissipated power is stabilizing towards a limiting value. This property can allow exploiting the memristive behaviour of the YBCO/Al interface while keeping the resistance of the channel unchanged. On the other hand, by increasing the dissipated power, one can tune the properties of the channel without affecting the memristive functions. This ability can be used for current-limiting applications and for the protection of superconducting circuitry or for the engineering of reconfigurable Josephson junctions for sensing applications.

The envisioned devices, prior to the characterization, were designed as the active element of a superconducting radio frequency switch for cryogenic superconducting electronics. However, the non-reversible and monotonic decrease of the T_C while applying voltage gates is a hindrance to a fully operational resistive-switching element. Nonetheless, a reversible modulation of the resistance of the YBCO channel from a finite value (in the normal state) to zero (in the superconducting state) through a controlled chemical redox reaction might be achievable by modifying the geometry and/or materials of the device. This can be done by reducing the thickness of the YBCO channel and utilizing a reducing material that requires a lower voltage to start the redox process, to prevent from potential thermal effects (Joule heating).

2. Magnetic tuning in superconducting spin valve structures

In the second part of this thesis, we have shown that the superconducting properties of YBCO can be tuned magnetically in a superconducting spin valve (SSV) structure, consisting in two ferromagnetic layers sandwiching a superconducting thin spacer. Analogous to the well-known giant magnetoresistance (GMR) effect in conventional spin valves, the resistive state of the device can be switched between a low-conductive state and a high-conductive state by changing the relative orientations of the two ferromagnets (FMs) from parallel (P) to anti-parallel (AP). In this thesis, SSVs in the form of YBCO/ FM_1/ YBCO/ FM_2/ YBCO multilayers were investigated using magneto-transport experiments, with FM a half-metallic material, namely $La_{1-x}Sr_xMnO_3$ (LSMO) or $La_{1-x}Ca_xMnO_3$ (LCMO). Half-metals are promising materials that can be used in conjunction with cuprate superconductors for their similar crystal structures related to the perovskite family leading to highly transparent epitaxial interfaces as well as their ideal $100\ \%$ spin-polarized property. In particular, YBCO/LSMO and YBCO/LCMO interfaces have been thoroughly investigated the last two decades for the generation of equal-spin triplet Cooper pairs, of particular interest in the field of superconducting spintronics [104], *i.e.* the study of pure spin-polarized supercurrents.

The multilayers were patterned through a multi-step clean-room fabrication process to design current-perpendicular-to-plane junctions whose geometry allows for a 4-probe characterization of the transport properties. The junctions exhibited a unique feature: the possibility to induce a reversal of the magnetoresistance between a positive spin valve effect (with $\Delta R > 0$) and a negative spin valve effect (with $\Delta R < 0$) by decreasing the temperature below a reversal temperature threshold that

strongly depends on the middle YBCO layer's thickness. It was shown that the positive-to-negative polarity reversal is likely induced by superconducting exchange coupling: when decreasing the temperature below the reversal temperature, the YBCO spacer becomes superconducting, and the exchange fields generated by the FMs couple and enhance each other in the P configuration, quenching superconductivity.

These devices are particularly fitted for the design of cryogenic magnetic memories. In fact, being able to store non-volatile information in the resistive state of the junction depending on the relative orientations of the FMs' magnetization can be used to encode bits for data storage applications. Moreover, the unique property of the studied SSVs to switch between a positive and a negative SVE can add novel functionalities, allowing to write and read information differently depending on the temperature or the injected current.

The interest of the observed effects calls for further investigations to get a deeper understanding of the switching process. Notably, stability, relaxation and scalability experiments are required to fully characterize the switching phenomena and allow for the design of electrical components that can be integrated in superconducting circuitry. These experiments should include a dynamic characterization, for example by applying fast magnetic pulses of increasing amplitudes to study the memristive (cumulative) switching, or high-frequency switching to exploit the spin valve effect in electromagnetic detection.

Annexes

1. Annexes: electrochemical tuning of YBCO superconducting properties

1.1. Fabrication process recipes

The fabrication of the transistor-like structures of **Chapter 4** was performed on commercial $150\ nm$-thick YBCO (001) grown on r-cut sapphire substrates and capped with a $100\ nm$-thick layer of gold (CERACO ceramic coating GmbH). Moreover, a buffer layer of cerium oxide was included between the YBCO and sapphire layers. The lithography digital masks were all designed using the software KLayout.

1.1.1. Step 1: Etching of the bars

The first step consists in the lithography and etching of the YBCO bars (see **Fig. 6.1**). Each bar contains ten transistor-like devices, each device having the exact same geometry as well as identical aluminium and YBCO thicknesses.

- **Cleaning:** 5 minutes in acetone followed by 5 minutes in propanol while using an ultrasonic bath.
- **Dehydration:** 5 minutes on a heating plate at 100 °C.
- **Resist coating:** 6 seconds at 500 rotations per minute followed by 45 seconds at 4000 rotations per minute with SPR700 (1.0).
- **Softbake:** 1 minute on a heating plate at 95 °C.
- **Optical projection lithography:** 2 seconds of exposure time using a x5 lens and a digital mask.
- **Hardbake:** 1 minute on a heating plate at 115 °C.
- **Development:** 45 seconds in MF319 followed by 30 seconds in deionized water while agitating the sample.
- **Ion beam etching:** 28 minutes of etching time. Parameters: $V = 300\ V$, $I = 50\ mA$, $J = 0.3\ mA.cm^{-2}$, $\theta = 30$ °(sample holder's tilt), $T = 5\ °C$ (sample holder's temperature). SIMS: Au, Cu, Ba.
- **Plasma cleaning:** 10 minutes of plasma time. Parameters: $P = 0.2\ Torr$ (chamber's pressure), $d_m(Ar) = 14\ sccm$ (Argon flow rate), $d_m(O_2) = 100\ sccm$ (Oxygen flow rate), $Pw = 1000\ W$.

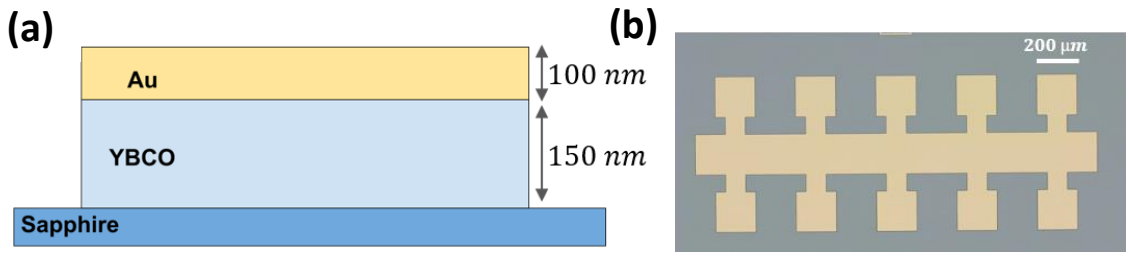

Fig. 6.1: (a) Side-view schematic of the sample after step 1 has been performed. The bars are defined by etching the layers down to the cerium oxide buffer layer. (b) Microscope picture of a typical bar following step 1. In the end, each bar will have 10 transistor-like structures.

- **Cleaning:** 5 minutes in acetone followed by 5 minutes in propanol while using an ultrasonic bath.

1.1.2. Step 2: Etching of the transistors' channels

The second step is the etching of the transistors' channels (see **Fig. 6.2**). The remaining thickness of YBCO will depend on the etching rate and therefore the etching time. Thus, this step is to be done independently on every bar for a thickness of YBCO ranging from $20\ nm$ to $150\ nm$.

- **Cleaning:** 5 minutes in acetone followed by 5 minutes in propanol while using an ultrasonic bath.
- **Dehydration:** 5 minutes on a heating plate at 100 °C.
- **Resist coating:** 6 seconds at 500 rotations per minute followed by 45 seconds at 4000 rotations per minute with SPR700 (1.0).
- **Softbake:** 1 minute on a heating plate at 95 °C.
- **Optical projection lithography:** 1,4 seconds of exposure time using a x5 lens and a digital mask.
- **Hardbake:** 1 minute on a heating plate at 115 °C.
- **Development:** 45 seconds in MF319 followed by 30 seconds in deionized water while agitating the sample.
- **Ion beam etching:** x minutes of etching time, $x \in [7,27]$. Parameters: $V = 300\ V$, $I = 50\ mA$, $J = 0.3\ mA.cm^{-2}$, $\theta = 30$ °(sample holder's tilt), $T = 5\ °C$ (sample holder's temperature). SIMS: Au, Cu, Ba.
- **Plasma cleaning:** 10 minutes of plasma time. Parameters: $P = 0.2\ Torr$ (chamber's pressure), $d_m(Ar) = 14\ sccm$ (Argon flow rate), $d_m(O_2) = 100\ sccm$ (Oxygen flow rate), $Pw = 1000\ W$.
- **Cleaning:** 5 minutes in acetone followed by 5 minutes in propanol while using an ultrasonic bath.

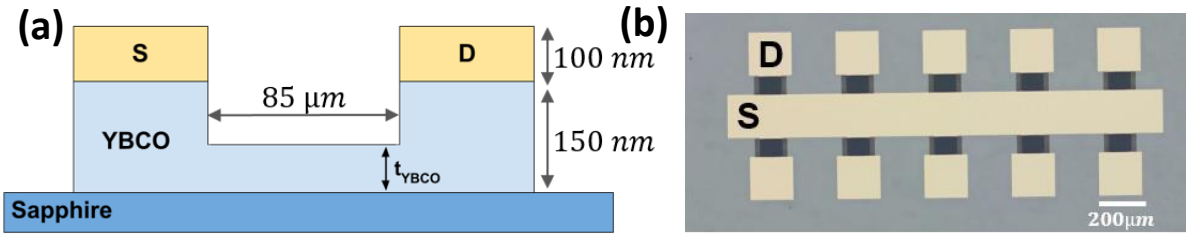

Fig. 6.2: (a) Side-view schematic of the sample after step 2 has been performed. The transistor's channel is defined by etching the gold and YBCO layers using IBE until the desired thickness t_{YBCO} remains via a time-controlled IBE process. (b) Microscope picture of a typical bar following step 2. The black part represents the top of the YBCO channel.

1.1.3. Step 3: Gate and contacts deposition

The third and last step consists in the deposition of the aluminium gate and the gold contacts (see **Fig. 6.3**).

- **Cleaning:** 5 minutes in acetone followed by 5 minutes in propanol while using an ultrasonic bath.
- **Dehydration:** 5 minutes on a heating plate at 100 °C.
- **Resist coating:** 6 seconds at 500 rotations per minute followed by 45 seconds at 4000 rotations per minute with SPR700 (1.0).
- **Softbake:** 1 minute on a heating plate at 95 °C.
- **Chlorobenzene:** 12 minutes in a chlorobenzene bath followed by 1 minute in deionized water.
- **Optical projection lithography:** 4 seconds of exposure time using a x5 lens and a digital mask.
- **Development:** 45 seconds in MF319 followed by 30 seconds in deionized water while agitating the sample.
- **Sputtering deposition:**
  - For the deposition of aluminium: $P = 2.5 \times 10^{-3}\ mbar$, $P_W = 65\ W$, $d_m(Ar) = 60\ sccm$ and $r = 1.25\ \text{Å}.s^{-1}$.
  - For the deposition of gold: $P = 2.5 \times 10^{-3}\ mbar$, $P_W = 95\ W$, $d_m(Ar) = 60\ sccm$ and $r = 9\ \text{Å}.s^{-1}$.
- **Lift-off:** 1h in an acetone bath followed by a few seconds in an ultrasonic bath. Then 5 minutes in propanol.
- **Cleaning:** 5 minutes in acetone followed by 5 minutes in propanol while using an ultrasonic bath.

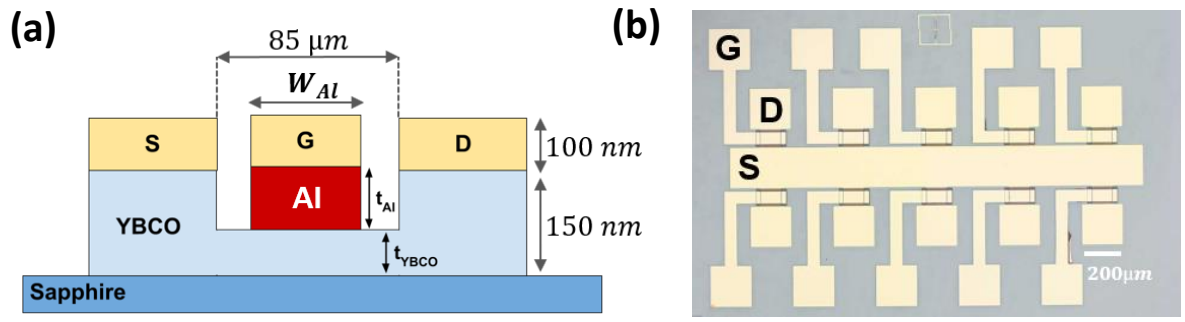

Fig. 6.3: (a) Side-view schematic of the sample after step 3 has been performed. The gate made of aluminium ($t_{Al} = 2\ nm$ or $t_{Al} = 10\ nm$) and gold ($t_{Au} = 100\ nm$) has been deposited using magnetron sputtering. (b) Microscope picture of a typical bar following step 3. The gate contacts are deported far from the Al/YBCO interface to prevent the degradation of the interface while bonding before the transport experiments.

1.2. Aluminium thickness calculations

Chapter 4 is dedicated to the study of the electrochemical properties of transistor-like devices made of the high-temperature cuprate superconductor and aluminium. Aluminium has been chosen for its very low reduction potential ($E^{\circ}(Al) = -1.676\ eV$) compared to the reduction potential of YBCO ($E^{\circ}(YBCO) = 2.4\ eV$). This difference of reduction potential makes the interface between YBCO and Al particularly fitting for the study of oxygen migration mechanisms, such as redox reactions, electromigration and/or thermomigration. In order to estimate the thicknesses of the YBCO and aluminium layers, this annex presents the calculations performed prior to the fabrication processes, based on crystallographic arguments.

Fig. 6.4(a) shows the basic representation of the mathematical problem: the YBCO oxygen-depleted region is generated by oxygen exchanges at the YBCO/Al interface and has a thickness t_d. The main objective is to determine the thickness t_{Al} of Al required to fully deplete the YBCO layer, i.e. to obtain $t_d = t_{YBCO}$.

YBCO crystallizes in an orthorhombic crystal structure due to the CuO chains distortion on the crystallographic parameters [364]. The geometrical constants in the case of YBCO are $a_{YBCO} = 0.382\ nm$, $b_{YBCO} = 0.389\ nm$ and $c_{YBCO} = 1.168\ nm$, leading to the volume of the unit cell (denoted with a lower case v_{YBCO}) being equal to:

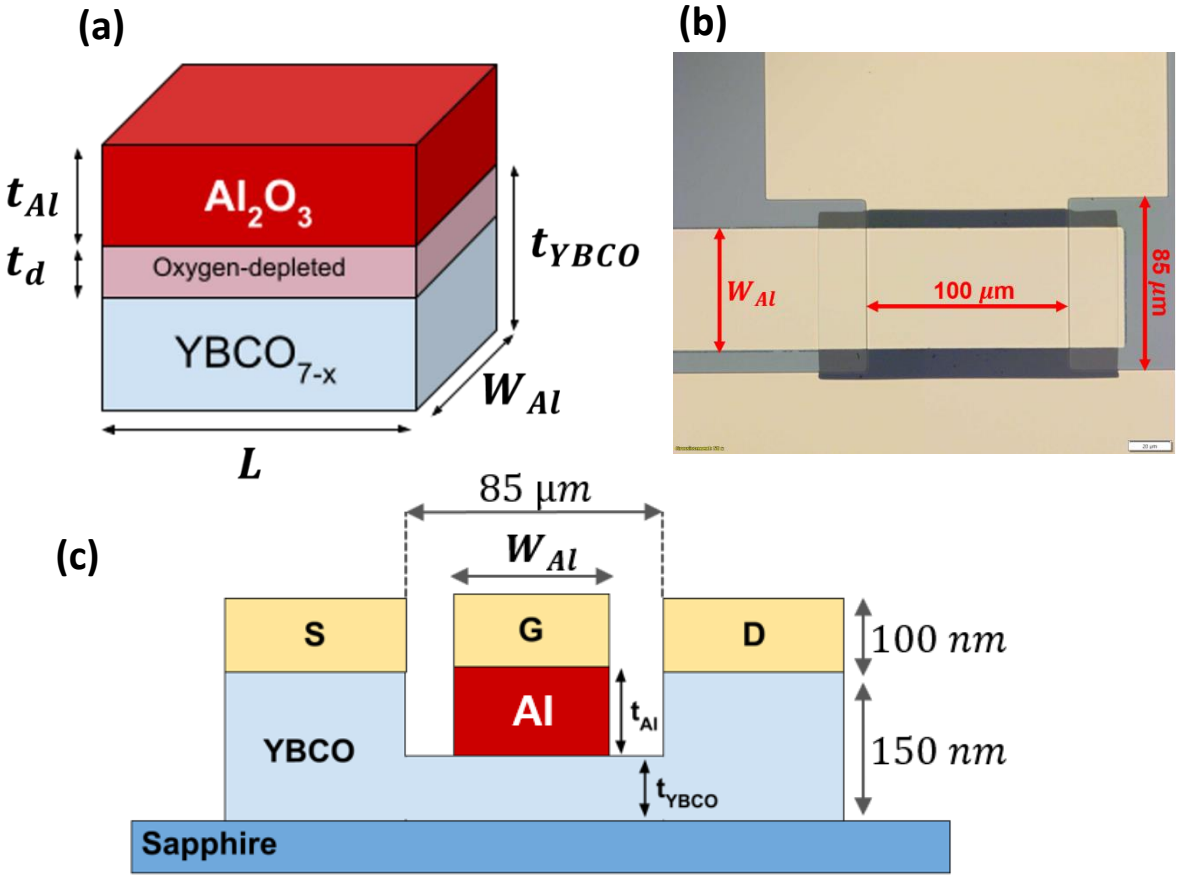

Fig. 6.4: (a) Schematic representation of the interface between aluminium and YBCO. Aluminium pumps oxygen atoms out from the YBCO layer, generating an oxygen-depleted region below the aluminium layer, with a thickness equal to t_d. (b) Microscope picture of a typical device after deposition of the aluminium and gold gating. The distance between the source and drain contacts ($85\ \mu m$) and the lateral dimension of the channel ($L = 100\ \mu m$) are fixed, while the distance W_{Al} is equal to $5\ \mu m$ or $60\ \mu m$. (c) Side-view schematic picture of a superconducting transistor and a summary of the typical distances.

$$v_{YBCO} = a_{YBCO} \cdot b_{YBCO} \cdot c_{YBCO} = 1.736 \times 10^{-28}\ m^3 \quad (6.1)$$

Aluminium oxide Al_2O_3 crystallizes in a trigonal crystal structure with parameters $a_{Al} = b_{Al} = 0.479\ nm$ and $c_{Al} = 1.299\ nm$. These parameters give the volume of the aluminium oxide unit cell:

$$v_{Al} = {a_{Al}}^2 \cdot c_{Al} \cdot \sin(60\ °) = 2.58 \times 10^{-28}\ m^3 \quad (6.2)$$

To oxidize, aluminium requires 3 oxygen atoms per unit cell to be pumped from the YBCO layer. As a consequence, the total number of oxygen atoms required to fully oxidize the full thickness of aluminium is equal to:

$$N = 3 \cdot \frac{V_{Al}}{v_{Al}} \quad (6.3)$$

with $V_{Al} = L \cdot t_{Al} \cdot W_{Al}$ the total volume of the deposited aluminium layer.

Therefore, if one oxygen atom per YBCO unit cell is given to the aluminium for oxidation purposes, we obtain that the total volume of the oxygen-depleted YBCO region is equal to:

$$L \cdot t_d \cdot W_{Al} = N \cdot v_{YBCO} \quad (6.4)$$

After further simplification, we obtain the following relation between t_d and t_{Al}:

$$t_{Al} = \frac{t_d \times v_{Al}}{3 v_{YBCO}} \quad (6.5)$$

During the fabrication process of the transistor-like devices, the thickness of the YBCO channel was thinned down to values of $20\ nm < t_{YBCO} < 150\ nm$. This range of t_{YBCO} leads to the following range for t_{Al} from **Eq. 6.5**:

$$9.9\ nm < t_{Al} < 74.4\ nm \quad (6.6)$$

In conclusion, with the hypothesis that three oxygen atoms per unit cell is needed to oxidize Al and that one oxygen atom per unit cell is taken from YBCO, the required thickness of the Al needed to fully deplete $20\ nm$ of YBCO is equal to $t_{Al} \approx 10\ nm$. This value has been chosen for the work presented in **Chapter 4**, and samples with an aluminium thickness of $2\ nm$ were also fabricated for comparison purposes. Considering the simplicity of the calculations above, this thickness is a rough approximation of the real oxygen-depleted region's thickness. Indeed, as expected from the phase diagram of YBCO, a difference in hole doping equals to $p = 0.1$ is enough to induce a switching between the optimally doped superconducting phase to an insulating behaviour. Consequently, it is possible that less than one oxygen atom per unit cell is expected to migrate to participate in the redox reaction. Moreover, this calculation may not hold true in the case of electro- and thermomigration processes, which require much higher current densities and may alter the reversibility of the switching process, inducing disorder on a much larger length scale compared to the softer redox chemical reactions.

1.3. Microscope pictures of the devices after characterization

This annex presents the microscope pictures obtained on two distinct devices after applying $V_{write} = 11\,V$ for **Fig. 6.5(a)** and $V_{write} = 26\,V$ for **Fig. 6.5(b)**. Both devices displayed the simultaneous reversible and non-reversible effects of the Al/YBCO interface and the YBCO channel as discussed in **Chapter 4, Sect. 4.1.** However, only the second device [**Fig. 6.5(b)**] was studied for voltages high enough to observe a reversible switching of R_{SD} as seen for example in **Fig. 4.29(b)**. This device shows clear signs of degraded areas, particularly pronounced close to the periphery of the Al/YBCO interface, while the first device seems to be almost unchanged by the applied voltages.

In **Chapter 4**, it is shown that the thermomigration of oxygen ions due to high dissipated powers and energies lead to the non-reversible degradation of the superconducting channel. In fact, oxygen ions represent the lighter elements within the YBCO structure and are expected to migrate first when exposed to external stimuli, although at very high voltages and temperature gradients, it is difficult to discard the possibility that other elements (copper, yttrium and barium) may be affected. Here, looking at **Fig. 6.5(b)**, it is evident that for very high voltages the degradation of the YBCO channel is not only governed by the thermomigration of oxygen, as even the gold layer is visibly affected by the application of the writing cycles. Therefore, these microscope pictures indicate that for an intermediate range of voltages, while both reversible and non-reversible effects are concomitantly observed, the device is not visibly degradated by the voltage cycles [**Fig. 6.5(a)**] corroborating the hypothesis that only a motion of oxygen is initially triggered.

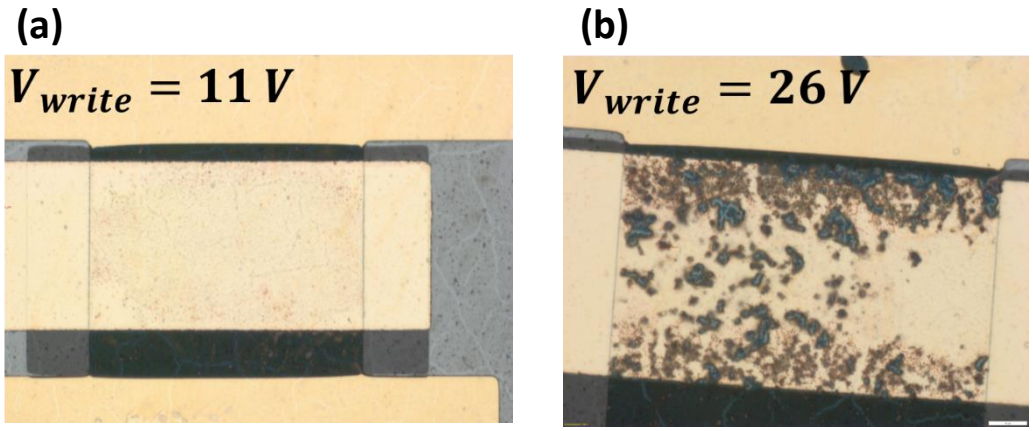

*Fig. 6.5: Microscope pictures of a device after consecutive $G_G(V_{write})$ switching loops up to (a) $-11\,V < V_{write} < 11\,V$ and (b) $-26\,V < V_{write} < 26\,V$. For the former, even though a clear switching of the gate was observed, the device doesn't show any sign of degradation. However, the second device [**Fig. 6.5(b)**] exhibits clear signatures of degradation, with degraded areas more pronounced close to the periphery of the Al/YBCO interface, further supporting the conclusion of a thermally activated migration of oxygen and/or other species at very high voltages.*

2. Annexes: magnetic switching in superconducting spin valve structures

2.1. Fabrication process recipes

In **Fig. 5.12**, I present the various steps of the clean-room microfabrication process and define the two methods that were used for the design of the SSVs. Here, only detail the recipes of method 2 will be presented, considering that both methods had very similar (if not identical) sets of parameters and that method 2 was the one yielding the more reproducible and consistent results. The fabrication was performed on multi-layers STO (001)// YBCO ($30\ nm$)/ LSMO ($15\ nm$)/ YBCO (t_{YBCO})/ FM_2 ($5\ nm$)/ YBCO ($30\ nm$)/ Au ($30\ nm$) samples. The multi-stack was deposited with PLD at the UMR CNRS/Thales as described in **Chapter 3, Sect. 1.**, using the following parameters:

(iv) **For the deposition of YBCO:** $t_{PLD} = 3\ min$ for $\sim 30\ nm$, $P_{O_2} = 0.36\ mbar$, $d_{ts} = 50.85\ mm$, $\rho_{laser} = 8.5\ mJ.mm^{-2}$, $T_{surface} \approx 680\ °C$.

(v) **For the deposition of LSMO:** $t_{PLD} = 2.25\ min$ for $\sim 15\ nm$, $P_{O_2} = 0.2\ mbar$, $d_{ts} = 54.85\ mm$, $\rho_{laser} = 27.5\ mJ.mm^{-2}$, $T_{surface} \approx 660\ °C$.

(vi) **For the deposition of gold:** $t_{PLD} = 10\ min$ for $\sim 30\ nm$, $P_{O_2} = 2 \times 10^{-6}\ mbar$, $d_{ts} = 43.85\ mm$.

2.1.1. Step 1: Etching of the vertical pillars and alignment marks

The first step consists in the etching of the vertical pillars, as well as the alignment marks that will be used for the subsequent alignment of the lithography masks (see **Fig. 6.6**) using ion beam etching IBE. The vertical junctions have a squared cross-section, with a typical size of either $W = 10\ \mu m$ or $W = 20\ \mu m$. As can be seen in **Fig. 6.6(b)**, the size of the junctions alternates between $10 \times 10\ \mu m^2$ and $20 \times 20\ \mu m^2$.

- **Cleaning:** 5 minutes in acetone followed by 5 minutes in propanol while using an ultrasonic bath.
- **Dehydration:** 5 minutes on a heating plate at 95 °C.
- **Resist coating:** 30 seconds at 4000 rotations per minutes with SPR700 (1.0).
- **Softbake:** 1 minute on a heating plate at 95 °C.
- **Laser lithography:** Parameters: $E = 20$, $V = 3$, $O.L = 76\ \%$, $z = 5.88$, $t = 4\ h\ 42\ min$.
- **Development:** 10 seconds in MFCD26 followed by 30 seconds in deionized water while agitating the sample.
- **Ion beam etching:** Parameters: $V = 300\ V$, $I = 45\ mA$, $J = 0.3\ mA.cm^{-2}$, $\theta = 30$ °(sample holder's tilt), $T = 2\ °C$ (sample holder's temperature). SIMS: Au, Ba, La.
- **Plasma cleaning:** 10 minutes of plasma time. Parameters: $P = 0.2\ Torr$ (Chamber's pressure), $d_m(Ar) = 14\ sccm$ (Argon flow rate), $d_m(O_2) = 100\ sccm$ (Oxygen flow rate), $Pw = 1000\ W$.
- **Cleaning:** 5 minutes in acetone followed by 5 minutes in propanol while using an ultrasonic bath.

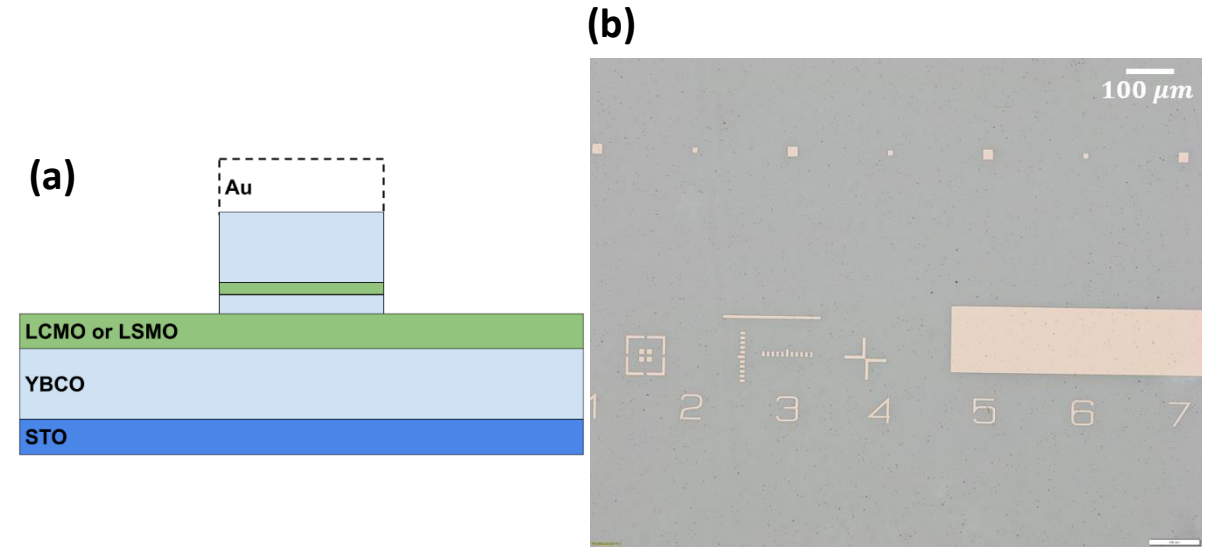

Fig. 6.6: (a) Side-view schematic of the sample after step 1 has been performed. The magnetic pillars have been defined using photolithography and IBE while monitoring the etching process with a SIMS. (b) Microscope picture of the alignment marks and the pillars after step 1. The pillars can be seen in the top part of the picture and alternate between $10x10\ \mu m^2$ *and* $20x20\ \mu m^2$ *junctions.*

2.1.2. Step 2: Etching of the bars

The second step is the etching of the measuring bars down to the STO substrate (see **Fig. 6.7**). A sample is made of four different measuring bars, each bar containing twelve junctions, half of them having a $10 \times 10\ \mu m^2$ pillar size and the other half having a $20 \times 20\ \mu m^2$ pillar size.

- **Cleaning:** 5 minutes in acetone followed by 5 minutes in propanol while using an ultrasonic bath.
- **Dehydration:** 5 minutes on a heating plate at 95 °C.
- **Resist coating:** 30 seconds at 4000 rotations per minutes with SPR700 (1.0).

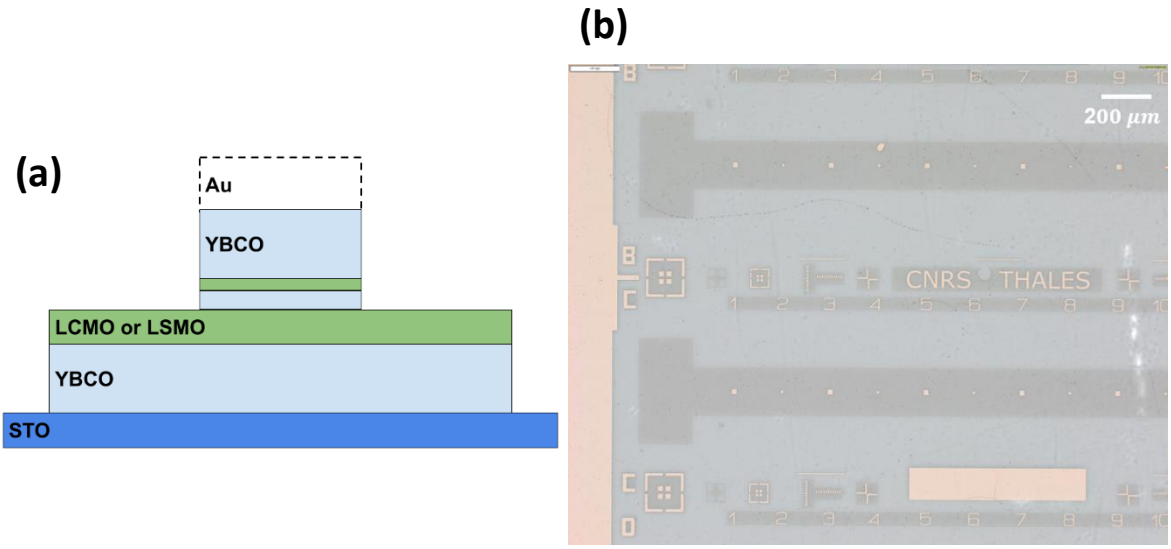

Fig. 6.7: (a) Side-view schematic of the sample after step 2 has been performed. IBE is used to shape the measuring bars. (b) Microscope picture of the sample after step 2. Two bars are visible in ***Fig. 5(b)*** *as well as the alignment marks that have been protected with resist coating.*

- **Softbake:** 1 minute on a heating plate at 95 °C.
- **Laser lithography:** Parameters: $E = 20, V = 3, O.L = 76\ \%, z = 5.88, t = \ min.$
- **Development:** 12 seconds in MFCD26 followed by 30 seconds in deionized water while agitating the sample.
- **Ion beam etching:** Parameters: $V = 300\ V, I = 45\ mA, J = 0.3\ mA.cm^{-2}, \theta = 30$ °(sample holder's tilt), $T = 2\ °C$ (sample holder's temperature). SIMS: Au, Ba, La.
- **Plasma cleaning:** 10 minutes of plasma time. Parameters: $P = 0.2\ Torr$ (Chamber's pressure), $d_m(Ar) = 14\ sccm$ (Argon flow rate), $d_m(O_2) = 100\ sccm$ (Oxygen flow rate), $Pw = 1000\ W$.
- **Cleaning:** 5 minutes in acetone followed by 5 minutes in propanol while using an ultrasonic bath.

2.1.3. Step 3: Top contacts definition

In this third step, IBE is used to etch the top gold layer in order to define the top contacts of each junction (see **Fig. 6.8**). This step is crucial for the geometry of the system, as it allows 4-point measurements to be performed.

- **Cleaning:** 5 minutes in acetone followed by 5 minutes in propanol while using an ultrasonic bath.
- **Dehydration:** 5 minutes on a heating plate at 95 °C.
- **Resist coating:** 30 seconds at 4000 rotations per minutes with SPR700 (1.0).
- **Softbake:** 1 minute on a heating plate at 95 °C.
- **Laser lithography:** Parameters: $E = 20, V = 2, O.L = 76\ \%, z = 5.88, t = \ min.$
- **Development:** 10 seconds in MFCD26 followed by 30 seconds in deionized water while agitating the sample.
- **Ion beam etching:** Parameters: $V = 300\ V, I = 45\ mA, J = 0.3\ mA.cm^{-2}, \theta = 30$ °(sample holder's tilt), $T = 2\ °C$ (sample holder's temperature). SIMS: Au, Ba, La.

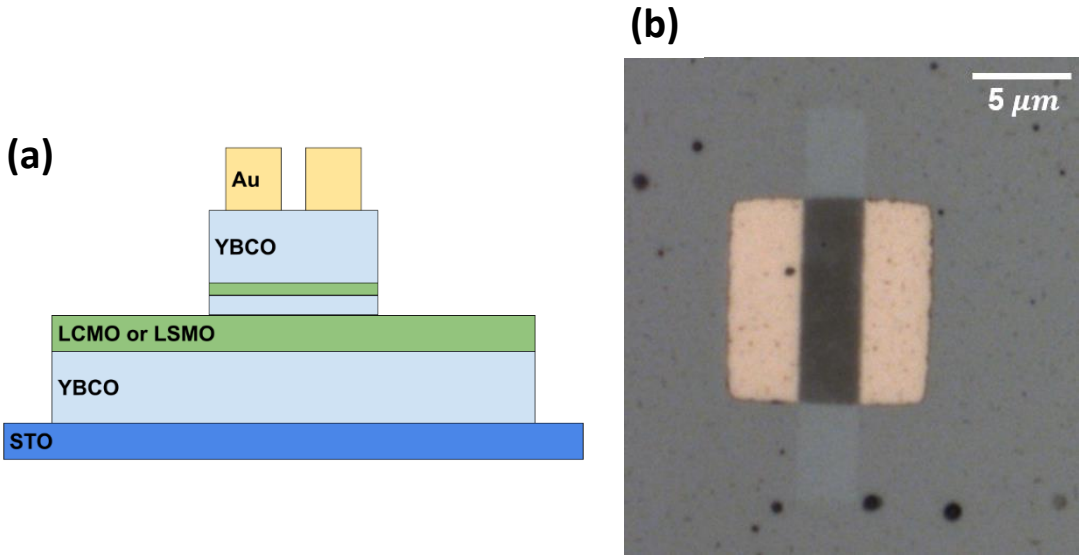

Fig. 6.8: (a) Side-view schematic of the sample after step 3 has been performed. The top gold layer has been divided into two distinct contacts to allow for a 4-probe measurement of the SSVs. (b) Microscope picture of a junction of step 3. We ca clearly distinguish between the two top contacts.

- **Plasma cleaning:** 10 minutes of plasma time. Parameters: $P = 0.2\ Torr$ (Chamber's pressure), $d_m(Ar) = 14\ sccm$ (Argon flow rate), $d_m(O_2) = 100\ sccm$ (Oxygen flow rate), $Pw = 1000\ W$.
- **Cleaning:** 5 minutes in acetone followed by 5 minutes in propanol while using an ultrasonic bath.

2.1.4. Step 4: Opening of junctions and permanent bake

Step 4 consists in protecting the whole sample with resist and opening a hole on top of each junction in order to subsequently deposit the contact layer during the next step (see **Fig. 6.9**). After the aperture is opened, the resist is permanently baked.

- **Cleaning:** 5 minutes in acetone followed by 5 minutes in propanol while using an ultrasonic bath.
- **Dehydration:** 5 minutes on a heating plate at 95 °C.
- **Resist coating:** 30 seconds at 4000 rotations per minutes with S1805 50/50.
- **Softbake:** 1 minute on a heating plate at 110 °C.
- **Laser lithography:** Parameters: $E = 12, V = 1, O.L = 50\ \%, z = 5.88, t = 6\ h\ 21\ min.$
- **Hardbake:** 1 minute on a heating plate at 110 °C.
- **Development:** 5 seconds in MF319 followed by 30 seconds in deionized water while agitating the sample.
- **Plasma cleaning:** 2 minutes of plasma time. Parameters: $P = 0.2\ Torr$ (Chamber's pressure), $d_m(Ar) = 14\ sccm$ (Argon flow rate), $d_m(O_2) = 100\ sccm$ (Oxygen flow rate), $Pw = 1000\ W$.
- **Permanent bake:** 1 minute on a heating plate at 170 °C.

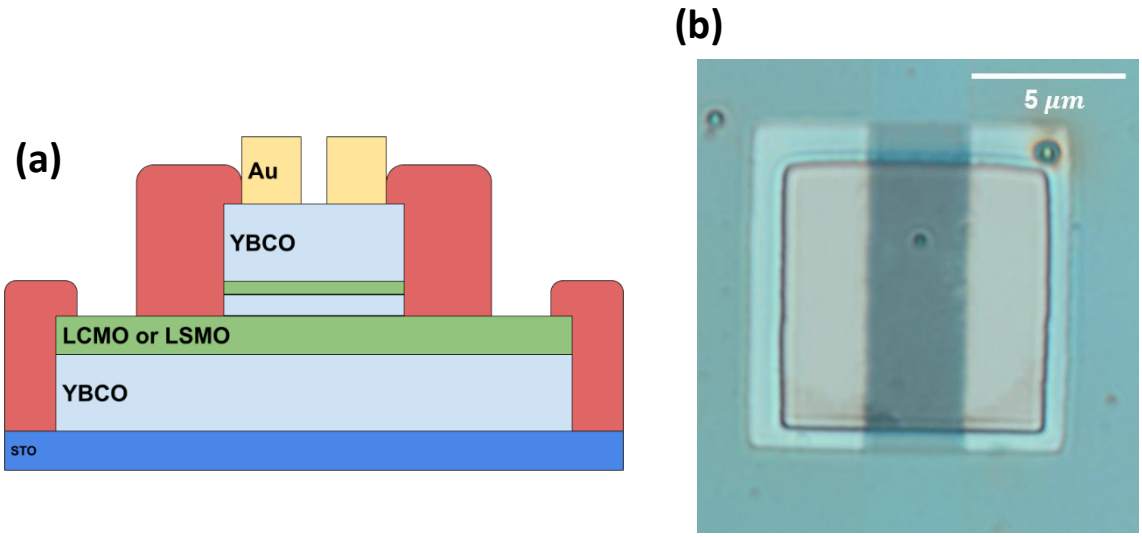

Fig. 6.9: (a) Side-view schematic of the sample after step 4 has been performed. The resist S1805 is used to coat most of the sample's surface: only a small aperture on top of each junction has been unscathed. Then the resist is permanently baked by heating the sample with a high enough temperature.

2.1.5. Step 5: Top electrodes deposition

The last fabrication step consists in the deposition of the deported top electrodes on top of the permanently baked insulating resist (see **Fig. 6.10**).

- **Cleaning:** 5 minutes in acetone followed by 5 minutes in propanol while using an ultrasonic bath.
- **Dehydration:** 5 minutes on a heating plate at 95 °C.
- **Resist coating:** 30 seconds at 4000 rotations per minutes with SPR700 (1.0).
- **Softbake:** 1 minute on a heating plate at 95 °C.
- **Chlorobenzene:** 12 minutes in a chlorobenzene bath followed by 1 minute in deionized water.
- **Hardbake:** 1 minute on a heating plate at 95 °C.
- **Laser lithography:** Parameters: $E = 20, V = 3, O.L = 76\ \%, z = 5.88, t = 3\ h\ 44\ min.$
- **Development:** 45 seconds in MFCD26 followed by 30 seconds in deionized water while agitating the sample.
- **Deposition:**
- **Lift-off:** 1h in an acetone bath followed by a few seconds in an ultrasonic bath. Then 5 minutes in propanol.

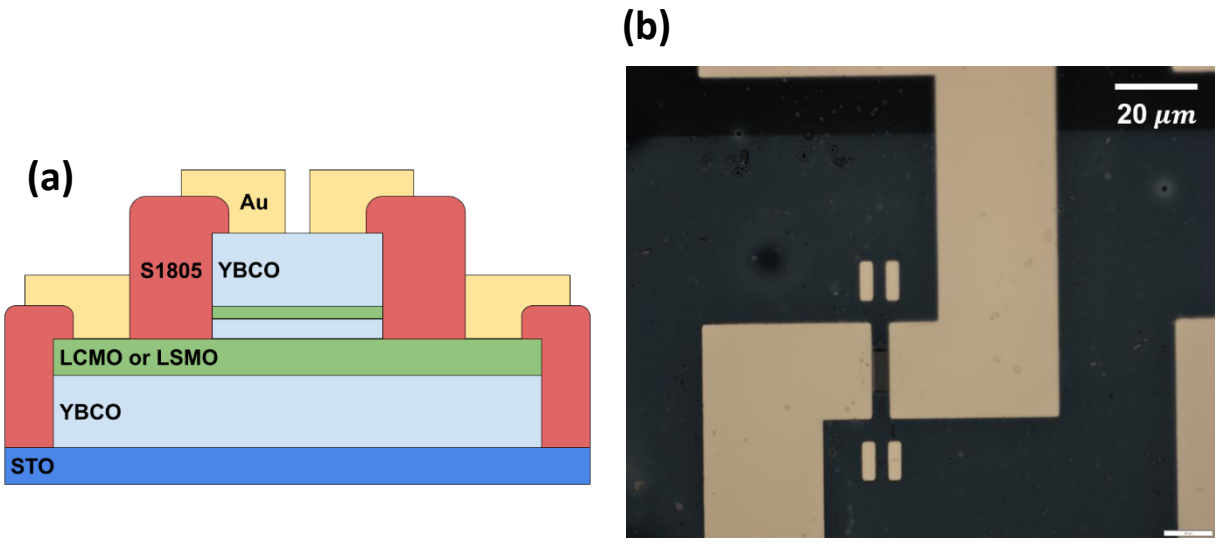

Fig. 6.10: (a) Side-view schematic of the sample after step 5 has been performed. The deported contact electrodes are deposited on top of the insulating resist. (b) Microscope picture of the top electrodes. In the middle, we can notice the top part of the magnetic pillar.

2.2. Magnetoresistance reversal with temperature

In **Fig. 5.17**, the reversal of the magnetoresistance from positive to negative was observed while decreasing the temperature and the injected current for a particular SSV. In this annex, the magnetoresistance measurements for all temperatures and all currents are shown for the sake of completeness. The temperature was varied between $15\ K$ and $60\ K$ with two different biasing currents: $I = 0.2\ mA$ (**Fig. 6.11**) and $I = 0.15\ mA$ (**Fig. 6.12**).

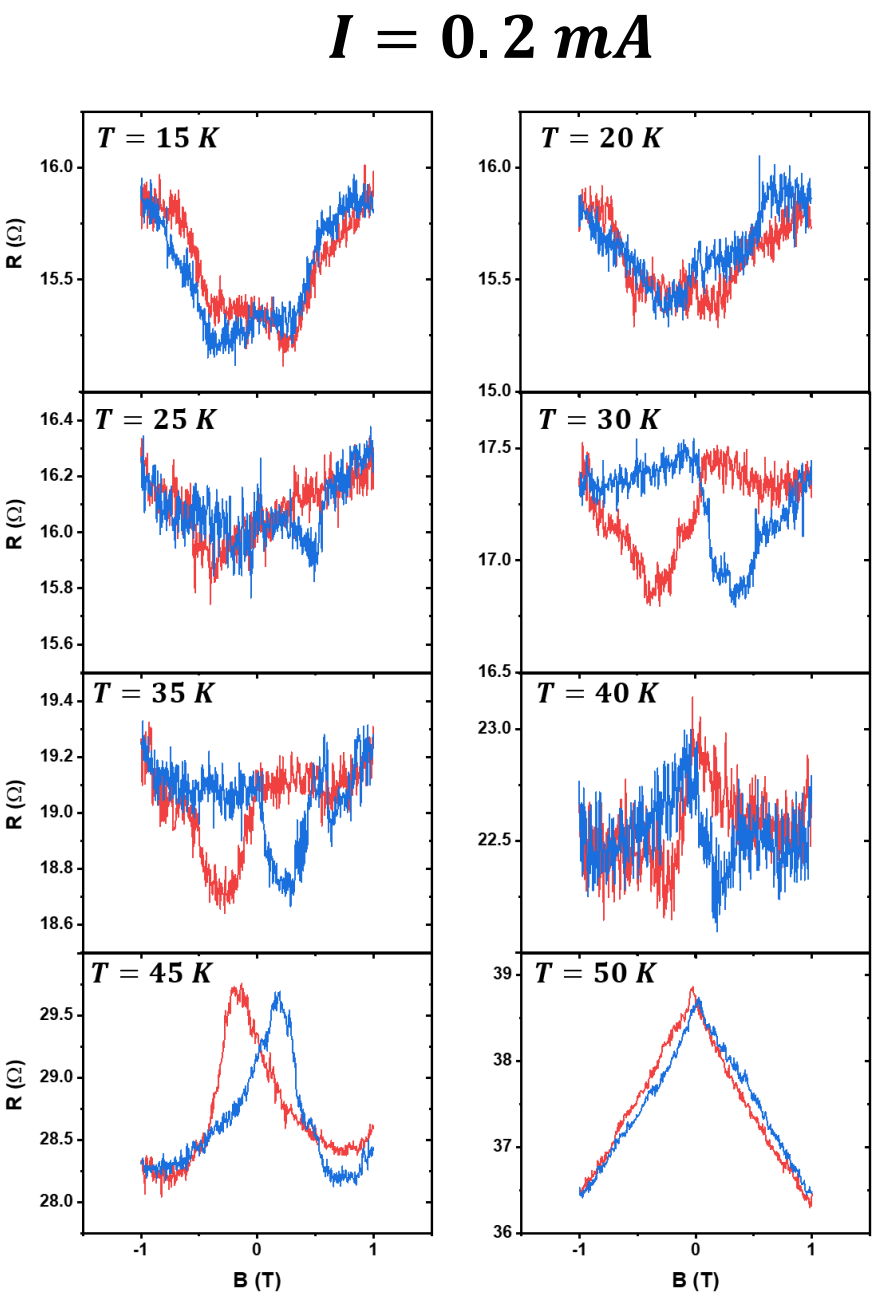

Fig. 6.11: Magnetoresistance measurements done on a SSV from sample SY2 ($t_{YBCO} = 5\ nm$) with a biasing current of $I = 0.20\ mA$ for $15\ K < T < 50\ K$.

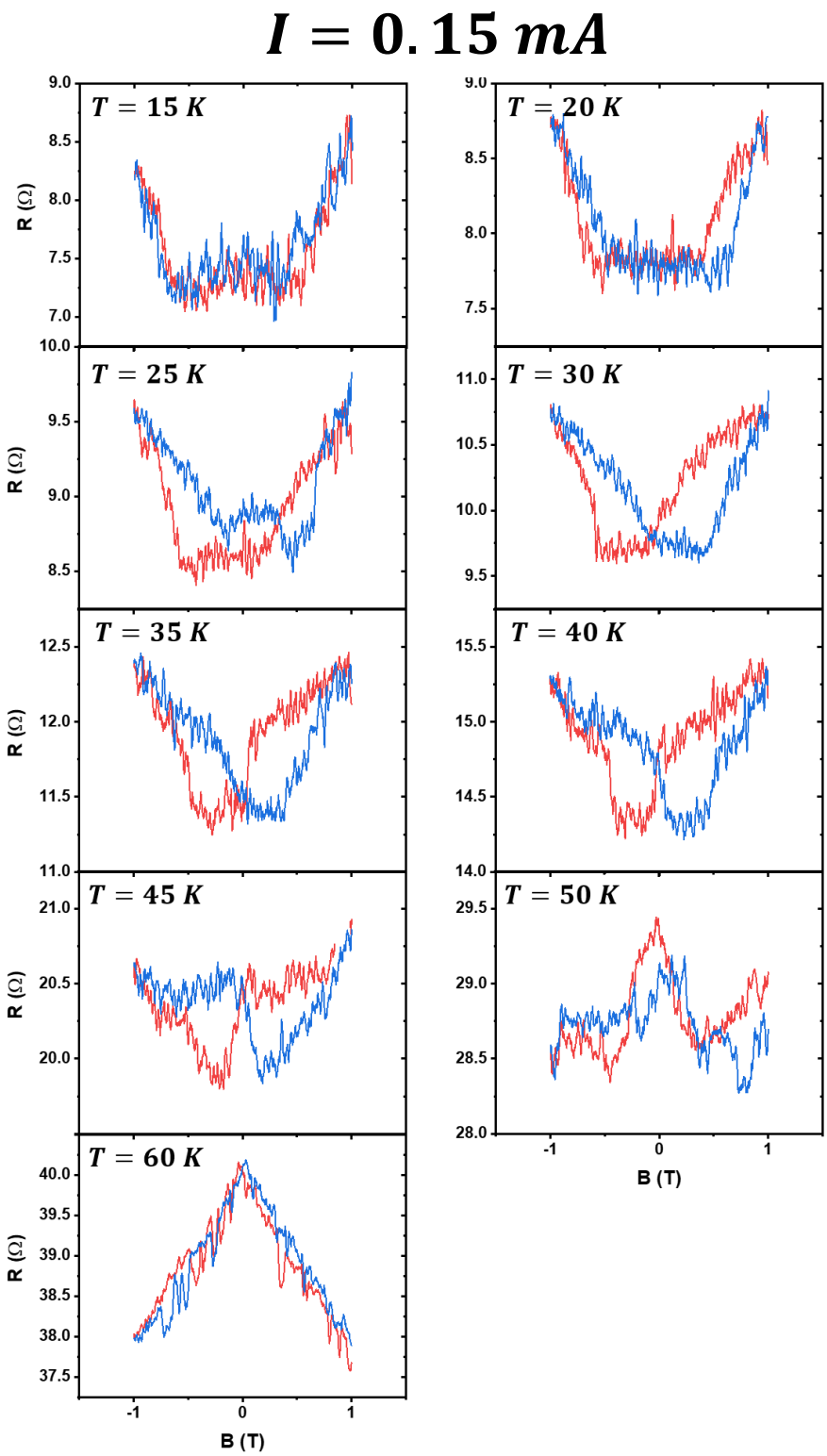

Fig. 6.12: Magnetoresistance measurements done on a SSV from sample SY2 ($t_{YBCO} = 5\ nm$) with a biasing current of $I = 0.15\ mA$ for $15\ K < T < 50\ K$.

2.3. Fitting of the magnetization hysteresis loop at $15\ K$

The magnetization hysteresis loop of type-II superconductors under application of an external magnetic field is well described by Bean's critical state model [365], later extended by Kim *et al.* [366] and Anderson *et al.* [367] into what is now known as the Kim-Anderson (KA) model [368]. In this model, the total magnetization of the film is equal to:

$$M_{KA}(B) = M_{c0}\frac{1}{1+{|B|}/{B_0}} \tag{6.7}$$

where M_{c0} and B_0 are constants.

On the other hand, one of the typical model used to describe the behaviour of a FMs' magnetization is called the Jiles-Atherton (JA) model [25], developed in 1986. In the simplest possible picture, considering an isotropic ferromagnetic material, the magnetization takes the mathematical form:

$$M_{JA}(B) = M_S\left(\coth\left(\frac{B}{a}\right) - \frac{a}{B}\right) \tag{6.8}$$

where M_S is the saturation magnetization in $A\cdot m^{-1}$ and a (also in $A\cdot m^{-1}$) is characteristic of the domain wall density in the magnetic material.

Fig. 6.13 shows the fitting of the magnetization in the superconducting state, taken from **Fig. 5.24(b),** by assuming that the magnetization is the sum of **Eq. 6.7** and **Eq. 6.8**. Although the final fitting (red dotted line) does not seem to simulate all of the features of the $M(B)$ curve, it gives a good approximation of the expected shape of the magnetization.

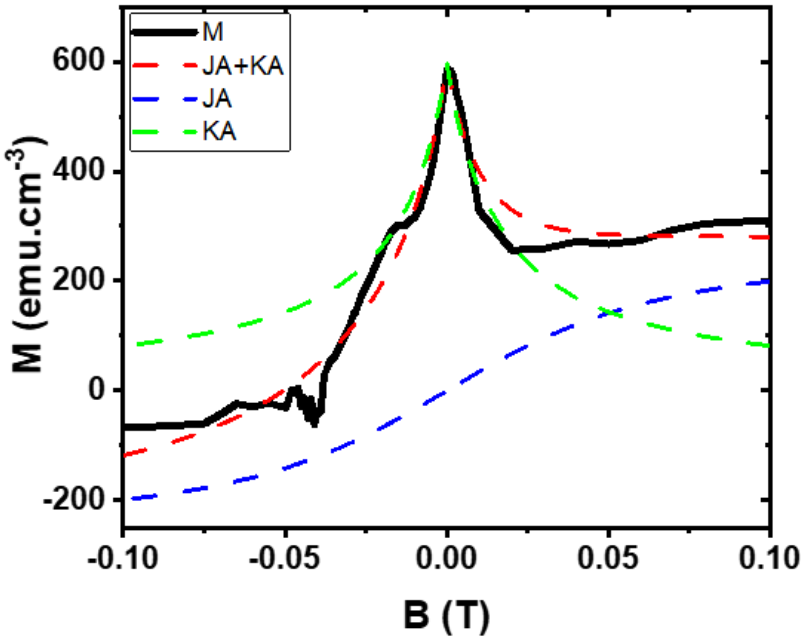

*Fig. 6.13: Fitting of the $M(B)$ hysteresis loop [taken from **Fig. 5.24(b)**] as the sum of a superconducting contribution (green dashed line, Kim-Anderson model) and a ferromagnetic contribution (blue dashed line, Jiles-Atherton model). The sum of both contributions equals to the red dotted line, roughly simulating the behaviour of the observed magnetization.*

2.4. $R(T)$, current-voltage characteristics and diode-like behaviour of *ex-situ* samples

Fig. 6.14 displays typical $R(T)$ measurements in semi-log scale [**Fig. 6.14(a)**] and in linear scale [**Fig. 6.14(b)**] of a SSV from sample REAL3 (*ex-situ*) with $t_{YBCO} = 8\,nm$. Although the resistance is decreasing by two orders of magnitude between $110\,K$ and $10\,K$, the $R(T)$ doesn't show a clear superconducting transition. The inset of **Fig. 6.14(a)** displays the first derivative of the main figure as a function of temperature. Below $90\,K$, two distinct peaks can be distinguished, for temperatures of $T_{C1} = 80\,K$ and $T_{C2} = 21\,K$. These two temperatures probably correspond to the superconducting T_C of two distinct superconducting layers, the highest one ($T_{c1} = 80\,K$) corresponding to the bottom and top YBCO layers while the lowest one ($T_{c2} = 21\,K$) might characterize the superconducting YBCO spacer.

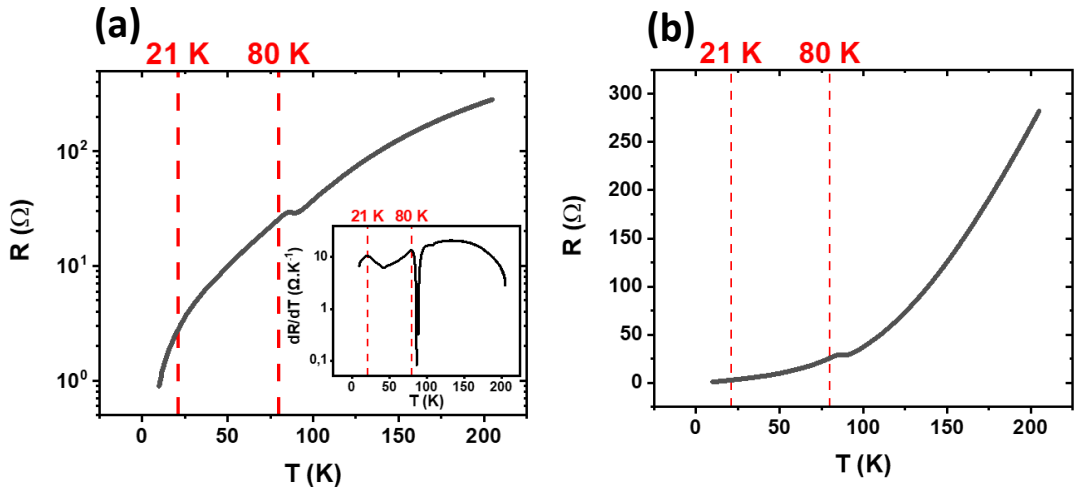

*Fig. 6.14: Measurements done on a SSV from sample REAL3 with $t_{YBCO} = 8\,nm$ displaying the $R(T)$ in a (a) semi-log scale and (b) linear scale. The first derivative of the $R(T)$ is shown in the inset of **Fig. 6.14(a)**. We can distinguish two peaks below $90\,K$, giving two critical temperatures of $80\,K$ and $21\,K$, probably corresponding to the bottom/top layers ($30\,nm$) and the YBCO spacer, respectively.*

I-V characteristics for the same junction as the one studied in **Fig. 6.14** are shown in **Fig. 6.15(a)**, while the inset is the same set of data in log-log scale. Two main features appear from this figure:

(i) The measured voltage spans on more than 2 orders of magnitude (from $10^{-4}\,V$ to $8 \times 10^{-7}\,V$) at low current for temperatures between $120\,K$ and $10\,K$. This very high difference is likely to be induced by the superconducting transition of the YBCO layer, leading to a strong decrease of the voltage (or equivalently, the resistance).

(ii) A recurring feature of this type of experiment on *ex-situ* samples is the highly asymmetric shape of the I-V characteristics. At higher positive current bias, a clear bending of the current-voltage characteristics is seen for all temperatures. As this behaviour is present at temperatures higher than the optimal superconducting critical temperature of YBCO of $\sim 93\,K$, superconductivity can be ruled out from playing a major role in this phenomenon. It can be attributed to the presence of a diode-like behaviour of the YBCO/Au interface (with Au being deposited by magnetron sputtering) leading to Joule heating for high injected positive current. This kind of semiconducting effects can arise at the interface between a metal and a semiconductor.

The diode current I_D is defined in this experiments as the value of the current for which the diode-like behaviour arises and is plotted as a function of the temperature in **Fig. 6.15(c)** for 5 different SSVs showing the same behaviour as the one described in **Fig. 6.15(a)**. For low temperatures, we first observe an increase of I_D followed by a gradual decrease after reaching a temperature threshold that is device-dependent.

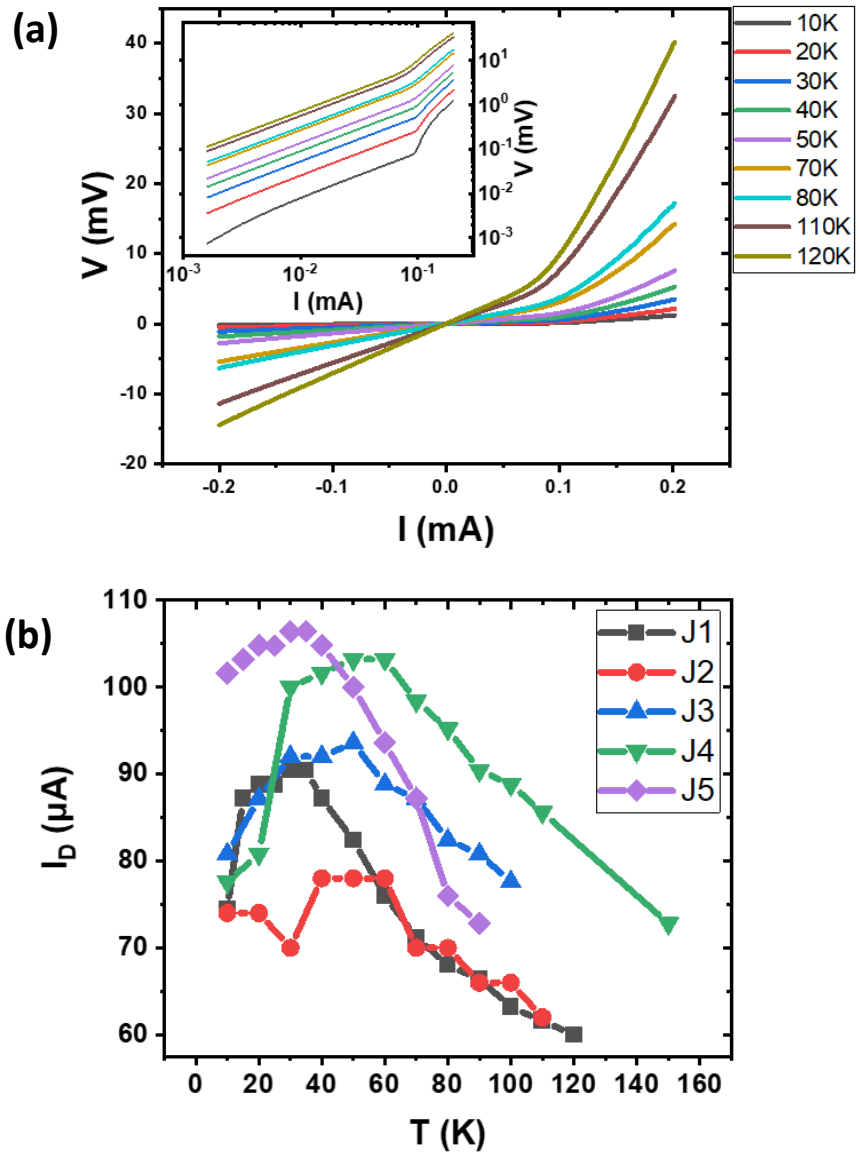

Fig. 6.15: (a) I-V characteristics typical of junctions from ex-situ samples for $10\ K < T < 120\ K$. The inset shows the identical set of measurements in a log-log scale illustrating that the junction's resistance goes down by more than two orders of magnitude between $120\ K$ and $10\ K$, hinting to the presence of a superconducting transition. Moreover, for all temperatures (and strikingly above $93\ K$) the curves are highly asymmetric. This behaviour might be due to the presence of a diode-like behaviour of the YBCO/Au interface, leading to Joule heating above the diode current I_D. (b) $I_D(T)$ for five junctions from sample REAL3, labelled J1 to J5. First, for low temperatures, this current is rising to a maximum that is device-dependent before reducing with increasing temperatures.

2.5. Magnetoresistance reversal with current

In **Chapter 5, Sect. 4.4.2.**, it is shown that a reversal of the magnetoresistance was observed while decreasing the temperature. A similar reversal was also observed while decreasing the injected current at a fixed temperature. This effect is illustrated in **Fig. 6.16**, showing the magnetoresistance measured at $10\ K$ for a junction with $t_{YBCO} = 8\ nm$ for two different currents: $I = 100\ \mu A$ [**Fig. 6.16(a)**] and $I = 10\ \mu A$ [**Fig. 6.16(b)**]. Although the values of the switching field $B_S^{\pm} \approx \pm 45\ mT$ for both currents, the sign of the SVE is reversed [$\Delta R > 0$ in **Fig. 6.16(a)** and $\Delta R < 0$ in **Fig. 6.16(b)**], showing that reducing the current and reducing the temperature yield the same reversal behaviour.

Interestingly, **Fig. 6.16(c)** shows that for the same absolute value of the current $|I| = 100\ \mu A$, the sign of the SVE can be opposite. This effect is probably caused by the local heating of the sample due to the semiconducting diode-like barrier discussed in **Annexes, Sect. 2.4.** In fact, we can observe from the I-V characteristic in **Fig. 6.16(d)** that $I_D \approx 90\ \mu A$, meaning that a current of $100\ \mu A$ can trigger thermal runaway leading to an increase of the local temperature of the junction via Joule heating. The rise in temperature can lead to the reversal of the sign of the spin valve effect in the same way it could be reversed from positive to negative by decreasing the temperature in **Fig. 5.26**. However, for a current of $-100\ \mu A$, the diode effect is not triggered, and the SVE is observed.

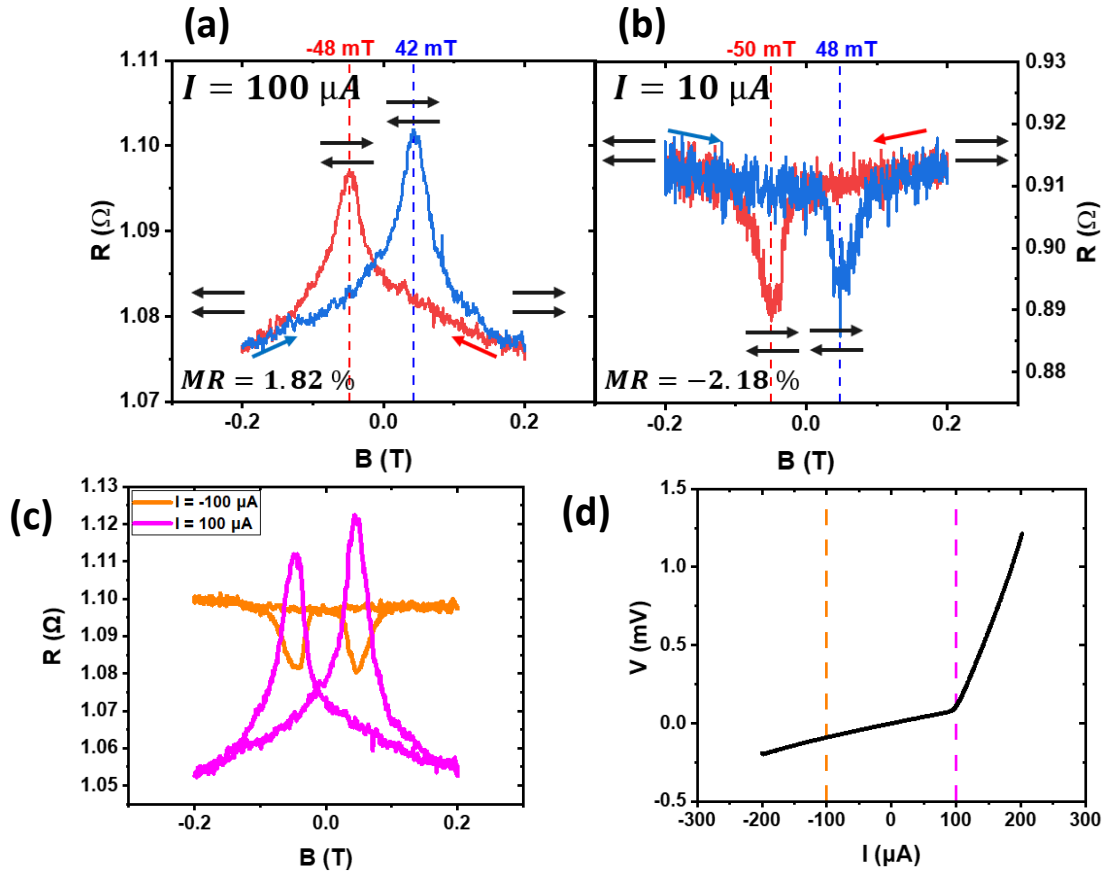

*Fig. 6.16: Measurements done on a SSV from sample REAL3 with $t_{YBCO} = 8\ nm$ at $10\ K$, displaying the magnetoresistance for a biasing current of (a) $100\ \mu A$ and (b) $10\ \mu A$. The magnetoresistance reverses between a positive SVE to a negative SVE. (c) Magnetoresistance for a current of $+100\ \mu A$ (purple curve) and $-100\ \mu A$ (orange curve). For the same absolute value of the current, the polarity of the SVE is opposite. (d) I-V characteristic at $T = 10\ K$ showing the diode-like behaviour of the I-V for currents above $I_D = 90\ \mu A$. The purple and orange dashed lines represent the values of $I = \pm 100\ \mu A$ used to measure the magnetoresistance displayed in **Fig. 6.16(a)**.*

2.6. Evolution of the switching magnetic field with temperature

As is demonstrated numerous times in the magnetoresistance measurements presented in **Chapter 5**, the peaks and dips characteristic of the positive and negative SVEs are reaching maxima and minima for switching magnetic fields that are temperature-dependent [see for example **Fig. 5.17**, **Fig. 5.18** and **Fig. 5.26**]. I demonstrated that the values of the switching fields $B_S^{\pm}$ coincide with the AP configuration of the spin valve in **Fig. 5.28**. Therefore, as the coercive fields are getting enlarged with decreasing temperatures, it is expected for the switching fields to equally vary with temperature.

Typically, the temperature-dependence of B_C of various ferromagnets has been shown to follow an exponential law in various papers [369,370]:

$$B_C(T) = B_0 \exp(^{-T}/_{T_0}) \tag{6.9}$$

Fig. 6.17 shows a 2d-colorplot of the normalized 4-probe resistance of a junction from sample REAL3 with $t_{YBCO} = 8\,nm$ as a function of the temperature (y-axis) and the magnetic field (x-axis), measured with a biasing current of $I = 10\ \mu A$. This particular junction did not exhibit any signatures of a negative SVE even for low temperatures. However, the broadening of the switching magnetic field as the temperature decreases is clear, increasing from $B_S^{\pm} = \pm 15\,mT$ at $90\,K$ to $B_S^{\pm} = \pm 50\,mT$ at $10\,K$. The fitting of the exponential law from **Eq. 6.9** is plotted in red dotted points in **Fig. 6.17** with fitting parameters of $B_0 = 0.061\,T$ and $T_0 = 60.04\,K$. The exponential law does not seem to properly fit the shape of $B_C(T)$. In fact, we observe that the coercive field is almost constant for temperatures above $\sim 40\,K$ and increases faster for lower temperatures, a feature that indicates that superconductivity might play a role in the fast increase of B_C. The MR measurements that were used to plot **Fig. 6.17** are shown for all temperatures in **Fig. 6.18**.

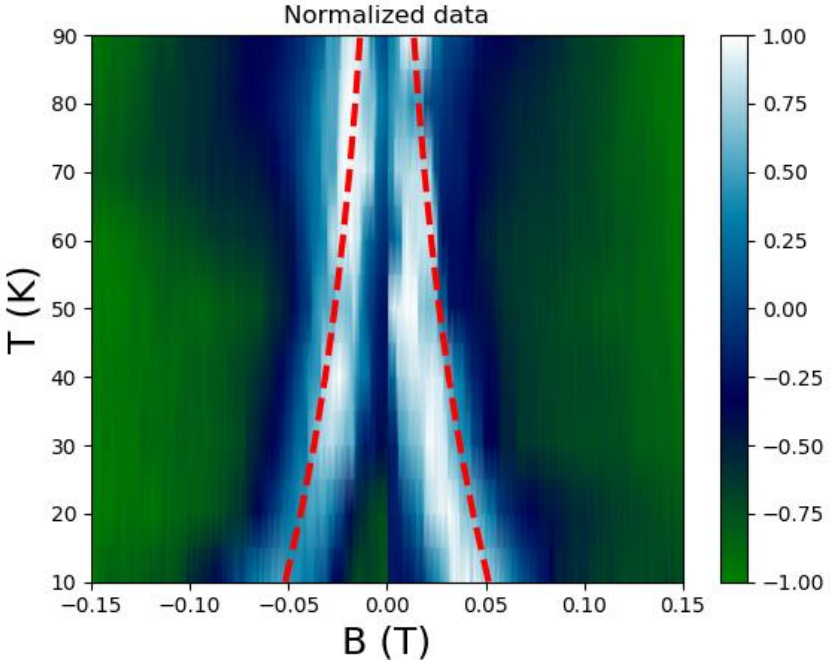

*Fig. 6.17: 2d-colorplot of the normalized resistance of a SSV from sample REAL3 ($t_{YBCO} = 8\,nm$) measured with a biasing current of $10\ \mu A$ as a function of the temperature (y-axis) and the magnetic field (x-axis). The red dashed lines represent the fitting of the switching magnetic field as a function of the temperature calculated from the exponential law (**Eq. 6.9**).*

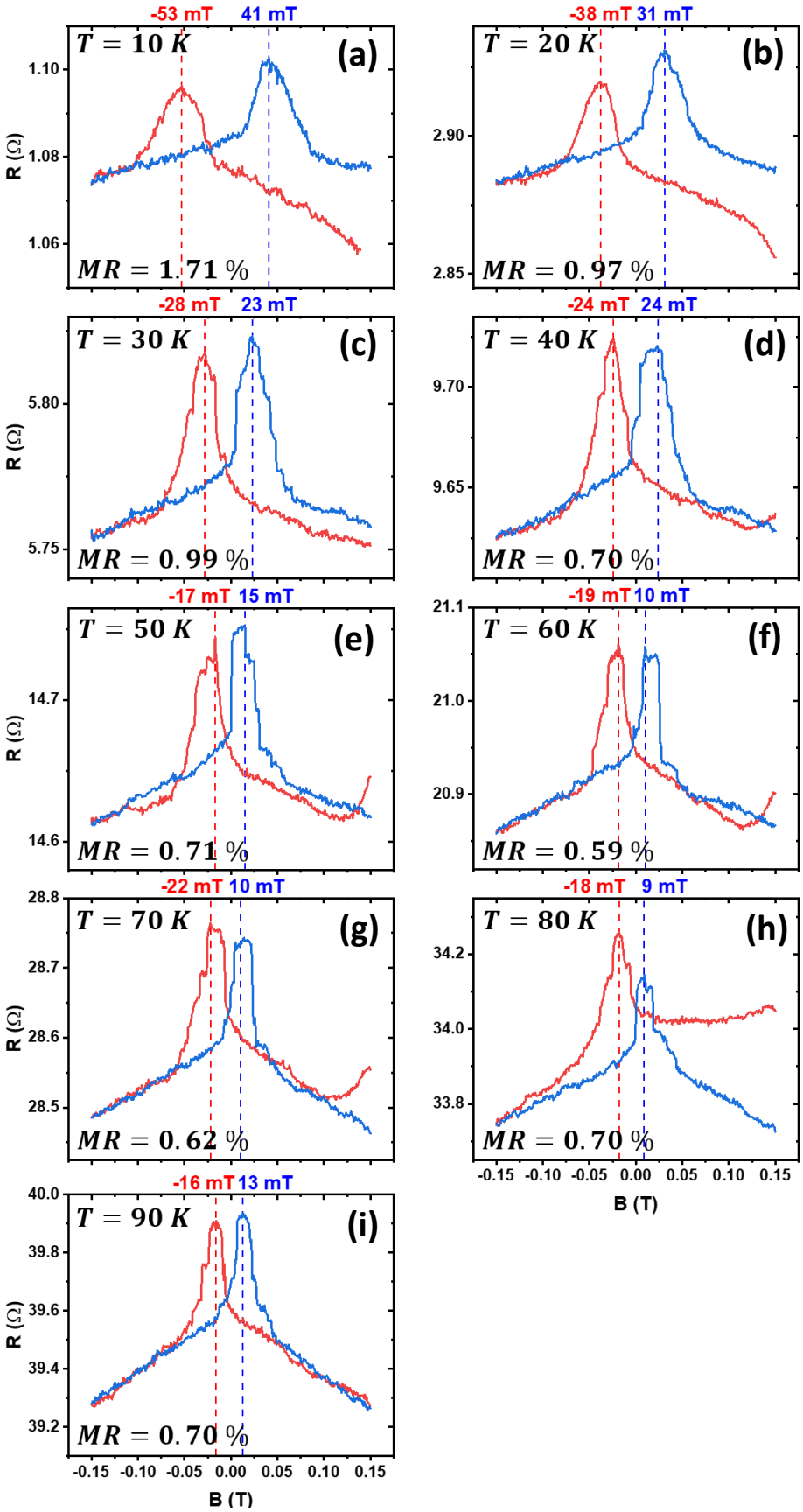

Fig. 6.18: Magnetoresistance measured for a SSV from sample REAL3 with $t_{YBCO} = 8\ nm$ and $I = 10\ \mu A$ for fixed temperatures between $10\ K$ and $90\ K$. The values of $B_S^{\pm}$ are shown via the vertical dashed lines and one can observe a clear increase of the switching fields for decreasing temperatures.

2.7. Magnetoresistance measurements, sample REAL1

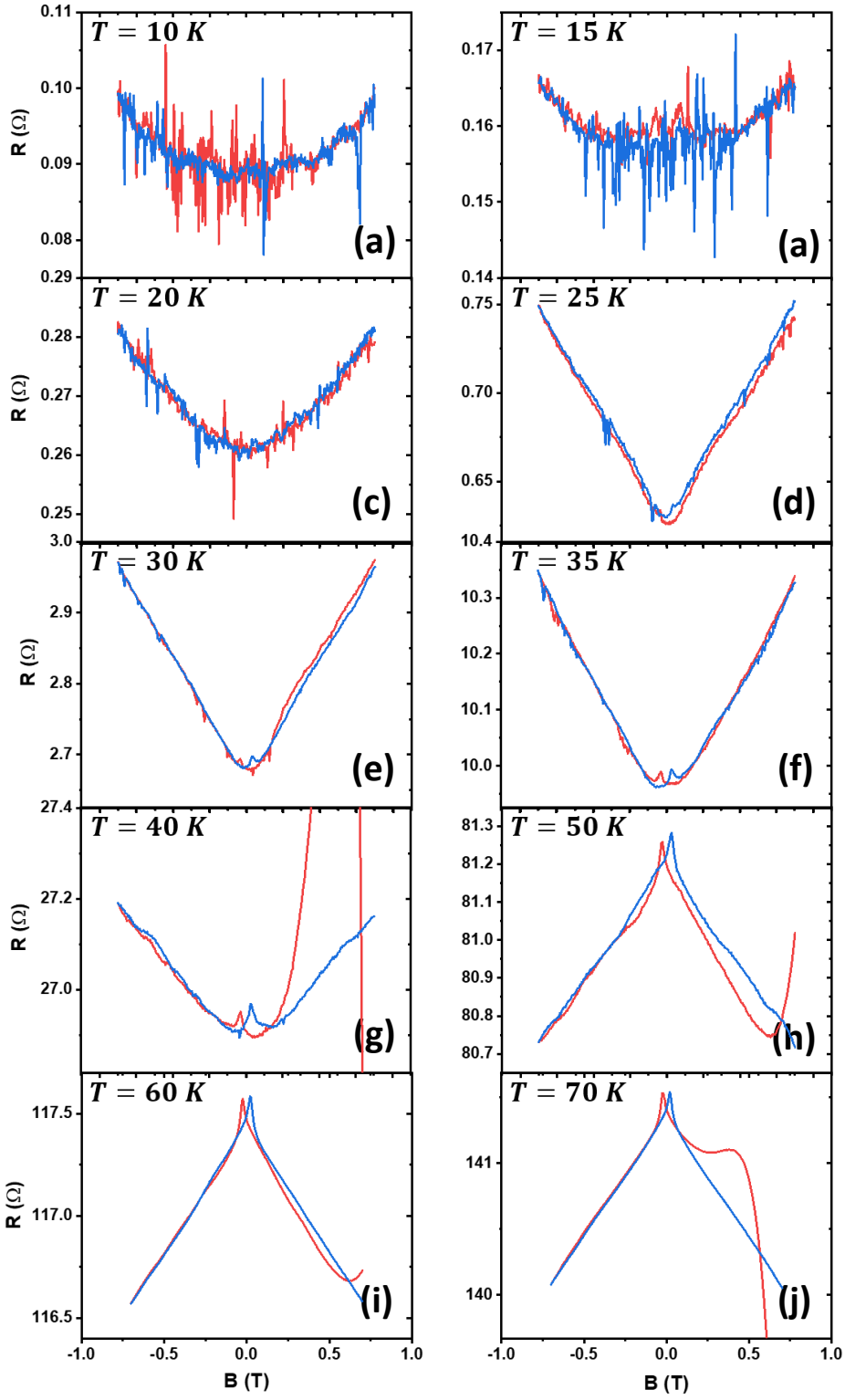

Fig. 6.19: Magnetoresistance measurements done for a SSV from sample REAL1 with $t_{YBCO} = 3$ nm with a biasing current of $100\ \mu A$ for $10\ K < T < 70\ K$. The large variations of the red curves for (g), (h) and (j) for high magnetic fields represent a spurious experimental effect due to an unstable temperature at the start of the data acquisition.

2.8. Magnetoresistance reversal with angle

Magnetoresistance measurements as a function of the in-plane angle θ of the applied magnetic field were carried on various SSVs from batches 3 and 4. Interestingly, a reversal of the SVE from positive to negative could be observed for some junctions while rotating the in-plane magnetic field. This property is depicted in **Fig. 6.20**, showing the magnetoresistance measured at $30\,K$ with $I = 10\,\mu A$ for an incident angle of $\theta = 15\,°$ [**Fig. 6.20(a)**] and $\theta = 75\,°$ [**Fig. 6.20(b)**] on a junction from sample REAL3 with $t_{YBCO} = 8\,nm$. It is important to mention that the behaviour described in this section was observed while measuring only two particular SSVs and that the general shape of the magnetoresistance was untypical compared to the reproducible magnetoresistance reversal with temperature presented in **Chapter 5, Sect. 4.4.2.**

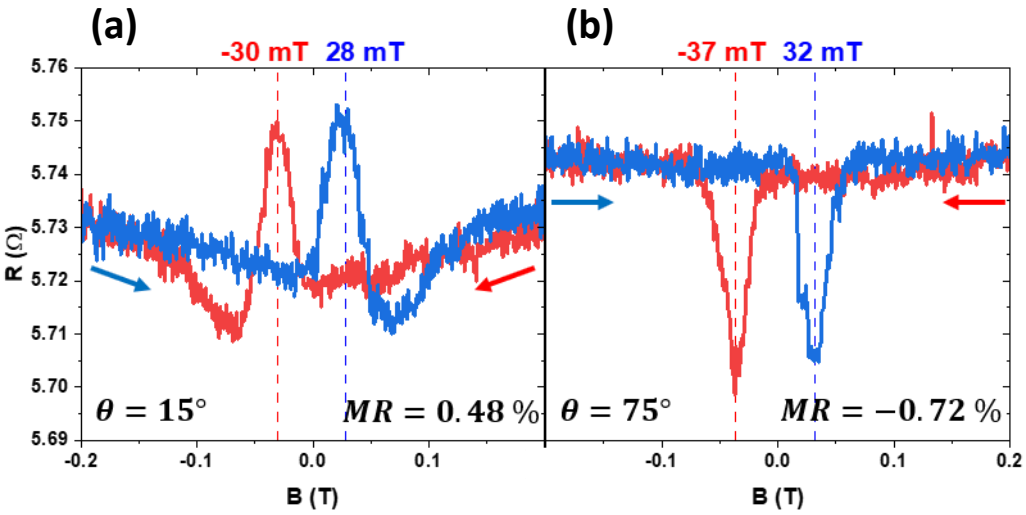

Fig. 6.20: Measurements done at $30\,K$ with a biasing current of $10\,\mu A$ for a SSV from sample REAL3 with $t_{YBCO} = 8\,nm$. (a) Magnetoresistance for $\theta = 15\,°$ showing a positive SVE. (b) Magnetoresistance for $\theta = 75\,°$ showing a negative SVE.

A more complete view of the reversal process as a function of the angle is depicted in **Fig. 6.21**, showing the 2d-colorplot of the normalized resistance R_N between $+1$ and -1 as a function of the angle between $0\,°$ and $360\,°$ (y-axis) and the in-plane magnetic field (x-axis) for three different temperatures after subtraction of the background. These 2d-colorplots were calculated numerically from a set of twenty-five MR curves measured with a constant angle-step of $15\,°$ between $0\,°$ and $360\,°$. In this representation, the positive SVE is characterized by the red areas, corresponding to a peak of the magnetoresistance, while the negative SVE is characterized by the blue areas, corresponding to a minimum of the magnetoresistance. The expected hard and easy axes for an LSMO thin layer are $\theta = 0\,° + n \times 90\,°$ and $\theta = 45\,° + n \times 90\,°$ with n an integer, respectively. This property was demonstrated in **Chapter 5, Sect. 4.4.1.** by studying the magnetic properties of the SSVs at high temperature.

(i) For $T = 30\,K$ [**Fig. 6.21(a)**], one can observe a $180\,°$ symmetry of the reversal mechanism, with alternating positive and negative SVEs (blue and red areas). For $\theta = 0\,°$, *i.e.* for a magnetic field perpendicular to the measuring bar, the junction exhibits a clear positive SVE. However, rotating the magnetic field from $\theta = 0\,°$ to $\theta = 90\,°$ induces a reversal of the polarity of the SVE from positive to negative. Moreover, we can observe that the peaks and dips of the magnetoresistance are broadest for the hard axes. This property is illustrated by the lateral size of the red and blue dots in **Fig. 6.21(a)**.

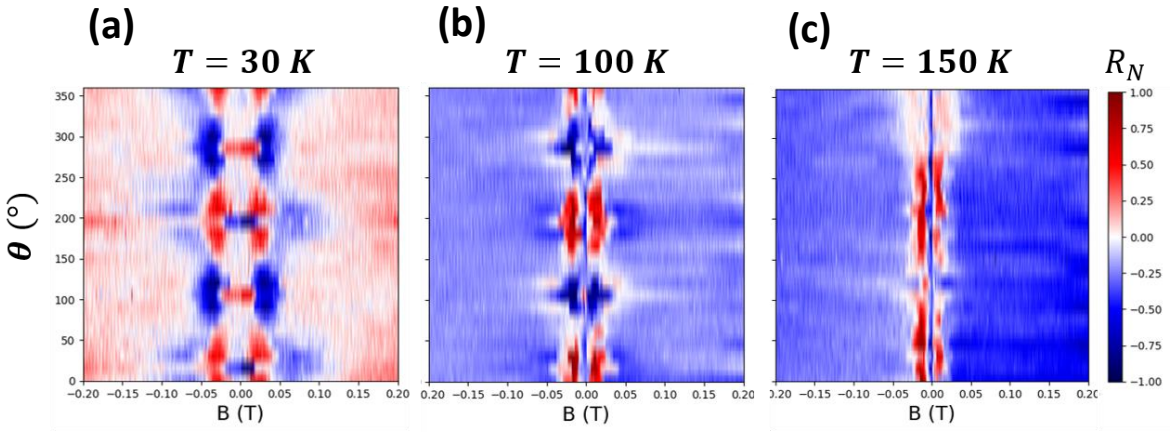

Fig. 6.21: Measurements done on a SSV from sample REAL3 with $t_{YBCO} = 8\ nm$ displaying 2d-colorplots of R_N measured in 4-probe as a function of θ (y-axis) and B (x-axis) for a biasing current of $10\ \mu A$ and for three different temperatures: (a) $30\ K$, (b) $100\ K$ and (c) $150\ K$. One can observe the reversal from a positive SVE (characterized by the red spots) and the negative SVE (characterized by the blue spots) for varying θ. Strikingly, the reversal is still observed above $90\ K$, the optimal T_C of YBCO, although the reversal behaviour seems to vanish at $150\ K$ and above.

(ii) For $T = 100\ K$ [**Fig. 6.21(b)**], the general behaviour of the magnetoresistance is very similar to the previous temperature, except for the value of the switching fields that is reduced from approximately $\pm 30\ mT$ at 30 K to $\pm 15\ mT$ at 100 K. This is consistent with the behaviour of the coercive fields assessed from the SQUID measurements conducted on the unpatterned samples and displayed in **Fig. 5.24**.

(iii) For $T = 150\ K$ [**Fig. 6.21(c)**], the magnetoresistance only exhibits a positive SVE, although some blurred areas seem to remain for angles where a negative SVE was previously observed. This feature indicates that although the temperature is well above T_C, some remnants of the effect persist. The switching fields of $\pm 10\ mT$ are slightly smaller compared to the previous temperature.

Strikingly, the reversal effect between negative and positive SVEs with respect to θ is observed at the temperature of $T = 100\ K$, which is above the optimal superconducting critical temperature of YBCO ($T_C \approx 93\ K$), indicating that, although superconductivity might play a role in the reversal process at low-temperatures, it is possible to observe this switching without involving superconductivity. **Fig. 6.22, Fig. 6.24** and **Fig. 6.25** show an exhaustive set of magnetoresistance measurements obtained on the same SSV as the one illustrated in **Fig. 6.20** and **Fig. 6.21** for three different temperatures, namely $T = 30, 100$ and $150\ K$, for varying angles $0\ ° < \theta < 105\ °$.

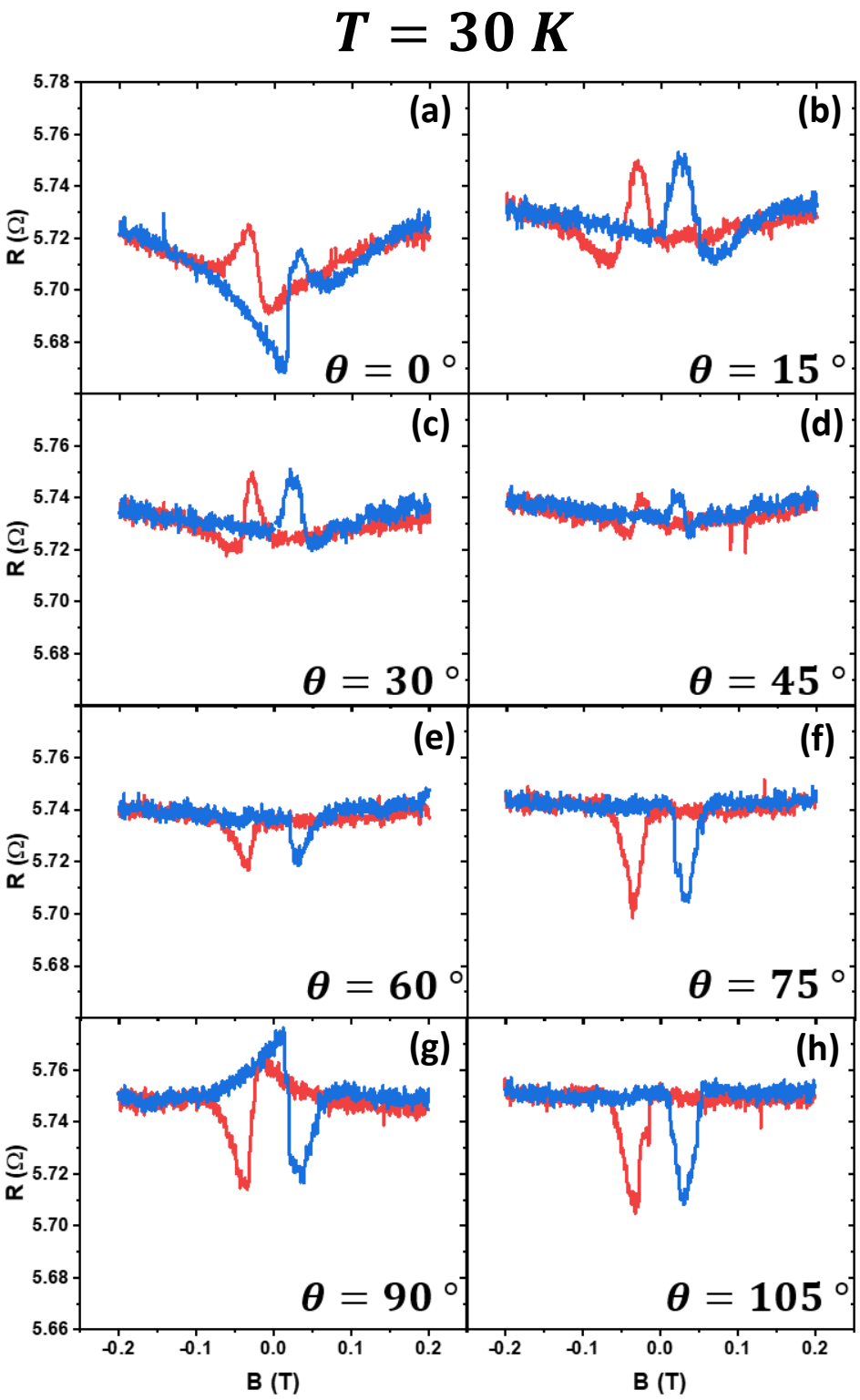

*Fig. 6.22: Measurements done at $30\ K$ with a biasing current of $10\ \mu A$ for a SSV from sample REAL3 with $t_{YBCO} = 8\ nm$ for different angles $0\ ° < \theta < 105\ °$. One can observe a reversal of the SVE from positive [see for example **Fig. 6.22(b)**] to negative [see for example **Fig. 6.22(f)**] while varying the angle from $\theta = 15\ °$ to $\theta = 75\ °$.*

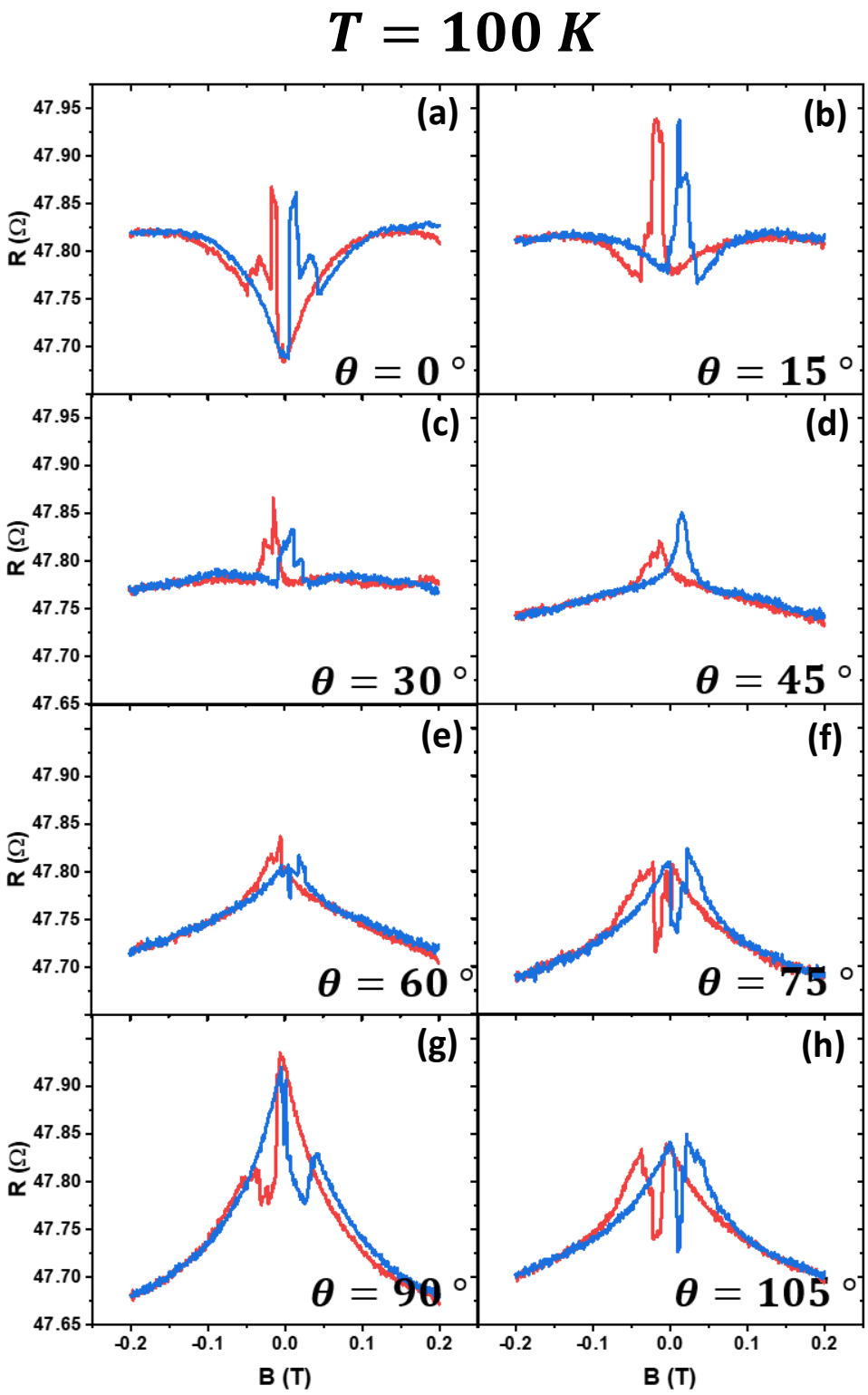

Fig. 6.23: Measurements done at $100\ K$ *with a biasing current of* $10\ \mu A$ *for a junction from sample REAL3 with* $t_{YBCO} = 8\ nm$ *for different angle* $0\ ° < \theta < 105\ °$*. One can observe a reversal of the SVE from positive [see for example* ***Fig. 6.23(b)****] to negative [see for example* ***Fig. 6.23(g)****] while varying the angle from* $\theta = 45\ °$ *to* $\theta = 90\ °$*.*

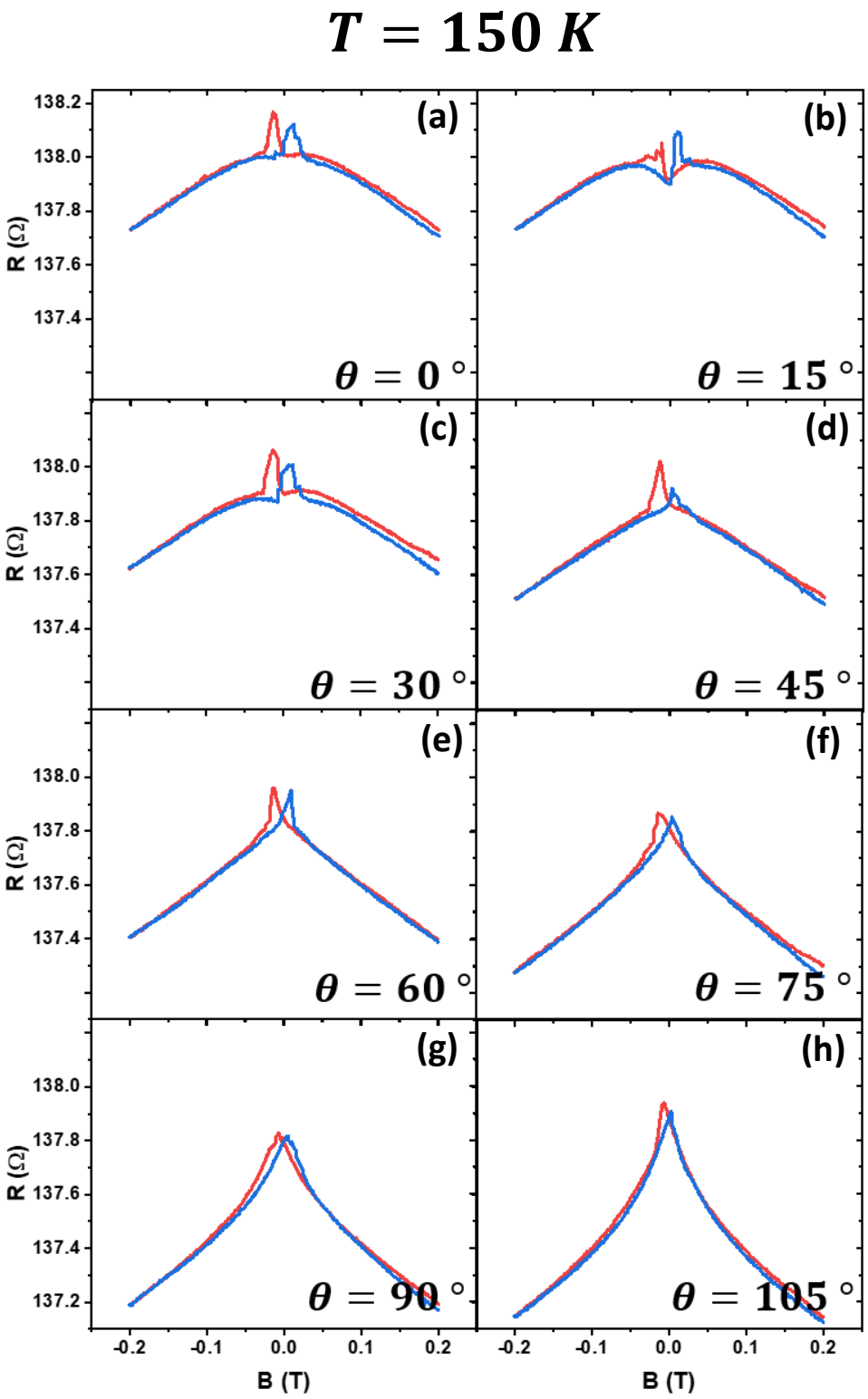

Fig. 6.24: Measurements done at $150\ K$ *with a biasing current of* $10\ \mu A$ *for a junction from sample REAL3 with* $t_{YBCO} = 8\ nm$ *for different angle* $0\ ° < \theta < 105\ °$*. At this temperature, no clear signatures of the negative SVE are observed.*

The possible origin of the angle-dependent reversal of the magnetoresistance is now discussed. Most importantly, this behaviour is seen for $T = 100\ K$, *i.e.* above the optimal critical temperature of YBCO and the shape of the positive and negative SVEs are drastically different from the superconducting SVE discussed **in Chapter 5, Sect. 5.**, pointing to a different origin for the reversal mechanism. Before giving a possible explanation for this phenomenon, I would like to highlight some key observations:

(i) Although $\theta = 0\ °$ [010] and $\theta = 90\ °$ [100] both represent the expected hard axes, it is important to note that they are not equivalent from the viewpoint of the bottom LSMO layer: whereas the top LSMO layer has a square cross-section $W \times W$ with $W = 10 \text{ or } 20\ \mu m$, the bottom LSMO layer has a rectangular shape of $2.96 \times 0.2\ mm^2$. Therefore, it is expected for the LSMO bottom layer to have a lower coercive field while applying an external magnetic field along the [010] (alongside the measuring bar) crystalline direction compared to the [100] direction (perpendicular to the measuring bar).

(ii) A second geometry factor that needs to be considered originates from the first microfabrication step: the thickness of the bottom LSMO layer can vary between different samples and measuring bars, depending on the IBE parameters and the etching time. Consequently, the magnetizations of the FMs may be affected differently by the external magnetic field, yielding device-to-device variations.

In order to understand the angle-dependent measurements, the subsequent discussion will be focused on the description of three particular magnetoresistance curves measured with $I = 10\ \mu A$ at $T = 100\ K$ for three different angles: $\theta = 0\ °$ [hard axis [010], **Fig. 6.25(a)**], $\theta = 45\ °$ [easy axis [110], **Fig. 6.25(b)**] and $\theta = 90\ °$ [hard axis [100], **Fig. 6.25(c)**].

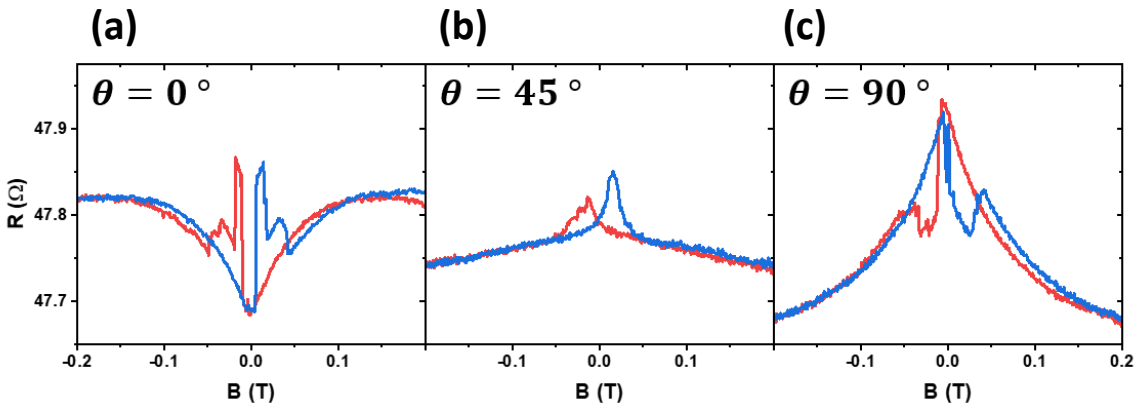

*Fig. 6.25: Magnetoresistance measurements done at 100 K with a biasing current of 10 μA for a SSV from sample REAL3 with $t_{YBCO} = 8\ nm$ for (a) $\theta = 0\ °$, (b) $\theta = 0\ °$ and (c) $\theta = 0\ °$. Figures taken from **Fig. 6.23**.*

For $\theta = 45\,°$, the $R(B)$ curve exhibits a typical manganite-like shape, identical to the magnetoresistance plots of SSVs at high temperature as seen previously in **Fig. 5.25**, for example. In fact, $\theta = 45\,°$ corresponds to the easy axis of the FMs, and therefore, the magnetoresistance plot can be simply understood by dividing the reversal process into four consecutive regimes. In regime 1 [**Fig. 6.26, (1)**], the magnetizations of both FMs (depicted by the blue and green arrows) are saturated in the direction of the external magnetic field, *i.e.* in a P configuration, yielding a low resistance of the junction. Then, decreasing B does not lead to any change in magnetization considering that the magnetizations are already aligned with the easy axis [**Fig. 6.26, (2)**]. While applying a negative B [**Fig. 6.26, (3)**], the thicker LSMO layer is expected to reverse first, leading to the appearance of an AP alignment and an increase of the resistance. Finally, as the magnetic field increases (in absolute values) above B_C of the second LSMO layer, a new P configuration is reached and the resistance decreases [**Fig. 6.26, (4)**].

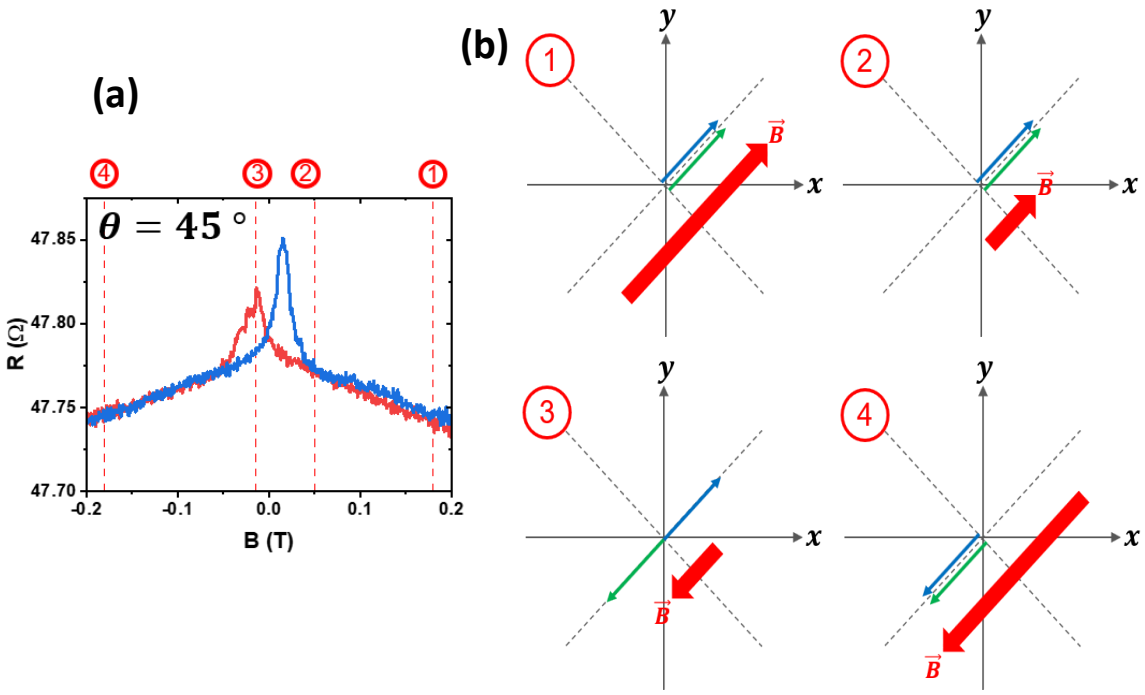

Fig. 6.26: (a) Magnetoresistance measurements done at $100\ K$ with a biasing current of $10\ \mu A$ for a junction from sample REAL3 with $t_{YBCO} = 8\ nm$ for $\theta = 45\,°$. (b) Step-by-step reversal process of the magnetizations of the FMs depending on the strength and direction of the external magnetic fields.

For $\theta = 0\,°$, an unusual shape of the magnetoresistance is observed in **Fig. 6.27(a)**. This behaviour can be understood through a step by step reversal of the magnetizations. An example of such a process is shown in **Fig. 6.27**. For this explanation, I consider the x-axis ($\theta = 90°$) to be an additional easy axis of one or both FMs, due to the large rectangular shape of the bottom LSMO electrode. Starting with a high applied magnetic field alongside the y-axis, I consider that applying $0.2\,T$ is not sufficient to saturate both magnetizations and therefore the SSV is in a AP configuration at the start of the experiment [**Fig. 6.27, (1)**]. As the applied field is decreased, the magnetization of the saturated FM will gradually reverse to the $\theta = 45\,°$ easy axis, yielding a decrease of the resistance [**Fig. 27, (2)**]. Then, I consider a 3-step reversal process as depicted in **Fig. 6.27, (3)**, **Fig. 6.27, (4)** and **Fig. 6.27, (5)** leading to a new P state with two consecutive decrease of the resistance. This is consistent with the shape of the measured magnetoresistance [see the close-up of **Fig. 6.27 (b)**], with two abrupt decrease of the resistance for $B \approx -19\,mT$ and $B \approx -50\,mT$. Finally, a new AP state is defined for high negative magnetic fields [**Fig. 6.27, (6)**] as the resistance increases.

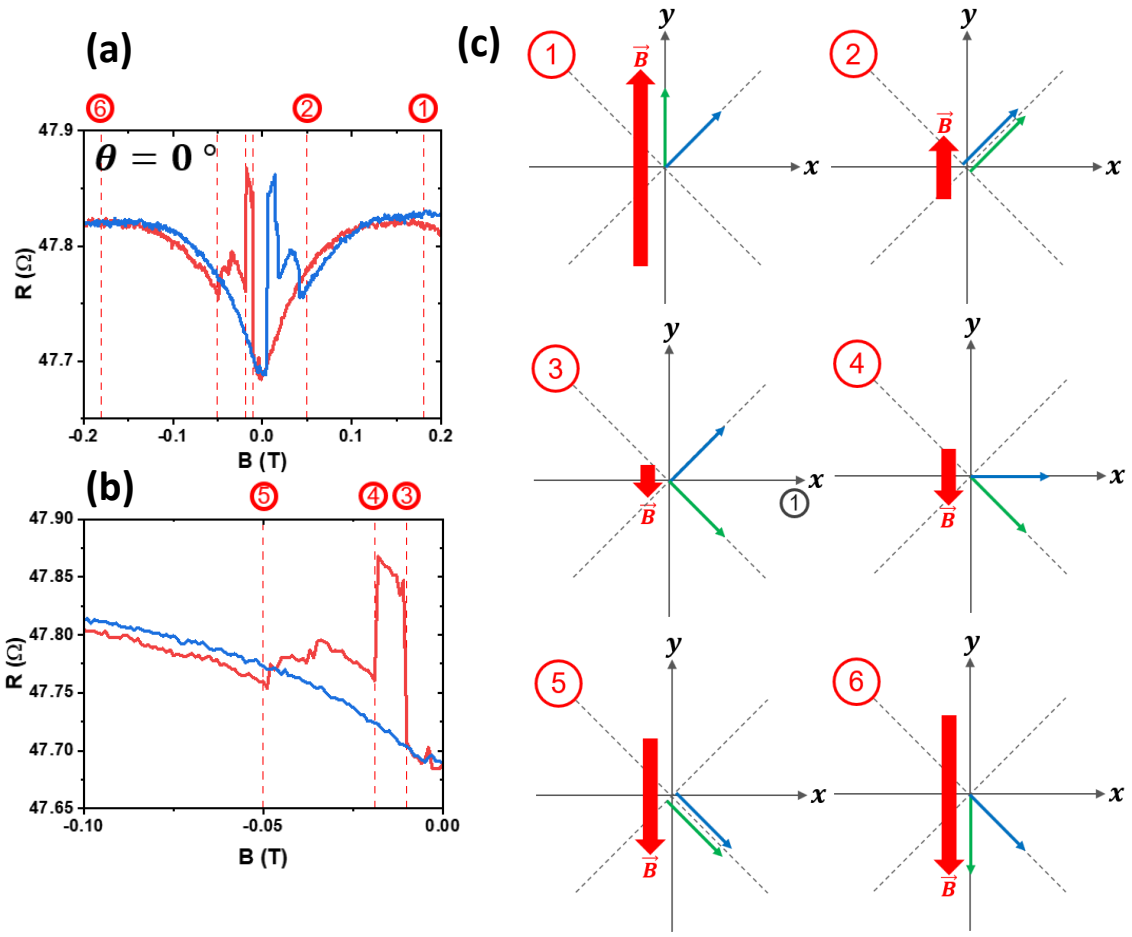

*Fig. 6.27: (a) Magnetoresistance measurements done at $100\,K$ with a biasing current of $10\,\mu A$ for a junction from sample REAL3 with $t_{YBCO} = 8\,nm$ for $\theta = 0\,°$. (b) Close-up of **Fig. 6.27(a)** for $-0.1\,T < B < 0\,T$. (c) Step-by-step reversal process of the magnetizations of the FMs depending on the strength and direction of the external magnetic fields.*

For $\theta = 90\,°$, a negative SVE is observed in **Fig. 6.28(a)**. For high applied magnetic fields, considering that the x-axis ($\theta = 90°$) is an additional easy-axis of the FMs, it is expected that both ferromagnetic layers are saturated and the magnetization form a P configuration, leading to a low global resistance. The non-linear evolution of the magnetoresistance as the magnetic field is reduced indicates that the increase of the resistance is probably due to CMR and an additional contribution caused by the GMR effect as an AP configuration is defined. An example of this step-by-step reversal process is illustrated in [**Fig. 6.28, (2)**] and [**Fig. 6.28, (3)**]. Then, as a negative magnetic field is applied [**Fig. 6.28, (4)**], a P configuration is achieved and the global resistance of the junction decreases. Finally, as the negative magnetic field increases (in absolute values) the resistance rises once more as the magnetization reverses in **Fig. 6.28, (5)** before reaching a final P configuration.

Therefore, we can conclude that the behaviour of the magnetoresistance as a function of the angle θ can be explained through a step-by-step reversal process between the various easy and hard axes of the system. Note that the scenarios discussed above in **Fig. 6.26**, **Fig. 6.27** and **Fig. 6.28** are only examples of particular reversal processes that potentially simulate the observed behaviour of the MR and do not represent an absolute answer. In particular, more complex reversal mechanisms may exist if the easy and hard axes of the two FMs are completely different.

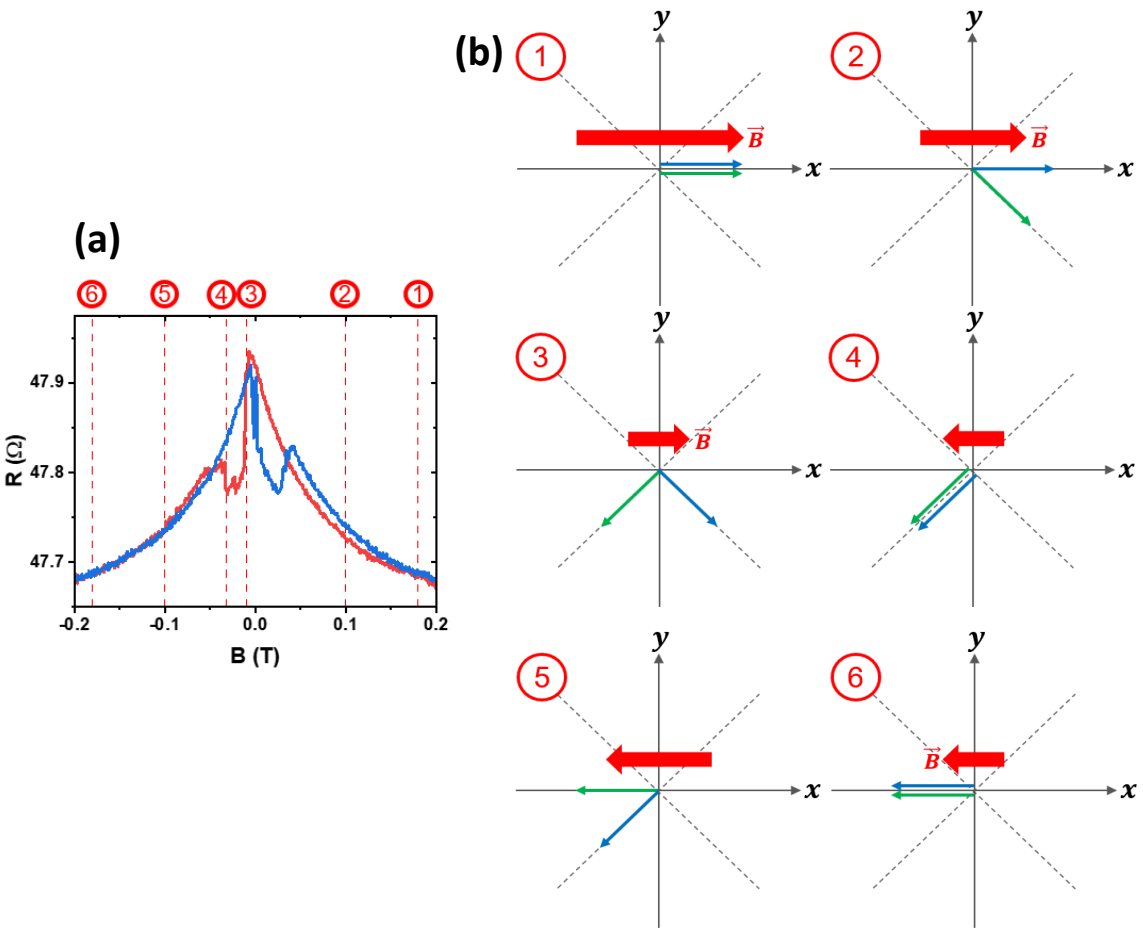

Fig. 6.28: (a) Magnetoresistance measurements done at $100\ K$ with a biasing current of $10\ \mu A$ for a junction from sample REAL3 with $t_{YBCO} = 8\ nm$ for $\theta = 95\,°$. (b) Step-by-step reversal process of the magnetizations of the FMs depending on the strength and direction of the external magnetic fields.

Bibliography

[1] H. Kamerlingh Onnes, *The Condensation of Helium [1]*, Nature.

[2] G. B. Yntema, *Superconducting Winding for Electromagnet*, in *Minutes of the 1955 Annual Meeting Held at New York City, January 27-29, 1955* (1955), p. 1197.

[3] J. E. Kunzler, E. Buehler, F. S. L. Hsu, and J. H. Wernick, *Erratum: Superconductivity in Nb3Sn at High Current Density in a Magnetic Field of 88 Kgauss (Physical Review Letters (1961) 7, 5)*, Physical Review Letters.

[4] J. G. Bednorz and K. A. Müller, *Possible High Tc Superconductivity in the Ba-La-Cu-O System*, Zeitschrift Für Phys. B Condens. Matter **64**, 189 (1986).

[5] M. K. Wu, J. R. Ashburn, C. J. Torng, P. H. Hor, R. L. Meng, L. Gao, Z. J. Huang, Y. Q. Wang, and C. W. Chu, *Superconductivity at 93 K in a New Mixed-Phase Yb-Ba-Cu-O Compound System at Ambient Pressure*, Phys. Rev. Lett. **58**, 908 (1987).

[6] J. Bardeen, L. N. Cooper, and J. R. Schrieffer, *Theory of Superconductivity*, Phys. Rev. **108**, 1175 (1957).

[7] B. Keimer, S. A. Kivelson, M. R. Norman, S. Uchida, and J. Zaanen, *From Quantum Matter to High-Temperature Superconductivity in Copper Oxides*, Nature.

[8] L. Taillefer, *Scattering and Pairing in Cuprate Superconductors*, Annu. Rev. Condens. Matter Phys. **1**, 51 (2010).

[9] D. P, *CRC Handbook of Chemistry and Physics*, J. Mol. Struct. **268**, 320 (1992).

[10] S. Khoobiar, J. L. Carter, and P. J. Lucchesi, *The Electronic Properties of Aluminum Oxide and the Chemisorption of Water, Hydrogen, and Oxygen*, J. Phys. Chem. **72**, 1682 (1968).

[11] P. A. Lee, N. Nagaosa, and X. G. Wen, *Doping a Mott Insulator: Physics of High-Temperature Superconductivity*, Rev. Mod. Phys. **78**, 17 (2006).

[12] M. N. Baibich, J. M. Broto, A. Fert, F. Nguyen, V. Dau, F. Petroff, P. Eitenne, G. Creuzet, A. Friederich, and J. Chazelas, *Giant Magnetoresistance of (001)Fel(001) Cr Magnetic Snperlattices*, Phys. Rev. Lett. **61**, 2472 (1988).

[13] G. Binasch, P. Grünberg, F. Saurenbach, and W. Zinn, *Enhanced Magnetoresistance in Layered Magnetic Structures with Antiferromagnetic Interlayer Exchange*, Phys. Rev. B **39**, 4828 (1989).

[14] P. G. De Gennes, *Coupling between Ferromagnets through a Superconducting Layer*, Phys. Lett. **23**, 10 (1966).

[15] L. R. Tagirov, *Low-Field Superconducting Spin Switch Based on a Superconductor/Ferromagnet Multilayer*, Phys. Rev. Lett. **83**, 2058 (1999).

[16] A. I. Buzdin, A. V. Vedyayev, and N. V. Ryzhanova, *Spin-Orientation-Dependent Superconductivity in F/S/F Structures*, Europhys. Lett. **48**, 686 (1999).

[17] M. C. Ramírez Camacho, C. F. Sánchez Valdés, M. Curiel, J. L. Sánchez Llamazares, J. M. Siqueiros, and O. Raymond Herrera, *Superparamagnetic State in La0.7Sr0.3MnO3 Thin Films Obtained by Rf-Sputtering*, Sci. Rep. **10**, (2020).

[18] C. H. Lin, P. A. Friddle, C. H. Ma, A. Daga, and H. Chen, *Effects of Thickness on the Electrical Properties of Metalorganic Chemical Vapor Deposited Pb(Zr, Ti)O3 (25-100 Nm) Thin Films on LaNiO3 Buffered Si*, J. Appl. Phys. **90**, 1509 (2001).

[19] D. Sánchez, M. Directores, J. Santamaría Sánchez-Barriga, C. León, and Y. Madrid, *Nanoestructuras de Óxidos Para Espintrónica Superconductora*, (2021).

[20] Z. Liao, M. Huijben, G. Koster, and G. Rijnders, *Uniaxial Magnetic Anisotropy Induced Low Field Anomalous Anisotropic Magnetoresistance in Manganite Thin Films*, APL Mater. **2**, (2014).

[21] S. Ghosh, R. G. Tanguturi, P. Pramanik, D. C. Joshi, P. K. Mishra, S. Das, and S. Thota, *Low-Temperature Anomalous Spin Correlations and Kondo Effect in Ferromagnetic SrRuO3/LaNiO3/La0.7Sr0.3MnO3 Trilayers*, Phys. Rev. B **99**, (2019).

[22] P. Perna, D. Maccariello, F. Ajejas, R. Guerrero, L. Méchin, S. Flament, J. Santamaria, R. Miranda, and J. Camarero, *Engineering Large Anisotropic Magnetoresistance in La0.7Sr0.3MnO3 Films at Room Temperature*, Adv. Funct. Mater. **27**, (2017).

[23] A. Urushibara, Y. Moritomo, T. Arima, A. Asamitsu, G. Kido, and Y. Tokura, *Insulator-Metal Transition and Giant Magnetoresistance in La1-XSrxMnO3*, Phys. Rev. B **51**, 14103 (1995).

[24] Y. Suzuki, Y. Wu, J. Yu, U. Ruediger, A. D. Kent, T. K. Nath, and C. B. Eom, *Domain Structure and Magnetotransport in Epitaxial Colossal Magnetoresistance Thin Films*, J. Appl. Phys. **87**, 6746 (2000).

[25] D. C. Jiles and D. L. Atherton, *Theory of Ferromagnetic Hysteresis*, J. Magn. Magn. Mater. **61**, 48 (1986).

[26] P. Rani, A. K. Hafiz, and V. P. S. Awana, *Temperature Dependence of Lower Critical Field of YBCO Superconductor*, in *AIP Conference Proceedings*, Vol. 1953 (2018).

[27] Z. Sefrioui, D. Arias, V. Peña, J. E. Villegas, M. Varela, P. Prieto, C. León, J. L. Martinez, and J. Santamaria, *Ferromagnetic/Superconducting Proximity Effect in La0.7Ca0.3MnO3/YBa2Cu3O7−δ Superlattices*, Phys. Rev. B - Condens. Matter Mater. Phys. **67**, (2003).

[28] F. S. Bergeret, A. F. Volkov, and K. B. Efetov, *Odd Triplet Superconductivity and Related Phenomena in Superconductor- Ferromagnet Structures*, Rev. Mod. Phys. **77**, 1321 (2005).

[29] P. H. E. Meijer, *Kamerlingh Onnes and the Discovery of Superconductivity*, Am. J. Phys. **62**, 1105 (1994).

[30] P. F. Dahl, *Kamerlingh Onnes and the Discovery of Superconductivity: The Leyden Years, 1911–1914*, Hist. Stud. Phys. Sci. **15**, 1 (1984).

[31] J. N. Rjabinin and L. W. Shubnikow, *Magnetic Properties and Critical Currents of Supraconducting Alloys [3]*, Nature.

[32] X. Palermo, *Proximity and Flux Pinning Effects in Superconductor-Ferromagnet Hybrids*, (2019).

[33] A. A. Abrikosov, *The Magnetic Properties of Superconducting Alloys*, J. Phys. Chem. Solids **2**, 199 (1957).

[34] S. Pittard, P. Feenan, and W. Vennart, *Superconducting Magnets for Magnetic Resonance Imaging*, Appl. Supercond. **1**, 1827 (1993).

[35] Y. Huang and J. Kinsinger, *Applications of a Superconducting Magnet on High Performance Fourier Transform Mass Spectrometers*, IEEE Trans. Magn. **21**, 694 (1985).

[36] P. Schmuser, *Superconducting Magnets for Particle Accelerators*, Reports Prog. Phys. **54**, 683 (1991).

[37] L. N. Cooper, *Bound Electron Pairs in a Degenerate Fermi Gas [1]*, Physical Review.

[38] B. D. Josephson, *The Discovery of Tunneling Supercurrents*, Science (80-.). **184**, 527 (1974).

[39] P. W. Anderson and J. M. Rowell, *Probable Observation of the Josephson Superconducting Tunneling Effect*, Phys. Rev. Lett. **10**, 230 (1963).

[40] I. F. Quercia, *Physics and Applications of the Josephson Effect*, Nuovo Cim. D **4**, 411 (1984).

[41] R. P. Giffard, J. C. Gallop, and B. W. Petley, *Applications of the Josephson Effects*, Prog. Quantum Electron. **4**, 301 (1976).

[42] P. Russer and J. A. Russer, *Nanoelectronic RF Josephson Devices*, IEEE Trans. Microw. Theory Tech. **59**, 2685 (2011).

[43] A. Spratt, *Tigecycline: Present and Future Applications*, Biomed. Sci. 1064 (2006).

[44] A. I. Braginski, *Superconductor Electronics: Status and Outlook*, J. Supercond. Nov. Magn. **32**, 23 (2019).

[45] H. London, *High-Frequency Resistance of Superconducting Tin*, Nature.

[46] Tinkham, *Tinkham M. Introduction to Superconductivity (2ed., MGH, 1996)(K)(T)(ISBN 0070648786)(472s).Pdf*, Book.

[47] T. Noguchi, A. Dominjon, M. Kroug, S. Mima, and C. Otani, *Characteristics of Very High Q Nb Superconducting Resonators for Microwave Kinetic Inductance Detectors*, IEEE Trans. Appl. Supercond. **29**, (2019).

[48] D. E. Oates, M. A. Hein, P. J. Hirst, R. G. Humphreys, G. Koren, and E. Polturak, *Nonlinear Microwave Surface Impedance of YBCO Films: Latest Results and Present Understanding*, in *Physica C: Superconductivity and Its Applications*, Vols. 372–376 (2002), pp. 462–468.

[49] S. Li et al., *A 12-Pole Narrowband Highly Selective High-Temperature Superconducting Filter for the Application in the Third-Generation Wireless Communications*, IEEE Trans. Microw. Theory Tech. **55**, 754 (2007).

[50] D. D. Bai, J. Du, T. Zhang, and Y. S. He, *A Compact High Temperature Superconducting Bandpass Filter for Integration with a Josephson Mixer*, J. Appl. Phys. **114**, 133906 (2013).

[51] N. El-Hinnawy et al., *12.5 THz Fco GeTe Inline Phase-Change Switch Technology for Reconfigurable RF and Switching Applications*, in *Technical Digest - IEEE Compound Semiconductor Integrated Circuit Symposium, CSIC* (2014).

[52] B. Jeanneret and S. P. Benz, *Application of the Josephson Effect in Electrical Metrology*, European Physical Journal: Special Topics.

[53] S. Shapiro, *Josephson Currents in Superconducting Tunneling: The Effect of Microwaves and Other Observations*, Phys. Rev. Lett. **11**, 80 (1963).

[54] S. Matarazzo, S. Barbanera, V. Boffa, R. Bruzzese, F. Ciciulla, U. Gambardella, F. Murtas, S. Pagano, M. Penna, and C. Romeo, *DC SQUIDs Based on YBCO Step Edge Junctions*, J. Supercond. **6**, 391 (1993).

[55] E. R. Pawlowski, J. Kermorvant, D. Crété, Y. Lemaître, B. Marcilhac, C. Ulysse, F. Couëdo, C. Feuillet-Palma, N. Bergeal, and J. Lesueur, *Static and Radio Frequency Magnetic Response of High T c Superconducting Quantum Interference Filters Made by Ion Irradiation*, Supercond. Sci. Technol. **31**, (2018).

[56] R. C. Jaklevic, J. Lambe, A. H. Silver, and J. E. Mercereau, *Quantum Interference Effects in Josephson Tunneling*, Phys. Rev. Lett. **12**, 159 (1964).

[57] M. Schmelz, V. Zakosarenko, A. Chwala, T. Schönau, R. Stolz, S. Anders, S. Linzen, and H. G. Meyer, *Thin-Film-Based Ultralow Noise SQUID Magnetometer*, IEEE Trans. Appl. Supercond. **26**, (2016).

[58] R. Kraus, M. Espy, P. Magnelind, and P. Volegov, *Ultra-Low Field Nuclear Magnetic Resonance*, Ultra-Low Field Nuclear Magnetic Resonance.

[59] D. Cohen, *Magnetic Fields of the Human Body*, Phys. Today **28**, 34 (1975).

[60] Y. Lin and G. I. Ogilvie, *Ohmic Dissipation in the Earth's Outer Core Resulting from the Free Inner Core Nutation*, Earth Planet. Sci. Lett. **530**, (2020).

[61] S. P. Singh, *Magnetoencephalography: Basic Principles*, Ann. Indian Acad. Neurol. **17**, S107 (2014).

[62] L. P. Lee, K. Char, M. S. Colclough, and G. Zaharchuk, *Monolithic 77 K Dc SQUID Magnetometer*, Appl. Phys. Lett. **59**, 3051 (1991).

[63] J. Clarke, *High-Tc Squids*, Curr. Opin. Solid State Mater. Sci. **2**, 3 (1997).

[64] M. I. Faley, J. Dammers, Y. V. Maslennikov, J. F. Schneiderman, D. Winkler, V. P. Koshelets, N. J. Shah, and R. E. Dunin-Borkowski, *High-Tc SQUID Biomagnetometers*, Superconductor Science and Technology.

[65] F. Ludwig, D. Koelle, E. Dantsker, D. T. Nemeth, A. H. Miklich, J. Clarke, and R. E. Thomson, *Low Noise YBa2Cu3O7-x-SrTiO3-YBa 2Cu3O7-x Multilayers for Improved Superconducting Magnetometers*, Appl. Phys. Lett. 373 (1995).

[66] D. Drung et al., *Integrated YBa2Cu3O7-x Magnetometer for Biomagnetic Measurements*, Appl. Phys. Lett. **68**, 1421 (1996).

[67] M. I. Faley, U. Poppe, K. Urban, D. N. Paulson, T. N. Starr, and R. L. Fagaly, *Low Noise HTS Dc-SQUID Flip-Chip Magnetometers and Gradiometers*, in *IEEE Transactions on Applied Superconductivity*, Vol. 11 (2001), pp. 1383–1384.

[68] M. I. Faley et al., *High-Tc DC SQUIDs for Magnetoencephalography*, IEEE Trans. Appl. Supercond. **23**, 1600705 (2013).

[69] C. Pfeiffer, S. Ruffieux, L. M. Andersen, A. Kalabukhov, D. Winkler, R. Oostenveld, D. Lundqvist, and J. F. Schneiderman, *On-Scalp MEG Sensor Localization Using Magnetic Dipole-like Coils: A Method for Highly Accurate Co-Registration*, Neuroimage **212**, (2020).

[70] C. P. Foley, S. Lam, K. E. Leslie, K. H. Müller, R. A. Binks, L. Macks, and G. J. Sloggett, *Excess Low-Frequency Noise in YBCO Rf SQUIDs in Weak Magnetic Fields*, Appl. Supercond. **6**, 669 (1999).

[71] F. Qaderi, F. Shanehsazzadeh, B. Mazdouri, and M. Fardmanesh, *HTS YBCO Resonator Configuration with a Coplanar Optimized Flux Concentrator Strongly Coupled to Rf SQUID*, IEEE Trans. Appl. Supercond. **28**, (2018).

[72] A. Tsukamoto, S. Adachi, Y. Oshikubo, and K. Tanabe, *Design and Fabrication of Directly-Coupled HTS-SQUID Magnetometer with a Multi-Turn Input Coil*, IEEE Trans. Appl. Supercond. **23**, (2013).

[73] Y. Zhang, M. Muck, A. I. Braginski, and H. Topfer, *High-Sensitivity Microwave RF SQUID Operating at 77 K*, Supercond. Sci. Technol. **7**, 269 (1994).

[74] D. Bera, L. Qian, T. K. Tseng, and P. H. Holloway, *Quantum Dots and Their Multimodal Applications: A Review*, Materials.

[75] R. Zitko, *Superconducting Quantum Dot and the Sub-Gap States*, in (2018), p. 58.

[76] A. l. Efros and A. l. Efros, *Interband Light Absorption in Semiconductor Spheres*, Sov. Physics. Semicond. **16**, 772 (1982).

[77] Ah. A. H. Abdellatif, H. M. Tawfeek, M. A. Younis, M. Alsharidah, and O. Al Rugaie, *Biomedical Applications of Quantum Dots: Overview, Challenges, and Clinical Potential*, Int. J. Nanomedicine **17**, 1951 (2022).

[78] M. A. Cotta, *Quantum Dots and Their Applications: What Lies Ahead?*, ACS Applied Nano Materials.

[79] D. Loss and D. P. DiVincenzo, *Quantum Computation with Quantum Dots*, Phys. Rev. A - At. Mol. Opt. Phys. **57**, 120 (1998).

[80] J. A. Van Dam, Y. V. Nazarov, E. P. A. M. Bakkers, S. De Franceschi, and L. P. Kouwenhoven, *Supercurrent Reversal in Quantum Dots*, Nature **442**, 667 (2006).

[81] S. De Franceschi, L. Kouwenhoven, C. Schönenberger, and W. Wernsdorfer, *Hybrid Superconductor-Quantum Dot Devices*, Nature Nanotechnology.

[82] S. V. Polonsky, V. K. Semenov, P. I. Bunyk, A. F. Kirichenko, A. Y. Kidiyarova-Shevchenko, O. A. Mukhanov, P. N. Shevchenko, D. F. Schneider, D. Y. Zinoviev, and K. K. Likharev, *New Rsfq Circuits*, IEEE Transactions on Applied Superconductivity.

[83] O. A. Mukhanov et al., *Superconductor Digital-RF Receiver Systems*, IEICE Trans. Electron. **E91**-**C**, 306 (2008).

[84] J. H. Kang, *Single Flux Quantum Signal Transmission Techniques in Building Practical RSFQ Circuits*, in *Cryogenics*, Vol. 43 (2003), pp. 543–547.

[85] L. O. Chua, *Memristor—The Missing Circuit Element*, IEEE Trans. Circuit Theory **18**, 507 (1971).

[86] D. B. Strukov, G. S. Snider, D. R. Stewart, and R. S. Williams, *The Missing Memristor Found*, Nature **453**, 80 (2008).

[87] J. J. Yang, M. D. Pickett, X. Li, D. A. A. Ohlberg, D. R. Stewart, and R. S. Williams, *Memristive Switching Mechanism for Metal/Oxide/Metal Nanodevices*, Nat. Nanotechnol. **3**, 429 (2008).

[88] Y. Ho, G. M. Huang, and P. Li, *Nonvolatile Memristor Memory: Device Characteristics and Design Implications*, IEEE/ACM Int. Conf. Comput. Des. Dig. Tech. Pap. ICCAD 485 (2009).

[89] S. Parajuli, R. K. Budhathoki, and H. Kim, *Nonvolatile Memory Cell Based on Memristor*, Univers. J. Electr. Electron. Eng. **7**, 110 (2020).

[90] B. Mouttet, *Proposal for Memristors in Signal Processing*, Lect. Notes Inst. Comput. Sci. Soc. Telecommun. Eng. **3 LNICST**, 11 (2009).

[91] Y. Zhong et al., *A Memristor-Based Analogue Reservoir Computing System for Real-Time and Power-Efficient Signal Processing*, Nat. Electron. **5**, 672 (2022).

[92] H. T. Zhang et al., *Organismic Materials for beyond von Neumann Machines*, Appl. Phys. Rev. **7**, 011309 (2020).

[93] R. El Hage, V. Humbert, V. Rouco, A. Sander, J. Charliac, S. Mesoraca, J. Trastoy, J. Briatico, J. Santamaría, and J. E. Villegas, *Superconducting Bimodal Ionic Photo-Memristor*, in (2022).

[94] J. Grollier, D. Querlioz, K. Y. Camsari, K. Everschor-Sitte, S. Fukami, and M. D. Stiles, *Neuromorphic Spintronics*, Nature Electronics.

[95] A. Mehonic and A. J. Kenyon, *Brain-Inspired Computing Needs a Master Plan*, Nature **604**, 255 (2022).

[96] A. N. Burkitt, *A Review of the Integrate-and-Fire Neuron Model: I. Homogeneous Synaptic Input*, Biol. Cybern. **95**, 1 (2006).

[97] N. M. Samardzic, J. S. Bajic, D. L. Sekulic, and S. Dautovic, *Volatile Memristor in Leaky Integrate-and-Fire Neurons: Circuit Simulation and Experimental Study*, Electron. **11**, (2022).

[98] A. Fert, *Origin, Development, and Future of Spintronics (Nobel Lecture)*, in *Angewandte Chemie - International Edition*, Vol. 47 (2008), pp. 5956–5967.

[99] C. Chappert, A. Fert, and F. N. Van Dau, *The Emergence of Spin Electronics in Data Storage*, Nat. Mater. **6**, 813 (2007).

[100] M. Julliere, *Tunneling between Ferromagnetic Films*, Phys. Lett. A **54**, 225 (1975).

[101] T. Miyazaki and N. Tezuka, *Spin Polarized Tunneling in Ferromagnet/Insulator/Ferromagnet Junctions*, J. Magn. Magn. Mater. **151**, 403 (1995).

[102] M. G. Flokstra, *Proximity Effects in Superconducting Spin-Valve Structures*, PhD Thesis 144 (2010).

[103] M. Eschrig, *Spin-Polarized Supercurrents for Spintronics: A Review of Current Progress*, Reports Prog. Phys. **78**, (2015).

[104] J. Linder and J. W. A. Robinson, *Superconducting Spintronics*, Nat. Phys. **11**, 307 (2015).

[105] R. S. Keizer, S. T. B. Goennenwein, T. M. Klapwijk, G. Miao, G. Xiao, and A. Gupta, *A Spin Triplet Supercurrent through the Half-Metallic Ferromagnet CrO 2*, Nature **439**, 825 (2006).

[106] D. Sanchez-Manzano et al., *Extremely Long-Range, High-Temperature Josephson Coupling across a Half-Metallic Ferromagnet*, Nat. Mater. **21**, 188 (2022).

[107] N. Banerjee, C. B. Smiet, R. G. J. Smits, A. Ozaeta, F. S. Bergeret, M. G. Blamire, and J. W. A. Robinson, *Evidence for Spin Selectivity of Triplet Pairs in Superconducting Spin Valves*, Nat. Commun. **5**, (2014).

[108] P. V. Leksin, N. N. Garif'Yanov, I. A. Garifullin, Y. V. Fominov, J. Schumann, Y. Krupskaya, V. Kataev, O. G.

Schmidt, and B. Büchner, *Evidence for Triplet Superconductivity in a Superconductor-Ferromagnet Spin Valve*, Phys. Rev. Lett. **109**, (2012).

[109] M. Rogers et al., *Spin-Singlet to Triplet Cooper Pair Converter Interface*, Commun. Phys. **4**, (2021).

[110] J. W. A. Robinson, J. D. S. Witt, and M. G. Blamire, *Controlled Injection of Spin-Triplet Supercurrents into a Strong Ferromagnet*, Science (80-.). **329**, 59 (2010).

[111] M. S. Anwar, F. Czeschka, M. Hesselberth, M. Porcu, and J. Aarts, *Long-Range Supercurrents through Half-Metallic Ferromagnetic CrO 2*, Phys. Rev. B - Condens. Matter Mater. Phys. **82**, (2010).

[112] A. Singh, S. Voltan, K. Lahabi, and J. Aarts, *Colossal Proximity Effect in a Superconducting Triplet Spin Valve Based on the Half-Metallic Ferromagnet CrO2*, Phys. Rev. X **5**, (2015).

[113] M. Varela, A. R. Lupini, S. J. Pennycook, Z. Sefrioui, and J. Santamaria, *Nanoscale Analysis of YBa2Cu3O7-x/La 0.67Ca0.33MnO3 Interfaces*, Solid. State. Electron. **47**, 2245 (2003).

[114] F. L. H. London, *The Electromagnetic Equations of the Supraconductor*, Proc. R. Soc. London. Ser. A - Math. Phys. Sci. **149**, 71 (1935).

[115] K. Steinberg, M. Scheffler, and M. Dressel, *Quasiparticle Response of Superconducting Aluminum to Electromagnetic Radiation*, in *Physical Review B - Condensed Matter and Materials Physics*, Vol. 77 (2008).

[116] T. Klein et al., *Thermodynamic Phase Diagram of Fe (Se0.5 Te0.5) Single Crystals in Fields up to 28 Tesla*, Phys. Rev. B - Condens. Matter Mater. Phys. **82**, (2010).

[117] R. F. Kiefl et al., *Direct Measurement of the London Penetration Depth in YBa2 Cu3 O6.92 Using Low-Energy MsR*, Phys. Rev. B - Condens. Matter Mater. Phys. **81**, (2010).

[118] R. Prozorov, R. W. Giannetta, A. Carrington, P. Fournier, R. L. Greene, P. Guptasarma, D. G. Hinks, and A. R. Banks, *Measurements of the Absolute Value of the Penetration Depth in High-Tc Superconductors Using a Low-Tc Superconductive Coating*, Appl. Phys. Lett. **77**, 4202 (2000).

[119] S. Kamal, R. Liang, A. Hosseini, D. Bonn, and W. Hardy, *Magnetic Penetration Depth and Surface Resistance in Ultrahigh-Purity Crystals*, Phys. Rev. B - Condens. Matter Mater. Phys. **58**, R8933 (1998).

[120] V. L. Ginzburg, *On the Theory of Superconductivity*, Nuovo Cim. Ser. 10 **2**, 1234 (1955).

[121] P. C. Hohenberg and A. P. Krekhov, *An Introduction to the Ginzburg-Landau Theory of Phase Transitions and Nonequilibrium Patterns*, Physics Reports.

[122] J. Trastoy, V. Rouco, C. Ulysse, R. Bernard, G. Faini, J. Lesueur, J. Briatico, and J. E. Villegas, *Nanostructuring of High-TC Superconductors via Masked Ion Irradiation for Efficient Ordered Vortex Pinning*, Phys. C Supercond. Its Appl. **506**, 195 (2014).

[123] A. Abou El Hassan, A. Labrag, A. Taoufik, M. Bghour, H. El Ouaddi, A. Tirbiyine, B. Lmouden, A. Hafid, and H. El Hamidi, *Magnetic Penetration Depth and Coherence Length in a Single-Crystal YBa2Cu3O7−δ*, Phys. Status Solidi Basic Res. **258**, (2021).

[124] Y. Asada and H. Nosé, *Superconductivity of Niobium Films*, J. Phys. Soc. Japan **26**, 347 (1969).

[125] H. Fröhlich, *Interaction of Electrons with Lattice Vibrations*, Proc. R. Soc. London. Ser. A. Math. Phys. Sci. **215**, 291 (1952).

[126] L. P. Gor'Kov, *The Critical Supercooling Field in Superconductivity Theory*, in *Selected Papers of Lev P. Gor'kov* (2014), pp. 35–41.

[127] T. le quang, Investigating the Possibility of Triplet Supercurrent in Lateral Cobalt Junctions, 2011.

[128] G. E. Blonder, M. Tinkham, and T. M. Klapwijk, *Transition from Metallic to Tunneling Regimes in Superconducting Microconstrictions: Excess Current, Charge Imbalance, and Supercurrent Conversion*, Phys. Rev. B **25**, 4515 (1982).

[129] G. Eilenberger, *Transformation of Gorkov's Equation for Type II Superconductors into Transport-like Equations*, Zeitschrift Für Phys. **214**, 195 (1968).

[130] K. D. Usadel, *Generalized Diffusion Equation for Superconducting Alloys*, Phys. Rev. Lett. **25**, 507 (1970).

[131] F. Konschelle, *Transport Equations for Superconductors in the Presence of Spin Interaction*, Eur. Phys. J. B **87**, (2014).

[132] G. Grissonnanche et al., *Direct Measurement of the Upper Critical Field in Cuprate Superconductors*, Nat. Commun. **5**, (2014).

[133] C. Proust and L. Taillefer, *The Remarkable Underlying Ground States of Cuprate Superconductors*, Annu. Rev. Condens. Matter Phys. **10**, 409 (2019).

[134] A. Schilling, M. Cantoni, J. D. Guo, and H. R. Ott, *Superconductivity above 130 K in the Hg-Ba-Ca-Cu-O System*, Nature **363**, 56 (1993).

[135] M. Bibes, J. E. Villegas, and A. Barthélèmy, *Ultrathin Oxide Films and Interfaces for Electronics and Spintronics*, Adv. Phys. **60**, 5 (2011).

[136] I. H. Lone, J. Aslam, N. R. E. Radwan, A. H. Bashal, A. F. A. Ajlouni, and A. Akhter, *Multiferroic ABO3 Transition Metal Oxides: A Rare Interaction of Ferroelectricity and Magnetism*, Nanoscale Res. Lett. **14**, 142 (2019).

[137] S. A. Siddiqui, D. Hong, J. E. Pearson, and A. Hoffmann, *Antiferromagnetic Oxide Thin Films for Spintronic Applications*, Coatings **11**, (2021).

[138] N. G. Bebenin, *Ferromagnetic Lanthanum Manganites*, in *Journal of Magnetism and Magnetic Materials*, Vol. 324 (2012), pp. 3593–3596.

[139] S. Er-Rahmany, M. Loulidi, A. El Kenz, A. Benyoussef, and M. Azzouz, *From Mott Insulators to Quantum Metals*, ArXiv (2020).

[140] M. Biagini, C. Calandra, and S. Ossicini, *Electronic Structure of PrBa2Cu3O7: A Local-Spin-Density Approximation with on-Site Coulomb Interaction*, Phys. Rev. B **52**, 10468 (1995).

[141] A. Sawa, *Resistive Switching in Transition Metal Oxides*, Materials Today.

[142] M. Bibes and A. Barthélémy, *Oxide Spintronics*, IEEE Trans. Electron Devices **54**, 1003 (2007).

[143] G. Biswal and K. L. Mohanta, *A Recent Review on Iron-Based Superconductor*, in *Materials Today: Proceedings*, Vol. 35 (2021), pp. 207–215.

[144] G. Pacchioni, *Nickelates Enter the Scene*, Nature Reviews Materials.

[145] A. Bhaumik, R. Sachan, and J. Narayan, *A Novel High-Temperature Carbon-Based Superconductor: B-Doped Q-Carbon*, J. Appl. Phys. **122**, (2017).

[146] Y. Kamihara, H. Hiramatsu, M. Hirano, R. Kawamura, H. Yanagi, T. Kamiya, and H. Hosono, *Iron-Based Layered Superconductor: LaOFeP*, J. Am. Chem. Soc. **128**, 10012 (2006).

[147] J. F. Ge, Z. L. Liu, C. Liu, C. L. Gao, D. Qian, Q. K. Xue, Y. Liu, and J. F. Jia, *Superconductivity above 100 K in Single-Layer FeSe Films on Doped SrTiO3*, Nat. Mater. **14**, 285 (2015).

[148] M. Ainslie, *Transport AC Loss in High Temperature Superconducting Coils Doctor of Philosophy*, (2016).

[149] G. Uimin, *Order and Disorder in the Ensemble of Cu-O Chain Fragments in Oxygen-Deficient Planes of YBa2Cu3O6+x*, Phys. Rev. B **50**, 9531 (1994).

[150] J. M. Tranquada et al., *Neutron-Diffraction Determination of Antiferromagnetic Structure of Cu Ions in YBa2Cu3O6+x with X=0.0 and 0.15*, Phys. Rev. Lett. **60**, 156 (1988).

[151] M. Magnuson, T. Schmitt, V. N. Strocov, J. Schlappa, A. S. Kalabukhov, and L. C. Duda, *Self-Doping Processes between Planes and Chains in the Metal-to-Superconductor Transition of YBa2Cu3O6.9*, Sci.

Rep. **4**, (2014).

[152] N. M. Strickland, A. Semwal, G. V. M. Williams, D. T. Verebelyi, and W. Zhang, *Optimizing the Doping State of YBCO Coated Conductors*, in *Superconductor Science and Technology*, Vol. 17 (2004).

[153] A. Palau et al., *Electrochemical Tuning of Metal Insulator Transition and Nonvolatile Resistive Switching in Superconducting Films*, ACS Appl. Mater. Interfaces **10**, 30522 (2018).

[154] V. Rouco et al., *Quasiparticle Tunnel Electroresistance in Superconducting Junctions*, Nat. Commun. **11**, 658 (2020).

[155] S. Marinković et al., *Direct Visualization of Current-Stimulated Oxygen Migration in YBa2Cu3O7-ΔThin Films*, ACS Nano **14**, 11765 (2020).

[156] X. D. A. Baumans, A. Fernández-Rodríguez, N. Mestres, S. Collienne, J. Van de Vondel, A. Palau, and A. V. Silhanek, *Electromigration in the Dissipative State of High-Temperature Superconducting Bridges*, Appl. Phys. Lett. **114**, 012601 (2019).

[157] E. Trabaldo, A. Kalaboukhov, R. Arpaia, E. Wahlberg, F. Lombardi, and T. Bauch, *Mapping the Phase Diagram of a YBa2Cu3 O7-δ Nanowire Through Electromigration*, Phys. Rev. Appl. **17**, 024021 (2022).

[158] J. Lesueur, P. Nedellec, H. Bernas, J. P. Burger, and L. Dumoulin, *Depairing-like Variation of Tc in YBa2Cu3O7-δ*, Phys. C Supercond. Its Appl. **167**, 1 (1990).

[159] J. A. N. Bruin, H. Sakai, R. S. Perry, and A. P. Mackenzie, *Similarity of Scattering Rates in Metals Showing T-Linear Resistivity*, Science (80-.). **339**, 804 (2013).

[160] T. Timusk and B. Statt, *The Pseudogap in High-Temperature Superconductors: An Experimental Survey*, Reports Prog. Phys. **62**, 61 (1999).

[161] M. Franz, *Superconductivity: Importance of Fluctuations*, Nature Physics.

[162] V. J. Emery and S. A. Kivelson, *Importance of Phase Fluctuations in Superconductors with Small Superfluid Density*, Nature **374**, 434 (1995).

[163] P. Armitage, *Theory of Correlated Superconductors : S - vs . d - Wave Acknowledgments*, (2011).

[164] N. E. Bickers, D. J. Scalapino, and R. T. Scalettar, *Cdw and Sdw Mediated Pairing Interactions*, Int. J. Mod. Phys. B **01**, 687 (1987).

[165] M. Inui, S. Doniach, P. J. Hirschfeld, and A. E. Ruckenstein, *Coexistence of Antiferromagnetism and Superconductivity in a Mean-Field Theory of High-Tc Superconductors*, Phys. Rev. B **37**, 2320 (1988).

[166] C. Gros, D. Poilblanc, T. M. Rice, and F. C. Zhang, *Superconductivity in Correlated Wavefunctions*, Phys. C Supercond. Its Appl. **153**–**155**, 543 (1988).

[167] Z. X. Shen et al., *Anomalously Large Gap Anisotropy in the A-b Plane of Bi2Sr2CaCu2O8+*, Phys. Rev. Lett. **70**, 1553 (1993).

[168] W. N. Hardy, D. A. Bonn, D. C. Morgan, R. Liang, and K. Zhang, *Precision Measurements of the Temperature Dependence of in YBa2Cu3O6.95: Strong Evidence for Nodes in the Gap Function*, Phys. Rev. Lett. **70**, 3999 (1993).

[169] F. Lombardi, F. Tafuri, F. Ricci, F. M. Granozio, A. Barone, G. Testa, E. Sarnelli, J. R. Kirtley, and C. C. Tsuei, *Intrinsic [Formula Presented]-Wave Effects in [Formula Presented] Grain Boundary Josephson Junctions*, Phys. Rev. Lett. **89**, (2002).

[170] S. Maekawa, Y. Isawa, and H. Ebisawa, *Effects of Magnetic and Non-Magnetic Impurities on Anisotropic Singlet Superconductors*, Jpn. J. Appl. Phys. **26**, L771 (1987).

[171] J. M. D. Coey, *Magnetism and Magnetic Materials*, Vol. 9780521816 (2010).

[172] D. R. Inglis, *The Heisenberg Theory of Ferromagnetism [6]*, Phys. Rev. **42**, 442 (1932).

[173] L. Néel, *Propriétés Magnétiques de l'état Métallique et Énergie d'interaction Entre Atomes Magnétiques*, Ann. Phys. (Paris). **11**, 232 (1936).

[174] J. S. Smart, *The Néel Theory of Ferrimagnetism*, Am. J. Phys. **23**, 356 (1955).

[175] S. Seki and M. Mochizuki, *Observation of Skyrmions in Magnetic Materials*, in (2016), pp. 15–31.

[176] I. Lemesh, F. Büttner, and G. S. D. Beach, *Accurate Model of the Stripe Domain Phase of Perpendicularly Magnetized Multilayers*, Phys. Rev. B **95**, (2017).

[177] T. Jourdan, F. Lançon, and A. Marty, *Pinning of Magnetic Domain Walls to Structural Defects in Thin Layers within a Heisenberg-Type Model*, Phys. Rev. B - Condens. Matter Mater. Phys. **75**, (2007).

[178] *Encyclopedia of Physical Science and Technology*, Choice Rev. Online **39**, 39 (2002).

[179] R. Kubo, *Solid State Physics*, Physics Today.

[180] R. A. De Groot, F. M. Mueller, P. G. V. Engen, and K. H. J. Buschow, *New Class of Materials: Half-Metallic Ferromagnets*, Phys. Rev. Lett. **50**, 2024 (1983).

[181] M. I. Katsnelson, V. Y. Irkhin, L. Chioncel, A. I. Lichtenstein, and R. A. De Groot, *Half-Metallic Ferromagnets: From Band Structure to Many-Body Effects*, Rev. Mod. Phys. **80**, 315 (2008).

[182] L. Vinet and A. Zhedanov, *A "missing" Family of Classical Orthogonal Polynomials*, Vol. 44 (2011).

[183] A. Kakizaki, *Spin-Resolved Photoemission Spectroscopy*, Acta Phys. Pol. A **91**, 649 (1997).

[184] K. Elphick, W. Frost, M. Samiepour, T. Kubota, K. Takanashi, H. Sukegawa, S. Mitani, and A. Hirohata, *Heusler Alloys for Spintronic Devices: Review on Recent Development and Future Perspectives*, Science and Technology of Advanced Materials.

[185] A. P. Ramirez, *Colossal Magnetoresistance*, Journal of Physics Condensed Matter.

[186] Y. Tokura and Y. Tomioka, *Colossal Magnetoresistive Manganites*, J. Magn. Magn. Mater. **200**, 1 (1999).

[187] DISMUKES JP, MARTIN DF, EKSTROM L, WANG CC, and COUTTS MD, *Ferromagnetic Chromium Dioxide for Magnetic Tape*, Ind Eng Chem Prod Res Dev. **10**, 319 (1971).

[188] M. S. Hasan, J. Alom, M. Asaduzzaman, M. B. Ahmed, M. D. Hossain, A. S. M. Saem, J. Masud, J. Thakare, and M. A. Hossain, *Recent Criterion on Stability Enhancement of Perovskite Solar Cells*, Processes.

[189] H. Fujishiro, T. Fukase, and M. Ikebe, *Charge Ordering and Sound Velocity Anomaly in La1-XSrxMnO3 (X ≥ 0.5)*, J. Phys. Soc. Japan **67**, 2582 (1998).

[190] H. Fujishiro, T. Fukase, and M. Ikebe, *Anomalous Lattice Softening at X = 0.19 and 0.82 in La1-XCaxMnO3*, J. Phys. Soc. Japan **70**, 628 (2001).

[191] A. J. Millis, B. I. Shraiman, and R. Mueller, *Dynamic Jahn-Teller Effect and Colossal Magnetoresistance in La1-XSrxMnO3*, Phys. Rev. Lett. **77**, 175 (1996).

[192] P. Orgiani et al., *Multiple Double-Exchange Mechanism by Mn2⊃+ Doping in Manganite Compounds*, Phys. Rev. B - Condens. Matter Mater. Phys. **82**, (2010).

[193] H. Keller, A. Bussmann-Holder, and K. A. Müller, *Jahn-Teller Physics and High-Tc Superconductivity*, Materials Today.

[194] Y. Tokura, *Critical Features of Colossal Magnetoresistive Manganites*, Reports Prog. Phys. **69**, 797 (2006).

[195] M. Bowen et al., *Using Half-Metallic Manganite Interfaces to Reveal Insights into Spintronics*, J. Phys. Condens. Matter **19**, (2007).

[196] M. Bowen, A. Barthélémy, M. Bibes, E. Jacquet, J. P. Contour, A. Fert, F. Ciccacci, L. Duò, and R. Bertacco, *Spin-Polarized Tunneling Spectroscopy in Tunnel Junctions with Half-Metallic Electrodes*, Phys.

Rev. Lett. **95**, (2005).

[197] M. Bowen, J. L. Maurice, A. Barthélémy, P. Prod'homme, E. Jacquet, J. P. Contour, D. Imhoff, and C. Colliex, *Bias-Crafted Magnetic Tunnel Junctions with Bistable Spin-Dependent States*, Appl. Phys. Lett. **89**, (2006).

[198] Y. Song, C. Chai, Q. Fan, W. Zhang, and Y. Yang, *Lateral Magnetic Tunnel Junctions with a Heterointerface-induced Half-metallic Electrode*, J. Phys. Chem. Solids **167**, (2022).

[199] C. Hordequin, J. P. Nozières, and J. Pierre, *Half Metallic NiMnSb-Based Spin-Valve Structures*, J. Magn. Magn. Mater. **183**, 225 (1998).

[200] S. Bhatti, R. Sbiaa, A. Hirohata, H. Ohno, S. Fukami, and S. N. Piramanayagam, *Spintronics Based Random Access Memory: A Review*, Materials Today.

[201] N. Maciel, E. Marques, L. Naviner, Y. Zhou, and H. Cai, *Magnetic Tunnel Junction Applications*, Sensors (Switzerland).

[202] Y. Tanaka and S. Kashiwaya, *Theory of Tunneling Spectroscopy of D-Wave Superconductors*, Phys. Rev. Lett. **74**, 3451 (1995).

[203] S. Kashiwaya and Y. Tanaka, *Theory for Tunneling Spectroscopy of Anisotropic Superconductors*, Phys. Rev. B - Condens. Matter Mater. Phys. **53**, 2667 (1996).

[204] C. Chen, *Scanning Tunneling Spectroscopy Studies of High-Temperature Cuprate Superconductors*, **2006**, 181 (2006).

[205] S. Kashiwaya, M. Koyanagi, M. Matsuda, and K. Kajimura, *Study of Zero-Bias Conductance Peaks in YBCO Films by LT-STM*, Phys. B Phys. Condens. Matter **194**–**196**, 2119 (1994).

[206] S. Sinha and K.-W. Ng, *Magnetic-Field Dependence of the Zero-Bias Conductance Peak Observed in Pb/BSCCO Junctions*, Europhys. Lett. **44**, 648 (1998).

[207] W. Yu, R. Haenel, M. A. Rodriguez, S. R. Lee, F. Zhang, M. Franz, D. I. Pikulin, and W. Pan, *Zero-Bias Conductance Peak in Dirac Semimetal-Superconductor Devices*, Phys. Rev. Res. **2**, (2020).

[208] S. Cho, R. Zhong, J. A. Schneeloch, G. Gu, and N. Mason, *Kondo-like Zero-Bias Conductance Anomaly in a Three-Dimensional Topological Insulator Nanowire*, Sci. Rep. **6**, (2016).

[209] L. Fu and C. L. Kane, *Superconducting Proximity Effect and Majorana Fermions at the Surface of a Topological Insulator*, Phys. Rev. Lett. **100**, (2008).

[210] A. I. Buzdin, *Proximity Effects in Superconductor-Ferromagnet Heterostructures*, Rev. Mod. Phys. **77**, 935 (2005).

[211] J. W. A. Robinson, F. Chiodi, M. Egilmez, G. B. Halász, and M. G. Blamire, *Supercurrent Enhancement in Bloch Domain Walls*, Sci. Rep. **2**, 1 (2012).

[212] P. Fulde and R. A. Ferrell, *Superconductivity in a Strong Spin-Exchange Field*, Phys. Rev. **135**, (1964).

[213] A. I. Larkin and Y. N. Ovchinnikov, *Nonuniform State of Superconductors*, Zh. Eksp. Teor. Fiz. **47**, 1136 (1964).

[214] M. Eschrig and T. Löfwander, *Triplet Supercurrents in Clean and Disordered Half-Metallic Ferromagnets*, Nat. Phys. **4**, 138 (2008).

[215] R. Eason, *Pulsed Laser Deposition of Thin Films: Applications-Led Growth of Functional Materials* (2006).

[216] Andor, *Introduction to Optical Diagnostics for PLD*, https://andor.oxinst.com/learning/view/article/pulsed-laser-deposition.

[217] Horiba Scientific, *The Analytical Companion Tool for Magnetron Sputtering Deposition*, https://www.horiba.com/int/scientific/applications/material-sciences/pages/gdoes-the-analytical-companion-tool-for-magnetron-sputtering-deposition/.

[218] M. Dawber, *Sputtering Techniques for Epitaxial Growth of Complex Oxides*, in *Epitaxial Growth of Complex Metal Oxides* (2015), pp. 31–45.

[219] R. Asmatulu and W. S. Khan, *Characterization of Electrospun Nanofibers*, in *Synthesis and Applications of Electrospun Nanofibers* (2019), pp. 257–281.

[220] Opus, *160AC-NA*, https://www.opustips.com/AFM-Tip-160AC-NA.

[221] Semiconductor Technology, *Dry Etching: Dry Etch Processes*, Semicond. Technol. (n.d.).

[222] Z. Cheng et al., *Experimental Observation of High Intrinsic Thermal Conductivity of AlN*, Phys. Rev. Mater. **4**, (2020).

[223] J. L. Routbort and S. J. Rothman, *Oxygen Diffusion in Cuprate Superconductors*, J. Appl. Phys. **76**, 5615 (1994).

[224] M. T. Yurtcan, O. Simsek, M. Yilmaz, U. C. Hasar, M. Ertugrul, and O. S. Bayram, *Influence of Deposition Pressure (O2) on the YBCO (Y123) Thin Films Prepared by Pulsed Laser Deposition*, J. Supercond. Nov. Magn. **26**, 1873 (2013).

[225] H. Guerlac, *Lavoisier—the Crucial Year* (Cornell University Press, 2019).

[226] R. J. Cava, B. Batlogg, K. M. Rabe, E. A. Rietman, P. K. Gallagher, and L. W. Rupp, *Structural Anomalies at the Disappearance of Superconductivity in Ba2YCu3O7-δ: Evidence for Charge Transfer from Chains to Planes*, Phys. C Supercond. Its Appl. **156**, 523 (1988).

[227] A. M. Perez-Muñoz et al., *In Operando Evidence of Deoxygenation in Ionic Liquid Gating of YBa2Cu3O7-X*, Proc. Natl. Acad. Sci. U. S. A. **114**, 215 (2017).

[228] G. Dubuis, Y. Yacoby, H. Zhou, X. He, A. T. Bollinger, D. Pavuna, R. Pindak, and I. Božović, *Oxygen Displacement in Cuprates under Ionic Liquid Field-Effect Gating*, Sci. Rep. **6**, 32378 (2016).

[229] P. D. Murray et al., *Interfacial-Redox-Induced Tuning of Superconductivity in YBa2Cu3O7-Î´*, ACS Appl. Mater. Interfaces **12**, 4741 (2020).

[230] D. G. Pierce and P. G. Brusius, *Electromigration: A Review*, Microelectronics Reliability.

[231] M. K. Rahman, A. M. M. Musa, B. Neher, K. A. Patwary, M. A. Rahman, and M. S. Islam, *A Review of the Study on the Electromigration and Power Electronics*, J. Electron. Cool. Therm. Control **06**, 19 (2016).

[232] L. Cao, K. J. Ganesh, L. Zhang, O. Aubel, C. Hennesthal, M. Hauschildt, P. J. Ferreira, and P. S. Ho, *Grain Structure Analysis and Effect on Electromigration Reliability in Nanoscale Cu Interconnects*, Appl. Phys. Lett. **102**, (2013).

[233] I. A. Blech and C. Herring, *Stress Generation by Electromigration*, Appl. Phys. Lett. **29**, 131 (1976).

[234] S. Vitta, M. A. Stan, J. D. Warner, and S. A. Alterovitz, *Electromigration Failure in YBa2Cu3O7-x Thin Films*, Appl. Phys. Lett. **58**, 759 (1991).

[235] K. Govinda Rajan, P. Parameswaran, J. Janaki, and T. S. Radhakrishnan, *Electromigration of Oxygen in YBa2Cu3O7-Δ*, J. Phys. D. Appl. Phys. **23**, 694 (1990).

[236] E. Trabaldo, A. Garibaldi, F. Lombardi, and T. Bauch, *Electromigration Tuning of the Voltage Modulation Depth in YBa2Cu3O7-Δnanowire-Based SQUIDs*, Supercond. Sci. Technol. **34**, 104001 (2021).

[237] B. H. Moeckly, R. A. Buhrman, and P. E. Sulewski, *Micro-Raman Spectroscopy of Electromigration-Induced Oxygen Vacancy Aggregation in YBa2Cu3O7-δ*, Appl. Phys. Lett. **64**, 1427 (1994).

[238] B. H. Moeckly, D. K. Lathrop, and R. A. Buhrman, *Electromigration Study of Oxygen Disorder and Grain-Boundary Effects in YBa2Cu3O7- Thin Films*, Phys. Rev. B **47**, 400 (1993).

[239] H. Strauven, J. P. Locquet, O. B. Verbeke, and Y. Bruynseraede, *Oxygen Evolution from YBa2Cu3O6.85 High Tc Superconductors*, Solid State Commun. **65**, 293 (1988).

[240] Y. Bruynseraede, J. P. Locquet, I. K. Schuller, and C. Van Haesendonck, *Oxygen Disorder Effects in High T>c Superconductors*, Phys. Scr. **1989**, 100 (1989).

[241] A. C. Basaran, J. E. Villegas, J. S. Jiang, A. Hoffmann, and I. K. Schuller, *Mesoscopic Magnetism and Superconductivity*, MRS Bulletin.

[242] X. Leng, J. Garcia-Barriocanal, S. Bose, Y. Lee, and A. M. Goldman, *Electrostatic Control of the Evolution from a Superconducting Phase to an Insulating Phase in Ultrathin YBa2Cu3O7-x Films*, Phys. Rev. Lett. **107**, 6 (2011).

[243] S. Marinković, E. Trabaldo, S. Collienne, F. Lombardi, T. Bauch, and A. V. Silhanek, *Oxygen Ordering in Untwinned YBa2Cu3 O7-δ Films Driven by Electrothermal Stress*, Phys. Rev. B **107**, 14208 (2023).

[244] W. B. J. Zimmerman, *Introduction To Comsol Multiphysics*, Multiphysics Model. with Finite Elem. Methods 1 (2006).

[245] E. A. Tholén, A. Ergül, E. M. Doherty, F. M. Weber, F. Grégis, and D. B. Haviland, *Nonlinearities and Parametric Amplification in Superconducting Coplanar Waveguide Resonators*, Appl. Phys. Lett. **90**, (2007).

[246] R. G. Seed, C. Vittoria, and A. Widom, *Heterodyne Microwave Mixing in a Superconducting YBa2Cu 3O7-x Coplanar Waveguide Circuit Containing a Single Engineered Grain Boundary Junction*, J. Appl. Phys. **76**, 6962 (1994).

[247] M. Mirhosseini, E. Kim, V. S. Ferreira, M. Kalaee, A. Sipahigil, A. J. Keller, and O. Painter, *Superconducting Metamaterials for Waveguide Quantum Electrodynamics*, Nat. Commun. **9**, (2018).

[248] V. Humbert et al., *An Oxygen Vacancy Memristor Ruled by Electron Correlations*, Adv. Sci. **9**, 1 (2022).

[249] D. Marković, A. Mizrahi, D. Querlioz, and J. Grollier, *Physics for Neuromorphic Computing*, Nat. Rev. Phys. **2**, 499 (2020).

[250] R. Arpaia, E. Andersson, E. Trabaldo, T. Bauch, and F. Lombardi, *Probing the Phase Diagram of Cuprates with YBa2Cu3 O7-δ Thin Films and Nanowires*, Phys. Rev. Mater. **2**, (2018).

[251] O. Cyr-Choinière et al., *Pseudogap Temperature T∗ of Cuprate Superconductors from the Nernst Effect*, Phys. Rev. B **97**, (2018).

[252] C. Gao, T. Li, T. Wang, and X. Cao, *Memristor-Based Logic Gate Circuit*, 2020 IEEE 3rd Int. Conf. Comput. Commun. Eng. Technol. CCET 2020 330 (2020).

[253] J. J. Yang, D. B. Strukov, and D. R. Stewart, *Memristive Devices for Computing*, Nature Nanotechnology.

[254] A. A. Faisal, L. P. J. Selen, and D. M. Wolpert, *Noise in the Nervous System*, Nature Reviews Neuroscience.

[255] N. Locatelli, A. F. Vincent, and D. Querlioz, *Use of Magnetoresistive Random-Access Memory as Approximate Memory for Training Neural Networks*, in *2018 25th IEEE International Conference on Electronics Circuits and Systems, ICECS 2018* (2019), pp. 553–556.

[256] Z. Wang et al., *Fully Memristive Neural Networks for Pattern Classification with Unsupervised Learning*, Nat. Electron. **1**, 137 (2018).

[257] E. Dagotto, *Brief Introduction to Giant Magnetoresistance (GMR)*, in (2003), pp. 395–405.

[258] P. Drude, *Zur Elektronentheorie Der Metalle*, Ann. Phys. **306**, 566 (1900).

[259] J. H. Davies, *Scattering Rates: The Golden Rule*, in *The Physics of Low-Dimensional Semiconductors*, edited by J. H. Davies (Cambridge University Press, Cambridge, 2012), pp. 290–328.

[260] J. a Berezovsky, Optical Control and Detection of Spin Coherence in Semiconductor Nanostructures, 2007.

[261] Z. Yang, D. Han, S. Mao, H. Wang, G. Al-Jumaily, P. J. Ryan, P. A. Crozier, S. C. Y. Tsen, M. McCartney,

and M. Scheinfein, *A Study on Pinned Layer Magnetization Processes in Different Antiferromagnetic Coupling Systems of Spin-Valves*, J. Appl. Phys. **87**, 5729 (2000).

[262] J. Nogués and I. K. Schuller, *Exchange Bias*, J. Magn. Magn. Mater. **192**, 203 (1999).

[263] N. M. Nemes, C. Visani, Z. Sefrioui, C. Leon, J. Santamaría, M. Iglesias, F. Mompean, and M. García-Hernández, *Exchange-Bias-Modulated Inverse Superconducting Spin Switch in CoO/Co/ YBa2 Cu3 O7-δ / La0.7 Ca 0.3 MnO3 Thin Film Hybrids*, Phys. Rev. B - Condens. Matter Mater. Phys. **81**, (2010).

[264] M. L. Kulić and M. Endres, *Ferromagnetic-Semiconductor-Singlet-(or Triplet) Superconductor-Ferromagnetic-Semiconductor Systems as Possible Logic Circuits and Switches*, Phys. Rev. B - Condens. Matter Mater. Phys. **62**, 11846 (2000).

[265] J. Y. Gu, C. Y. You, J. S. Jiang, J. Pearson, Y. B. Bazaliy, and S. D. Bader, *Magnetization-Orientation Dependence of the Superconducting Transition Temperature in the Ferromagnet-Superconductor-Ferromagnet System: [Formula Presented]*, Phys. Rev. Lett. **89**, 1 (2002).

[266] A. Potenza and C. H. Marrows, *Superconductor-Ferromagnet CuNi/Nb/CuNi Trilayers as Superconducting Spin-Valve Core Structures*, Phys. Rev. B - Condens. Matter Mater. Phys. **71**, (2005).

[267] I. C. Moraru, W. P. Pratt, and N. O. Birge, *Magnetization-Dependent Tc Shift in Ferromagnet/Superconductor/Ferromagnet Trilayers with a Strong Ferromagnet*, Phys. Rev. Lett. **96**, 1 (2006).

[268] I. C. Moraru, W. P. Pratt, and N. O. Birge, *Observation of Standard Spin-Switch Effects in Ferromagnet/Superconductor/ Ferromagnet Trilayers with a Strong Ferromagnet*, Phys. Rev. B - Condens. Matter Mater. Phys. **74**, (2006).

[269] G. X. Miao, A. V. Ramos, and J. S. Moodera, *Infinite Magnetoresistance from the Spin Dependent Proximity Effect in Symmetry Driven Bcc-Fe/V/Fe Heteroepitaxial Superconducting Spin Valves*, Phys. Rev. Lett. **101**, (2008).

[270] J. Zhu, X. Cheng, C. Boone, and I. N. Krivorotov, *Origin of the Inverse Spin Switch Effect in Superconducting Spin Valves*, Phys. Rev. Lett. **103**, (2009).

[271] P. V. Leksin, N. N. Garif'Yanov, I. A. Garifullin, J. Schumann, H. Vinzelberg, V. Kataev, R. Klingeler, O. G. Schmidt, and B. Büchner, *Full Spin Switch Effect for the Superconducting Current in a Superconductor/Ferromagnet Thin Film Heterostructure*, Appl. Phys. Lett. **97**, (2010).

[272] J. Zhu, I. N. Krivorotov, K. Halterman, and O. T. Valls, *Angular Dependence of the Superconducting Transition Temperature in Ferromagnet-Superconductor-Ferromagnet Trilayers*, Phys. Rev. Lett. **105**, (2010).

[273] P. V. Leksin, N. N. Garif'Yanov, A. A. Kamashev, Y. V. Fominov, J. Schumann, C. Hess, V. Kataev, B. Büchner, and I. A. Garifullin, *Superconducting Spin-Valve Effect and Triplet Superconductivity in Co Ox/Fe1/Cu/Fe2/Cu/Pb Multilayer*, Phys. Rev. B - Condens. Matter Mater. Phys. **91**, (2015).

[274] A. A. Jara, E. Moen, O. T. Valls, and I. N. Krivorotov, *Bias Current Dependence of Superconducting Transition Temperature in Superconducting Spin-Valve Nanowires*, Phys. Rev. B **100**, (2019).

[275] Y. Gu, G. Halász, J. W. A. Robinson, and M. G. Blamire, *Large Superconducting Spin Valve Effect and Ultrasmall Exchange Splitting in Epitaxial Rare-Earth-Niobium Trilayers*, Phys. Rev. Lett. **115**, (2015).

[276] B. Li, N. Roschewsky, B. A. Assaf, M. Eich, M. Epstein-Martin, D. Heiman, M. Münzenberg, and J. S. Moodera, *Superconducting Spin Switch with Infinite Magnetoresistance Induced by an Internal Exchange Field*, Phys. Rev. Lett. **110**, 1 (2013).

[277] Y. Zhu, A. Pal, M. G. Blamire, and Z. H. Barber, *Superconducting Exchange Coupling between Ferromagnets*, Nat. Mater. **16**, 195 (2017).

[278] A. Di Bernardo, S. Komori, G. Livanas, G. Divitini, P. Gentile, M. Cuoco, and J. W. A. Robinson, *Nodal Superconducting Exchange Coupling*, Nat. Mater. **18**, 1194 (2019).

[279] S. Komori, A. Di Bernardo, A. I. Buzdin, M. G. Blamire, and J. W. A. Robinson, *Magnetic Exchange Fields and Domain Wall Superconductivity at an All-Oxide Superconductor-Ferromagnet Insulator Interface*, Phys. Rev. Lett. **121**, 77003 (2018).

[280] M. Van Zalk, M. Veldhorst, A. Brinkman, J. Aarts, and H. Hilgenkamp, *Magnetization-Induced Resistance-Switching Effects in La0.67 Sr0.33 MnO3 / YBa2 Cu3 O7-δ Bi- and Trilayers*, Phys. Rev. B - Condens. Matter Mater. Phys. **79**, 1 (2009).

[281] V. Peña, Z. Sefrioui, D. Arias, C. Leon, J. Santamaria, J. L. Martinez, S. G. E. Te Velthuis, and A. Hoffmann, *Giant Magnetoresistance in Ferromagnet/Superconductor Superlattices*, Phys. Rev. Lett. **94**, 3 (2005).

[282] N. M. Nemes et al., *Origin of the Inverse Spin-Switch Behavior in Manganite/Cuprate/Manganite Trilayers*, Phys. Rev. B - Condens. Matter Mater. Phys. **78**, 3 (2008).

[283] R. Steiner and P. Ziemann, *Magnetic Switching of the Superconducting Transition Temperature in Layered Ferromagnetic/Superconducting Hybrids: Spin Switch versus Stray Field Effects*, Phys. Rev. B - Condens. Matter Mater. Phys. **74**, (2006).

[284] T. Hu, H. Xiao, C. Visani, J. Santamaria, and C. C. Almasan, *Stray Field and the Superconducting Surface Spin Valve Effect in La0.7Ca0.3MnO3/YBa2Cu3O7?Bilayers*, New J. Phys. **13**, (2011).

[285] D. Stamopoulos, N. Moutis, M. Pissas, and D. Niarchos, *Effective Ferromagnetic Coupling between a Superconductor and a Ferromagnet in LaCaMnO/Nb Hybrids*, Phys. Rev. B - Condens. Matter Mater. Phys. **72**, (2005).

[286] C. Bell, S. Turşucu, and J. Aarts, *Flux-Flow-Induced Giant Magnetoresistance in All-Amorphous Superconductor-Ferromagnet Hybrids*, Phys. Rev. B - Condens. Matter Mater. Phys. **74**, (2006).

[287] V. Rouco et al., *Competition between Superconductor-Ferromagnetic Stray Magnetic Fields in YBa2Cu3O7-x Films Pierced with Co Nano-Rods /639/301/119/1003 /639/301/357/997 /639/925/357/997 /639/766/119/1003 /120 /123 /142/126 /119 /128 /140/146 Article*, Sci. Rep. **7**, (2017).

[288] G. Carapella, F. Russo, and G. Costabile, *Low-Field Transport Measurements in Superconducting Co/Nb/Co Trilayers*, Phys. Rev. B - Condens. Matter Mater. Phys. **78**, (2008).

[289] T. J. Hwang and D. H. Kim, *Influence of Stray Fields and the Proximity Effect in Ferromagnet/Superconductor/Ferromagnet Spin Valves*, J. Korean Phys. Soc. **61**, 1628 (2012).

[290] B. Stoddart-Stones, X. Montiel, M. G. Blamire, and J. W. A. Robinson, *Competition between the Superconducting Spin-Valve Effect and Quasiparticle Spin-Decay in Superconducting Spin-Valves*, Commun. Phys. **5**, 224 (2022).

[291] I. Asulin, O. Yuli, G. Koren, and O. Millo, *Evidence for Crossed Andreev Reflections in Bilayers of (100) YBa2 Cu3 O7-δ and the Itinerant Ferromagnet SrRuO3*, Phys. Rev. B - Condens. Matter Mater. Phys. **74**, (2006).

[292] J. L. Webb, B. J. Hickey, and G. Burnell, *Numerical Model of Crossed Andreev Reflection and Charge Imbalance*, Phys. Rev. B - Condens. Matter Mater. Phys. **86**, (2012).

[293] D. Beckmann and H. V. Löhneysen, *Negative Four-Terminal Resistance as a Probe of Crossed Andreev Reflection*, Appl. Phys. A Mater. Sci. Process. **89**, 603 (2007).

[294] D. Beckmann, E. B. Weber, and H. V. Löhneysen, *Evidence for Crossed Andreev Reflection in Superconductor-Ferromagnet Hybrid Structures*, Phys. Rev. Lett. **93**, (2004).

[295] G. Deutscher and D. Feinberg, *Coupling Superconducting-Ferromagnetic Point Contacts by Andreev Reflections*, Appl. Phys. Lett. **76**, 487 (2000).

[296] A. Kleine, A. Baumgartner, J. Trbovic, and C. Schönenberger, *Contact Resistance Dependence of Crossed Andreev Reflection*, Europhys. Lett. **87**, (2009).

[297] W. J. Herrera, A. L. Yeyati, and A. Martín-Rodero, *Long-Range Crossed Andreev Reflections in High-*

Temperature Superconductors, Phys. Rev. B - Condens. Matter Mater. Phys. **79**, (2009).

[298] V. Peña, Z. Sefrioui, D. Arias, C. Leon, J. Santamaria, M. Varela, S. J. Pennycook, and J. L. Martinez, *Coupling of Superconductors through a Half-Metallic Ferromagnet: Evidence for a Long-Range Proximity Effect*, Phys. Rev. B - Condens. Matter Mater. Phys. **69**, (2004).

[299] S. F. Lee et al., *Current-Perpendicular and Current-Parallel Giant Magnetoresistances in Co/Ag Multilayers*, Phys. Rev. B **52**, 15426 (1995).

[300] W. P. Pratt, S. F. Lee, J. M. Slaughter, R. Loloee, P. A. Schroeder, and J. Bass, *Perpendicular Giant Magnetoresistances of Ag/Co Multilayers*, Phys. Rev. Lett. **66**, 3060 (1991).

[301] J. Y. Gu, J. A. Caballero, R. D. Slater, R. Loloee, and W. P. Pratt, *Direct Measurement of Quasiparticle Evanescent Waves in a Dirty Superconductor*, Phys. Rev. B - Condens. Matter Mater. Phys. **66**, 1 (2002).

[302] Y. V. Fominov, A. A. Golubov, T. Y. Karminskaya, M. Y. Kupriyanov, R. G. Deminov, and L. R. Tagirov, *Superconducting Triplet Spin Valve*, JETP Lett. **91**, 308 (2010).

[303] Z. Devizorova and S. Mironov, *Crossover between Standard and Inverse Spin-Valve Effect in Atomically Thin Superconductor/Half-Metal Structures*, Phys. Rev. B **100**, (2019).

[304] I. A. Garifullin, *Superconducting Spin-Valve and Triplet Superconductivity*, JETP Lett. **106**, 57 (2017).

[305] R. R. Gaifullin, V. N. Kushnir, R. G. Deminov, L. R. Tagirov, M. Y. Kupriyanov, and A. A. Golubov, *Proximity Effect in a Superconducting Triplet Spin Valve S1/F1/S2/F2*, Phys. Solid State **61**, 1535 (2019).

[306] S. Mironov and A. Buzdin, *Triplet Proximity Effect in Superconducting Heterostructures with a Half-Metallic Layer*, Phys. Rev. B - Condens. Matter Mater. Phys. **92**, (2015).

[307] K. Halterman and M. Alidoust, *Half-Metallic Superconducting Triplet Spin Valve*, Phys. Rev. B **94**, (2016).

[308] G. A. Ovsyannikov, K. Y. Constantinian, V. V. Demidov, and Y. N. Khaydukov, *Magnetic Proximity Effect and Superconducting Triplet Correlations at the Cuprate Superconductor and Oxide Spin Valve Interface*, Low Temp. Phys. **42**, 873 (2016).

[309] V. I. Zdravkov et al., *Experimental Observation of the Triplet Spin-Valve Effect in a Superconductor-Ferromagnet Heterostructure*, Phys. Rev. B - Condens. Matter Mater. Phys. **87**, (2013).

[310] C. Visani, Z. Sefrioui, J. Tornos, C. Leon, J. Briatico, M. Bibes, A. Barthélémy, J. Santamaría, and J. E. Villegas, *Equal-Spin Andreev Reflection and Long-Range Coherent Transport in High-Temperature Superconductor/Half-Metallic Ferromagnet Junctions*, Nat. Phys. **8**, 539 (2012).

[311] M. Eschrig, J. Kopu, J. C. Cuevas, and G. Schön, *Theory of Half-Metal/Superconductor Heterostructures*, Phys. Rev. Lett. **90**, 4 (2003).

[312] V. N. Krivoruchko, *Local Spin-Triplet Superconductivity in Half-Metallic Manganites: A Perspective Platform for High-Temperature Topological Superconductivity*, Low Temp. Phys. **47**, 901 (2021).

[313] A. A. Kamashev and I. A. Garifullin, *Proximity Effect in Heterostructures Based on a Superconductor/Half-Metal System*, JETP Lett. **113**, 194 (2021).

[314] F. A. Cuellar, D. Hernandez-Martin, J. Tornos, F. Gallego, G. Orfila, A. Rivera-Calzada, Z. Sefrioui, C. Leon, and J. Santamaria, *Interface Magnetism in La0.7Ca0.3MnO3/PrBa2Cu3O7 Epitaxial Heterostructures*, Phys. Status Solidi Appl. Mater. Sci. **215**, (2018).

[315] A. Kreisler, J.-C. Villegier, and A. Dégardin, *PrBaCuO/YBaCuO/PrBaCuO Ultrathin Film Constrictions : Nanostructuration and Superconducting Properties for Hot Electron Bolometer Applications at Terahertz Frequencies*, (2011).

[316] N. Didier, C. Dubourdieu, A. Rosova, B. Chenevier, V. Galindo, and O. Thomas, *Twinning Behaviour in YBCO and PBCO Thin Films and in PBCO-YBCO Superlattices*, J. Alloys Compd. **251**, 322 (1997).

[317] H. Sharma, A. Tulapurkar, and C. V. Tomy, *Electric Field Controlled Magnetization and Transport Properties of La0.7Ca0.3MnO3 Ultrathin Film*, Mater. Chem. Phys. **186**, 523 (2017).

[318] H. O. Wang, P. Zhao, J. J. Sun, W. S. Tan, K. P. Su, S. Huang, and D. X. Huo, *Investigation of Magnetic Response of Charge Ordering in Half-Doped La0.5Ca0.5MnO3 Manganite*, J. Mater. Sci. Mater. Electron. **29**, 13176 (2018).

[319] A. C. Basaran, C. Monton, J. Trastoy, R. Bernard, K. Bouzehouane, J. E. Villegas, and I. K. Schuller, *Emergence of Exchange Bias and Giant Coercive Field Enhancement by Internal Magnetic Frustration in La0.67Sr0.33MnO3 Thin Films*, J. Magn. Magn. Mater. **550**, (2022).

[320] S. Ju and Z. Y. Li, *Study of the Temperature Dependence of Giant Magnetoresistance in Metallic Granular Composite*, J. Magn. Magn. Mater. **250**, 295 (2002).

[321] J. W. Yoo, C. Y. Chen, H. W. Jang, C. W. Bark, V. N. Prigodin, C. B. Eom, and A. J. Epstein, *Spin Injection/Detection Using an Organic-Based Magnetic Semiconductor*, Nat. Mater. **9**, 638 (2010).

[322] T. Hagler, R. Kinder, and G. Bayreuther, *Temperature Dependence of Tunnel Magnetoresistance*, J. Appl. Phys. **89**, 7570 (2001).

[323] C. Enderlein, J. F. de Oliveira, D. A. Tompsett, E. B. Saitovitch, S. S. Saxena, G. G. Lonzarich, and S. E. Rowley, *Superconductivity Mediated by Polar Modes in Ferroelectric Metals*, Nat. Commun. **11**, (2020).

[324] M. Azadi and G. Lopez, *Spin Curves for MicroChem S1800 (1805, 1813,1818) Series Positive Resist*, in Vol. 1800 (2016).

[325] I. Benguettat-EL Mokhtari, Y. Roussigné, T. Petrisor, F. Zighem, F. Kail, L. Chahed, V. Pierron, L. Méchin, M. Gabor, and M. Belmeguenai, *Spin Pumping and Magnetic Anisotropy in La2/3Sr1/3MnO3/Pt Systems*, Phys. Status Solidi Basic Res. **257**, (2020).

[326] N. M. Nemes et al., *Thickness Dependent Magnetic Anisotropy of Ultrathin LCMO Epitaxial Thin Films*, IEEE Trans. Magn. **44**, 2926 (2008).

[327] M. R. Koblischka, T. H. Johansen, and M. Murakami, *Field-Cooled Magnetization Measurements of Nd-123 Bulk Superconductors*, Supercond. Sci. Technol. **13**, 745 (2000).

[328] P. Przyslupski, A. Tsarou, P. Dluzewski, W. Paszkowicz, R. Minikayev, K. Dybko, M. Sawicki, B. Dabrowski, and C. Kimaball, *Interplay of Superconductivity and Ferromagnetism in YBa2Cu 3O7/ La1-XSrxMnO3 Heterostructures*, Supercond. Sci. Technol. **19**, S38 (2006).

[329] P. Przyslupski, *Magnetism and Superconductivity in Oxide Ferromagnet/Superconductor Heterostructures*, Phys. Status Solidi C Conf. **2**, 1625 (2005).

[330] N. Kambhala and S. Angappane, *Anisotropic Magnetotransport Properties of La0.67Sr0.33MnO3 Thin Film*, in *Physics Procedia*, Vol. 54 (2014), pp. 164–167.

[331] D. Fadil et al., *Direct Observation of Magnetization Reversal and Low Field Magnetoresistance of Epitaxial La 0.7Sr 0.3MnO 3/SrTiO 3 (001) Thin Films at Room Temperature*, J. Appl. Phys. **112**, (2012).

[332] M. Ziese and S. P. Sena, *Anisotropic Magnetoresistance of Thin La0.7Ca0.3MnO3 Films*, J. Phys. Condens. Matter **10**, 2727 (1998).

[333] M. Egilmez, K. H. Chow, and J. A. Jung, *Anisotropic Magnetoresistance in Perovskite Manganites*, Modern Physics Letters B.

[334] M. Trushin, K. Výborný, P. Moraczewski, A. A. Kovalev, J. Schliemann, and T. Jungwirth, *Anisotropic Magnetoresistance of Spin-Orbit Coupled Carriers Scattered from Polarized Magnetic Impurities*, Phys. Rev. B - Condens. Matter Mater. Phys. **80**, (2009).

[335] S. M. Kumawat et al., *Magnetic Field Enhancement in Critical Current and Possible Triplet Superconductivity in LSMO/YBCO/LSMO Heterostructures*, J. Phys. Chem. C **127**, 6861 (2022).

[336] K. Dybko, K. Werner-Malento, P. Aleshkevych, M. Wojcik, M. Sawicki, and P. Przyslupski, *Possible Spin-Triplet Superconducting Phase in the La0.7 Sr0.3 MnO3 / YBa2 Cu3 O7 / La0.7 Sr0.3 MnO3 Trilayer*, Phys. Rev. B - Condens. Matter Mater. Phys. **80**, (2009).

[337] Y. Kalcheim, T. Kirzhner, G. Koren, and O. Millo, *Long-Range Proximity Effect in La2/3Ca1/3MnO 3/(100)YBa2Cu3O7-δ Ferromagnet/Superconductor Bilayers: Evidence for Induced Triplet Superconductivity in the Ferromagnet*, Phys. Rev. B - Condens. Matter Mater. Phys. **83**, (2011).

[338] G. Blatter, M. V. Feigel'man, V. B. Geshkenbein, A. I. Larkin, and V. M. Vinokur, *Vortices in High Temperature Superconductors: The Statistical Mechanics and Dynamics of Strings*, Phys. A Stat. Mech. Its Appl. **200**, 341 (1993).

[339] S. J. Chapman and D. R. Heron, *The Motion of Superconducting Vortices in Thin Films of Varying Thickness*, SIAM J. Appl. Math. **58**, 1808 (1998).

[340] J. E. Villegas, Z. Sefrioui, M. Varela, E. M. Gonzalez, J. Santamaria, and J. L. Vicent, *Interface Barriers for Flux Motion in High-Temperature Superconducting Superlattices*, Phys. Rev. B - Condens. Matter Mater. Phys. **69**, (2004).

[341] A. Gupta, G. Singh, D. Kumar, H. Kishan, and R. C. Budhani, *Giant Coercivity Enhancement and Dimensional Crossover of Superconductivity in Co2FeSi-NbN Nanoscale Bilayers*, Appl. Phys. Lett. **103**, (2013).

[342] V. O. Yagovtsev, N. G. Pugach, and M. Eschrig, *The Inverse Proximity Effect in Strong Ferromagnet–Superconductor Structures*, Supercond. Sci. Technol. **34**, (2021).

[343] D. B. Jan, J. Y. Coulter, M. E. Hawley, L. N. Bulaevskii, M. P. Maley, Q. X. Jia, B. B. Maranville, F. Hellman, and X. Q. Pan, *Flux Pinning Enhancement in Ferromagnetic and Superconducting Thin-Film Multilayers*, Appl. Phys. Lett. **82**, 778 (2003).

[344] M. Z. Cieplak, Z. Adamus, M. Kończykowski, L. Y. Zhu, X. M. Cheng, and C. L. Chien, *Tuning Vortex Confinement by Magnetic Domains in a Superconductor/ Ferromagnet Bilayer*, Phys. Rev. B - Condens. Matter Mater. Phys. **87**, (2013).

[345] J. Fritzsche, R. B. G. Kramer, and V. V. Moshchalkov, *Visualization of the Vortex-Mediated Pinning of Ferromagnetic Domains in Superconductor-Ferromagnet Hybrids*, Phys. Rev. B - Condens. Matter Mater. Phys. **79**, (2009).

[346] J. G. Caputo, L. Gozzelino, F. Laviano, G. Ghigo, R. Gerbaldo, J. Noudem, Y. Thimont, and P. Bernstein, *Screening Magnetic Fields by Superconductors: A Simple Model*, J. Appl. Phys. **114**, (2013).

[347] D. S. Holmes, A. L. Ripple, and M. A. Manheimer, *Energy-Efficient Superconducting Computing—Power Budgets and Requirements*, IEEE Trans. Appl. Supercond. **23**, 1701610 (2013).

[348] A. L. Robinson, *Superconducting Electronics: Toward an Ultrafast Computer*, Science (80-.). **201**, 602 (1978).

[349] I. I. Soloviev, N. V. Klenov, S. V. Bakurskiy, V. V. Bol'ginov, V. V. Ryazanov, M. Y. Kupriyanov, and A. A. Golubov, *Josephson Magnetic Rotary Valve*, Appl. Phys. Lett. **105**, (2014).

[350] S. V. Bakurskiy, N. V. Klenov, I. I. Soloviev, M. Y. Kupriyanov, and A. A. Golubov, *Superconducting Phase Domains for Memory Applications*, Appl. Phys. Lett. **108**, (2016).

[351] S. E. Shafraniuk, I. P. Nevirkovets, and O. A. Mukhanov, *Modeling Computer Memory Based on Ferromagnetic/Superconductor Multilayers*, Phys. Rev. Appl. **11**, (2019).

[352] A. Neilo, S. Bakurskiy, N. Klenov, I. Soloviev, and M. Kupriyanov, *Superconducting Valve Exploiting Interplay between Spin-Orbit and Exchange Interactions*, Nanomaterials **12**, (2022).

[353] E. Ilin, X. Song, I. Burkova, A. Silge, Z. Guo, K. Ilin, and A. Bezryadin, *Supercurrent-Controlled Kinetic Inductance Superconducting Memory Element*, Appl. Phys. Lett. **118**, (2021).

[354] N. Klenov, Y. Khaydukov, S. Bakurskiy, R. Morari, I. Soloviev, V. Boian, T. Keller, M. Kupriyanov, A. Sidorenko, and B. Keimer, *Periodic Co/Nb Pseudo Spin Valve for Cryogenic Memory*, Beilstein Journal of Nanotechnology.

[355] N. G. Pugach, D. M. Heim, D. V. Seleznev, A. I. Chernov, and D. Menzel, *Switchable Spiral Josephson*

Junction: A Superconducting Spin-Valve Proposal, Supercond. Sci. Technol. **35**, (2022).

[356] O. O. Shvetsov, Y. S. Barash, A. V. Timonina, N. N. Kolesnikov, and E. V. Deviatov, *Josephson Spin-Valve Realization in the Magnetic Nodal-Line Topological Semimetal Fe3GeTe2*, JETP Lett. **115**, 267 (2022).

[357] E. C. Gingrich, B. M. Niedzielski, J. A. Glick, Y. Wang, D. L. Miller, R. Loloee, W. P. Pratt, and N. O. Birge, *Controllable 0-π Josephson Junctions Containing a Ferromagnetic Spin Valve*, Nat. Phys. **12**, 564 (2016).

[358] B. Baek, W. H. Rippard, S. P. Benz, S. E. Russek, and P. D. Dresselhaus, *Hybrid Superconducting-Magnetic Memory Device Using Competing Order Parameters*, Nat. Commun. **5**, (2014).

[359] T. Yamashita, K. Tanikawa, S. Takahashi, and S. Maekawa, *Superconducting π Qubit with a Ferromagnetic Josephson Junction*, Phys. Rev. Lett. **95**, (2005).

[360] A. Hirohata, K. Yamada, Y. Nakatani, L. Prejbeanu, B. Diény, P. Pirro, and B. Hillebrands, *Review on Spintronics: Principles and Device Applications*, Journal of Magnetism and Magnetic Materials.

[361] M. L. Schneider, C. A. Donnelly, S. E. Russek, B. Baek, M. R. Pufall, P. F. Hopkins, P. D. Dresselhaus, S. P. Benz, and W. H. Rippard, *Ultralow Power Artificial Synapses Using Nanotextured Magnetic Josephson Junctions*, Sci. Adv. **4**, (2018).

[362] M. L. Schneider, C. A. Donnelly, and S. E. Russek, *Tutorial: High-Speed Low-Power Neuromorphic Systems Based on Magnetic Josephson Junctions*, J. Appl. Phys. **124**, (2018).

[363] S. H. Jo, T. Chang, I. Ebong, B. B. Bhadviya, P. Mazumder, and W. Lu, *Nanoscale Memristor Device as Synapse in Neuromorphic Systems*, Nano Lett. **10**, 1297 (2010).

[364] R. Hott, *Materials Aspects of High-Temperature Superconductors for Applications*, (2003).

[365] C. P. Bean, *Magnetization of Hard Superconductors*, Phys. Rev. Lett. **8**, 250 (1962).

[366] Y. B. Kim, C. F. Hempstead, and A. R. Strnad, *Magnetization and Critical Supercurrents*, Phys. Rev. **129**, 528 (1963).

[367] P. W. Anderson, *Theory of Flux Creep in Hard Superconductors*, Phys. Rev. Lett. **9**, 309 (1962).

[368] K. Yamamoto, H. Mazaki, and H. Yasuoka, *Magnetization of Type-II Superconductors in the Kim-Anderson Model*, Phys. Rev. B **47**, 915 (1993).

[369] D. Pajić, K. Zadro, R. Ristić, I. Ivković, Ž. Skoko, and E. Babić, *Thermal Relaxation of Magnetic Clusters in Amorphous Hf57Fe 43 Alloy*, J. Phys. Condens. Matter **19**, (2007).

[370] K. Mbela, T. Moyo, and N. S. E. Osman, *Effect of Annealing on Exchange Bias in Mg0.2FexCr1.8−xO3 Nano Oxides*, J. Mater. Sci. Mater. Electron. **27**, 8916 (2016).